

*The Many Aspects Of Amphiphilic
Complexes*

DISSERTATION

zur Erlangung des akademischen Grades eines
Doktors der Naturwissenschaften (Dr. rer. nat.)
an der Fakultät für Biologie, Chemie und Geowissenschaften
der Universität Bayreuth

vorgelegt von

Johannes Weihermüller

aus *Bamberg*

Bayreuth, 2019

Die vorliegende Arbeit wurde in der Zeit von *Januar 2015* bis *März 2019* in Bayreuth an der Professur Anorganische Chemie IV unter Betreuung von Frau Professorin Dr. *Birgit Weber* angefertigt.

Vollständiger Abdruck der von der Fakultät für Biologie, Chemie und Geowissenschaften der Universität Bayreuth genehmigten Dissertation zur Erlangung des akademischen Grades eines Doktors der Naturwissenschaften (*Dr. rer. nat.*).

Dissertation eingereicht am: 27.03.2019

Zulassung durch die Promotionskommission: 24.04.2019

Wissenschaftliches Kolloquium: 02.08.2019

Amtierender Dekan: Prof. Dr. Stefan Peiffer

Prüfungsausschuss:

Prof. Dr. Birgit Weber	(Gutachterin)
Prof. Dr. Rainer Schobert	(Gutachter)
Prof. Dr. Markus Retsch	(Vorsitz)
Prof. Dr. Seema Agarwal	

*“Life’s not about how hard of a hit you can give...
it’s about how many you can take, and still keep moving forward”*

– Rocky (Sylvester Stallone)

Table of Contents

Abbreviations	V
Acknowledgement.....	IX
1. Summary	1
2. Zusammenfassung	3
3. Introduction	5
3.1 Principles of the spin crossover phenomenon	5
3.2 General concept of liquid crystalline systems.....	8
3.3 SCO in nanostructures and thin films	11
3.4 Multifunctional SCO systems	13
3.4.1 Luminescent and photoswitchable SCO complexes	14
3.4.2 Electrical conductivity in SCO systems	15
3.4.3 Porous SCO polymers and chemical sensing	16
3.4.4 Metallomesogens exhibiting SCO behaviour.....	16
3.5 The Jäger type ligand system	20
3.6 References	23
4. Synopsis	33
5. Individual contributions to joint publications	49
5.1 Kinetic trapping effects in amphiphilic iron(II) spin crossover compounds.....	49
5.2 Amphiphilic iron(II) spin crossover coordination polymers: crystal structures and phase transition properties.....	50
5.3 Behaviour of Cu(II) and Ni(II) Schiff base-like complexes with long, branched alkyl chains in solution and in the solid state: Micelle formation, CISSS, and liquid crystallinity...	51
6. Kinetic trapping effects in amphiphilic iron(II) spin crossover compounds.....	53
6.1 Abstract	53
6.2 Introduction	53

6.3	Experimental section.....	55
6.4	Results.....	57
6.4.1	Synthesis of the complexes	57
6.4.2	Mössbauer measurements	58
6.4.3	X-ray structure analysis	59
6.4.4	Magnetic properties.....	64
6.5	Discussion	69
6.6	Conclusion	70
6.7	Associated content	71
6.8	Supporting Information.....	72
6.9	References.....	81
7.	Amphiphilic Iron(II) Spin Crossover Coordination Polymers: Crystal Structures and Phase Transition Properties	85
7.1	Abstract	85
7.2	Introduction.....	86
7.3	Results and Discussion.....	88
7.3.1	Synthesis	88
7.3.2	X-ray Structure Analysis.....	89
7.3.3	Magnetic properties.....	96
7.3.4	TGA and DSC	100
7.3.5	Polarized Optical Microscopy.....	104
7.3.6	Processing as thin films.....	106
7.4	Conclusion	109
7.5	Conflicts of interest.....	110
7.6	Acknowledgements.....	110
7.7	Supporting Information.....	111
7.8	References.....	139

8.	Behaviour of Cu(II) and Ni(II) Schiff base-like complexes with long, branched alkyl chains in solution and in the solid state: Micelle formation, CISSS, and liquid crystallinity	143
8.1	Abstract	143
8.2	Introduction	143
8.3	Synthesis.....	144
8.4	Results and discussion.....	145
8.4.1	¹ H-NMR spectroscopy	145
8.4.2	DLS measurements	147
8.4.3	TEM measurements.....	150
8.4.4	UV-Vis spectroscopy	151
8.4.5	Magnetic properties.....	155
8.4.6	TGA and DSC measurements	156
8.4.7	Polarised optical microscopy	158
8.4.8	PXRD patterns.....	161
8.4.9	SEM measurements.....	164
8.5	Conclusion.....	165
8.6	Experimental Part.....	166
8.7	Supporting Information	170
8.8	References	175
9.	Publications	177
10.	Conferences	178
11.	(Eidesstattliche) Versicherungen und Erklärungen.....	179

Abbreviations

(in alphabetical order)

ac	acetate
AFM	atomic force microscopy
approx.	approximately
apy	4-aminopyridine
ATR	attenuated total reflection
ax	axial
azpy	4,4'-azopyridine
bimm	bis(1 <i>H</i> -imidazol-1-yl)methane
bipy	bipyridine
bpea	1,2-bis(4-pyridyl)ethane
bpee	1,2-di(4-pyridyl)ethylene/1,2-bis(4-pyridyl)ethene
bpey	bis(4-pyridyl)acetylene/1,2-bis(4-pyridyl)ethyne
bpma	bis(pyridin-4-ylmethyl)amine
bpms	bis(pyridin-4-ylmethyl)sulfane
bppa	1,3-bis(pyridin-4-yl)propane
btpyb	1,4-bis(2,2':6',2''-terpyridin-4'-yl)benzene
bzimpy	2,6-di(1 <i>H</i> -benzo[d]imidazol-2-yl)pyridine
<i>c</i>	<i>columnar</i>
<i>c</i>	concentration in mg/mL
calcd.	calculated
CCDC	Cambridge Crystallographic Data Centre
CDCl ₃	deuterated chloroform
CHCl ₃	chloroform
CISSS	coordination induced spin state switch
χ_M	molar magnetic susceptibility
<i>cpp</i>	critical packing parameter
CRISPR	clustered regularly interspaced short palindromic repeats
cryo	cryogenic
C _x	alkyl chain with a number of x carbon atoms in it
D	<i>discotic</i>
δ (Mössbauer)	isomer shift
δ (NMR)	chemical shift
DCM	dichloromethane
ΔE_{HL}	difference of the zero point energies
DEI	desorption electron ionisation
ΔE_Q	quadrupole splitting
ΔH	enthalpy
DHP	dihexadecyl phosphate
DLS	dynamic light scattering
dmap	4-(dimethylamino)pyridine
DMF	dimethylformamide
dmit	2-thioxo-1,3-dithiol-4,5-dithiolato
Δ_o	ligand field splitting parameter in an octahedral coordination sphere
ΔS	entropy
DSC	differential scanning calorimetry
<i>e. g.</i>	<i>exempli gratia</i> (lat.) = for example
endo	endothermic

eq	equatorial
eq./equiv.	equivalents
ESI	electrospray ionisation
<i>et al.</i>	<i>et alii/aliae/alia</i> (lat.) = and others
EtOH	ethanol
exo	exothermic
$\Gamma/2$	half width at half maximum
χ_{HS}	high spin fraction
h	<i>hexagonal</i>
H ₂ O	water
HS	high spin
hydr. dyn.	hydro dynamic
IR	infra-red
L	ligand
λ	wave length
LB	Langmuir-Blodgett
LC	liquid crystalline
LCP	liquid crystalline polymer
LIESST	light induced excited spin state trapping
LS	low spin
μ_{B}	Bohr magneton
μ_{eff}	effective magnetic moment
MeOH	methanol
MEPE	metallo-supramolecular coordination polyelectrolyte
MOF	metal organic framework
MRI	magnetic resonance imaging
MS	mass spectrometry
μ_{so}	spin-only magnetic moment
N	<i>nematic</i>
NBS	<i>N</i> -bromosuccinimide
NMR	nuclear magnetic resonance
<i>o</i>	<i>ortho</i>
ODT	4-octadecyl-1,2,4-triazole
ODTS	octadecyltrichlorosilane
<i>P</i>	spin pairing energy
PAC	polyelectrolyte-amphiphile complex
PBA	Prussian blue analogue
PDI	poly dispersity index
PEG	polyethylene glycol
phen	phenanthroline
pina	<i>N</i> -(pyridin-4-yl)isonicotinamide
POM	polarised optical microscopy
PPh ₃	triphenylphosphane
PS-P4VP	polystyrene-poly-4-vinylpyridine
PT	phase transition
ptz	1-propyltetrazole
PVA	polyvinyl alcohol
PVP	polyvinylpyrrolidone
PXRD	powder X-ray diffraction
py	pyridine
pz	pyrazine

pzo	pyrazole
r_{ML}	metal-to-ligand distance
RMS	root mean square
RT	room temperature
S	<i>smectic</i>
S	spin number
Σ	octahedral distortion parameter
sal ₂ -trien	bis-salicylaldehyde-triethylenetetramine
<i>sap</i>	self-assembly parameter
SCO	spin crossover
SEM	scanning electron microscope
SLS	swiss light source
S_N2	substitution nucleophilic (bi-molecular)
SQUID	superconducting quantum interference device
STM	scanning tunneling microscopy
T	Temperature
$T_{1/2}$	spin transition temperature
TEM	transmission electron microscopy
TGA	thermogravimetric analysis
TIESST	temperature induced excited spin state trapping
trz	triazole
TTF	tetrathiafulvalene
T_{TIESST}	TIESST temperature
UV-Vis	ultraviolet-visible
VdW	Van der Waal
XPS	X-ray photoelectron spectroscopy
XRD	X-ray diffraction
XRPD	X-ray powder diffraction

Acknowledgement

I would like to thank my supervisor Prof. Dr. Birgit Weber for giving me the opportunity to work in her group on my research project. I'm very grateful for her overall support, the scientific discussions we had, and the freedom to focus on subprojects of my choice. In particular, I'm thankful for the possibilities to present my results at various national and international conferences.

—

My thanks also go to my colleagues Ottokar Klimm, Charles Lochenie, Katja Dankhoff, Christoph Göbel, and Sophie Schöpfung. I thank my predecessor Stephan Schlamp whose work formed the foundation of my thesis. A special thanks go to René Nowak who shared the laboratory with me and was a good, supportive friend and to Hannah Kurz who encouraged me to stay focused and cheered me up during hard times.

—

I would like to thank my student interns Christian Heber, Patrick Hofmann, Jannik Petry, Joan Sander, Daniel Schmidmeier, and Daniel Wagner for their assistance. Here, I want to emphasise the contributions of Stella Buchmann and Victoria Müller who both did a great work during their bachelor thesis and their practical courses.

—

Collaborations were possible thanks to Felix Krohn, Julia Kronawitt, Paul Pineda, and Ling Peng who measured TGA and DSC, Florian Puchtler who measured PXR, Christine Denner and Ottokar Klimm who measured SEM, and Christoph Göbel who measured TEM of my samples. Basic analytics were supported by Ulrike Lacher with MS measurements and Anna-Maria Dietel who took good care of the elemental analysis device. Special measurements were done by Kerstin Hannemann who did paramagnetic NMR, Markus Hund who measured AFM, Wolfgang Milius who measured temperature dependent PRD, and Birger Dittrich who measured a very thin crystal at the SLS synchrotron and solved the structure. I very appreciated the work of Philipp Ramming and that he used his time during his master thesis for spin coating and AFM measurements of my samples.

—

I would like to express my special thanks to my parents and to my brother for their support and encouragement throughout my studies and my PhD work.

—

I thank my friends Sebastian Brahmman, Christoph Hartmann, Stefan Hüttner, Hannah Lammel, Thomas Metzner, Lisa Reinwand, Ralf Schlossmacher, and Christian Unglaub from Bamberg and Sebastian Bruckner, Peter Kolb, Raphael Kunz, Markus Petermichl, Nils Schieschke, and Laura Schwinger I know from Bayreuth. You and many other friends supported me with a lot of fun and pleasant moments during my time at the University of Bayreuth.

—

I appreciate the support of the mechanics, the glassblowers, the chemistry counter, and the purchasing department. In particular, I thank the laboratory assistants Anna-Maria Dietel, Christine Fell, and Heidi Maisel and our secretary Marlies Schilling.

—

Financial support was provided by the University of Bayreuth, the German Research Foundation DFG (WE 3546/5-1 and SFB 840), and the University of Bayreuth Graduate School.

1. Summary

In this work, metallomesogenic complexes were synthesised and their properties were investigated. For this, a selection of alkyl chains with different lengths was attached to an equatorial Schiff base-like ligand to obtain an amphiphilic system. The reaction with Fe(II) acetate, Cu(II) acetate, or Ni(II) acetate yielded the corresponding complexes. The amphiphilicity resulted in an interesting order in the solid phase, in the melt, and in solution. A variation of the axial ligands and the metal centres gave rise to further remarkable attributes.

In the first part, an Fe(II) system with C12 alkyl chains attached to the tetradentate equatorial ligand was studied. The reaction with dmap or bipy as axial ligands resulted in monomeric or polymeric octahedral complexes, respectively. Crystallographic data of the monomeric **[FeL(12)(dmap)₂]** complex, a partially converted **[FeL(12)(dmap)(MeOH)]** complex, and also an oxidised Fe(III) species **[μ -O-{FeL(12)}₂(dmap)]** were obtained. **[FeL(12)(dmap)(MeOH)]** and **[μ -O-{FeL(12)}₂(dmap)]** showed a lipid layer-like arrangement in the crystal packing due to *van der Waals* interactions between the alkyl chains. This is in consistency with the *sap* of around 1.00 from previous work. **[FeL(12)(dmap)₂]** displayed a lipid layer-like arrangement which was slightly disarranged due to a relatively high *sap* value of 1.12. It was suggested that this value is on the border for the formation of those structures. The magnetic measurements of **[FeL(12)(dmap)₂]** and **[FeL(12)bipy]_n** revealed SCO properties with hysteretic behaviour for both complexes. TIESST measurements showed that the HS species of both complexes could be trapped in a metastable state by rapid cooling. Heating up resulted in a T_{TIESST} of 121 K for **[FeL(12)(dmap)₂]** and 101 K for **[FeL(12)bipy]_n**. The width of the hysteresis was strongly depending on the scan rate of the measurement which was confirmed for **[FeL(12)bipy]_n** by kinetic measurements in the region of the SCO. As a result, a hysteresis without kinetic effects was obtained.

In the next part, the influence of the length of the alkyl chains on the SCO properties was investigated. Fe(II) complexes with C16, C18, C20, and C22 alkyl chains attached to the equatorial ligand were synthesised. Bridging bisonodentate axial ligands were used to form more stable coordination polymers. The rigidity of the coordination polymers was varied for the complexes with a C22 chain by using axial ligands with a single (bpea), a double (bpee), or a triple bond (bpey) as a bridge. For comparison purpose the four corresponding Fe(III) μ -O-complexes were synthesised and characterised, as well. Crystallographic data was obtained for **[FeL(22)bpea]_n**, **[FeL(22)bpey]_n**, and the precursor complex **[FeL(20)(MeOH)₂]**. Lipid layer-like arrangements were again observed in the crystal packing which were in agreement with the *sap* values. The PXRD measurements confirmed a similar crystal packing for the six Fe(II) coordination polymers.

Magnetic measurements showed an abrupt irreversible SCO above room temperature for all Fe(II) complexes. A second reversible SCO around 220 K was observed for the Fe(II) complexes with bpey as axial ligand. Temperature dependent PXRD, DSC and POM measurements showed that the SCO was related to a phase transition which was triggered by a reorientation of the alkyl chains in the crystal packing. In addition, birefringent structures were observed after crystallisation from the melt in the POM measurements. These were correlated with a liquid crystalline phase in the solid. Furthermore, the film formation behaviour was tested with $[\mu\text{-O-}\{\text{FeL(16)}\}_2]$ which was a first step towards the application as a multifunctional sensor. Homogenous films with a thickness of 15 and 30 nm were obtained by spin coating. A delamination procedure of the crystalline powder of $[\text{FeL(22)bpey}]_n$ was tested, too, and resulted in small platelets with a thickness roughly between 75 and 260 nm.

In the last part, the ligand system was modified to bear branched alkyl chains. It was expected that switching to a conical complex shape would reduce the phase transition temperatures and bring them closer to room temperature. Additionally, the conical shape ought to be advantageous for the formation of micelles. Cu(II) and Ni(II) complexes were synthesised first to investigate their behaviour in solution and their phase transition properties as they were easier to handle under air than an Fe(II) system. In *n*-hexane both complexes formed micelles with the addition of MeOH and NaCN which was confirmed by DLS and TEM. UV-Vis and $^1\text{H-NMR}$ studies showed a CISSS for $[\text{NiL(27)}]$ in $\text{CHCl}_3/\text{CDCl}_3$ with the stepwise addition of the coordinating solvent pyridine/pyridine- d_5 . Preliminary test demonstrated that micelle formation and a CISSS can be obtained at the same time. DSC and POM measurements revealed a melting process over a broad temperature range for both complexes and the formation of birefringent spherulitic structures when the samples were cooled from the melt. Moreover, $[\text{CuL(27)}]$ formed a second phase of well-defined six armed stars which has to be further investigated.

2. Zusammenfassung

In dieser Arbeit wurden metallomesogene Komplexe hergestellt und deren Eigenschaften untersucht. Hierfür wurde eine Auswahl von unterschiedlich langen Alkylketten an einen äquatorialen Schiff-Base ähnlichen Liganden angebracht, um amphiphile Eigenschaften zu erhalten. Dieser wurde mit Fe(II)-acetat, Cu(II)-acetat oder Ni(II)-acetat zu den entsprechenden Komplexen umgesetzt. Die Amphiphilität ergab eine interessante Ordnung im Feststoff, in der Schmelze und in Lösung. Durch eine Abänderung der axialen Liganden und des Metallzentrums wurden weitere herausragende Eigenschaften erhalten.

Im ersten Teil dieser Arbeit wurden Fe(II) Systeme untersucht an deren vierzähligen, äquatorialen Liganden C12 Alkylketten angebracht wurden. Die Umsetzung mit dmap oder bipy resultierte in den entsprechenden monomeren oder polymeren oktaedrischen Komplexen. Die kristallographischen Daten des monomeren **[FeL(12)(dmap)₂]** Komplexes, einem nur teilweise umgesetzten **[FeL(12)(dmap)(MeOH)]** Komplexes und einer oxidierten Fe(III) Spezies **[μ -O-{FeL(12)}₂(dmap)]** wurden erhalten. **[FeL(12)(dmap)(MeOH)]** und **[μ -O-{FeL(12)}₂(dmap)]** zeigten auf Grund von *van der Waals* Wechselwirkungen zwischen den Alkylketten eine lipidschichtähnliche Anordnung in der Kristallpackung. Dies ist in Übereinstimmung mit einem *sap* von circa 1.00 aus vorhergehenden Studien. **[FeL(12)(dmap)₂]** zeigte ebenfalls eine lipidschichtähnliche Anordnung, welche jedoch wegen einem relativ hohem *sap*-Wert von 1.12 leicht verschoben war. Es wird vermutet, dass der Wert an der Grenze zur Ausbildung dieser Strukturen war. Die Magnetmessungen von **[FeL(12)(dmap)₂]** und **[FeL(12)bipy]_n** zeigten SCO-Eigenschaften mit dem Auftreten einer Hysterese für beide Komplexe. TIESST Messungen ergaben, dass die HS Spezies beider Komplexe durch ein rapides Abkühlen in einem metastabilen Zustand eingefangen werden konnte. Hochheizen resultierte in einer T_{TIESST} von 121 K für **[FeL(12)(dmap)₂]** und 101 K für **[FeL(12)bipy]_n**. Die Breite der Hysterese hing stark von der Messgeschwindigkeit ab, was für **[FeL(12)bipy]_n** durch kinetische Messungen in der SCO-Region bestätigt wurde. Als Ergebnis wurde eine von kinetischen Effekten bereinigte Hysterese erhalten. Im nächsten Teil wurde der Einfluss der Alkylkettenlänge auf die SCO-Eigenschaften untersucht. Hierfür wurden Fe(II) Komplexe mit einer Alkylkettenlänge von C16, C18, C20 und C22 am äquatorialen Liganden hergestellt. Hierfür wurden verbrückende, zweizählige, axiale Liganden eingesetzt, die stabilere Koordinationspolymere bilden. Die Steifheit der Koordinationspolymere wurde für die Komplexe mit einer C22 Kette durch den Einsatz von axialen Liganden mit einer Einfach- (bpea), einer Zweifach- (bpee) oder einer Dreifachbindung (bpey) als Brücke variiert. Für Vergleichszwecke wurden die vier entsprechenden Fe(III) μ -O-Komplexe ebenfalls hergestellt und charakterisiert. Kristallographischen Daten wurden für **[FeL(22)bpea]_n**, **[FeL(22)bpey]_n** und

dem Präkursorkomplex **[FeL(20)(MeOH)₂]** erhalten. Es wurden ebenfalls lipidschichtähnliche Anordnungen in der Kristallpackung beobachtet, welche mit den *sap*-Werten übereinstimmten. Die PXRD Messungen bestätigten eine ähnliche Kristallpackung für die sechs Fe(II) Koordinationspolymere. Magnetmessungen zeigten für alle Fe(II) Komplexe einen abrupten, irreversiblen SCO oberhalb von Raumtemperatur. Einen zweiten, reversiblen SCO um die 220 K wurde für die Fe(II) Komplexe mit bpey als axialer Ligand beobachtet. Temperaturabhängige PXRD, DSC und POM Messungen zeigten, dass der SCO mit einem Phasenübergang verknüpft ist, der durch eine Neuausrichtung der Alkylketten in der Kristallpackung ausgelöst wurde. Zusätzlich wurden doppelbrechende Strukturen nach der Kristallisation aus der Schmelze in der POM Messung beobachtet. Diese wurden einer flüssigkristallinen Phase im Feststoff zugeordnet. Des Weiteren wurde das Filmbildungsverhalten von **[μ-O-{FeL(16)}₂]** getestet, was ein erster Schritt in Richtung Anwendung als multifunktionalen Sensor ist. Homogene Filme mit einer Schichtdicke von 15 und 30 nm wurden durch Rotationsbeschichtung erhalten. Ein Delaminierungsprozess des kristallinen Pulvers von **[FeL(22)bpey]_n** wurde ebenfalls getestet und es wurden kleine Plättchen mit einer Dicke zwischen 75 und 260 nm erhalten.

Im letzten Teil der Arbeit wurde verzweigte Alkylketten an das Ligandensystem angebracht. Es wurde davon ausgegangen, dass die Änderung hin zu einer kegelförmigen Komplexform die Phasenübergangstemperaturen reduzieren und sie in die Nähe von Raumtemperatur bringen würde. Zusätzlich sollte die kegelförmige Form vorteilhaft für die Bildung von Mizellen sein. Es wurden zuallererst die Cu(II) und Ni(II) Komplexe hergestellt, um deren Eigenschaften in Lösung und deren Phasenübergangsverhalten zu untersuchen, da diese sehr viel einfacher unter Luft handzuhaben waren als ein Fe(II) System. In *n*-Hexan bildeten beide Komplexe unter Zugabe von MeOH und NaCN Mizellen, was durch DLS und TEM Messungen bestätigt wurde. UV-Vis und ¹H-NMR Messungen zeigten einen CISSS für **[NiL(27)]** in CHCl₃/CDCl₃ unter stufenweiser Zugabe des koordinierenden Lösungsmittels Pyridin/Pyridin-d₅. Vorläufige Tests demonstrierten, dass die Bildung von Mizellen und ein CISSS gleichzeitig erreicht werden können. DSC und POM Messungen zeigten für beide Komplexe einen Schmelzprozess über einen weiten Temperaturbereich und die Bildung von doppelbrechenden, spherulitischen Strukturen, wenn die Probe aus der Schmelze wieder abgekühlt wurde. Darüber hinaus bildete **[CuL(27)]** eine zweite Phase aus, die aus gut ausgeprägten, sechsarmigen Sternen bestand, welche noch weiter untersucht werden muss.

3. Introduction

In the last decades and even centuries the advances of human research in all kinds of technological fields proceeded at elusive speed. Be it the first atomic model of Bohr and Rutherford considering quantum mechanics in 1913^[1] to the first absorption imaging of a single atom by Streed *et al.* in 2012^[2] or the basic work of Mendel about the rules of heredity in 1866^[3] to the establishment of the clustered regularly interspaced short palindromic repeats (CRISPR) method by Jinek *et al.* in 2012 to tailor life itself.^[4] Many more examples could be mentioned, however, most of them are about a better understanding and a higher control at the molecular and sub molecular level. This work presents another small step forward in the huge field of research, in particular, in the area of spin crossover (SCO) systems.

3.1 Principles of the spin crossover phenomenon

The SCO phenomenon is a magnetic effect first observed and described by Cambi and Szegő in 1931 on tris(N,N'-alkyldithiocarbamate) iron(III) complexes.^[5] Till this day, the phenomenon was observed for metals such as Fe(II),^[6] Fe(III),^[7] Co(II),^[8] Co(III),^[9] Mn(II),^[10] Mn(III),^[11] and Cr(II).^[12] In general, it can occur for 3d⁴ to 3d⁷ transition metals in an octahedral coordination sphere. As shown in **Figure 1**, with a 3d⁶ system like Fe(II), the electrons can be arranged in the orbitals in different ways.^[13,14]

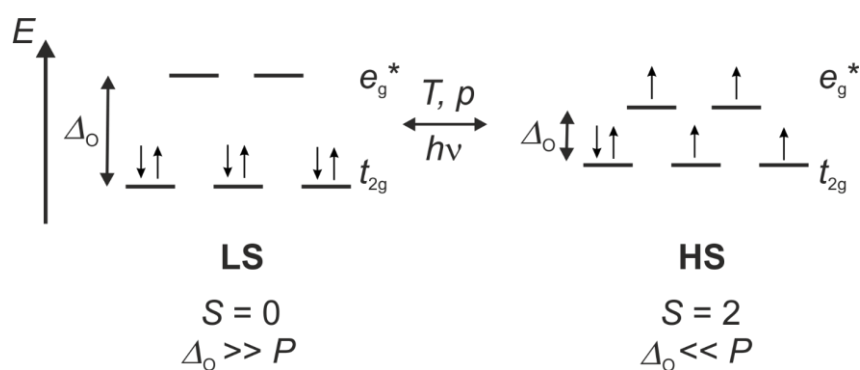


Figure 1: Schematic representation of a SCO between the LS and the HS state of a 3d⁶ transition metal (*e.g.* Fe(II)) in an octahedral coordination sphere. The electrons are distributed in the orbitals to give the minimum (LS state) and the maximum (HS state) number of unpaired electrons.

The minimum number of unpaired electrons leads to the low spin (LS) state while the maximum number leads to the high spin (HS) state. Which spin state is observed depends on the ligand field splitting parameter Δ_o and the spin pairing energy P . If Δ_o is much higher than P the LS state occurs, and if Δ_o is much lower than P the HS state occurs. When both energies are in the same region the system is bistable and it is possible to switch between these two states. Changes in temperature T

or pressure p ,^[15] or the irradiation with light $h\nu$ can trigger the SCO.^[16,17,18] The most prominent and most investigated one is by far the temperature dependent SCO. As a result of a SCO, the properties of the complex can change drastically. With the occupation of the antibonding e_g^* orbitals in the HS state the bond lengths increase. This is illustrated in the Jablonski diagram (**Figure 2**). Here, the 1A_1 potential well of the LS state and the 5T_2 potential well of the HS state have their energetic minimum at different metal-to-ligand distances r_{ML} .^[13,14] A transition between 1A_1 and 5T_2 is possible, if the difference of the zero point energies ΔE_{HL} is in an accessible energetic region.

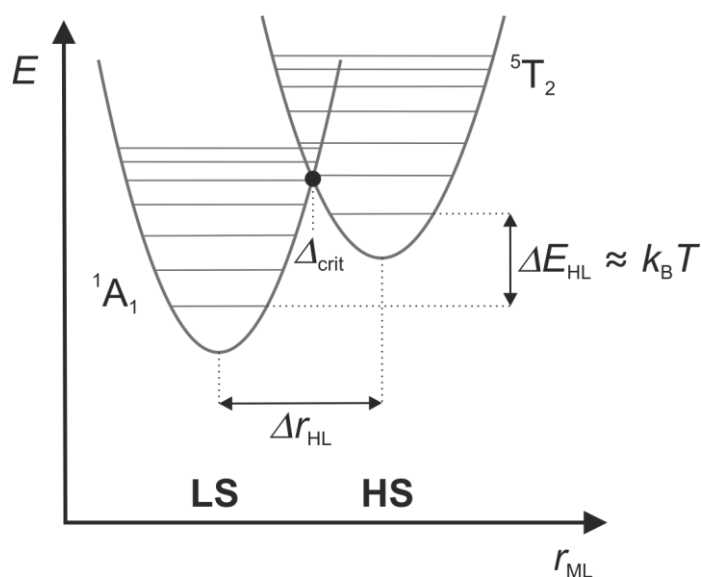
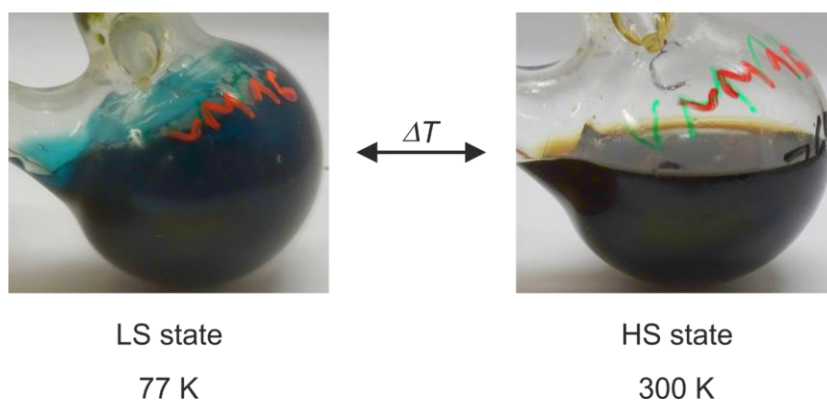


Figure 2: Jablonski diagram of the potential wells of the LS and the HS state of a $3d^6$ complex. The energetic states are shown in relation to the metal ligand distance r_{ML} .

Furthermore, with the modification of the electronic structure the colour changes, too. This is shown as an example in **Figure 3** with one of the complexes synthesised during this PhD work.



LS state

77 K

HS state

300 K

Figure 3: SCO complex in a Schlenk flask after (left) and before (right) dipping it into liquid nitrogen.

However, the most investigated effect caused by the SCO is a change in the magnetic properties. While the LS state of a $3d^6$ system in an octahedral coordination sphere is diamagnetic the HS state is paramagnetic. The transition between the two spin states can occur in many different ways as shown in **Figure 4**. Here, the magnetic behaviour of different SCO systems is compared by plotting $\chi_M T$, where χ_M is the molar magnetic susceptibility, against the temperature T . An important parameter is the temperature $T_{1/2}$, where 50% of the molecules did change the spin state. The most common SCO is gradual over a large temperature range and appears due to a lack of cooperativity.^[19] In principle, it is a Boltzmann distribution of the thermal spin state equilibrium. SCO phenomena in solution are a good example for this, as the complex molecules are isolated by the solvent. With a higher cooperativity between the metal centres the SCO becomes abrupt. It is even possible that a hysteresis appears, where the transition from HS to LS occurs at lower temperatures than the transition from LS to HS.^[20,21,22] This results in a memory effect which is most interesting for applications. Depending on the molecular structure and/or the crystal structure multi step or incomplete SCO are possible, too. Usually two different sites^[23] or special structural changes, *e. g.* solvent loss in the crystal structure,^[24] are responsible for it. Defects in the crystal can cause incomplete SCO behaviour, as well. The SCO phenomenon can also occur for systems which simply cannot become completely diamagnetic, like the $3d^5$ system Fe(III)^[25] or the $3d^7$ system Co(II).^[26]

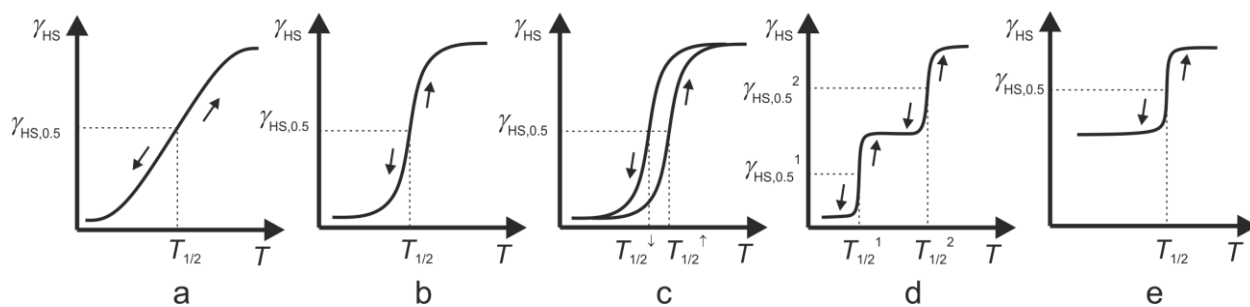


Figure 4: Different types of SCO: gradual (a), abrupt (b), with hysteresis (c), multi-step (d), and incomplete (e).

For certain SCO compounds the spin transition temperature is dependent on the scan rate used for the magnetic measurement. This was recently reported for Fe(II)^[27] and Co(II)^[28] SCO complexes. In some cases, the HS state can be trapped in a metastable state by cooling down very fast. This phenomenon is called temperature induced excited spin state trapping (TIESST) and is usually caused by slow phase transitions (PT). It was discussed by Buhks *et al.*^[29] in 1980 based on quantum mechanical studies and then first observed by Toftlund *et al.*^[30] in 1984 for Fe(II) complexes with tetradentate bis-2-(pyridylmethyl)diamine ligands. Until now, the highest observed TIESST temperature (T_{TIESST}) is 250 K for a polyanionic Fe(II) trimer.^[31]

A similar effect is the light induced excited spin state trapping (LIESST) effect which is represented in **Figure 5**. The first example of a LIESST effect was reported in 1984 by Decurtins *et al.* with $[\text{Fe}(\text{ptz})_6](\text{BF}_4)_2$ (ptz = 1-propyltetrazole).^[32] Nowadays many more are known.^[17,18,33] For the LIESST effect, the d electrons of the metal ion in the $^1\text{A}_1$ LS state can be excited with a green laser ($\lambda = 514 \text{ nm}$) to a ^1T state. After relaxation to the $^3\text{T}_1$ and further to the $^5\text{T}_2$ state the metal ion is in the HS state. A relaxation between the $^5\text{T}_2$ and the $^1\text{A}_1$ state is also possible. However, at low temperatures, more exactly below T_{LIESST} , the relaxation processes from ^1T to $^5\text{T}_2$ are much faster than from $^5\text{T}_2$ to $^1\text{A}_1$. This results in a quantitative photophysical electron pumping from the LS to the HS state.^[13,34] A reverse LIESST effect, where the electrons in the $^5\text{T}_2$ HS state are excited with a red laser ($\lambda = 820 \text{ nm}$) to the ^5E state which then relax back to the $^1\text{A}_1$ LS state, was also observed.^[35]

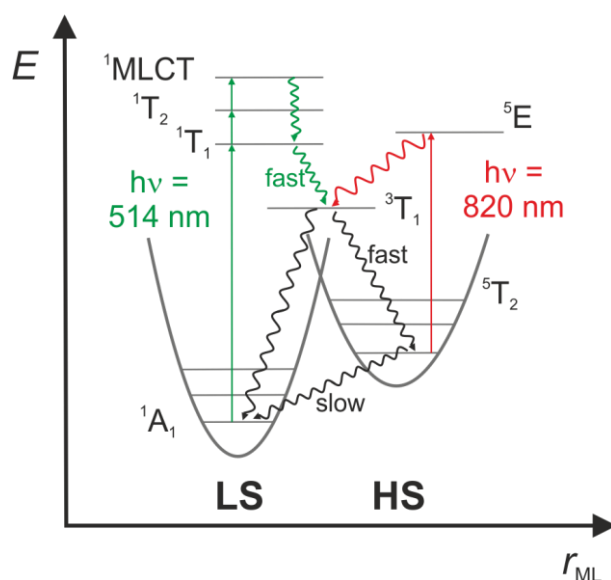


Figure 5: Schematic representation of the energy wells taking part in the LIESST (green) and the reverse LIESST (red) effect.

3.2 General concept of liquid crystalline systems

Liquid crystals, also called mesogens, are systems which have intermediate phases between the ordered solid and the disordered liquid phase. Those states are defined as mesophases. They combine properties of the crystalline phase, such as optical and electrical anisotropy, and the liquid phase, like molecular mobility and viscosity. They have a short-range order, but no long-range order. There are two different ways to obtain a mesophase: First, *thermotropic* liquid crystals which undergo mesophases by a variation of temperature and second, molecules which form anisotropic aggregates in combination with solvent, called *lyotropic* liquid crystals. Substances

which show both behaviours are *amphotropic*. The thermotropic liquid crystals can be classified in rod-like (*calamitic*) and disc-like (*discotic*) molecules. *Lyotropic* systems usually are amphiphilic compounds with a polar head group and nonpolar, aliphatic chains.^[36,37] This leads to the prerequisite of liquid crystals: the molecular structure, which introduces intermolecular attractive and repulsive (steric) forces to influence the packing and, as a result, the mesophase.^[38] In general, molecules with long, flexible alkyl chains attached to rigid, functional or aromatic groups are primarily used in literature.^[39] A simple and well known example is sodium stearate, one of the main ingredients of common soap. Basic examples of the three types of liquid crystalline molecules are shown in **Figure 6**.^[40]

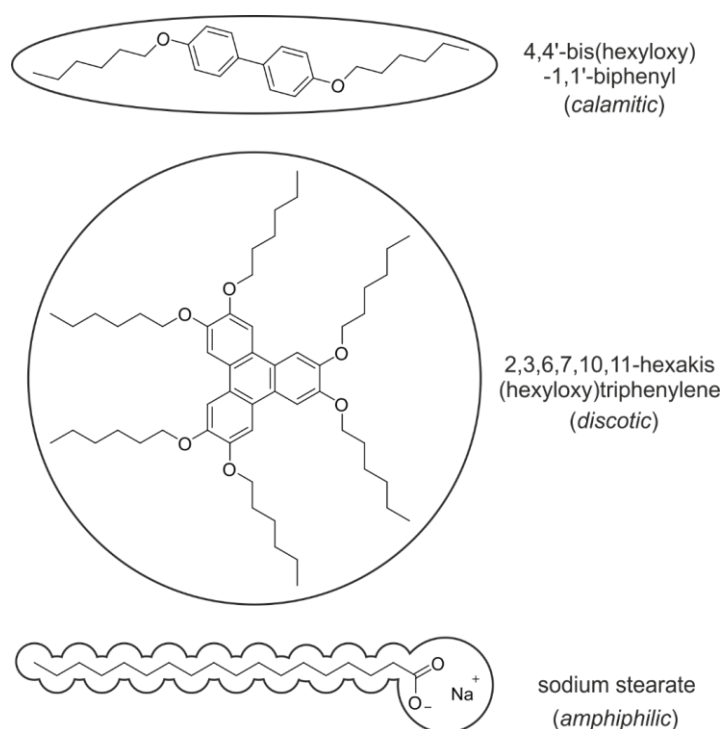


Figure 6: Basic examples for *calamitic*, *discotic*, and *amphiphilic* liquid crystalline molecules.

The three liquid crystalline mesophases *calamitic*, *discotic* and *lyotropic/amphiphilic* have characteristic molecular arrangements, as shown in **Figure 7**. Each mesophase has various subcategories. However, in this work only the typical subcategories will be shortly explained. More detailed explanations are given in literature.^[36,37,39,41–43] All mesophases have a certain degree of order which is usually in a temperature dependent sequence from highly ordered (low temperature) to less ordered (high temperature). Some liquid crystalline systems exhibit only one mesophase, others multiple.

The *calamitic* mesophase can be divided into the *nematic* (N) and the *smectic* (S) mesophase. In the *nematic* mesophase the rod-like molecules align parallel in the direction of vector \vec{n} . They can

move and rotate freely around this axis. The *smectic* mesophase possesses a higher structural order by forming layers in addition to the vector \vec{n} . *Discotic* mesophases behave similar to the *calamitic* mesophases. The disk-like molecules align again parallel in the direction of vector \vec{n} for the *nematic discotic* (N_D) mesophase which has the lowest order. In the *nematic columnar* (N_C) mesophase the molecules stack above each other to form columns. Those columns are ordered in a hexagonal way in the *discotic hexagonal* (D_H) mesophase. Amphiphilic molecules in the *lyotropic* mesophase interact with the solvent molecules and form separate layers, columns or spherical micelles. The structures formed by amphiphilic molecules were thoroughly investigated by Israelachvili *et al.* in 1976.^[44] It was shown that the thermodynamics, the interactions between the molecules, and the molecule geometry is of great importance. As a result, the critical packing parameter (cpp) was introduced to calculate the form of the macroscopic arrangement from the geometric parameters of the single molecules.

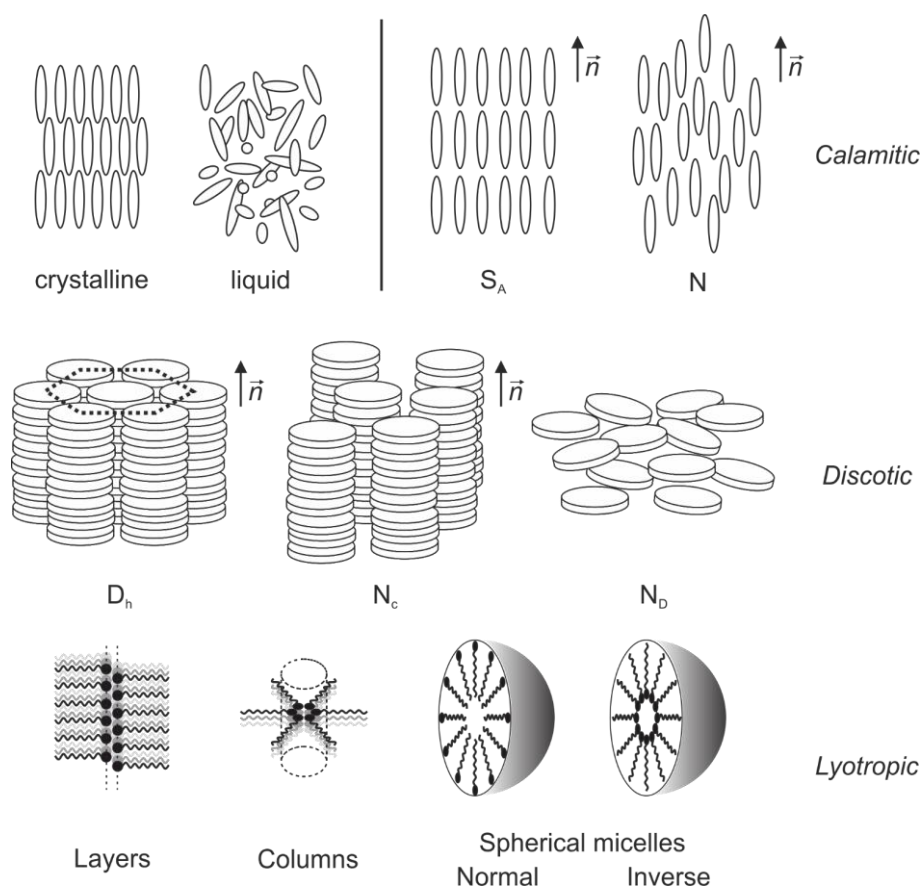


Figure 7: Schematic representation of different molecular arrangements in liquid crystalline mesophases. Top: Structural order in the crystalline and the liquid phase in comparison to the *calamitic* mesophases *smectic A* (S_A) and *nematic* (N). Centre: The *discotic* mesophases *discotic hexagonal* (D_H), *nematic columnar* (N_C), and *nematic discotic* (N_D). Bottom: The molecular formation of the *lyotropic* mesophases as layers, columns, and normal/inverse spherical micelles.

Liquid crystalline behaviour can occur not only in low molecular weight compounds, but also in macromolecular polymers. Those liquid crystalline polymers (LCPs) have a mesogenic unit either in their main chain or side chain.^[42] Mixtures and crosslinked LCPs are also possible. Due to the high variability of polymers a huge number of LCPs are known today and it is has become difficult to find simple categories to differentiate between them.^[45]

3.3 SCO in nanostructures and thin films

Nowadays, a lot of research revolves around meso- and nanostructuring. SCO systems are no exception as it allows additional modifications and is one step closer to future applications. Most of the approaches for SCO systems are *bottom up*, where the nanostructures grow from atomic or molecular level, in contrast to *top down* approaches, where macrostructures are etched or grinded to form nanostructures.^[46] In the end, it is important to obtain homogenous particles or layers with a well-defined size. In the region of the nanoscale, different particle sizes can also have different physical properties even though the material is exactly the same. One of the reasons for this is the size effect and, consequently, the surface effect. Molecules inside a homogenous particle have the same neighbours and interactions in all directions. Whereas, molecules on the surface have on one side vacuum, a gas phase, or solvent and therefore different kind of interactions which influence their physical properties, as shown in **Figure 8**. The size dependency can be explained by the ratio of molecules on to molecules below the surface of the particle. For big particles the number of molecules on the surface is small. However, the smaller the particle becomes, the larger gets the relative number of molecules on the surface. For example, a particle built like a 3x3x3 RUBIK'S CUBE[®] has 26 smaller molecules on the surface, but only one on the inside without surface effects. Of course, those effects can also occur when the particle is deposited on a matrix.

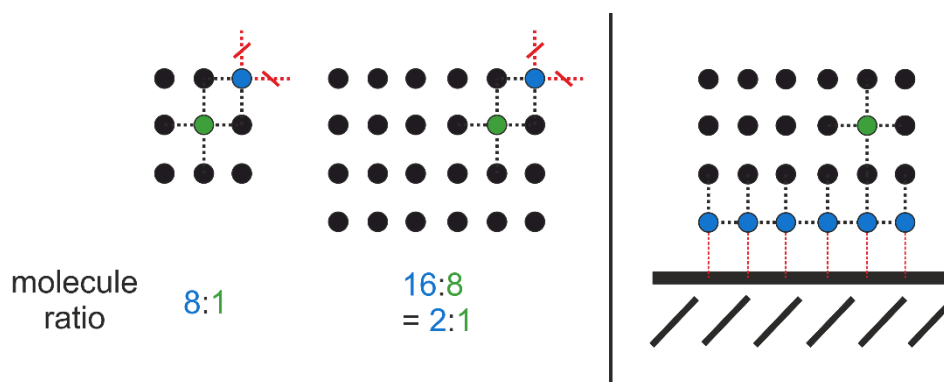


Figure 8: Schematic presentation of molecules in a small and a big particle in vacuum (left) and on a matrix (right). The green molecules are without, the blue molecules are with surface effects.

In the last years, SCO systems were intensively studied as nanostructures and the size effects were thoroughly discussed, as well.^[47] Even theoretical calculations about 1D chains with hysteresis loop,^[48] 3D frameworks of Fe(pz)[Pt(CN)₄] (pz = pyrazine),^[49] and 2D particles embedded in a polymer matrix^[50] were performed. Some SCO complexes had a thermal hysteresis loop in the bulk, but the SCO became gradual after nanostructuring.^[51] For other complexes the magnetic properties improved, as shown by Rohlf *et al.* in 2018.^[52] Here, the nanostructuring increased the TIESST temperature from 2 K to 100 K. It is also possible that the SCO properties are retained as nanomaterial which was shown with [Fe(HB(triazoly)3)₂].^[53]

Several methods for the synthesis of nanostructured SCO systems are known.^[54,55] A schematic overview of the major approaches is shown in **Figure 9**. Thin layers with a thickness in the nanoscale can be obtained by high vacuum evaporation,^[56] layer-by-layer deposition,^[57] or with a Langmuir-Blodgett (LB) trough.^[58,59] It was also shown that drop casted nanoparticles can be further processed with patterning to form parallel repeating linear structures on a silicon substrate.^[60] Solutions with [Fe(4-heptyl-1,2,4-trz)₃](OTs)₂ (trz = triazole) in CHCl₃ were used for spin coating and soft lithography.^[61] Furthermore, SCO nanoparticles were embedded in silica thin films via sol-gel technique.^[62] An interesting and facile approach is the inverse micelle technique.^[63,64] A water-in-oil system is stabilised with a surfactant like dioctyl sodium sulfosuccinate. The formed micelles can be used as microreactors which limit the size of crystal growth. Then, a metal precursor and a ligand are introduced to two separate emulsions. By mixing both emulsions homogenous nanoparticles can be obtained. Moreover, polymers can be used as stabilising agents. Mostly polyethylene glycol (PEG), polyvinylpyrrolidone (PVP), and polyvinyl alcohol (PVA) were combined with SCO compounds,^[64,65] where H-bonds and Van der Waals (VdW) interactions are responsible for the stability of the composite material. A new approach was reported by Weber *et al.* in 2016 with the block copolymer polystyrene-poly-4-vinylpyridine (PS-P4VP).^[55,66] The polymer itself is already known for micelle formation^[67] and the P4VP part is able to be a starting unit for SCO coordination polymers. This allows a better size control and improves the stability, as well.

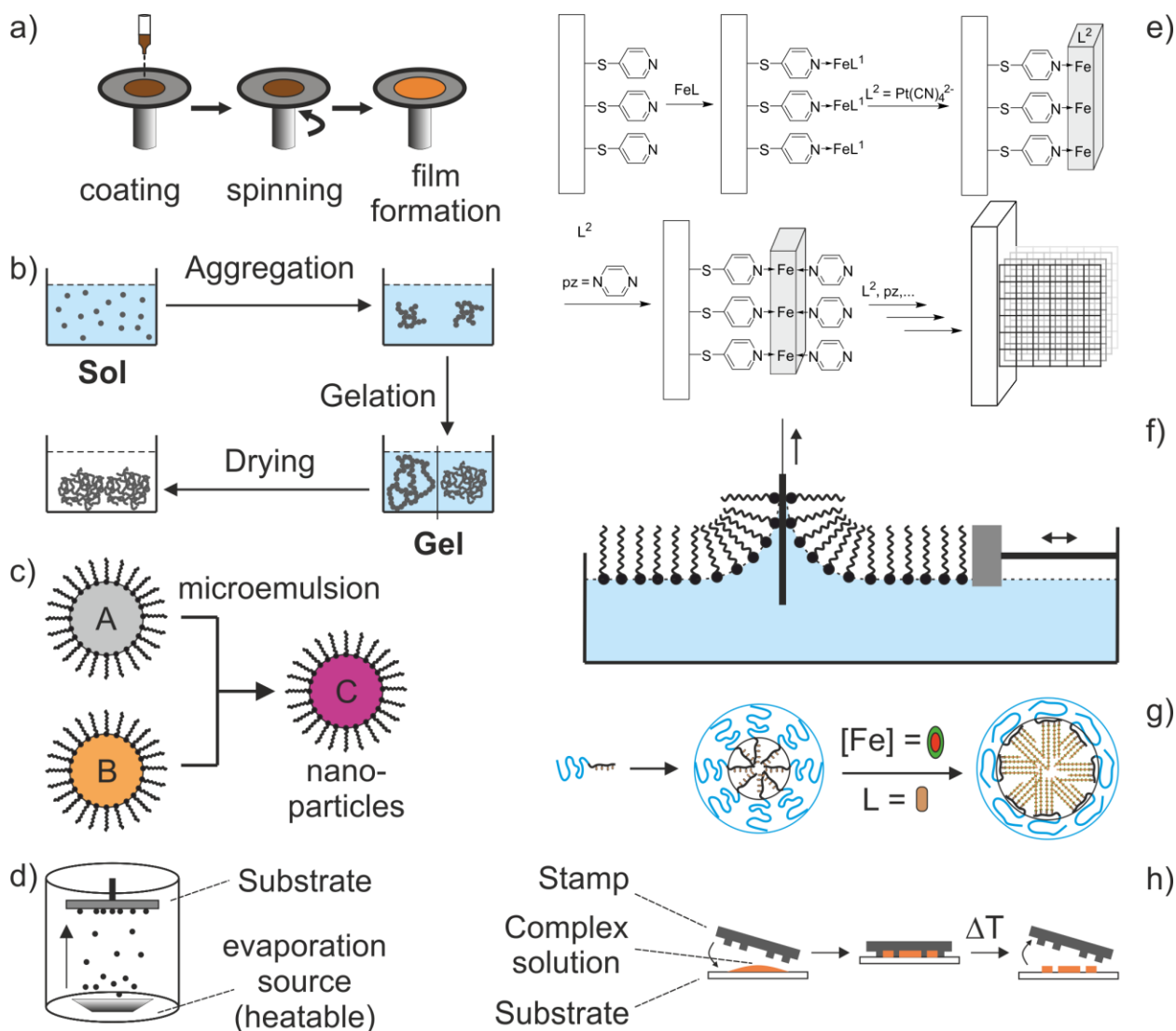


Figure 9: Schematic overview of different approaches for the synthesis of nanostructured SCO systems: a) spin coating, b) sol-gel-process, c) inverse micelle technique, d) high vacuum evaporation, e) layer-by-layer formation, f) Langmuir-Blodgett trough, g) block copolymer micelle method, h) soft-lithographic patterning.

3.4 Multifunctional SCO systems

SCO systems are undoubtedly an interesting field of science. Nevertheless, for applications it is of great benefit to combine them with other functional systems to obtain multifunctional SCO compounds.^[68] In principle, most applications for SCO systems centre around an input, a change of property, and finally a read-out possibility. The input, as mentioned under 1.1, is usually temperature, pressure, or light irradiation. In combination with other systems new kinds of input are possible, like electricity, chemical interactions, or liquid crystalline PTs.^[69] As for the change of property the SCO system can interact with the other system, *e. g.* with a change of magnetism or structure, or the other way round. The same applies for the read-out possibilities. The influence can modulate, inhibit, or even enhance the physical properties. This is not always successful as

sometimes both functions coexist without interactions.^[70] The general approaches for multifunctional SCO systems are either the fabrication of composite materials, *e. g.* by physically mixing the SCO system with the co-system, or the covalent binding of both systems within one molecule. In the following the most promising multifunctional SCO systems will be shortly discussed.

3.4.1 Luminescent and photoswitchable SCO complexes

Luminescent and SCO properties were mostly combined as composite materials. In 2014 Gros *et al.* prepared a heterostructure film consisting of the Prussian blue analogue Ni(II)[Cr(III)(CN)₆]_{0.7}·*n*H₂O (NiCr-PBA) and the Hofmann-like SCO system {Fe(azpy)[Pt(CN)₄]₂·*x*H₂O} (azpy = 4,4'-azopyridine) with the layer-by-layer deposition method.^[71] Light irradiation on the film resulted in a magnetisation change of the NiCr-PBA which was triggered by the coupling of the LIESST active SCO compound. It was also shown that SCO nanoparticles with a SiO₂ shell could be synthesised and post-functionalised with a fluorophore, like 3-(dansylamido)propyltrimethoxysilane^[72] or pyrene.^[73] In both cases the SCO properties were retained and a temperature dependent influence on the fluorescent moiety was observed. A more challenging attempt is the combination of both properties in one molecule by highly elaborate ligand design^[74,75] or by post functionalisation of a SCO system with fluorophores.^[76]

In principle, the composite materials and the bifunctional molecules have to exhibit a well-balanced donor-acceptor system, where the SCO element can function as a switch for the fluorophore element. The spectral overlap of the donor (fluorophore) and the acceptor (SCO metal ion) is large while in the LS state. Therefore, the luminescence is quenched by an energy transfer. Through the SCO the spectral overlap becomes smaller and the luminescence of the donor is preserved, as illustrated in **Figure 10**. Depending on the energetic levels, it is possible that the effect of the HS and the LS state on the fluorophore is *vice versa*. Additionally, an intermolecular electron transfer can occur in the case of bifunctional molecules and influence the quenching process of the luminescence.

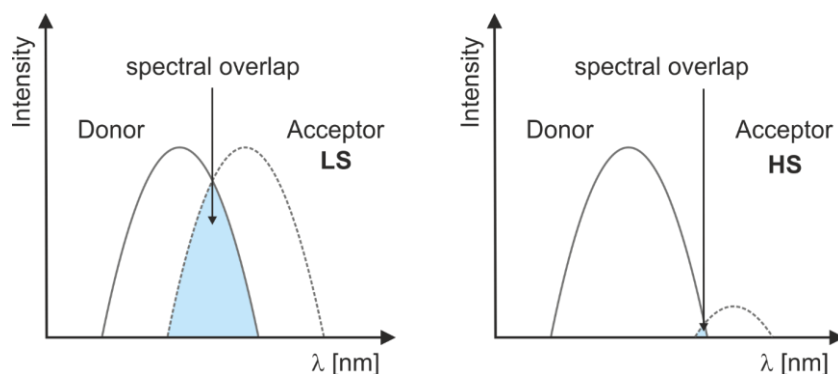
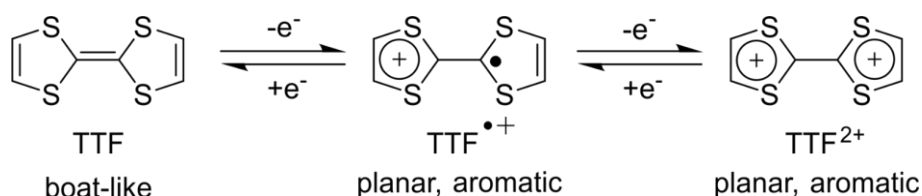


Figure 10: Illustration of the spectral overlap for a donor-acceptor system before and after the SCO phenomenon.

3.4.2 Electrical conductivity in SCO systems

Switching the electrical conductivity with a SCO system is a fascinating feature for future applications. Therefore, electrically conductive molecules were combined with SCO complexes. In 2005 Dorbes *et al.* presented the switchable SCO molecular conductor $[\text{Fe}(\text{sal}_2\text{-trien})][\text{Ni}(\text{dmit})_2]$ ($\text{sal}_2\text{-trien}$ = bis-salicylaldehyde-triethylenetetramine, dmit = 2-thioxo-1,3-dithiol-4,5-dithiolato).^[77] It was shown that cooperative effects, like π -stacking in the molecular structure, play an important role.^[77,78] In combination with LIESST active SCO complexes photoswitchable molecular conductors are even possible.^[79] A polythiophene based SCO systems was reported in 2009 by Djukic *et al.* with remarkable variable-temperature conductivity profiles.^[80] In recent years, the TTF (tetrathiafulvalene) ligand and its derivatives received attention in this field.^[81] While the TTF ligand itself has low conductive properties, the oxidised species is planar and aromatic which leads to a high electrical conductivity, as shown in **Scheme 1**. In general, charge-neutral systems are desired as counter ions increase the scattering of charge carriers which can be a problem for the electron transfer, *e. g.* in molecular junctions.^[82]



Scheme 1: Reversible redox states of the TTF ligand.

3.4.3 Porous SCO polymers and chemical sensing

Molecular structures with cavities in the nanoscale can be used as elements in chemical sensing. The size and the intermolecular forces of the cavities are very important to interact with the guest molecules. Furthermore, those interaction have to be selective for the target chemical substance. Bearing this in mind, porous SCO systems are an excellent material to combine both. In literature most examples were shown with the metal organic framework (MOF) $\{\text{Fe}(\text{L})[\text{M}(\text{CN})_4]\}$ ($\text{M} = \text{Ni}, \text{Pd}, \text{Pt}$; $\text{L} = \text{pz}, \text{bpee}$ (1,2-di(4-pyridyl)ethylene), bpey (bis(4-pyridyl)acetylene). The guest molecules influenced the spin state at room temperature (RT), which was easily detected by a change of colour due to absorption and desorption reactions. They also influenced the SCO temperature $T_{1/2}$. The flexibility in introducing various metal centre and bridging ligands resulted in the differentiation of many molecules, such as halogens, H_2O , CS_2 , thiourea, naphthalene, anthracene, and phenazine.^[83]

3.4.4 Metallomesogens exhibiting SCO behaviour

Metal containing liquid crystalline systems are called metallomesogens.^[43] In combination with a ligand group and a metal ion they can undergo SCO behaviour. Although, metallomesogens tend to need excessive ligand design and are often difficult to work up, they have many outstanding advantages. Due to their amphiphilic character self-assembled macrostructures, *e. g.* micelles, columns, or layers can be formed. A low melting point makes them processable from the melt and their remarkable spreading behaviour gives the possibility to obtain thin films by LB method, spin coating, and dip coating.^[43] In combination with SCO, additional properties such as thermochromism and photochromism are possible. The liquid crystallinity can further influence the SCO behaviour through external stimuli as electric- and magnetic-field-based methods.^[84] In the following, examples of metallomesogenic SCO systems will be discussed. Some of the molecular structures are presented in **Figure 11**.

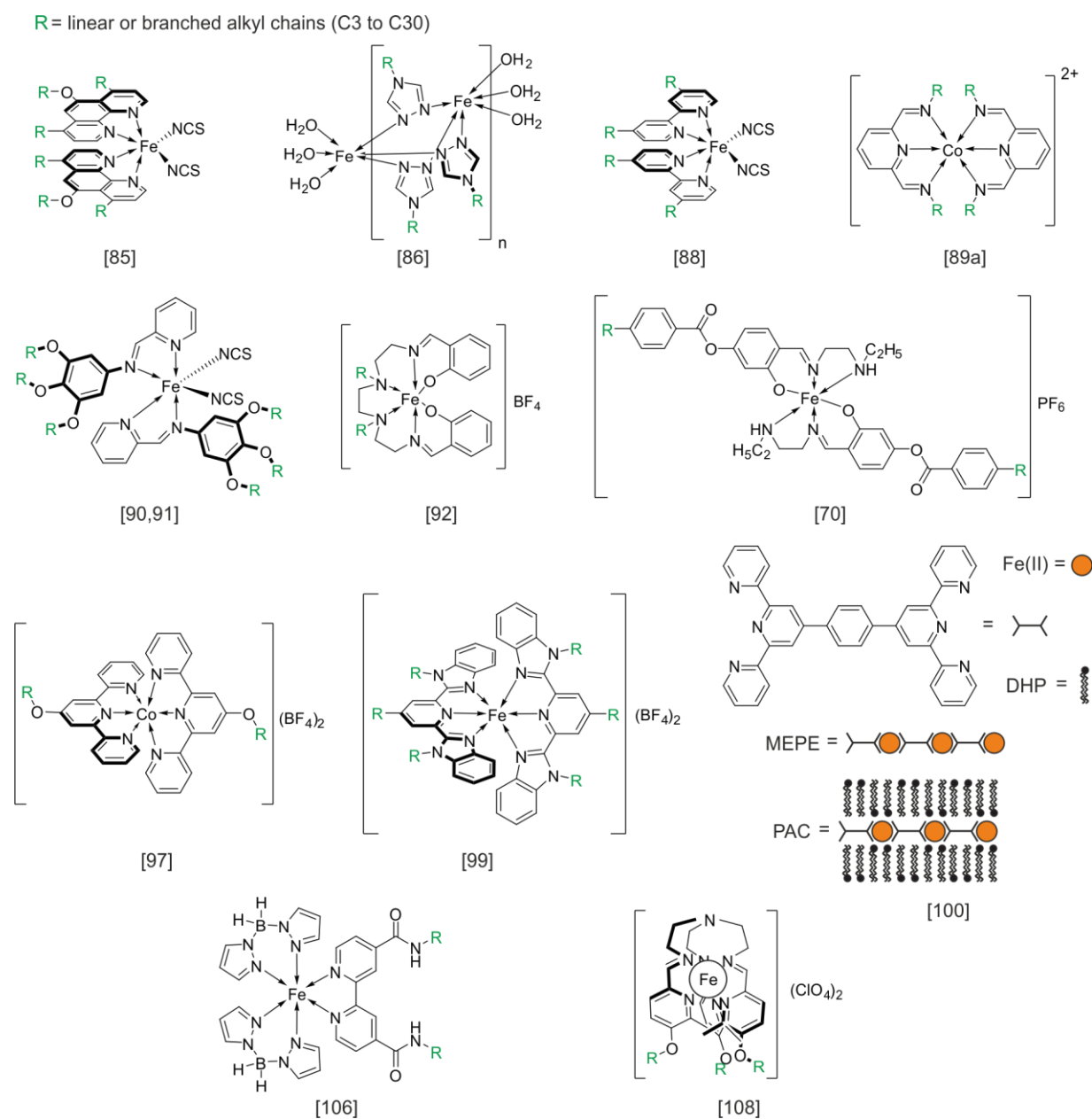


Figure 11: Molecular structures of some of the metallomesogenic SCO complexes discussed in the introduction of this work. The reference number is written below each structure in the order of appearance in the following text. substituent R stands for linear or branched alkyl chains (C3 to C30).

The first investigations on amphiphilic SCO systems were reported by Raudel-Teixier *et al.* in 1988.^[85] They used $[\text{Fe}(\text{phen})_2(\text{NCS})_2]$ (phen = phenanthroline) as initial structure, which was already well investigated at that time, and introduced three C18 alkyl chains on each phen ligand. LB films were obtained and SCO behaviour was confirmed by IR spectroscopy measurements at RT and at 77 K. Later, Armand *et al.* synthesised the amphiphilic, triazole-based Fe(II) coordination polymer $[\text{Fe}(\text{ODT})_3(\text{ClO}_4)_2]_n$ (ODT = 4-octadecyl-1,2,4-triazole).^[86] While the bulk showed the appearance of a SCO, the polymeric structure was not stable enough at the air-water interface of the LB film and, consequently, exhibited no SCO properties. This system was further studied by Roubeau *et al.* and the problems were stated to come from depolymerisation at the air-

water phase and recoordination of metal ions from the water subphase.^[87] The equilibrium was then shifted to the polymeric compound by dissolving $\text{Fe}(\text{NO}_3)_2$ in the water subphase and, as a result, SCO active LB films were obtained. By repeated vertical dipping of the substrates into a LB trough, multilayers ranging from 15 to 1100 layers were coated on the substrates, which was sufficient for XPS measurements, IR spectrometry, and magnetic measurements. $[\text{Fe}(\text{2,2}'\text{-bipy-alkyl})_2(\text{NCS})_2]$ (2,2'-bipy = 2,2'-bipyridine) and derivatives of this system were tested with formamide or KSCN in the water subphase to stabilise the LB monolayers.^[58] Here, the SCO behaviour was only followed by IR measurements. However, in 1999 Soyer *et al.* improved this system by attaching partially fluorinated alkyl chains on the bipy ligand.^[88] For the first time, the resulting LB film was investigated with magnetic measurements and it was shown that its special architecture has an influence on the SCO properties.

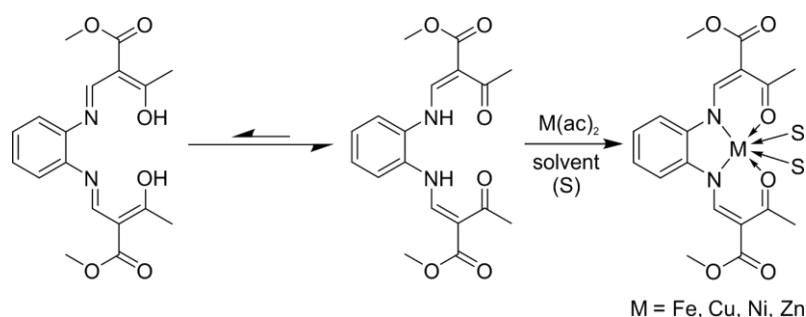
Several metallomesogenic SCO systems were studied in the bulk and, in general, the PT and the SCO can occur uncoupled or coupled. For the uncoupled systems an influence on the SCO is still observed due to the presence of the molecular structure needed for liquid crystalline behaviour, *e. g.* amphiphilic ligands.^[89,90-92] Some groups showed this by exchanging the alkyl chains of SCO active complexes for H-atoms, which lead to pure HS or LS complexes.^[92,93] However, more focus was set on obtaining compounds with coupled PT-SCO behaviour. The first example of an Fe(II) complex was shown by Galyametdinov *et al.* with a tridentate Schiff base ligand possessing one alkyl chain with twelve carbon atoms.^[70] Although, a coupling was observed more research was needed since the interplay was very weak. Systems with triazole^[94,95] and with Schiff base-like ligands followed^[96] and showed that a higher cooperativity with an abrupt SCO triggered by a PT is possible. Still, not all examples exhibited a complete LS to HS transition or were in the RT region which is an important asset for future applications. A new idea to couple PT with SCO came from Hayami *et al.*, where both phenomena have to be brought to the same temperature region.^[97] While the SCO phenomenon occurs mostly in the region below or even far below RT, PTs of metallomesogens occur usually above RT. Therefore, branched alkyl chains were introduced to a Co(II) complex with a terpyridine ligand. This is a well-established method to reduce the melting point of metallomesogens.^[43] As a result, an abrupt SCO coupled to a PT at $T_{1/2} = 288$ K during the heating mode was obtained. This approach was successfully implemented into triazole^[95,98] and bzimpy^[99] (bzimpy = 2,6-di(1H-benzo[d]imidazol-2-yl)pyridine) based systems. In 2003 Kurth *et al.* described a concept of two non-covalently bonded segments.^[100] $\text{Fe}(\text{ac})_2$ (ac = acetate) and btpyb (btpyb = 1,4-bis(2,2':6',2''-terpyridin-4'-yl)benzene) were reacted to form the rigid, rod-like metallosupramolecular coordination polyelectrolyte (MEPE). Amphiphilic dihexadecyl phosphate (DHP) was then added, which resulted in the formation of a

polyelectrolyte-amphiphile complex (PAC) via self-assembly. The magnetic properties of this lamellar superstructure were investigated in a LB multilayer and a SCO was observed.^[101] However, the SCO appeared to be incomplete due to reaching the temperature limit of the measurement device at 400 K. Further modifications of the MEPE unit shifted the SCO to lower temperatures at approximately 380 K.^[102] Studies on the ratio between MEPE and DHP showed an influence on the lamellar superstructure, that was found to change from a monolayer to a double layer.^[103] As a consequence, the SCO temperature changed, as well. Furthermore, self-assembly properties of amphiphilic complexes in solvents and their resulting magnetic behaviour were examined by various work groups. In 2008 Gandolfi *et al.* studied alkyl chain functionalised [Fe(sal₂trien)](PF₆) complexes.^[104] Temperature dependent UV-Vis spectra measured in dichloromethane (DCM) showed an abrupt SCO at approximately 235 K. This behaviour was very unusual as a gradual SCO with low cooperativity would have been expected in solution. DLS and cryo-SEM measurements showed the formation of spherical microparticles which were composed of rod-like assemblies. Those structures allow cooperative effects between the metal centres while still being in solution. Later, it was demonstrated that the alkyl chain length influenced the SCO temperature.^[105] By attaching a C30 alkyl chain to the sal₂trien ligand it was possible to increase the SCO temperature up to $T_{1/2} = 273$ K. In addition to that, fatigue effects of the reversibility of the SCO were inhibited which were observed for shorter alkyl chains after three heating-cooling cycles. The bulk material and vesicular nanospheres of [Fe(H₂Bpzo₂)₂(dialkyl-bipy)] (pzo = pyrazole) were investigated by Luo *et al.* in 2016.^[106] The nanospheres were obtained from hot water and characterised by DLS and TEM measurements. The system showed abrupt and complete SCO behaviour and a correlation between SCO temperature and chain length. While the SCO temperature of the bulk materials was roughly around 175 K, it was increased above RT to roughly 325 K for the lyophilised vesicular nanospheres.

An interesting new concept came from Hayami *et al.* in 2004, where three coexisting properties were combined in one system: the SCO phenomenon, liquid crystallinity, and the LIESST effect.^[90] The first approach with an Fe(II) complex consisting of two Schiff base ligands with three C16 alkyl chains and two NCS⁻ ligands ended in an uncoupled PT-SCO behaviour, with a gradual SCO, and only a partial LIESST excitation with a T_{LIESST} of 60 K. Further studies showed that through a variation of the alkyl chain length the light excited HS fraction of the system could be increased to 46% (C12 alkyl chain).^[91] Other systems followed^[107] of which the star-shaped Fe(II) complex presented by Seredyuk *et al.* in 2008 had with 80% the highest excitation fraction.^[108] The molecular structures of some of the metallomesogenic SCO systems which were discussed in the introduction of this work are presented in **Figure 11**.

3.5 The Jäger type ligand system

The ligand system discussed in this work is based on the Jäger type ligand system of L. Wolf and E. Jäger from 1966.^[109] Besides an interesting redox activity^[110] it was shown that the system exhibits SCO behaviour.^[111] The basic ligand has an N_2O_2 coordination sphere and can be easily obtained by reacting an *o*-diamine (*o* = *ortho*), like *o*-phenylenediamine, with a Claisen condensate as synthesised by L. Claisen in 1897.^[112] The Claisen condensate is synthesised by reacting methyl acetoacetate and trimethyl orthoformate in acetic anhydride. Following this, the pure Claisen condensate is distilled from the viscous mixture. A large range of ligands with several side groups can be synthesised by using different derivatives of the Claisen condensate. Though, it has to be noted that triethyl orthoformate should be used for some derivatives to prevent transesterification processes. The variation of the side groups has an influence on the ligand field splitting energy which makes this an excellent design for SCO complexes.^[113] The ligand is in an equilibrium between the enol-imine and the keto-enamine species as shown in **Scheme 2**.^[114] In literature, the terms Schiff base and Schiff base-like ligands are mostly used. The equilibrium of the Jäger type ligand is mainly on the Schiff base-like side and when metal ions are provided the tetradentate ligand forms a very stable metal chelate complex. Slightly basic conditions are beneficial as it increases the reaction speed by deprotonating the secondary amines. Up to now, Fe(II), Ni(II), Cu(II), and Zn(II) were used as metal ions.^[109,110,113,115] Fe(II) and Ni(II) prefer an octahedral coordination sphere. Therefore, additional solvent molecules are axially coordinated above and below the plane of the Jäger type ligand.



Scheme 2: Equilibrium of the enol-imine (left) and the keto-enamine (centre) species. The Jäger ligand can be reacted with a metal acetate to form a very stable chelate complex (right).

The ligand design was further developed by Weber *et al.* to increase the intermolecular interactions, such as π - π -stacking of aromatic carbon rings^[116] or H-bond networks through OH and ester groups.^[21,22,117] Dinuclear^[118] and luminescent^[75,115,119] systems were introduced, too.

The first metallomesogenic Jäger type ligand with two C16 alkyl chains was published by Schlamp *et al.* in 2011^[96] and more complexes followed.^[120] Data from X-ray structure analysis revealed that some of the amphiphilic complexes formed lipid layer-like arrangements in the crystal.^[121] At some point the data pool was big enough to find a correlation between the size of the polar head group and the length of the molecule. This is expressed in the self-assembly parameter *sap*, as shown in **Equation 1**.

$$sap = \frac{(H + B)}{L}$$

H: height of the head group
B: broadness of the head group
L: length of the molecule

Equation 1: The self-assembly parameter *sap* and its variables.

Lipid layer-like structures were only observed for an *sap* \approx 1. Consequently, it is possible to tune the *sap* by ligand design. As a result, the system possesses the advantage that the packing of the crystal structure can be predicted and controlled which can have a big impact on the magnetic properties. The basic structure of the Jäger type ligand, the amphiphilic derivatives, and some other derivatives are presented in **Figure 12**.

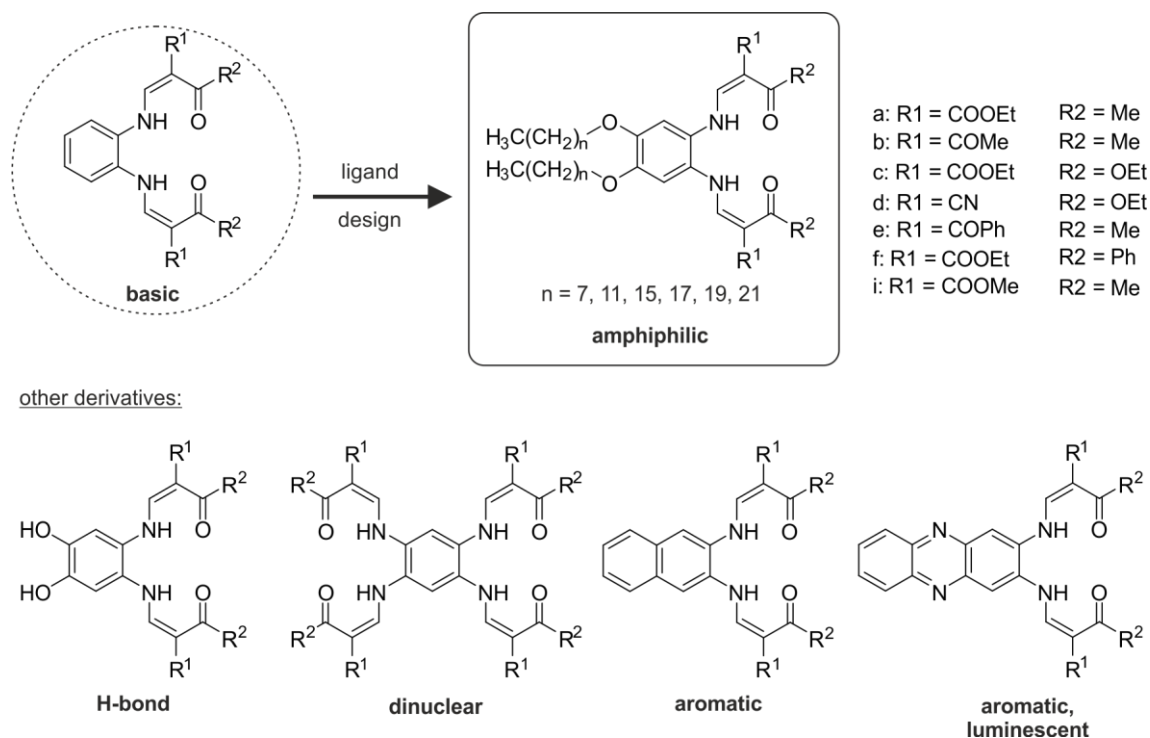


Figure 12: The basic structure of the Jäger type ligand and some of its derivatives. The amphiphilic ligand is emphasised with a box as it is the main ligand used in this work.

The axial ligands give an additional variability to the system. Most complexes were synthesised in methanol (MeOH) and have therefore MeOH as an axial ligand, at first. However, it is possible to obtain other complexes by ligand exchange. In principle, the axial ligand only needs a group

which coordinates stronger on the metal ion than MeOH. Imidazole or pyridine have been proven to be very effective for this purpose and many complexes were already synthesised.^[113] The complexes can also form 1D coordination polymers when bimonodentate ligands with two coordinating groups are used.^[122] The obtained coordination polymers were more stable under air and showed a higher cooperativity in the magnetic measurements. An overview of the axial ligands combined with the Jäger type ligand system are presented in **Figure 13**.

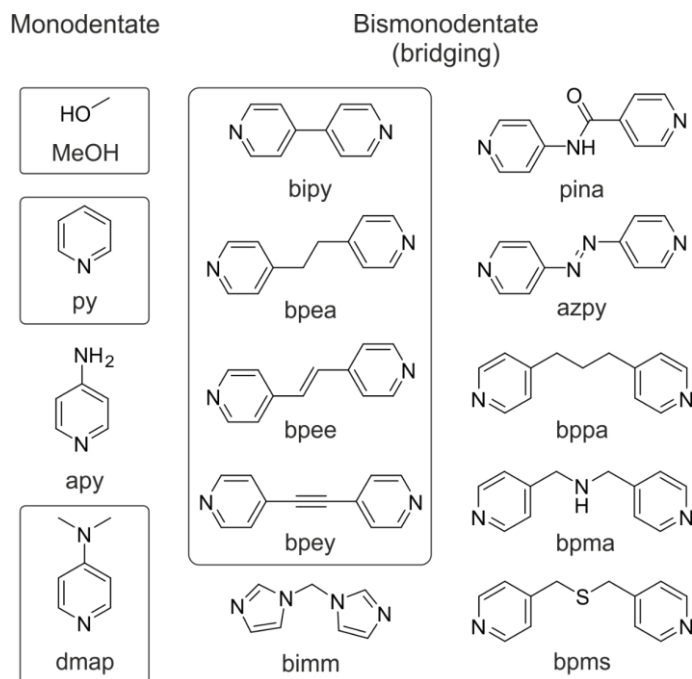


Figure 13: Overview of the axial ligands combined with the Jäger type ligand system. Monodentate ligands which form monomeric complexes (left) and bimonodentate ligands which form 1D coordination polymers (centre, right). The ligands in a box were used in this work.

3.6 References

- [1] a) N. Bohr, *Lond. Edinb. Dubl. Phil. Mag.* **1913**, *26*, 1–25; b) N. Bohr, *Lond. Edinb. Dubl. Phil. Mag.* **1913**, *26*, 857–875; c) N. Bohr, *Lond. Edinb. Dubl. Phil. Mag.* **1913**, *26*, 476–502.
- [2] E. W. Streed, A. Jechow, B. G. Norton, D. Kielpinski, *Nat. Commun.* **2012**, *3*, 1 - 5.
- [3] Gregor Mendel, *Verh. Naturf. Vereins Brünn* **1866**, 3–47.
- [4] M. Jinek, K. Chylinski, I. Fonfara, M. Hauer, J. A. Doudna, E. Charpentier, *Science* **2012**, *337*, 816–821.
- [5] L. Cambi, L. Szegö, *Ber. dtsch. Chem. Ges. A/B* **1931**, *64*, 2591–2598.
- [6] a) A. W. Addison, S. Burman, C. G. Wahlgren, O. A. Rajan, T. M. Rowe, E. Sinn, *J. Chem. Soc., Dalton Trans.* **1987**, 2621; b) E. V. Dose, M. A. Hoselton, N. Sutin, M. F. Tweedle, L. J. Wilson, *J. Am. Chem. Soc.* **1978**, *100*, 1141–1147; c) H. L.C. Feltham, A. S. Barltrop, S. Brooker, *Coord. Chem. Rev.* **2017**, *344*, 26–53; d) A.B. Gaspar, M. Seredyuk, P. Gütllich, *J. Mol. Struc.* **2009**, *924-926*, 9–19; e) I. A. Gass, S. R. Batten, C. M. Forsyth, B. Moubaraki, C. J. Schneider, K. S. Murray, *Coord. Chem. Rev.* **2011**, *255*, 2058–2067; f) P. Gütllich, Y. Garcia, H. A. Goodwin, *Chem. Soc. Rev.* **2000**, *29*, 419–427; g) J. Olgúin, S. Brooker, *Coord. Chem. Rev.* **2011**, *255*, 203–240.
- [7] a) L. Cambi, L. Szegö, *Ber. dtsch. Chem. Ges. A/B* **1933**, *66*, 656–661; b) D. J. Harding, P. Harding, W. Phonsri, *Coord. Chem. Rev.* **2016**, *313*, 38–61; c) S. Hayami, Z.-z. Gu, H. Yoshiki, A. Fujishima, O. Sato, *J. Am. Chem. Soc.* **2001**, *123*, 11644–11650; d) S. Hayami, K. Inoue, Y. Maeda, *Mol. Cryst. Liq. Cryst. Sci. Technol., Sect. A* **1999**, *335*, 573–582; e) Y. Maeda, H. Oshio, K. Toriumi, Y. Takashima, *J. Chem. Soc., Dalton Trans.* **1991**, *11*, 1227–1235; f) I. Nemeč, R. Herchel, R. Boča, Z. Trávníček, I. Svoboda, H. Fuess, W. Linert, *Dalton Trans.* **2011**, *40*, 10090–10099; g) M. Sorai, Y. Maeda, H. Oshio, *J. Phys. Chem. Solids* **1990**, *51*, 941–951; h) A. Tsukiashi, M. Nakaya, F. Kobayashi, R. Ohtani, M. Nakamura, J. M. Harrowfield, Y. Kim, S. Hayami, *Inorg. Chem.* **2018**, *57*, 2834–2842.
- [8] a) P. E. Figgins, D. H. Busch, *J. Am. Chem. Soc.* **1960**, *82*, 820–824; b) A. B. Gaspar, M. C. Muñoz, V. Niel, J. A. Real, *Inorg. Chem.* **2001**, *40*, 9–10; c) Y. Maeda, H. Ohshio, Y. Takashima, *Bull. Chem. Soc. Jpn.* **1982**, *55*, 3500–3505; d) L. G. Marzilli, P. A. Marzilli, *Inorg. Chem.* **1972**, *11*, 457–461.
- [9] a) W. Kläui, *J. Chem. Soc., Chem. Commun.* **1979**, 700; b) W. Kläui, W. Eberspach, P. Guetlich, *Inorg. Chem.* **1987**, *26*, 3977–3982; c) B. S. Manhas, B. C. Verma, S. B. Kalia, *Polyhedron* **1995**, *14*, 3549–3556.
- [10] a) J. H. Ammeter, R. Bucher, N. Oswald, *J. Am. Chem. Soc.* **1974**, *96*, 7833–7835; b) D. Cozak, F. Gauvin, *Organometallics* **1987**, *6*, 1912–1917; c) F. Franceschi, J. Hesschenbrouck,

- E. Solari, C. Floriani, N. Re, C. Rizzoli, A. Chiesi-Villa, *J. Chem. Soc., Dalton Trans.* **2000**, 593–604.
- [11] a) P. Guionneau, M. Marchivie, Y. Garcia, J. A. K. Howard, D. Chasseau, *Phys. Rev. B* **2005**, 72, 161; b) L. Kaustov, M. E. Tal, A. I. Shames, Z. Gross, *Inorg. Chem.* **1997**, 36, 3503–3511; c) P. G. Sim, E. Sinn, *J. Am. Chem. Soc.* **1981**, 103, 241–243.
- [12] a) D. M. Halepoto, D. G. L. Holt, L. F. Larkworthy, G. J. Leigh, D. C. Povey, G. W. Smith, *J. Chem. Soc., Chem. Commun.* **1989**, 1322; b) D. M. Halepoto, D. G. L. Holt, L. F. Larkworthy, D. C. Povey, G. W. Smith, G. J. Leigh, *Polyhedron* **1989**, 8, 1821–1822; c) H. Sitzmann, M. Schr, E. Dormann, M. Kelemen, *Z. Anorg. Allg. Chem.* **1997**, 623, 1850–1852.
- [13] B. Weber, *Koordinationschemie. Grundlagen und aktuelle Trends*, Springer Spektrum, Berlin **2014**.
- [14] B. Sieklucka, D. Pinkowicz, *Molecular Magnetic Materials: Concepts and Applications*, John Wiley and Sons Inc, Weinheim **2017**.
- [15] a) J. Jeftić, A. Hauser, *J. Phys. Chem. B* **1997**, 101, 10262–10270; b) V. Ksenofontov, H. Spiering, A. Schreiner, G. Levchenko, H. A. Goodwin, P. Gütllich, *J. Phys. Chem. Solids* **1999**, 60, 393–399; c) G. G. Levchenko, G. V. Bukin, A. B. Gaspar, J. A. Real, *Russ. J. Phys. Chem. A* **2009**, 83, 951–954; d) A. Tissot, H. J. Shepherd, L. Toupet, E. Collet, J. Sainton, G. Molnár, P. Guionneau, M.-L. Boillot, *Eur. J. Inorg. Chem.* **2013**, 1001–1008; e) D. Pinkowicz, M. Rams, M. Mišek, K. V. Kamenev, H. Tomkowiak, A. Katrusiak, B. Sieklucka, *J. Am. Chem. Soc.* **2015**, 137, 8795–8802.
- [16] a) S. Decurtins, P. Gütllich, C. P. Köhler, H. Spiering, A. Hauser, *Chem. Phys. Lett.* **1984**, 105, 1–4; b) A. Hauser, *Coord. Chem. Rev.* **1991**, 111, 275–290; c) A. Desaix, O. Roubeau, J. Jeftic, J.G. Haasnoot, K. Boukheddaden, E. Codjovi, J. Linarès, M. Noguès, F. Varret, *Eur. Phys. J. B* **1998**, 6, 183–193; d) C. Baldé, W. Bauer, E. Kaps, S. Neville, C. Desplanches, G. Chastanet, B. Weber, J. F. Létard, *Eur. J. Inorg. Chem.* **2013**, 2744–2750; e) N. F. Sciortino, S. M. Neville, C. Desplanches, J.-F. Létard, V. Martinez, J. A. Real, B. Moubaraki, K. S. Murray, C. J. Kepert, *Chemistry* **2014**, 20, 7448–7457; f) C. Sousa, C. de Graaf, A. Rudavskiy, R. Broer, *J. Phys. Chem. A* **2017**, 121, 9720–9727.
- [17] S. Decurtins, P. Gutlich, K. M. Hasselbach, A. Hauser, H. Spiering, *Inorg. Chem.* **1985**, 24, 2174–2178.
- [18] P. Gütllich, A. Hauser, H. Spiering, *Angew. Chem. Int. Ed.* **1994**, 33, 2024–2054.
- [19] a) E. W. Mueller, J. Ensling, H. Spiering, P. Guetlich, *Inorg. Chem.* **1983**, 22, 2074–2078; b) A. Real, J. Zarembowitch, O. Kahn, X. Solans, *Inorg. Chem.* **1987**, 26, 2939–2943; c) R. Kulmaczewski, O. Cespedes, M. A. Halcrow, *Inorg. Chem.* **2017**, 56, 3144–3148.

- [20] a) J.-F. Létard, P. Guionneau, E. Codjovi, O. Lavastre, G. Bravic, D. Chasseau, O. Kahn, *J. Am. Chem. Soc.* **1997**, *119*, 10861–10862; b) Z. J. Zhong, J.-Q. Tao, Z. Yu, C.-Y. Dun, Y.-J. Liu, X.-Z. You, *J. Chem. Soc., Dalton Trans.* **1998**, 327–328; c) B. Weber, W. Bauer, J. Obel, *Angew. Chem.* **2008**, *120*, 10252–10255.
- [21] W. Bauer, C. Lochenie, B. Weber, *Dalton Trans.* **2014**, *43*, 1990–1999.
- [22] C. Lochenie, W. Bauer, A. P. Railliet, S. Schlamp, Y. Garcia, B. Weber, *Inorg. Chem.* **2014**, *53*, 11563–11572.
- [23] B. Weber, C. Carbonera, C. Desplanches, J.-F. Létard, *Eur. J. Inorg. Chem.* **2008**, 1589–1598.
- [24] B. Weber, E. S. Kaps, C. Desplanches, J.-F. Létard, *Eur. J. Inorg. Chem.* **2008**, 2963–2966.
- [25] P. J. Koningsbruggen, Y. Maeda, H. Oshio, in: *Topics in Current Chemistry*, vol. 233-235 (Eds.: M.-L. Boillot, K. Boukheddaden, P. Gütllich, H. A. Goodwin, Y. Garcia), Springer, Berlin **2004**, 259–324.
- [26] P. Gütllich, H. A. Goodwin, *Spin Crossover in Transition Metal Compounds I-III*, Vols. 234, Springer, Berlin, Heidelberg **2004**.
- [27] a) T. Fujinami, K. Nishi, D. Hamada, K. Murakami, N. Matsumoto, S. Iijima, M. Kojima, Y. Sunatsuki, *Inorg. Chem.* **2015**, *54*, 7291–7300; b) R. Kulmaczewski, J. Olguín, J. A. Kitchen, Feltham, Humphrey L C, Jameson, Guy N L, J. L. Tallon, S. Brooker, *J. Am. Chem. Soc.* **2014**, *136*, 878–881; c) M. Seredyuk, M. C. Muñoz, M. Castro, T. Romero-Morcillo, A. B. Gaspar, J. A. Real, *Chem. Eur. J.* **2013**, *19*, 6591–6596.
- [28] R. G. Miller, S. Narayanaswamy, J. L. Tallon, S. Brooker, *New J. Chem.* **2014**, *38*, 1932.
- [29] E. Buhks, G. Navon, M. Bixon, J. Jortner, *J. Am. Chem. Soc.* **1980**, *102*, 2918–2923.
- [30] H. Toftlund, E. Pedersen, S. Yde-Andersen, M. Westdahl, *Acta Chem. Scand.* **1984**, *38a*, 693–697.
- [31] V. Gómez, C. Sáenz de Pipaón, P. Maldonado-Illescas, J. C. Waerenborgh, E. Martin, J. Benet-Buchholz, J. R. Galán-Mascarós, *J. Am. Chem. Soc.* **2015**, *137*, 11924–11927.
- [32] S. Decurtins, P. Gütllich, C. P. Köhler, H. Spiering, A. Hauser, *Chem. Phys. Lett.* **1984**, *105*, 1–4.
- [33] a) C.-C. Wu, J. Jung, P. K. Gantzel, P. Gütllich, D. N. Hendrickson, *Inorg. Chem.* **1997**, *36*, 5339–5347; b) K. D. Murnaghan, C. Carbonera, L. Toupet, M. Griffin, M. M. Dîrtu, C. Desplanches, Y. Garcia, E. Collet, J.-F. Létard, G. G. Morgan, *Chemistry* **2014**, *20*, 5613–5618.
- [34] P. Gütllich, *Coord. Chem. Rev.* **2001**, *219-221*, 839–879.
- [35] J. Kusz, H. Spiering, P. Gütllich, *J. Appl. Crystallogr.* **2001**, *34*, 229–238.

- [36] G. W. Gray, P. A. Winsor (Eds.) *Liquid crystals and plastic crystals - Physico-chemical properties and methods of investigation*, Horwood, Chichester **1974**.
- [37] G. W. Gray, P. A. Winsor (Eds.) *Liquid crystals and plastic crystals - Preparation, Constitution and Applications*, Horwood, Chichester **1974**.
- [38] M. A. Osman, *Z. Naturforsch. A* **1983**, 38.
- [39] C. Tschierske, T. Bellini, *Liquid crystals. Materials design and self-assembly*, Vols. 318, Springer, Heidelberg **2012**.
- [40] a) M. Sano, T. Kunitake, *Langmuir* **1992**, 8, 320–323; b) G. Cooke, V. Sage, T. Richomme, *Synth. Commun.* **1999**, 29, 1767–1771.
- [41] I. Mušević, *Liquid Crystal Colloids*, Springer International Publishing, Cham **2017**.
- [42] N. A. Platè (Ed.) *Liquid-Crystal polymers*, Plenum Press, New York **1993**.
- [43] J. L. Serrano, *Metallomesogens. Synthesis, properties, and applications*, VCH, Weinheim, New York **1996**.
- [44] J. N. Israelachvili, D. J. Mitchell, B. W. Ninham, *J. Chem. Soc., Faraday Trans. 2* **1976**, 72, 1525.
- [45] a) X.-J. Wang, Q.-F. Zhou, *Liquid crystalline polymers*, World Scientific, Singapore **2006**;
b) A. M. Donald, A. H. Windle, S. Hanna, *Liquid crystalline polymers*, Cambridge University Press, Cambridge **2006**.
- [46] H.-H. Gatzert, V. Saile, J. Leuthold, R. S. Muller, *Micro and nano fabrication. Tools and processes*, Springer, Berlin **2015**.
- [47] M. Mikolasek, G. Félix, W. Nicolazzi, G. Molnár, L. Salmon, A. Bousseksou, *New J. Chem.* **2014**, 38, 1834.
- [48] D. Chiruta, J. Linares, S. Miyashita, K. Boukheddaden, *J. Appl. Phys.* **2014**, 115, 194309.
- [49] D. Chiruta, J. Linares, M. Dimian, Y. Alayli, Y. Garcia, *Eur. J. Inorg. Chem.* **2013**, 5086–5093.
- [50] L. Stoleriu, A. Stancu, P. Chakraborty, A. Hauser, C. Enachescu, *J. Appl. Phys.* **2015**, 117, 17B307.
- [51] F. Volatron, L. Catala, E. Rivière, A. Gloter, O. Stéphan, T. Mallah, *Inorg. Chem.* **2008**, 47, 6584–6586.
- [52] S. Rohlf, M. Gruber, B. M. Flöser, J. Grunwald, S. Jarausch, F. Diekmann, M. Kalläne, T. Jasper-Toennies, A. Buchholz, W. Plass et al., *J. Phys. Chem. Lett.* **2018**, 9, 1491–1496.
- [53] V. Shalabaeva, S. Rat, M. D. Manrique-Juarez, A.-C. Bas, L. Vendier, L. Salmon, G. Molnár, A. Bousseksou, *J. Mater. Chem. C* **2017**, 5, 4419–4425.

- [54] a) A. Bousseksou, G. Molnár, L. Salmon, W. Nicolazzi, *Chem. Soc. Rev.* **2011**, *40*, 3313–3335; b) G. Molnár, S. Rat, L. Salmon, W. Nicolazzi, A. Bousseksou, *Adv. Mater.* **2018**, *30*.
- [55] B. Weber, *Chemistry* **2017**, *23*, 18093–18100.
- [56] a) T. Palamarciuc, J. C. Oberg, F. El Hallak, C. F. Hirjibehedin, M. Serri, S. Heutz, J.-F. Létard, P. Rosa, *J. Mater. Chem.* **2012**, *22*, 9690; b) S. Shi, G. Schmerber, J. Arabski, J.-B. Beaufrand, D. J. Kim, S. Boukari, M. Bowen, N. T. Kemp, N. Viart, G. Rogez et al., *Appl. Phys. Lett.* **2009**, *95*, 43303; c) H. Naggert, A. Bannwarth, S. Chemnitz, T. von Hofe, E. Quandt, F. Tuczek, *Dalton Trans.* **2011**, *40*, 6364–6366; d) K. Akabori, H. Matsuo, Y. Yamamoto, *J. Inorg. Nucl. Chem.* **1973**, *35*, 2679–2690; e) M. Atzori, L. Poggini, L. Squillantini, B. Cortigiani, M. Gonidec, P. Bencok, R. Sessoli, M. Mannini, *J. Mater. Chem. C* **2018**, *6*, 8885–8889.
- [57] S. Cobo, G. Molnár, J. A. Real, A. Bousseksou, *Angew. Chem. Int. Ed.* **2006**, *45*, 5786–5789.
- [58] H. Soyer, C. Mingotaud, M.-L. Boillot, P. Delhaes, *Langmuir* **1998**, *14*, 5890–5895.
- [59] J. F. Létard, O. Nguyen, H. Soyer, C. Mingotaud, P. Delhaès, O. Kahn, *Inorg. Chem.* **1999**, *38*, 3020–3021.
- [60] M. Cavallini, I. Bergenti, S. Milita, J. C. Kengne, D. Gentili, G. Ruani, I. Salitros, V. Meded, M. Ruben, *Langmuir* **2011**, *27*, 4076–4081.
- [61] C. M. Quintero, I.'y. A. Gural'skiy, L. Salmon, G. Molnár, C. Bergaud, A. Bousseksou, *J. Mater. Chem.* **2012**, *22*, 3745.
- [62] A. Tissot, J.-F. Bardeau, E. Rivière, F. Brisset, M.-L. Boillot, *Dalton Trans.* **2010**, *39*, 7806–7812.
- [63] a) E. Coronado, J. R. Galán-Mascarós, M. Monrabal-Capilla, J. García-Martínez, P. Pardo-Ibáñez, *Adv. Mater.* **2007**, *19*, 1359–1361; b) I. Boldog, A. B. Gaspar, V. Martínez, P. Pardo-Ibáñez, V. Ksenofontov, A. Bhattacharjee, P. Gütllich, J. A. Real, *Angew. Chem. Int. Ed.* **2008**, *47*, 6433–6437; c) T. Forestier, S. Mornet, N. Daro, T. Nishihara, S.-i. Mouri, K. Tanaka, O. Fouché, E. Freysz, J.-F. Létard, *Chem. Commun.* **2008**, 4327–4329.
- [64] V. Martínez, I. Boldog, A. B. Gaspar, V. Ksenofontov, A. Bhattacharjee, P. Gütllich, J. A. Real, *Chem. Mater.* **2010**, *22*, 4271–4281.
- [65] a) I.'y. A. Gural'skiy, C. M. Quintero, G. Molnár, I. O. Fritsky, L. Salmon, A. Bousseksou, *Chemistry* **2012**, *18*, 9946–9954; b) Y. Chen, J.-G. Ma, J.-J. Zhang, W. Shi, P. Cheng, D.-Z. Liao, S.-P. Yan, *Chem. Commun.* **2010**, *46*, 5073–5075; c) J. Laisney, A. Tissot, G. Molnár, L. Rechinat, E. Rivière, F. Brisset, A. Bousseksou, M.-L. Boillot, *Dalton Trans.* **2015**, *44*, 17302–17311.

- [66] a) C. Göbel, O. Klimm, F. Puchtler, S. Rosenfeldt, S. Förster, B. Weber, *Beilstein J. Nanotech.* **2017**, *8*, 1318–1327; b) O. Klimm, C. Göbel, S. Rosenfeldt, F. Puchtler, N. Miyajima, K. Marquardt, M. Drechsler, J. Breu, S. Förster, B. Weber, *Nanoscale* **2016**, *8*, 19058–19065.
- [67] S. Förster, M. Antonietti, *Adv. Mater.* **1998**, *10*, 195–217.
- [68] M. A. Halcrow (Ed.) *Spin-crossover materials. Properties and applications*, Wiley, Chichester **2013**.
- [69] a) A. B. Gaspar, V. Ksenofontov, M. Seredyuk, P. Gütllich, *Coord. Chem. Rev.* **2005**, *249*, 2661–2676; b) A. Bousseksou, G. Molnár, P. Demont, J. Menegotto, *J. Mater. Chem.* **2003**, *13*, 2069–2071; c) O. Kahn, C. J. Martinez, *Science* **1998**, *279*, 44–48; d) T. Mahfoud, G. Molnár, S. Cobo, L. Salmon, C. Thibault, C. Vieu, P. Demont, A. Bousseksou, *Appl. Phys. Lett.* **2011**, *99*, 53307; e) G. Molnár, L. Salmon, W. Nicolazzi, F. Terki, A. Bousseksou, *J. Mater. Chem. C* **2014**, *2*, 1360–1366.
- [70] Y. Galyametdinov, V. Ksenofontov, A. Prosvirin, I. Ovchinnikov, G. Ivanova, P. Gütllich, W. Haase, *Angew. Chem. Int. Ed.* **2001**, *40*, 4269–4271.
- [71] C. R. Gros, M. K. Peprah, B. D. Hosterman, T. V. Brinzari, P. A. Quintero, M. Sendova, M. W. Meisel, D. R. Talham, *J. Am. Chem. Soc.* **2014**, *136*, 9846–9849.
- [72] S. Titos-Padilla, J. M. Herrera, X.-W. Chen, J. J. Delgado, E. Colacio, *Angew. Chem. Int. Ed.* **2011**, *50*, 3290–3293.
- [73] I. Suleimanov, O. Kraieva, J. Sánchez Costa, I. O. Fritsky, G. Molnár, L. Salmon, A. Bousseksou, *J. Mater. Chem. C* **2015**, *3*, 5026–5032.
- [74] Y. Garcia, F. Robert, A. D. Naik, G. Zhou, B. Tinant, K. Robeyns, S. Michotte, L. Piraux, *J. Am. Chem. Soc.* **2011**, *133*, 15850–15853.
- [75] C. Lochenie, K. Schötz, F. Panzer, H. Kurz, B. Maier, F. Puchtler, S. Agarwal, A. Köhler, B. Weber, *J. Am. Chem. Soc.* **2018**, *140*, 700–709.
- [76] C.-F. Wang, R.-F. Li, X.-Y. Chen, R.-J. Wei, L.-S. Zheng, J. Tao, *Angew. Chem.* **2015**, *127*, 1594–1597.
- [77] S. Dorbes, L. Valade, J. A. Real, C. Faulmann, *Chem. Commun.* **2005**, 69–71.
- [78] K. Takahashi, H.-B. Cui, Y. Okano, H. Kobayashi, H. Mori, H. Tajima, Y. Einaga, O. Sato, *J. Am. Chem. Soc.* **2008**, *130*, 6688–6689.
- [79] K. Takahashi, H.-B. Cui, Y. Okano, H. Kobayashi, Y. Einaga, O. Sato, *Inorg. Chem.* **2006**, *45*, 5739–5741.
- [80] B. Djukic, M. T. Lemaire, *Inorg. Chem.* **2009**, *48*, 10489–10491.

- [81] a) M. Nihei, N. Takahashi, H. Nishikawa, H. Oshio, *Dalton Trans.* **2011**, *40*, 2154–2156; b) H.-Y. Wang, J.-Y. Ge, C. Hua, C.-Q. Jiao, Y. Wu, C. F. Leong, D. M. D'Alessandro, T. Liu, J.-L. Zuo, *Angew. Chem. Int. Ed.* **2017**, *56*, 5465–5470.
- [82] K. Senthil Kumar, M. Ruben, *Coord. Chem. Rev.* **2017**, *346*, 176–205.
- [83] a) G. Agustí, R. Ohtani, K. Yoneda, A. B. Gaspar, M. Ohba, J. F. Sánchez-Royo, M. C. Muñoz, S. Kitagawa, J. A. Real, *Angew. Chem. Int. Ed.* **2009**, *48*, 8944–8947; b) C. Bartual-Murgui, N. A. Ortega-Villar, H. J. Shepherd, M. C. Muñoz, L. Salmon, G. Molnár, A. Bousseksou, J. A. Real, *J. Mater. Chem.* **2011**, *21*, 7217; c) F. J. Muñoz Lara, A. B. Gaspar, D. Aravena, E. Ruiz, M. C. Muñoz, M. Ohba, R. Ohtani, S. Kitagawa, J. A. Real, *Chem. Commun.* **2012**, *48*, 4686–4688; d) F. J. Muñoz-Lara, A. B. Gaspar, M. C. Muñoz, M. Arai, S. Kitagawa, M. Ohba, J. A. Real, *Chemistry* **2012**, *18*, 8013–8018; e) M. Ohba, K. Yoneda, G. Agustí, M. C. Muñoz, A. B. Gaspar, J. A. Real, M. Yamasaki, H. Ando, Y. Nakao, S. Sakaki et al., *Angew. Chem. Int. Ed.* **2009**, *48*, 4767–4771; f) R. Ohtani, K. Yoneda, S. Furukawa, N. Horike, S. Kitagawa, A. B. Gaspar, M. C. Muñoz, J. A. Real, M. Ohba, *J. Am. Chem. Soc.* **2011**, *133*, 8600–8605; g) P. D. Southon, L. Liu, E. A. Fellows, D. J. Price, G. J. Halder, K. W. Chapman, B. Moubaraki, K. S. Murray, J.-F. Létard, C. J. Kepert, *J. Am. Chem. Soc.* **2009**, *131*, 10998–11009.
- [84] P. Gütllich, A. B. Gaspar, Y. Garcia, *Beilstein J. Org. Chem.* **2013**, *9*, 342–391.
- [85] A. Ruaudel-Teixier, A. Barraud, P. Coronel, O. Kahn, *Thin Solid Films* **1988**, *160*, 107–115.
- [86] F. Armand, C. Badoux, P. Bonville, A. Ruaudel-Teixier, O. Kahn, *Langmuir* **1995**, *11*, 3467–3472.
- [87] O. Roubeau, B. Agricole, R. Clérac, S. Ravaine, *J. Phys. Chem. B* **2004**, *108*, 15110–15116.
- [88] H. Soyer, E. Dupart, C. J. Gómez-García, C. Mingotaud, P. Delhaès, *Adv. Mater.* **1999**, *11*, 382–384.
- [89] a) N. Abdullah, N. L. M. Noor, A. R. Nordin, M. A. Halcrow, D. R. MacFarlane, M. A. Lazar, J. M. Pringle, D. W. Bruce, B. Donnio, B. Heinrich, *J. Mater. Chem. C* **2015**, *3*, 2491–2499; b) C. Gandolfi, T. Cotting, P. N. Martinho, O. Sereda, A. Neels, G. G. Morgan, M. Albrecht, *Dalton Trans.* **2011**, *40*, 1855–1865.
- [90] S. Hayami, K. Danjobara, K. Inoue, Y. Ogawa, N. Matsumoto, Y. Maeda, *Adv. Mater.* **2004**, *16*, 869–872.
- [91] S. Hayami, N. Motokawa, A. Shuto, N. Masuhara, T. Someya, Y. Ogawa, K. Inoue, Y. Maeda, *Inorg. Chem.* **2007**, *46*, 1789–1794.

- [92] P. N. Martinho, C. J. Harding, H. Müller-Bunz, M. Albrecht, G. G. Morgan, *Eur. J. Inorg. Chem.* **2010**, 675–679.
- [93] M. R. Karim, H. Takehira, M. M. Rahman, A. M. Asiri, M. K. Amin, R. Ohtani, S. Hayami, *J. Organomet. Chem.* **2016**, 808, 42–47.
- [94] a) T. Fujigaya, D.-L. Jiang, T. Aida, *J. Am. Chem. Soc.* **2003**, 125, 14690–14691; b) M. Seredyuk, A. B. Gaspar, V. Ksenofontov, Y. Galyametdinov, M. Verdaguer, F. Villain, P. Gülich, *Inorg. Chem.* **2008**, 47, 10232–10245.
- [95] R. Akiyoshi, R. Ohtani, M. Nakamura, S. Hayami, *J. Incl. Phenom. Macro.* **2018**.
- [96] S. Schlamp, B. Weber, A. D. Naik, Y. Garcia, *Chem. Commun.* **2011**, 47, 7152–7154.
- [97] S. Hayami, R. Moriyama, A. Shuto, Y. Maeda, K. Ohta, K. Inoue, *Inorg. Chem.* **2007**, 46, 7692–7694.
- [98] Y. H. Lee, Y. Komatsu, Y. Yamamoto, K. Kato, T. Shimizu, A. Ohta, T. Matsui, S. Hayami, *Inorg. Chem. Comm.* **2011**, 14, 1498–1500.
- [99] Y. H. Lee, A. Ohta, Y. Yamamoto, Y. Komatsu, K. Kato, T. Shimizu, H. Shinoda, S. Hayami, *Polyhedron* **2011**, 30, 3001–3005.
- [100] D. G. Kurth, A. Meister, A. F. Thünemann, G. Förster, *Langmuir* **2003**, 19, 4055–4057.
- [101] Y. Bodenthin, U. Pietsch, H. Möhwald, D. G. Kurth, *J. Am. Chem. Soc.* **2005**, 127, 3110–3114.
- [102] Y. Bodenthin, G. Schwarz, Z. Tomkowicz, T. Geue, W. Haase, U. Pietsch, D. G. Kurth, *J. Am. Chem. Soc.* **2009**, 131, 2934–2941.
- [103] G. Schwarz, Y. Bodenthin, Z. Tomkowicz, W. Haase, T. Geue, J. Kohlbrecher, U. Pietsch, D. G. Kurth, *J. Am. Chem. Soc.* **2011**, 133, 547–558.
- [104] C. Gandolfi, C. Moitzi, P. Schurtenberger, G. G. Morgan, M. Albrecht, *J. Am. Chem. Soc.* **2008**, 130, 14434–14435.
- [105] C. Gandolfi, G. G. Morgan, M. Albrecht, *Dalton Trans.* **2012**, 41, 3726–3730.
- [106] Y.-H. Luo, Q.-L. Liu, L.-J. Yang, Y. Sun, J.-W. Wang, C.-Q. You, B.-W. Sun, *J. Mater. Chem. C* **2016**, 4, 8061–8069.
- [107] a) M. Seredyuk, M. C. Muñoz, V. Ksenofontov, P. Gülich, Y. Galyametdinov, J. A. Real, *Inorg. Chem.* **2014**, 53, 8442–8454; b) S. Hayami, N. Motokawa, A. Shuto, R. Moriyama, N. Masuhara, K. Inoue, Y. Maeda, *Polyhedron* **2007**, 26, 2375–2380.
- [108] M. Seredyuk, A. B. Gaspar, V. Ksenofontov, Y. Galyametdinov, J. Kusz, P. Gülich, *J. Am. Chem. Soc.* **2008**, 130, 1431–1439.
- [109] L. Wolf, E.-G. Jäger, *Z. Anorg. Allg. Chem.* **1966**, 346, 76–91.

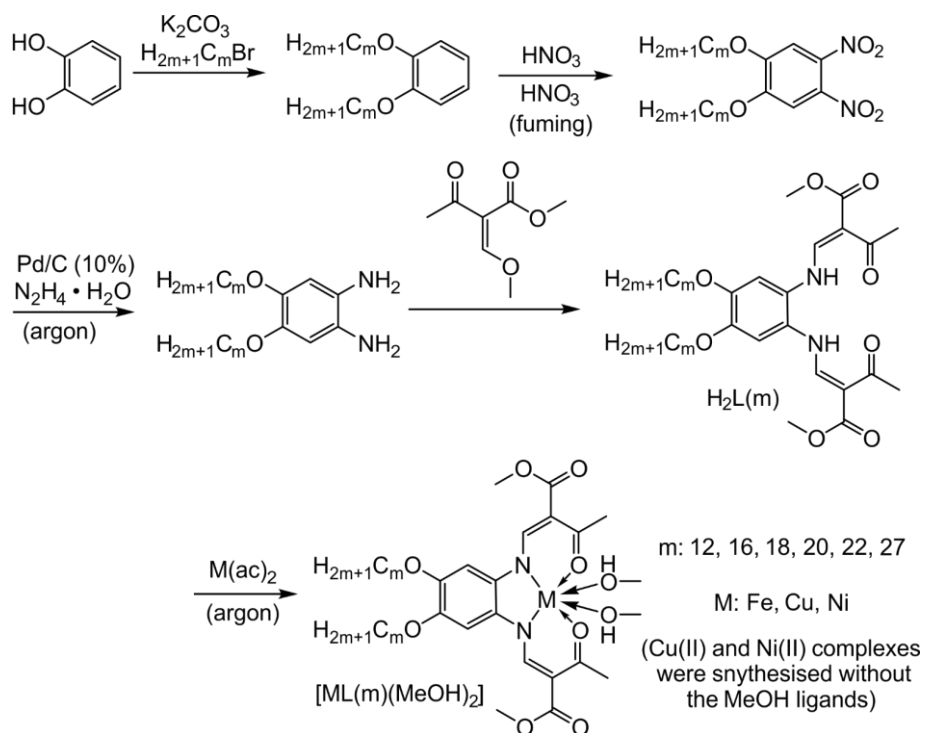
- [110] E.-G. Jäger, E. Häussler, M. Rudolph, A. Schneider, *Z. Anorg. Allg. Chem.* **1985**, 525, 67–85.
- [111] B. R. Müller, G. Leibelng, E.-G. Jäger, *Chem. Phys. Lett.* **2000**, 319, 368–374.
- [112] L. Claisen, *Liebigs Ann. Chem.* **1897**, 297, 1–98.
- [113] B. Weber, *Coord. Chem. Rev.* **2009**, 253, 2432–2449.
- [114] W. Bauer, T. Ossiander, B. Weber, *Z. Naturforsch. B* **2010**, 2010, 323–328.
- [115] C. Lochenie, K. G. Wagner, M. Karg, B. Weber, *J. Mater. Chem. C* **2015**, 3, 7925–7935.
- [116] a) C. Lochenie, J. Heinz, W. Milius, B. Weber, *Dalton Trans.* **2015**, 44, 18065–18077; b) C. Lochenie, A. Gebauer, O. Klimm, F. Puchtler, B. Weber, *New J. Chem.* **2016**, 40, 4687–4695.
- [117] a) B. Weber, W. Bauer, T. Pfaffeneder, M. M. Dîrtu, A. D. Naik, A. Rotaru, Y. Garcia, *Eur. J. Inorg. Chem.* **2011**, 3193–3206; b) B. Weber, E.-G. Jäger, *Z. Anorg. Allg. Chem.* **2009**, 635, 130–133; c) B. Weber, J. Obel, *Z. Anorg. Allg. Chem.* **2009**, NA-NA; d) B. Weber, J. Obel, D. Henner-Vásquez, W. Bauer, *Eur. J. Inorg. Chem.* **2009**, 5527–5534.
- [118] a) W. Bauer, S. Schlamp, B. Weber, *Chem. Commun.* **2012**, 48, 10222–10224; b) W. Bauer, B. Weber, *Inorg. Chim. Acta* **2009**, 362, 2341–2346.
- [119] H. Kurz, C. Lochenie, K. G. Wagner, S. Schneider, M. Karg, B. Weber, *Chem. Eur. J.* **2018**, 24, 5100–5111.
- [120] a) S. Schlamp, K. Dankhoff, B. Weber, *New J. Chem.* **2014**, 38, 1965–1972; b) S. Schlamp, P. Thoma, B. Weber, *Eur. J. Inorg. Chem.* **2012**, 2759–2768.
- [121] S. Schlamp, P. Thoma, B. Weber, *Chem. Eur. J.* **2014**, 20, 6462–6473.
- [122] a) W. Bauer, M. M. Dîrtu, Y. Garcia, B. Weber, *CrystEngComm* **2012**, 14, 1223–1231; b) W. Bauer, T. Pfaffeneder, K. Achterhold, B. Weber, *Eur. J. Inorg. Chem.* **2011**, 3183–3192; c) W. Bauer, W. Scherer, S. Altmannshofer, B. Weber, *Eur. J. Inorg. Chem.* **2011**, 2803–2818; d) R. Nowak, W. Bauer, T. Ossiander, B. Weber, *Eur. J. Inorg. Chem.* **2013**, 975–983; e) T. Pfaffeneder, W. Bauer, B. Weber, *Z. Anorg. Allg. Chem.* **2010**, 636, 183–187; f) T. M. Pfaffeneder, S. Thallmair, W. Bauer, B. Weber, *New J. Chem.* **2011**, 35, 691–700.

4. Synopsis

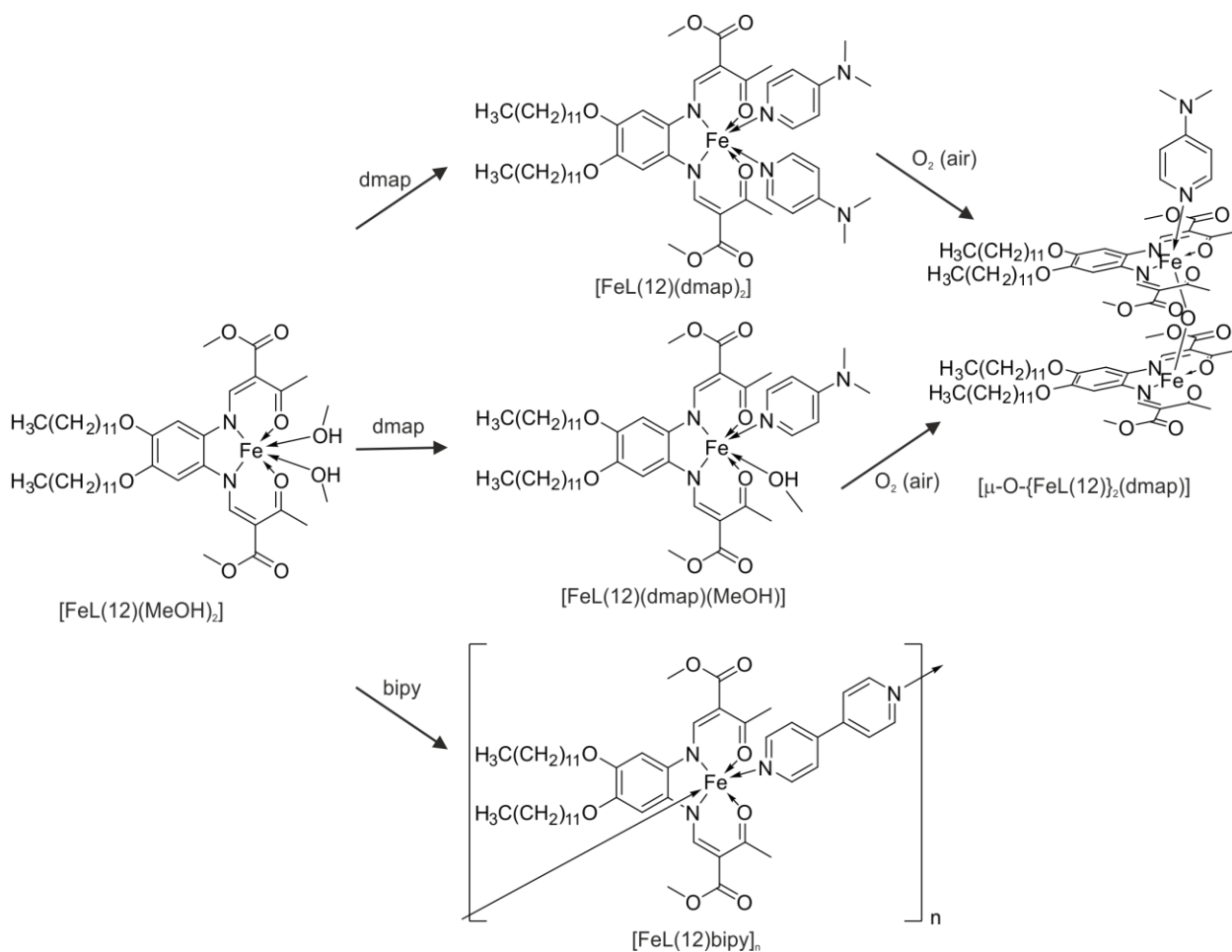
This thesis is based on the work of my predecessor Stephan Schlamp who introduced alkyl chains with a length of C8, C12, C16, and C22 to the Jäger type ligand system investigated in the group of Prof. Weber. With this modification he obtained amphiphilic Fe(II) SCO complexes which were mostly monomeric. The dissertation presented here centres around the better understanding of the influence of the alkyl chain length on the SCO and on the phase transition properties. In addition, the amphiphilicity of the system gave rise to a multitude of additional properties, such as liquid crystallinity, kinetic effects, self-assembly, and low melting points, which were investigated, as well. Moreover, possibilities for the application of the complexes as nanostructured material were tested with delamination processes, spin coating, and inverse micelle formation. In the following the work will be summarised in more detail.

The general synthesis of the amphiphilic ligands and the Fe(II), Cu(II), and Ni(II) complexes is shown in **Scheme 3**. In the first step two alkyl chains were attached to catechol. The mechanism proceeded by the *Williamson Ether Synthesis* (S_N2 reaction). For the alkyl bromide linear C12, C16, C18, C20, and C22 and branched C27 alkyl chains were used. Then, the aromatic ring was nitrated twice in para and in meta position to the alkyl ether groups through an electrophilic aromatic substitution. In the next step the nitro groups were reduced to amines with hydrazine and palladium on activated charcoal as a catalyst. The synthesis step took place under argon atmosphere as the diamine product was air sensitive and to prevent the evolving hydrogen to fiercely react with oxygen from the air during reflux. A keto-enol ether, which was synthesised through a Claisen condensation reaction, was coupled to each of the amines to obtain the tetradentate Schiff base-like ligand. The metal centre was introduced with the corresponding metal acetate by ligand exchange. Fe(II) complexes were always prepared and stored under an argon atmosphere to prevent the oxidation to an Fe(III) species. In MeOH Cu(II) and Ni(II) preferred a square planar coordination sphere while Fe(II) preferred an octahedral coordination sphere. As a result, the obtained Fe(II) complex possessed weakly bonded MeOH molecules as axial ligands. This made it an excellent precursor to be used in further reactions with different pyridyl derivatives which form stronger bonds.

Fe(II) complexes with a C12 alkyl chain attached to the Schiff base-like ligand and with either dmap or bipy as axial ligands are discussed in **Chapter 6**. The monomeric Fe(II) complex with dmap was found to be highly sensitive to air. The synthetic procedures of the complexes are shown in **Scheme 4**.



Scheme 3: General synthetic procedure for the metal complexes of **Chapter 6**, **Chapter 7**, and **Chapter 8** over five steps. The alkyl chains are linear for $m = 12 - 22$ and branched for $m = 27$. The Cu(II) and Ni(II) complexes are square planar and don't have MeOH as coordinating solvent.



Scheme 4: Synthesis of the complexes of **Chapter 6**.

X-ray crystal structure analysis showed that not only the expected **[FeL(12)(dmap)₂]** was crystallised but **[FeL(12)(dmap)(MeOH)_{0.5}] \times MeOH**, as well. This revealed that the equilibrium between dmap and the solvent MeOH coordinating on the Fe(II) centre is not far enough on the dmap side and can be influenced by factors such as the volume of MeOH, the eq. of dmap, or the crystallisation temperature. A third crystal structure showed an oxidised Fe(III) species which crystallised as the dimeric **[μ -O-{FeL(12)}₂(dmap)]** complex. It was fully characterised and used as a reference for the purity of the Fe(II) complexes. Furthermore, the **[FeL(12)(MeOH)₂]** precursor was reacted with bipy to form the polymeric **[FeL(12)bipy]_n** complex. However, no crystals suitable for X-ray crystal structure analysis were obtained for this compound. The crystal packing of the three obtained crystal structures is shown in **Figure 14**. The three complexes form lipid layer-like arrangements in which the head groups and the alkyl chains point away from each other. The structure is stabilised by *van der Waals* interactions between the alkyl chains. These arrangements were already observed by my predecessor for similar Jäger type complexes but not for all. A relation between the size of the head group and the length of the molecule was found to explain the tendency to form lipid-like layers. It was called the *self-assembly parameter* which is $sap = (H+B)/L$, where H is the height and B the broadness of the head group and L the length of the molecule. Values around 1.00 result in the formation of the arrangements. **[FeL(12)(dmap)(MeOH)_{0.5}] \times MeOH** and **[μ -O-{FeL(12)}₂(dmap)]** have *sap* values of 0.96/1.05 and 1.08, respectively. Consequently, lipid layer-like structures were observed. In contrast to this, **[FeL(12)(dmap)₂]** is a special case. It has a *sap* of 1.12 and the two alkyl chains are not ordered parallel to each other which is usually the case. They split slightly apart from each other and, as a result, the lipid layer-like arrangement is incomplete. Similar complexes with a *sap* of 1.20 or above didn't show lipid layer-like structures. Therefore, it can be concluded that **[FeL(12)(dmap)₂]** is on the border of forming these structures.

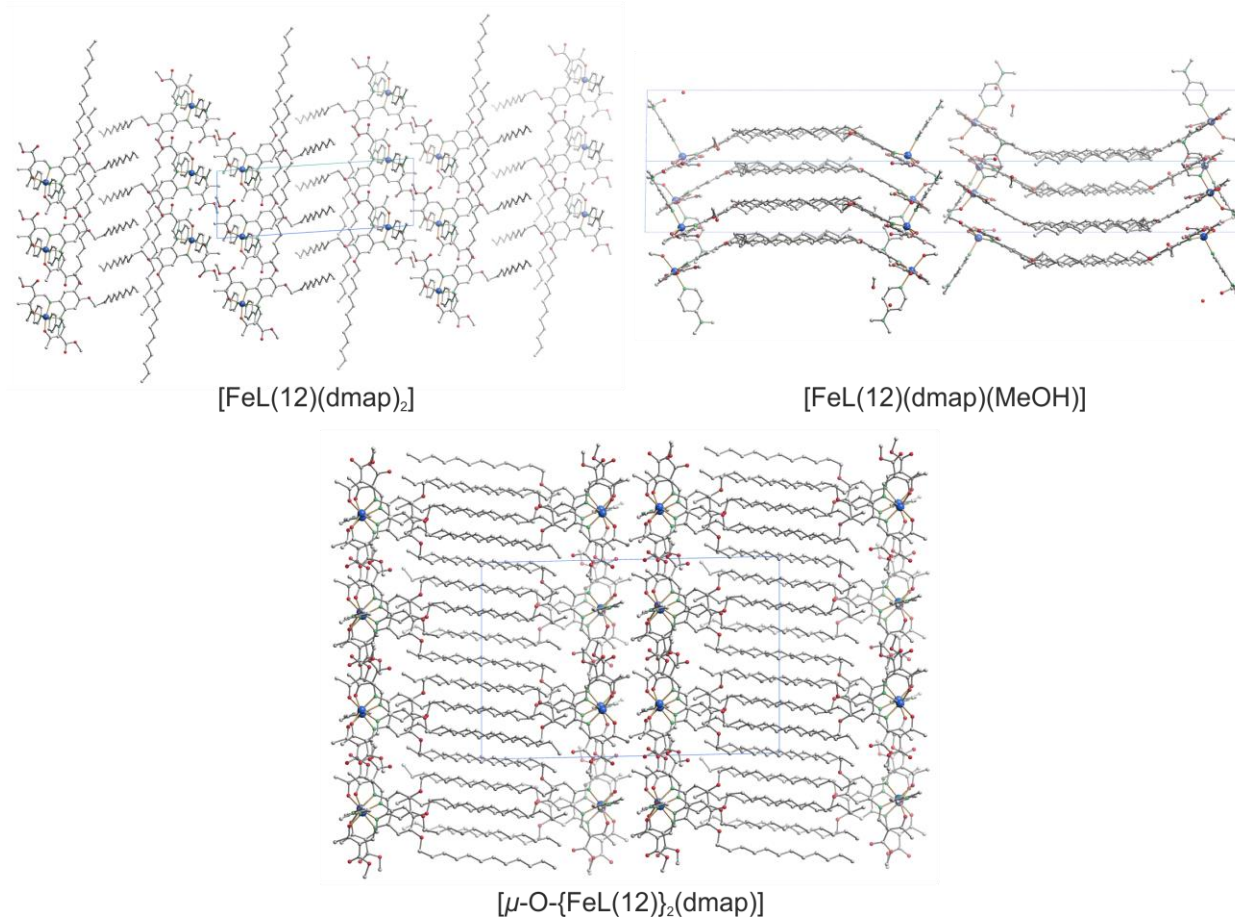


Figure 14: Molecular packing of $[\text{FeL}(\mathbf{12})(\text{dmap})_2]$ along $[0\ 1\ 0]$ (top, left), $[\text{FeL}(\mathbf{12})(\text{dmap})(\text{MeOH})]$ along $[1\ 1\ 0]$ (top, right), and $[\mu\text{-O-}\{\text{FeL}(\mathbf{12})\}_2(\text{dmap})]$ along $[1\ 0\ 0]$ (bottom). Hydrogen atoms are omitted for clarity.

The magnetic properties of $[\text{FeL}(\mathbf{12})(\text{dmap})_2]$ and $[\text{FeL}(\mathbf{12})\text{bipy}]_n$ are shown in **Figure 15**. They were SCO active and a hysteresis appeared for both complexes during the temperature dependent measurement in the sweep mode with a scan rate of 5 K/min. The hysteresis widths were 44 and 15 K, respectively. The measurements were repeated in the settle mode with a scan rate of 0.3 K/min. The hysteresis appeared slightly shifted with $T_{1/2}^\downarrow = 150\text{ K}$ and $T_{1/2}^\uparrow = 173\text{ K}$ for $[\text{FeL}(\mathbf{12})(\text{dmap})_2]$ and with $T_{1/2}^\downarrow = 126\text{ K}$ and $T_{1/2}^\uparrow = 136\text{ K}$ for $[\text{FeL}(\mathbf{12})\text{bipy}]_n$. Consequently, the complexes possessed a hysteresis loop with widths of 23 and 10 K, respectively. The shift was suspected to be caused by kinetic effects, such as the scan rate, which were then further investigated. The samples were rapidly cooled down from room temperature to 10 K. At this temperature point the $\chi_{\text{M}}T$ values were unexpectedly high and were more fitting to the HS state. When the samples were slowly heated up a drop in the $\chi_{\text{M}}T$ value was observed with a T_{TIESST} of 121 and 101 K, respectively. Below these temperatures the samples were kinetically trapped in a metastable HS state which was associated with the TIESST effect. This behaviour was not observed for similar Jäger type complexes without alkyl chains. Further heating up resulted in the continuation of the $\chi_{\text{M}}T$ values known from the settle measurement. Additionally, the real

hysteresis without kinetic effects was obtained for $[\text{FeL}(\mathbf{12})\text{bipy}]_n$. For this, the sample was cooled down from room temperature to specific temperatures (115 K, 120 K, 125 K, 130 K, 135 K, and 140 K) in the temperature range of the hysteresis and kept constant at this temperature for several hours while the magnetic susceptibility was recorded. The kinetically corrected hysteresis width was about 6 K broad.

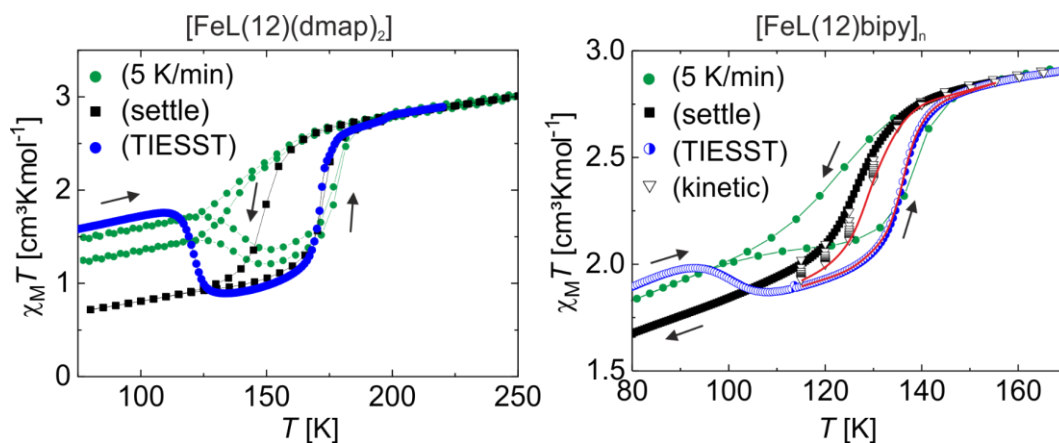
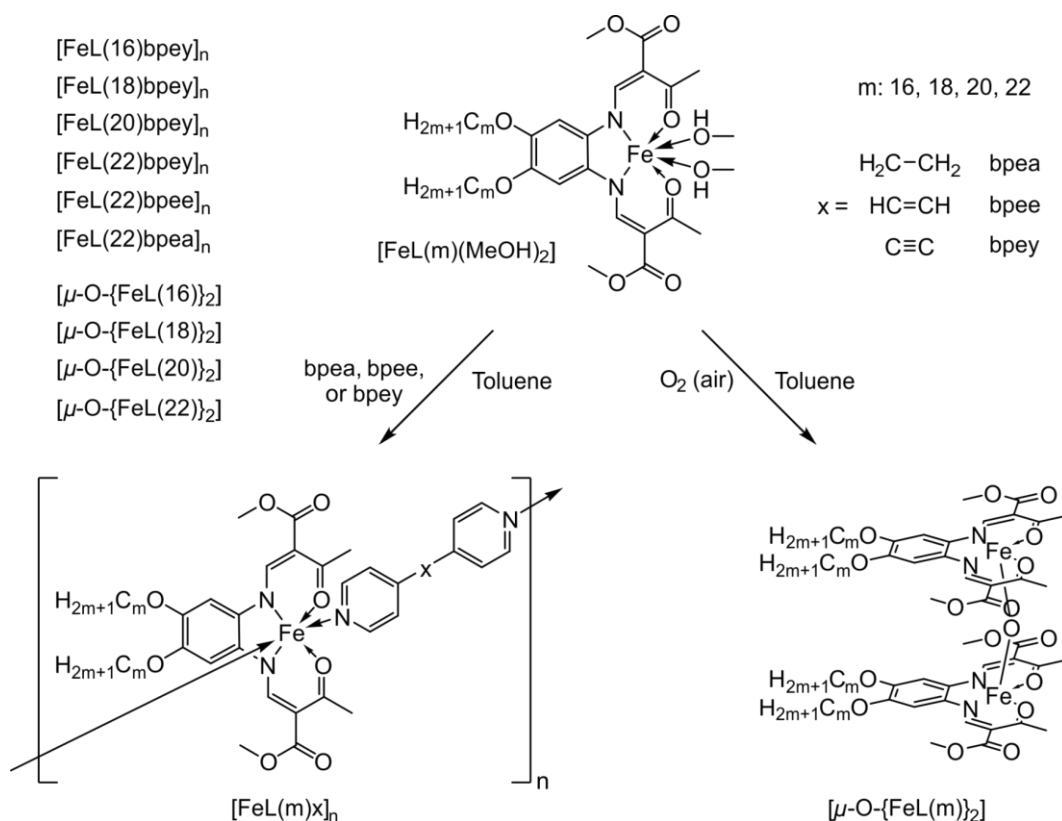


Figure 15: Magnetic measurements of $[\text{FeL}(\mathbf{12})(\text{dmap})_2]$ (left) and of $[\text{FeL}(\mathbf{12})\text{bipy}]_n$ (right) with $\chi_M T$ plotted against T . The green circles show the sweep mode with a scan rate of 5 K/min. The black squares show the measurement in the settle mode with a scan rate of 0.3 K/min. The blue circles represent the TIESST measurement where the samples were abruptly cooled down from room temperature to 10 K and slowly heated up with a scan rate of 0.3 K/min in the settle mode. The triangles show the real hysteresis width without the kinetic effects which is represented by the red line. Here, the sample was cooled down from room temperature to specific temperatures (115 K, 120 K, 125 K, 130 K, 135 K, 140 K) and kept at this temperature for several hours while the magnetic susceptibility was recorded.

In **Chapter 7** the Schiff base-like ligand system was extended to bear C16, C18, C20, and C22 alkyl chains as shown in **Scheme 5**. The Fe(II) centres were connected with a variety of different bridging ligands with increasing rigidity from bpea to bpee to bpey. Through this connection they formed coordination polymers similar to $[\text{FeL}(\mathbf{12})\text{bipy}]_n$ as reported in **Chapter 6**. The corresponding μ -O-Fe(III) complexes were synthesised and characterised, as well, to identify oxidation processes in the measurements.



Scheme 5: Synthesis procedure of the complexes of **Chapter 7**. The possible variation of the alkyl chain length and the bridging ligand is shown top, right. Not all combinations were successfully synthesised and in addition to the Fe(II) complexes Fe(III) complexes were synthesised, as well. The obtained and characterised Fe(II) and Fe(III) complexes are listed top, left.

Crystal structures were obtained for the precursor $[\text{FeL}(20)(\text{MeOH})_2]$ and for the coordination polymers $[\text{FeL}(22)\text{bpey}]_n$ and $[\text{FeL}(22)\text{bpea}]_n$ as shown with the molecular packing in **Figure 16**. The *sap* values for $[\text{FeL}(22)\text{bpey}]_n$ and $[\text{FeL}(22)\text{bpea}]_n$ were 1.0 and 0.9, respectively, and agree with the formation of the lipid layer-like arrangements in the crystal structure. However, the *sap* of $[\text{FeL}(20)(\text{MeOH})_2]$ is 0.7. Nevertheless, the lipid-like layers were observed, too. This was explained by the formation of H-bonds between the head groups. It was also suggested that for the formation of the lipid layer-like arrangements the *sap* can be lower than 1 as there were not many examples found in literature for this case.

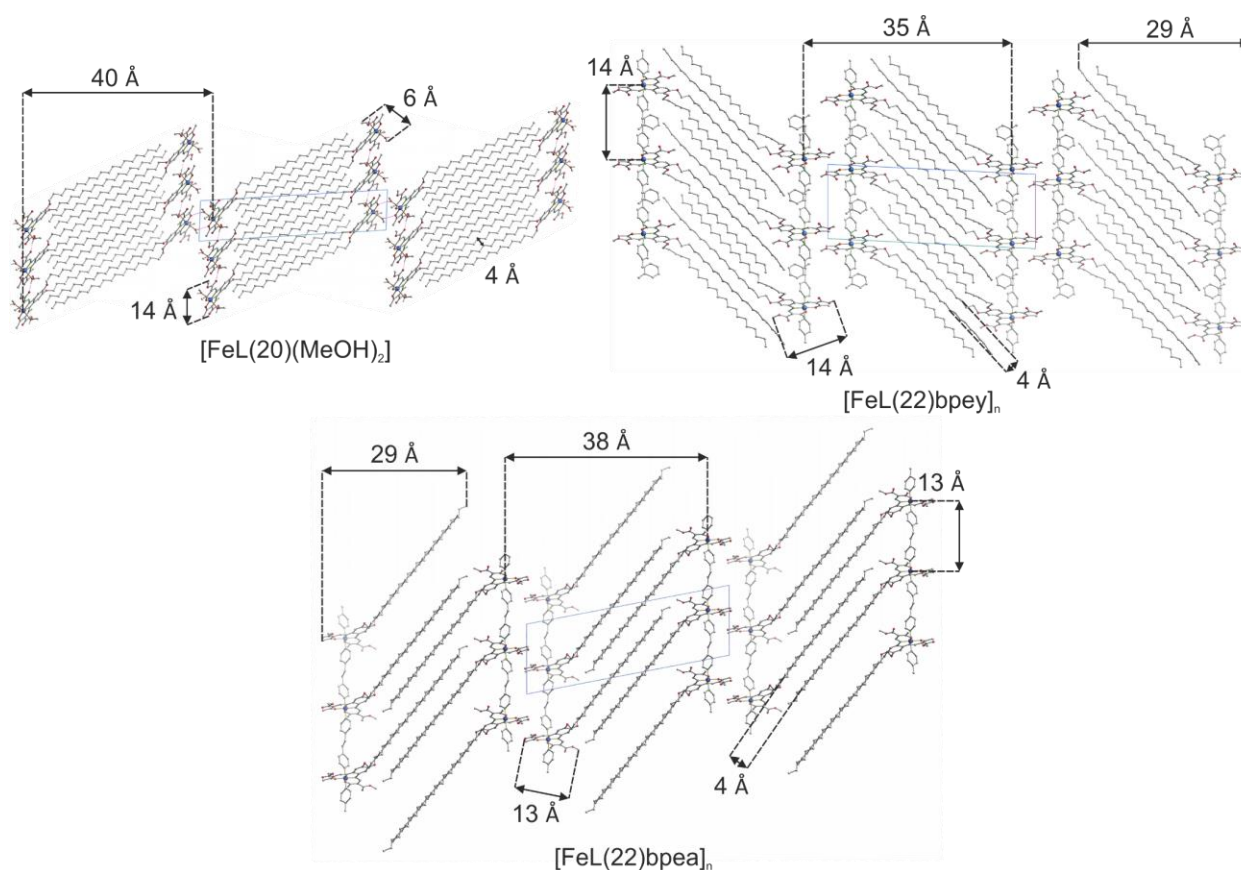


Figure 16: Molecular packing of $[\text{FeL}(20)(\text{MeOH})_2]$ along $[0.3\ 2.3\ 0.3]$ (top, left), $[\text{FeL}(22)\text{bpey}]_n$ along $[1\ 0\ 0]$ (top, right), and $[\text{FeL}(22)\text{bpea}]_n$ along $[1\ 0\ 0]$ (bottom). Selected intermolecular distances discussed in **Chapter 7** are indicated with arrows. Hydrogen atoms are omitted for clarity.

The Fe(II) coordination polymers showed an interesting connection between the magnetic properties and a phase transition as shown in **Figure 17** for $[\text{FeL}(22)\text{bpey}]_n$. The observations were supported by Mössbauer measurements, too. In general, the polymeric compounds were in the LS state at room temperature. Around 350 K all Fe(II) complexes had an abrupt, irreversible SCO which could be associated to a phase transition in the DSC measurements. Cooling down from 400 K to 50 K resulted an incomplete, reversible and gradual SCO with $T_{1/2}$ around 220 K. The enthalpy ΔH and the entropy ΔS calculated from the DSC measurement during the abrupt SCO were increasing with an increase of the chain length or the rigidity of the bridging ligand.

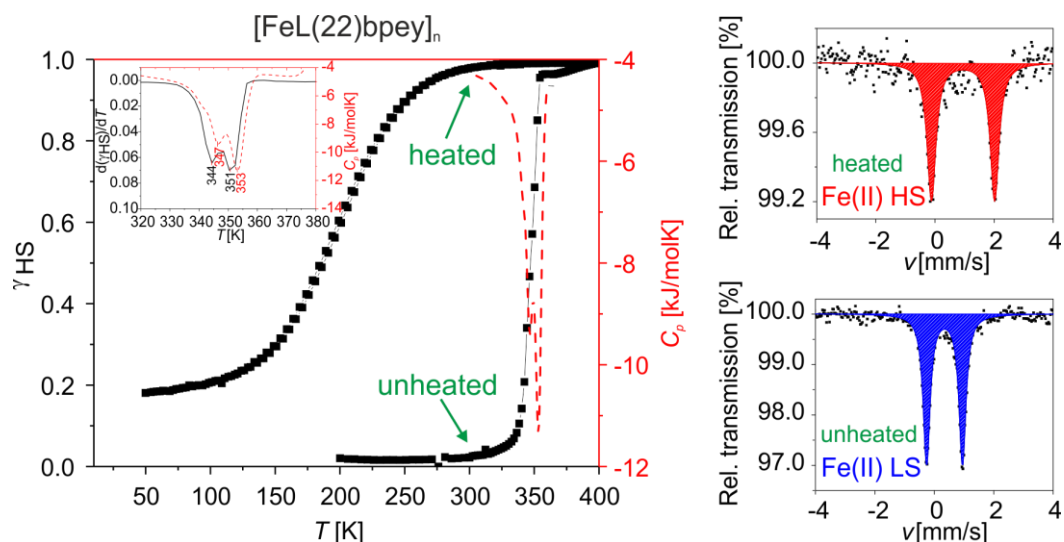


Figure 17: The magnetic measurements (left in black), the DSC measurements (left in red), and the Mössbauer studies (right) of $[\text{FeL}(22)\text{bpey}]_n$. The derivative of the γ_{HS} fraction and the heat capacity C_p are shown in the inset (left) to improve the identification of the thermal overlap.

The behaviour of the phase transition during the SCO was further studied by temperature dependent PXRD measurements. The 2θ values in the range of $2.0^\circ - 3.5^\circ$ were correlated to distances of two Fe atoms in neighbouring lipid-like layers with the help of the *Bragg's law*. $[\text{FeL}(22)\text{bpey}]_n$ has an Fe–Fe distance of 35 Å which is labelled in more detail in the molecular packing in **Figure 16**. The distance changed stepwise during the heating process as shown in **Figure 18**. This process took place during the same temperature as the SCO ($T_{1/2} = 344$ K/351 K). Repeating heating cycles in the PXRD measurement showed that the first phase transition was also irreversible. Therefore, it could be concluded that the structural rearrangement during the phase transition triggered the SCO.

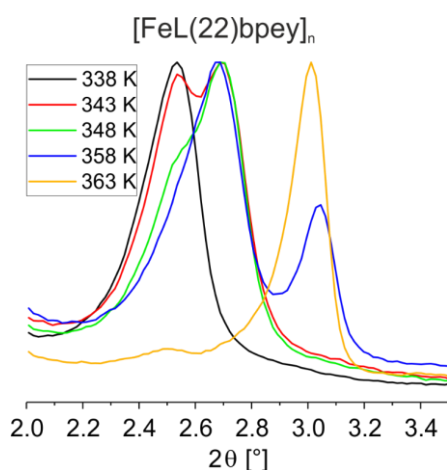


Figure 18: Temperature dependent PXRD patterns of $[\text{FeL}(22)\text{bpey}]_n$ in the range of $2.0^\circ - 3.5^\circ$ 2θ from **Chapter 7**.

The signals of the DSC measurement were also observed as a change of polarisation in the POM micrographs. This includes the phase transition during the SCO, the melting point, and the crystallisation to common liquid crystalline structures. Examples for birefringent spherulites and cross-like structures are given in **Figure 19** with $[\text{FeL}(20)\text{bpey}]_n$ and $[\text{FeL}(22)\text{bpey}]_n$.

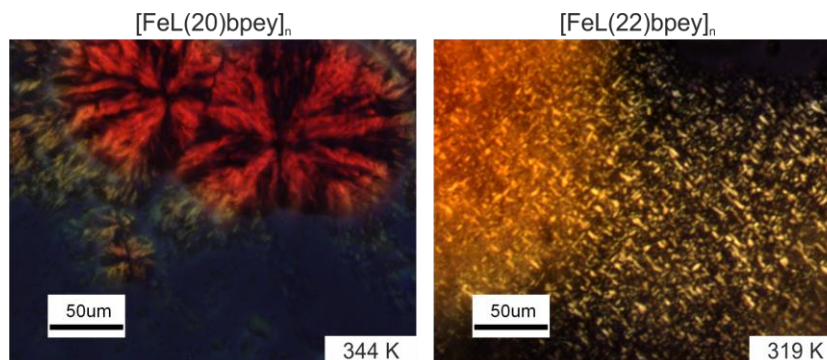


Figure 19: POM micrographs of $[\text{FeL}(20)\text{bpey}]_n$ and $[\text{FeL}(22)\text{bpey}]_n$ during the cooling process. In the solid phase spherulites (left) and cross-like structures (right) were observed for the complexes in **Chapter 7**.

The complexes were then tested for the formation of thin films as this can be a first step towards the application of multifunctional materials. For the spin coating procedure, the complexes had to be dissolved in a fast evaporating solvent such as toluene. The Fe(II) complexes have a high air sensitivity in solution. Therefore, $[\mu\text{-O-}\{\text{FeL}(16)\}_2]$ was used for spin coating. The obtained film was characterised by AFM afterwards. In low concentrations the complex formed networks where most of the silicon wafer was still visible. Increasing the concentration resulted in the successful formation of a homogenous film. Its thickness was measured by carving a small scratch with a needle in it. The film is shown in **Figure 20** and it had an average film thickness of 30 nm and a root mean square (RMS) roughness of 1.3 nm. It was even possible to halve the film thickness to 15 nm by increasing the spin speed from 2000 rpm to 5000 rpm.

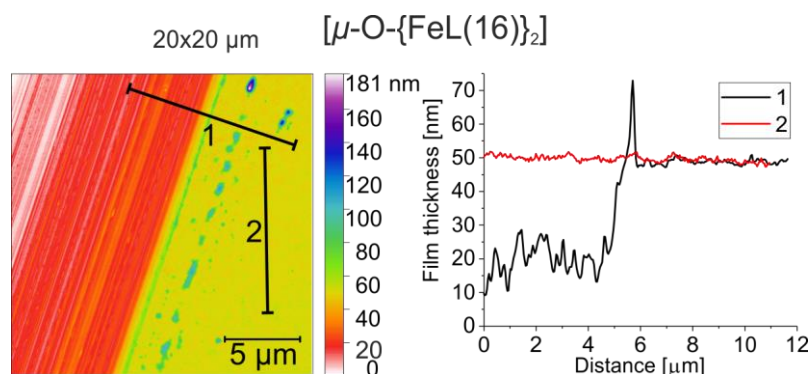


Figure 20: AFM measurement of a spin coated film of $[\mu\text{-O-}\{\text{FeL}(16)\}_2]$ of **Chapter 7** on which a scratch was implied with a needle. The AFM micrograph on the left side shows the film mostly in yellow and the silica wafer in red. The two extracted height profiles are presented on the right side.

The crystal structure and the SEM images of $[\text{FeL}(22)\text{bpey}]_n$ showed that the crystalline platelets themselves consisted of a pile of thin layers. Consequently, it was tested if the layers could be separated by delamination. For this, the crystalline powder was dispersed in iso-octane and shortly ultrasonicated. Subsequently, some drops were applied on a TEM grid or a mica plate and used for measurement. An advantage of the procedure was that the Fe(II) complex was not dissolved and kept its relatively high air resistance of the solid phase. The results are presented in **Figure 21**. Platelets consisting of very few layers can be observed in the TEM micrograph. In comparison to the SEM measurements they appeared to be much thinner and more separated. The thickness of the platelets was again determined by AFM. Small agglomerates of platelets with a more random stacking were observed. Due to this, the thickness could only be roughly determined between 75 and 250 nm and it was difficult to distinguish between thicker platelets and multistacking.

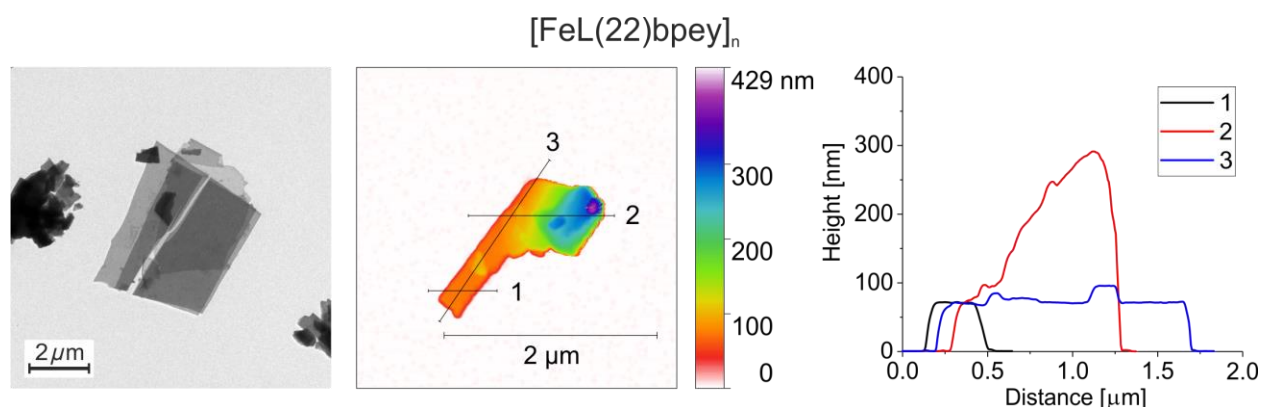
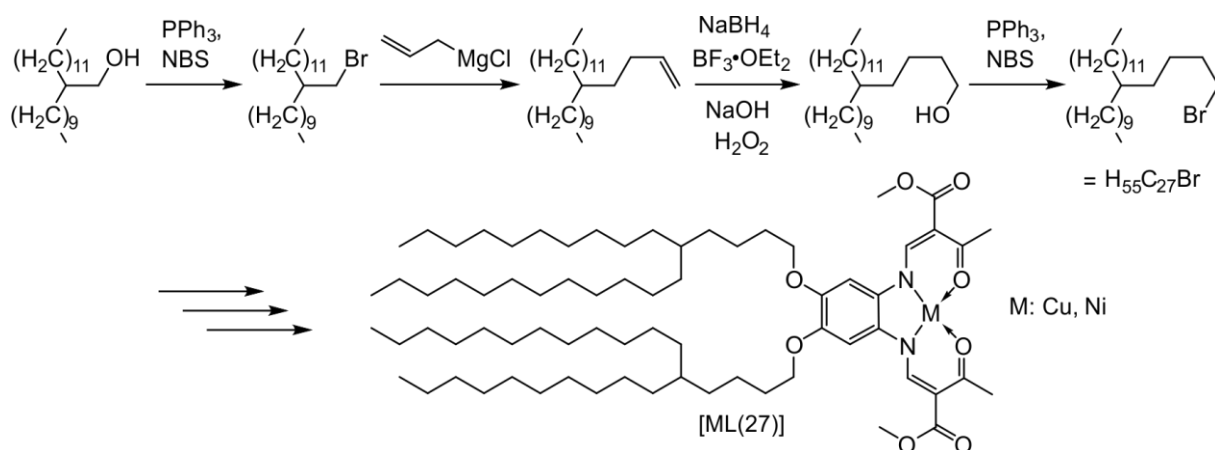


Figure 21: TEM (left) and AFM (centre) micrographs of $[\text{FeL}(22)\text{bpey}]_n$ after the delamination procedure from **Chapter 7**. Three extracted height profiles of the AFM measurement are shown on the right side.

The presented system of **Chapter 7** showed a high potential for future investigations. However, additional modifications seemed to be interesting to obtain further properties. Branched alkyl chains were introduced to the ligand system to have a higher focus on the amphiphilicity and on the self-assembly behaviour. Another important thought was to reduce the temperature of the abrupt SCO of the Fe(II) complexes of **Chapter 7** by reducing the phase transition temperature through a lower steric order of the branched alkyl chains. This would give an additional proof of the phase transition triggering the SCO and it would also bring the SCO closer to room temperature which is attractive for future applications. In **Chapter 8** the synthesis of the Schiff base-like ligand with long, branched alkyl chains and the corresponding Cu(II) and Ni(II) complexes is discussed. The complexes presented remarkable self-assembly behaviour and magnetic properties. The synthesis of Fe(II) complexes was carried out in prior tests, as well, but showed to be quite challenging. As a result, it will not be further discussed in this thesis.

The branched alkyl chains had to be elongated before attaching them to catechol. Without this procedure only one chain was attached due to steric hindrance of the branching. The synthesis is

shown in **Scheme 6**. In the first step the alcohol group was reacted with PPh₃ and NBS to the alkyl bromide. It is an *Appel* reaction based on an S_N2 mechanism. In the next step the chain of the alkyl bromide was elongated by reacting it with a *Grignard* reagent bearing an alkenyl group. The double bond was used in a hydroboration-oxidation reaction to form the alcohol. In the last step the alcohol group was again reacted with PPh₃ and NBS to the elongated alkyl bromide. Subsequently, it was reacted in the same way with catechol as the unbranched alkyl bromides as shown in **Scheme 3**. The following steps to the Cu(II) and the Ni(II) complexes proceeded accordingly, as well.



Scheme 6: Synthetic procedure for the elongation of the branched alkyl chains of **Chapter 8**. The following steps to the Cu(II) and the Ni(II) complex is schematically indicated with arrows. The synthesis steps are shown in more detail in **Scheme 3**.

Various measurements were done for the characterisation of the properties of [CuL(27)] and [NiL(27)]. In principle, they can be divided into measurements in solution and in the solid state. In solution the self-assembly of inverse micelles and the coordination induced spin state switching (CISSS) behaviour were studied. The complexes were first dissolved in *n*-hexane and examined in the DLS to see if they formed micellar structures. The head groups did not congregate and seemed to be nonpolar enough to be surrounded by *n*-hexane. Further tests with the addition of MeOH were carried out. The idea was that the complexes would act as a surfactant between the *n*-hexane and the MeOH phase. Indeed, the miscibility of both solvents improved in the presence of the complexes. However, no inverse micelles were observed. The self-assembly was to be improved with the addition of KSCN or NaCN to the MeOH phase. Their anions were able to coordinate to the metal centre which increased the polarity of the head group. The affinity of SCN⁻ still proved to be too weak. Nevertheless, the formation of inverse micelles was observed with the addition of CN⁻ for both complexes. [NiL(27)] formed more stable inverse micelles as the correlation function of the DLS measurement with [CuL(27)] started to collapse for higher MeOH/NaCN concentrations. The size distributions of [CuL(27)] and [NiL(27)] in *n*-hexane with

MeOH/NaCN are shown in **Figure 22**. The measurements with **[CuL(27)]** resulted in a bimodal distribution with hydrodynamic radii of 744 ± 203 nm and 6593 ± 1289 nm. It is important to note that the DLS device was only suited for monomodal distributions of spherical particles. Therefore, other structures, such as layers or tubes, were also possible but not detectable in the DLS. Inverse micelles with two different concentrations of MeOH/NaCN were observed for **[NiL(27)]**. 10 μ L MeOH/2 eq. NaCN and 20 μ L MeOH/4 eq. NaCN gave hydrodynamic radii of 772 ± 159 nm and 1173 ± 273 nm, respectively. This showed that the hydrodynamic radius of the inverse micelles can be adjusted with the amount of MeOH/NaCN added.

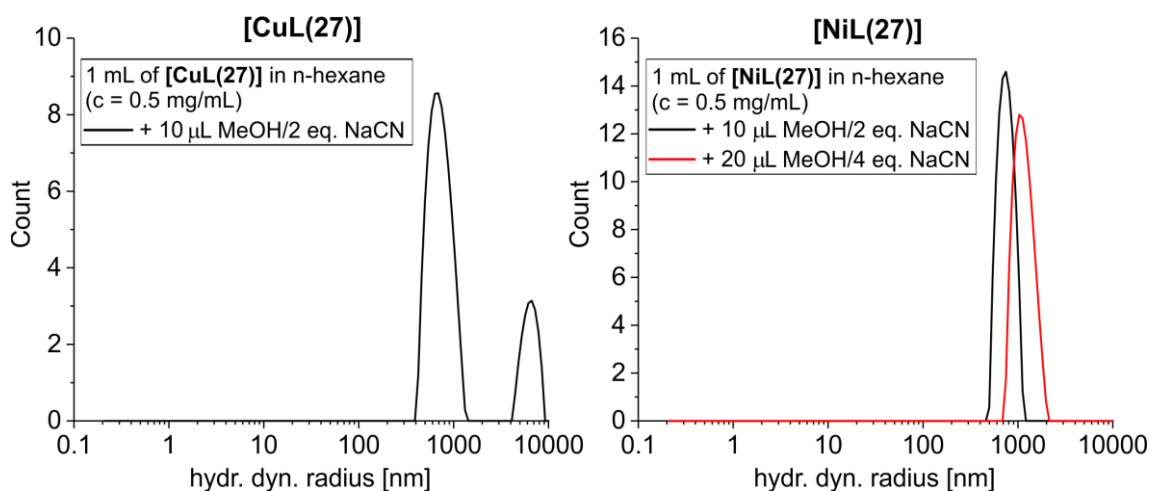


Figure 22: Size distributions from **Chapter 8** of the hydrodynamic radii of the inverse micelles obtained from the DLS measurements. For this **[CuL(27)]** (left) and **[NiL(27)]** (right) were dissolved in *n*-hexane and different amounts of MeOH/NaCN were added.

In addition to the DLS measurements, the solutions were prepared on copper grids and examined by TEM. In the obtained micrographs **[CuL(27)]** and **[NiL(27)]** did not form clear structures in *n*-hexane or in *n*-hexane with MeOH added. Nevertheless, both complexes formed spherical micelles when MeOH/NaCN was added to the *n*-hexane solution. The particle size was with 775 ± 561 nm for **[CuL(27)]** and 578 ± 386 nm for **[NiL(27)]** broadly distributed, but in agreement with the DLS measurements.

Ni(II) complexes are known for the CISSS effect. Here, a change in the coordination number influences the ligand field splitting and by this the magnetic properties of the complex. Thereby, it is possible to switch from a diamagnetic to a paramagnetic spin state as shown in **Figure 23**.

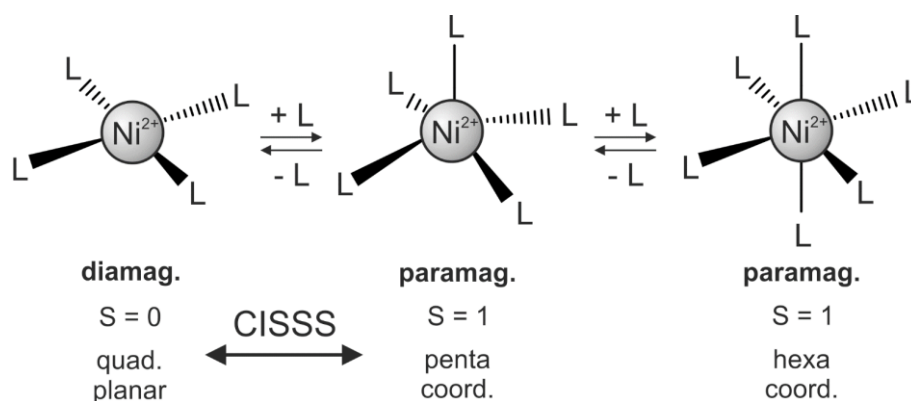


Figure 23: Schematic presentation of the CISSS for a Ni(II) complex with different numbers of ligands L. The magnetic properties change in correlation with the coordination sphere.

The different magnetic spin states were detected with $^1\text{H-NMR}$ studies in a non-coordinating (CDCl_3) and a coordinating solvent (pyridine- d_5). In CDCl_3 sharp signals of the diamagnetic species were observed. However, measuring in pyridine- d_5 resulted in a broadening and a low field shift of the signals which is typical for paramagnetic species. The effects were stronger for protons close to the Ni(II) centre.

The coordination of pyridine was also confirmed with UV-Vis measurements for $[\text{CuL}(27)]$ and for $[\text{NiL}(27)]$, when both complexes were dissolved in CHCl_3 and titrated with pyridine. The Cu(II) complex showed only a change in the d-d transition processes, whereas $[\text{NiL}(27)]$ had a change in the d-d transition and in the charge transfer processes.

It was tested if a CISSS could be observed under the same conditions as in the DLS measurements where micelles were formed. Due to the different precisions of the detectors in each device the concentrations had to be adjusted. It was not possible to use a high number of equivalents of NaCN as the miscibility of *n*-hexane and MeOH/NaCN reached its maximum very early. This could be a reason that no changes in the electronic transitions were observed for $[\text{CuL}(27)]$. Nevertheless, small changes were observed for $[\text{NiL}(27)]$ in the region of the d-d transition and the charge transfer processes. Consequently, it was shown that it is possible to obtain spherical micelles which exhibit the CISSS effect.

In the solid state the magnetic, the phase transition, and the liquid crystalline properties were investigated. The magnetic measurements were carried out in the temperature range of 50 to 400 K. $[\text{CuL}(27)]$ showed a paramagnetic signal corresponding to one unpaired electron while $[\text{NiL}(27)]$ showed a diamagnetic signal. Both signals did not change significantly over the whole temperature range.

TGA measurements showed a temperature stability of $[\text{CuL}(27)]$ and of $[\text{NiL}(27)]$ approximately until 568 K and 539 K, respectively. The DSC measurements showed several phase transition processes. $[\text{CuL}(27)]$ melted between 336 and 421 K and crystallised during the cooling process

between 397 and 355 K. For **[NiL(27)]** the temperature range of the melting process was 354 to 378 K and for the crystallisation process 375 to 368 K. A broad solid-solid phase transition was observed for both complexes in the heating and the cooling mode around 229 K and 231 K, respectively.

POM micrographs showed the different phase transitions in more detail. The melting processes of both complexes were observed in a similar region as in the DSC measurements. Discrepancies were possibly caused by the different scan rates or by the manual baseline correction of the DSC measurements. The cooling of the samples from the melt resulted for both complexes in the formation of spherulites which were associated with liquid crystalline structures. During the cooling process **[CuL(27)]** simultaneously formed a second phase consisting of well-defined six armed stars that slowly converted to the spherulitic phase until room temperature. The POM micrographs of the structures are shown in **Figure 24**.

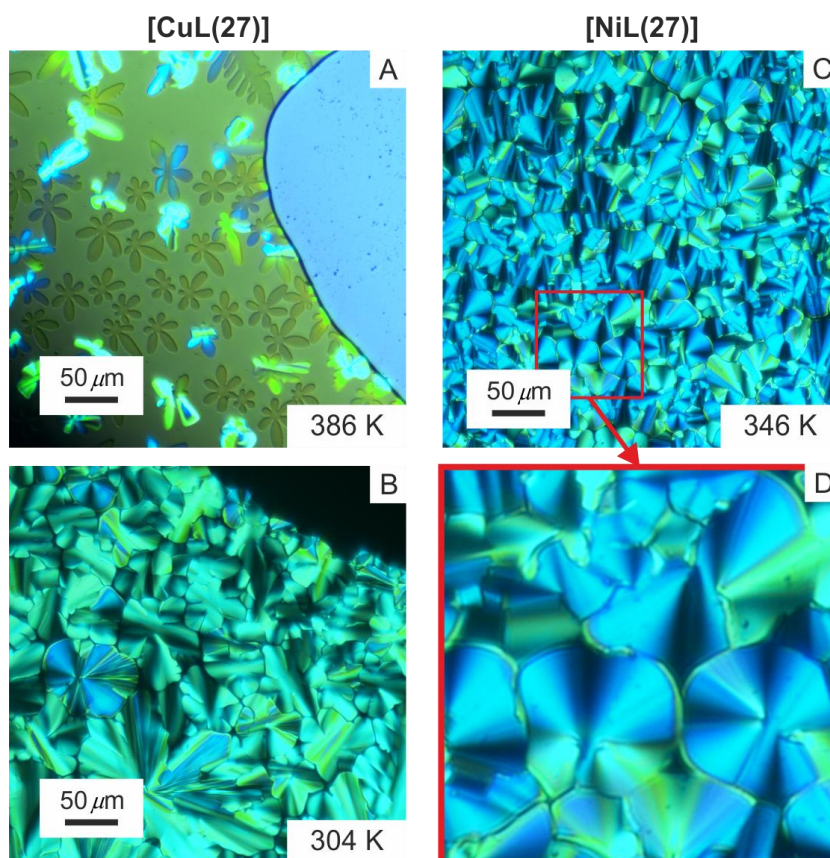


Figure 24: POM micrographs from **Chapter 8** of **[CuL(27)]** (A and B) and **[NiL(27)]** (C and D) of the crystallisation during the cooling process. Image D is a magnification of a part of image C.

Temperature dependent PXRD measurements showed weak changes in the distances during the heating and the cooling mode for both complexes. However, a distinct distance for this kind of amphiphilic system was shorter than expected and would better fit to alkyl chains with a length of C12 or shorter. Therefore, it was suggested that the order in the packing differed from that of the system with unbranched alkyl chains.

The surface of the wax-like complexes was investigated by SEM before and after melting the samples. For both complexes the surface was smooth with small wrinkles at the beginning. After annealing they formed homogenous thin films which have to be further studied by AFM. The property to form a homogenous thin film from the melt is an interesting aspect and a facile approach for the application as a functional material in surface coating.

5. Individual contributions to joint publications

The results presented in this thesis were obtained in collaboration with others. The contribution of each co-author and associate to the publications will be recognised and explained in this chapter. The state of progress of the publications will be labelled as published, accepted, submitted or to be submitted.

5.1 Kinetic trapping effects in amphiphilic iron(II) spin crossover compounds

The publication is presented in **Chapter 6**. This work *was published* in the Inorganic Chemistry and is referenced as *Inorg. Chem.* **2019**, 58, 1278–1289. The DOI name is 10.1021/acs.inorgchem.8b02763.

Johannes Weihermüller^a, Stephan Schlamp^a, Birger Dittrich^b, Birgit Weber^{a*}

^aDepartment of Chemistry, University of Bayreuth, 95440 Bayreuth, Germany

^bAnorganische Chemie und Strukturchemie II, Heinrich-Heine University Düsseldorf, Universitätsstr. 1, 40225 Düsseldorf, Germany

The project was based on prior studies done by Stephan Schlamp. He synthesised some of the complexes, carried out the magnetic measurements, and solved the crystal structure of **[μ -O-(FeL)₂(dmap)]**. I reproduced the complexes and the magnetic measurements. I carried out the Mössbauer measurements, solved and treated the crystal structure of **[FeL(dmap)₂]**, interpreted all data, and wrote discussion and the introduction including the abstract. Birger Dittrich solved and treated the crystal structure of **[FeL(dmap)(MeOH)]**. Birgit Weber was involved in scientific discussions and the correction of the manuscript.

5.2 Amphiphilic iron(II) spin crossover coordination polymers: crystal structures and phase transition properties

The publication is presented in **Chapter 7**. This work *was published* in the Journal of Material Chemistry C and is referenced as *J. Mater. Chem. C* **2019**, 7, 1151–1163. The DOI name is 10.1039/c8tc05580g.

Johannes Weihermüller,^a Stephan Schlamp,^a Wolfgang Milius,^b Florian Puchtler,^b Josef Breu,^b Philipp Ramming,^c Sven Hüttner,^c Seema Agarwal,^d Christoph Göbel,^a Markus Hund,^e Georg Papastavrou,^e and Birgit Weber^{a*}

^a Department of Chemistry, Inorganic Chemistry IV, Universität Bayreuth, Universitätsstrasse 30, NW I, 95440 Bayreuth, Germany E-mail: weber@unibayreuth.de.

^b Department of Chemistry, Inorganic Chemistry I, Universität Bayreuth, Universitätsstrasse 30, NW I, 95440 Bayreuth, Germany.

^c Department of Chemistry, Macromolecular Chemistry I, Universität Bayreuth, Universitätsstrasse 30, NW I, 95440 Bayreuth, Germany.

^d Department of Chemistry, Macromolecular Chemistry II, Universität Bayreuth, Universitätsstrasse 30, NW I, 95440 Bayreuth, Germany.

^e Department of Chemistry, Physical Chemistry II, Universität Bayreuth, Universitätsstrasse 30, NW I, 95440 Bayreuth, Germany.

The project was based on prior studies done by Stephan Schlamp who solved the crystal structure of **[FeL(22)bpea]_n**. I synthesised and characterised all compounds presented in this thesis by NMR spectroscopy, elemental analysis, MS spectrometry, and IR spectroscopy. I carried out the magnetic measurements, the Mössbauer spectroscopy, and the POM measurements and solved the crystal structure of **[FeL(22)bpey]_n** and of **[FeL(20)(MeOH)₂]**. TGA and DSC measurements were done in the chair of Seema Agarwal and interpreted by me. XRPD measurements were done by Florian Puchtler and Wolfgang Milius in the chair of Josef Breu and interpreted by me. Spin coating of **[μ-O-(FeL(16))₂]** and the characterisation by AFM were done by Philipp Ramming in the chair of Sven Hüttner in my presence and were interpreted by Philipp Ramming and me. TEM measurements were done by Christoph Göbel and interpreted by me. I prepared the delaminated **[FeL(22)bpey]_n** samples which were measured by Markus Hund in the chair of Georg Papastavrou in my presence and were interpreted by Markus Hund and me. I wrote the abstract, the discussion, the experimental part, and the conclusion. Birgit Weber wrote the introduction and was involved in scientific discussions and the correction of the manuscript.

5.3 Behaviour of Cu(II) and Ni(II) Schiff base-like complexes with long, branched alkyl chains in solution and in the solid state: Micelle formation, CISSS, and liquid crystallinity

The publication is presented in **Chapter 8**. This work is *to be submitted* to a scientific journal.

Johannes Weihermüller,^a Stella Buchmann,^a Victoria Müller,^a Wolfgang Milius,^b and Birgit Weber^{a*}

^aDepartment of Chemistry, Inorganic Chemistry IV, Universität Bayreuth, Universitätsstrasse 30, NW I, 95440 Bayreuth, Germany
E-mail: weber@uni-bayreuth.de.

^b Department of Chemistry, Inorganic Chemistry I, Universität Bayreuth,
Universitätsstrasse 30, NW I, 95440 Bayreuth, Germany.

The ligand and the complexes were synthesised and characterised by me or by Stella Buchmann and Victoria Müller under my supervision. Paramagnetic NMR studies were done by Kerstin Hannemann, TEM micrographs were obtained by Christoph Göbel, SEM micrographs were obtained by Christine Denner, TGA measurements were done by Julia Kronawitt, DSC measurements were done by Felix Krohn, and temperature dependent PXRD measurements were done by Wolfgang Milius. The DLS, the UV-Vis, the POM, and the magnetic measurements were carried out by me. The obtained data of each measurement was interpreted by me. I wrote the abstract, the introduction, the discussion, the experimental part, and the conclusion. Birgit Weber was involved in scientific discussions and the correction of the manuscript.

6. Kinetic trapping effects in amphiphilic iron(II) spin crossover compounds

Johannes Weihermüller^a, Stephan Schlamp^a, Birger Dittrich^b, Birgit Weber^{a*}

^aDepartment of Chemistry, University of Bayreuth, 95440 Bayreuth, Germany

^bAnorganische Chemie und Strukturchemie II, Heinrich-Heine University Düsseldorf, Universitätsstr. 1, 40225 Düsseldorf, Germany

Reprinted with permission from *Inorg. Chem.* **2019**, 58, 1278-1289. Copyright 2019 American Chemical Society.

6.1 Abstract

In this work, the synthesis of four new iron complexes with a Schiff base-like amphiphilic equatorial ligand (L) and dimethylaminopyridine (dmap) or 4,4'-bipyridine (bipy) as axial ligands is reported. Three of the complexes ($[\text{FeL}(\text{dmap})_2]$ **1**, $[\text{FeL}(\text{dmap})(\text{MeOH})_{0.5}] \cdot \text{MeOH}$ **2**, and $[\text{FeL}(\text{bipy})]_n$ **3**), have an iron(II) center, and two of those with an N_4O_2 coordination sphere (**1** and **3**) are spin crossover active. Both exhibit a thermal hysteresis (10 K with $T_{1/2} = 131$ K for **3** and 23 K with $T_{1/2} = 161$ K for **1**) where the width depends on the velocity used for the measurement. Additionally, in both cases, the high spin state is trapped by rapid cooling, and a T_{TIESST} was determined to be 121 K (**1**) and 101 K (**3**). Single crystals suitable for X-ray structure analysis were obtained for the three different complexes with dmap as axial ligand (**1S**, **2**, and $[\mu\text{-O}\{\text{FeL}\}_2(\text{dmap})]$ **4**). The complex **1S** has two dmap molecules in axial position, while the other two structures were obtained for a complex where a dmap ligand is exchanged by methanol and one where the iron(II) center is oxidized to iron(III) to form a dinuclear $\mu\text{-O}$ -complex. All three complexes were obtained under similar reaction conditions in the presence/absence of oxygen, and all three structures show the formation of lipid layer-like arrangements in the packing.

6.2 Introduction

Iron(II) spin crossover (SCO) complexes have the ability to reversibly switch between two different magnetic states – the paramagnetic high spin (HS) and the diamagnetic low spin (LS) state. This switching results in a change of chemical and physical properties, like color, magnetism, and size,^[1–3] and opens a way for new types of sensors,^[4] memory devices^[5] or contrast agents.^[6]

The spin transition can be triggered by a wide variety of physical or chemical stimuli such as temperature, pressure, light irradiation, or pH.^[1-3,7] The wide range of SCO complexes and their various areas of application has caught the attention of many researchers worldwide.^[8,9,10,11] Combining SCO with liquid crystallinity,^[11,12,13,14] fluorescence^[15,16] or redox activity leads to further exciting possibilities.^[17] Additionally, those systems are suitable for the synthesis of nanoparticles or the deposition of thin films on surfaces, further extending their application potential.^[18] Of the different types of SCO (gradual, abrupt, with hysteresis, step-wise) the one with a wide thermal hysteresis loop, if possible around or above room temperature, is the most searched for.^[8,19] Here, the two different magnetic states can be observed in the same temperature range depending on the previous sample treatment. Strong intermolecular interactions mediated by hydrogen bonds,^[20] π - π stacking,^[21] or a pronounced structural distortion^[14,22] can cause a high cooperativity between the metal centers and can increase the hysteresis width. In some cases the hysteresis width also depends on the scan rate used for the measurement, as recently shown for cobalt(II)^[23] and iron(II) complexes.^[12,24] For those complexes fast sample cooling can additionally lead to a trapping of the HS state, the so called TIESST (temperature induced excited spin state trapping) effect. The first example for rate-dependent spin crossover and a trapping of the high spin state was reported by Toftlund *et al.*,^[25] and the theoretical foundation for the understanding of this phenomenon were already made in 1980, when Buhks *et al.* investigated it based on quantum mechanical studies.^[26] Further examples followed, many focusing on complexes where the transition temperatures for the stable and the metastable HS state ($T_{1/2}$ and T_{TIESST}) are in a narrow temperature regime.^[27,28,29] For those systems $T_{1/2}$ and T_{TIESST} are usually in inverse proportion and a realization of T_{TIESST} above 100 K is rare. The highest T_{TIESST} observed so far is 250 K. It occurs in the central iron center of a trinuclear iron(II) complex.^[30] Remarkably slow transition dynamics are responsible for the easy trapping of the HS state and also for the observation of a wide thermal hysteresis loop.

In our group we have synthesized a wide variety of mononuclear, dimeric, and polymeric of iron(II) spin crossover complexes based on tetradentate N_2O_2 coordinating Schiff-base like ligands in combination with monodentate or bridging bidentate pyridine or imidazole ligands.^[31,32] All the different types of spin crossover mentioned above were realized by our group,^[31,32] however, so far only two examples for kinetic trapping effects were obtained.^[27,29] In both cases, the T_{TIESST} was significantly below 100 K. Here we report the synthesis of four different amphiphilic iron complexes, all with the same N_2O_2 coordinating Schiff-base like amphiphilic ligand. The impact of the amphiphilic nature of the ligand structure on the complex formation and the resulting magnetic properties is discussed.

6.3 Experimental section

The syntheses of the iron complexes were carried out under an argon atmosphere (argon 5.0) using Schlenk tube techniques. The solvents were purified as described in the literature^[33] and saturated with argon over one hour. The syntheses of $[\text{FeL}(\text{MeOH})_2]$ ^[14] is also described in the literature. 4-(dimethylamino)pyridine (dmap) (Merck, $\geq 99\%$) and 4,4'-bipyridine (Alfa Aesar, 98%) were purchased and used as received.

$[\text{FeL}(\text{dmap})_2]$ **1**: $[\text{FeL}(\text{MeOH})_2]$ (368 mg, 0.435 mmol) and dmap (1.680 g, 13.751 mmol, 32 equiv) were dissolved in MeOH (22 mL) and heated to reflux for 1 h. After three days at 6 °C crystals suitable for x-ray structure analysis were obtained from solution. According to X-ray structure analysis solvent molecules are included in the crystal packing of **1S**. The remaining dark brown crystals were filtered off, washed with MeOH (3x5 mL) and dried under vacuum to yield compound **1**. Yield: 320 mg (72%): $\text{C}_{56}\text{H}_{86}\text{FeN}_6\text{O}_8$ (1027.18): calcd. C 65.48, H 8.44, N 8.18; found C 64.72, H 8.50, N 7.45. Please note that the nitrogen content is lower than expected. This could be due to a partial oxidation as the sample is exposed to air during preparation for elemental analysis or due to an inclusion of solvent molecules. Partially oxidized samples of **1** are denoted as **1*** in the following. MS (DEI-+): m/z (%) 783 (20) ($[\text{FeL}]^+$), 725 (100) ($[\text{FeL}] - \text{C}_2\text{H}_3\text{O}_2^+$). IR: $\tilde{\nu} = 1709$ (s) (C=O), 1603 (s) (C=O), 1582 (s) (C=O) cm^{-1} .

$[\text{FeL}(\text{dmap})(\text{MeOH})_{0.5}] \cdot \text{MeOH}$ **2**: $[\text{FeL}(\text{MeOH})_2]$ (395 mg, 0.466 mmol) and dmap (1.825 g, 14.938 mmol, 32 equiv) were dissolved in MeOH (22 mL) and heated to reflux for 1 h. After 3 days at room temperature most of the solvent was removed and crystals suitable for X-ray structure analysis at a synchrotron were obtained. The synthesis was repeated using 570 mg, (0.673 mmol) $[\text{FeL}(\text{MeOH})_2]$ and 4.138 g (33.650 mmol, 50 equiv) dmap in 34 mL MeOH. Yield: 412 mg (65%) $\text{C}_{50}\text{H}_{80}\text{FeN}_4\text{O}_9$ (937.05): calcd. C 64.09, H 8.61, N 5.98; found C 64.22, H 8.65, N 5.73. MS (DEI-+): m/z (%) 782 (100) ($[\text{FeL}]^+$), 724 (48) ($[\text{FeL}] - \text{C}_2\text{H}_3\text{O}_2^+$). IR: $\nu = 1692$ (s) (C=O), 1600 (s) (C=O), 1571 (s) (C=O) cm^{-1} .

$[\text{FeL}(\text{bipy})]_n$ **3**: $[\text{FeL}(\text{MeOH})_2]$ (440 mg, 0.520 mmol) and bipy (2.210 g, 14.149 mmol, 27 equiv) were dissolved in MeOH (17 mL) and heated to reflux for 1 h. After cooling to room temperature, the red precipitate was filtered and dried under vacuum. Yield: 460 mg (94%). $\text{C}_{52}\text{H}_{74}\text{FeN}_4\text{O}_8 \times \text{bipy}$ (1095.19): calcd. C 67.99, H 7.55, N 7.67; found C 67.71, H 7.61, N 7.58. MS (DEI-+): m/z (%) 782 (100) ($[\text{FeL}]^+$), 724 (48) ($[\text{FeL}] - \text{C}_2\text{H}_3\text{O}_2^+$). IR: $\nu = 1689$ (s) (C=O), 1602 (s) (C=O), 1562 (s) (C=O) cm^{-1} .

$[\mu\text{-O-}\{\text{FeL}\}_2(\text{dmap})]$ **4**: $[\text{FeL}(\text{MeOH})_2]$ (190 mg, 0.224 mmol) and dmap (820 mg, 6.712 mmol, 30 equiv) were dissolved in MeOH (10 mL) and heated to reflux for 1 h. After three days at 6 °C crystals suitable for x-ray structure analysis were obtained from solution. X-ray structure analysis

revealed that during the synthesis oxidation of the iron center did occur. The synthesis was repeated allowing a purposeful oxidation of the complex. Yield: 10 mg (4%). $C_{84}H_{132}Fe_2N_4O_{17} \times 1.0 \text{ MeOH} \times 4.0 \text{ dmap}$ (2102.41): calcd. C 64.56, H 8.44, N 7.99; found C 64.56, H 9.24, N 7.60. MS (DEI-+): m/z (%) 783 (50) $([FeL])^+$, 725 (100) $([FeL] - C_2H_3O_2)^+$. IR: $\nu = 1709$ (s) (C=O), 1602 (s) (C=O), 1582 (s) (C=O) cm^{-1} .

Elemental Analysis: Carbon, hydrogen and nitrogen contents were measured using a Vario EL III. The samples were prepared in tin boats and acetanilide (Merck) was used as standard.

Mass Spectrometry: Mass spectra were recorded with a MS8500 sector field mass spectrometer from Thermo Finnigan. Direct injection was used and the measurement was done in a temperature range of room temperature to 330 °C.

Infrared Spectroscopy: Transmission infrared spectra were collected using a PerkinElmer Spectrum 100 FT-IR (ATR). The samples were measured as solids.

Single Crystal X-ray Diffraction: The single-crystal X-ray data collection of **1** was done on a STOE StadiVari diffractometer, the one of **4** was done on a Stoe IPDS II diffractometer. Both were using graphite-monochromatic Mo- K_α radiation. The data were corrected for Lorentzian and polarization effects. The structures were solved by direct methods (SIR-97, SIR2014)^[34] and refined by full matrix-least square techniques against F_0^2 (SHELXL-97)^[35] Hydrogen atoms were included at calculated positions with fixed displacement parameters. Due to pronounced disorder in **1** the included solvent could not be resolved and was “squeezed” with PLATON.^[36] Due to long lattice constants and difficulties of finding a sufficiently large single-crystal specimen structure solution of **2** was only successful after using microcrystals that were measured at the SLS synchrotron, beamline X10SA at the PSI in Villigen, Switzerland. SHELXT^[37] was used for structure solution and XDS^[38] for data reduction. Refinement was carried out with SHELXL^[39] with the graphical user interface ShelXle.^[40] ORTEP-III was used for the presentation of the asymmetric unit of the crystal structure and^[41] SCHAKAL-99 to illustrate the molecular packing.^[42] The supplementary crystallographic data for **1** (CCDC 1857855), for **2** (CCDC 1831460), and for **4** (CCDC 1857875) can be obtained free of charge from The Cambridge Crystallographic Data Centre via www.ccdc.cam.ac.uk/data_request/cif.

Powder X-ray Diffraction: Temperature dependent PXRD measurements of **3** were done on an X’Pert MPD Pro diffractometer from Panalytical (Bragg-Brentano geometry). Cu- K_α radiation was used. The samples were measured on a flat plate under nitrogen atmosphere in an XRK-900 chamber from Anton Paar.

Magnetic Measurements: Magnetic measurements were collected using a SQUID MPMS-XL5 instrument from Quantum Design. A field of 0.5 T was applied over the temperature range.

Gelatine capsules in a plastic straw were used for sample preparation. The diamagnetic parts of the sample holder and the organic ligand were corrected afterwards by using measured values and tabulated Pascal's constants.^[43]

Mössbauer Spectroscopy: ⁵⁷Fe Mössbauer spectra were recorded in transmission geometry at constant acceleration using a conventional Mössbauer spectrometer with a 50 mCi ⁵⁷Co(Rh) source. The samples were prepared under argon atmosphere. The spectra were fitted using Recoil 1.05 Mössbauer analysis software.^[44] Isomer shift values were reported with respect to α -Fe as a reference at room temperature.

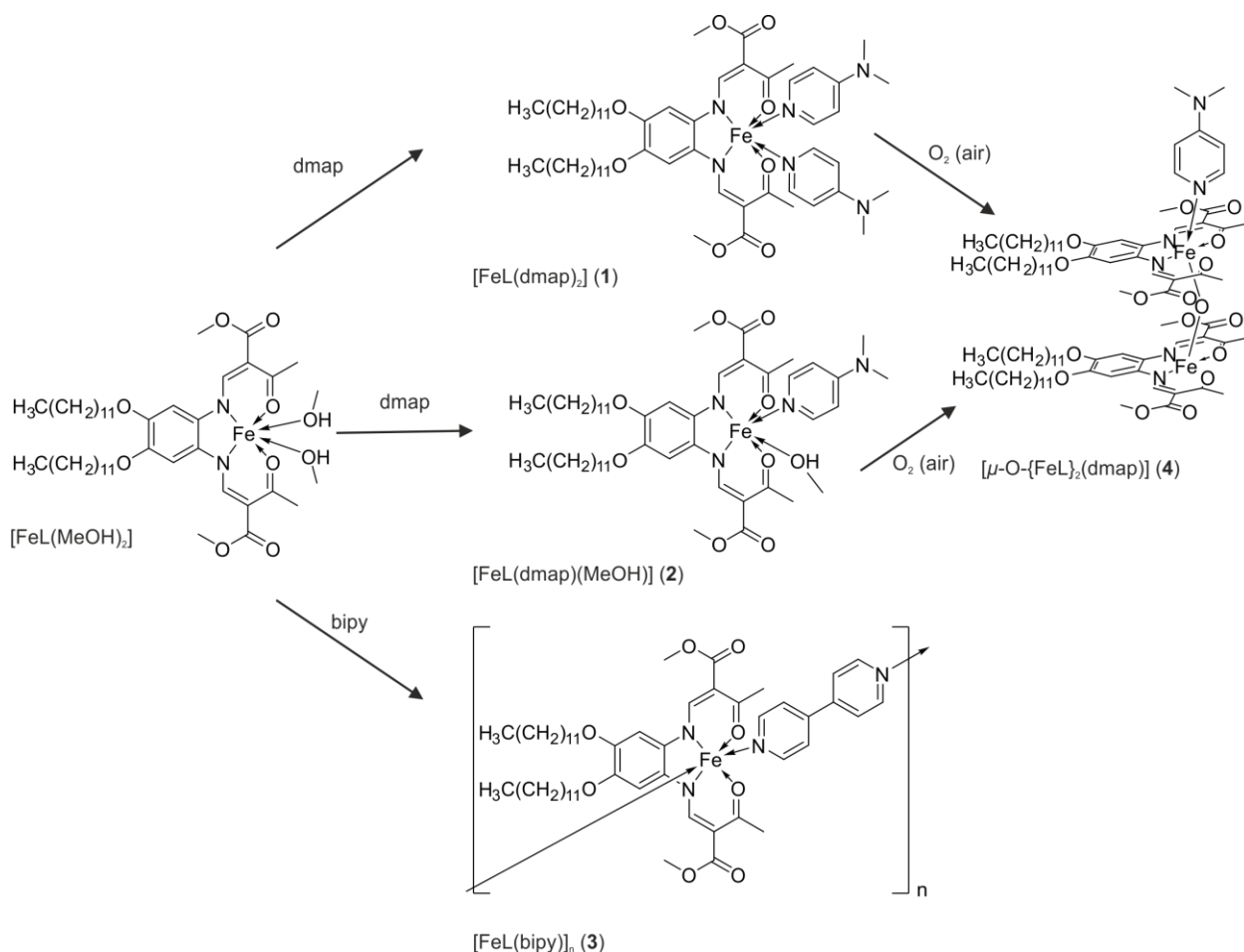
6.4 Results

6.4.1 Synthesis of the complexes

The general synthetic pathway for the iron complexes and the abbreviations used are shown in **Scheme 1**, and in **Table 1**, an overview over all discussed samples is given. The precursor iron(II) complex $[\text{FeL}(\text{MeOH})_2]$ was synthesized as reported previously.^[45] It was further converted in methanol with either dmap to yield the mononuclear complexes $[\text{FeL}(\text{dmap})_2]$ **1**, single crystals of **1** with unknown solvent contents (**1S**), $[\text{FeL}(\text{dmap})(\text{MeOH})_{0.5}] \cdot \text{MeOH}$ **2**, or the dinuclear complex $[\mu\text{-O-}\{\text{FeL}\}_2(\text{dmap})]$ **4**, depending on small changes in the reaction conditions. Especially **1** is highly air sensitive and partially oxidized samples of **1** (mixtures of **1** and **4**) are denoted as **1***.

Table 1: Overview of the complexes discussed in this work.

Compound	Formula	Origin
1	$[\text{FeL}(\text{dmap})_2]$	from synthesis, dried in vacuum
1S	$[\text{FeL}(\text{dmap})_2] \cdot \text{solvent}$	from synthesis, single crystal
1*	$[\text{FeL}(\text{dmap})_2]/[\mu\text{-O-}\{\text{FeL}\}_2(\text{dmap})]$	partially oxidized 1
2	$[\text{FeL}(\text{dmap})(\text{MeOH})_{0.5}] \cdot \text{MeOH}$	from synthesis
3	$[\text{FeL}(\text{bipy})]_n$	from synthesis
4	$[\mu\text{-O-}\{\text{FeL}\}_2(\text{dmap})]$	from synthesis



Scheme 1: Synthesis route of compounds $[\text{FeL}(\text{dmap})_2]$ **1**, $[\text{FeL}(\text{dmap})(\text{MeOH})_{0.5}] \cdot \text{MeOH}$ **2**, $[\text{FeL}(\text{bipy})]_n$ **3**, and $[\mu\text{-O-}\{\text{FeL}\}_2(\text{dmap})]$ **4** discussed in this work. Additionally, mixtures of **1** and **4** were obtained that are denoted as **1***. Single crystals of **1** contain additional solvent molecules and are denoted as **1S**.

The conversion with bipy yielded the coordination polymer $[\text{FeL}(\text{bipy})]_n$ **3**. The samples were characterized using Mössbauer spectroscopy and magnetic measurements including kinetic studies. Single crystals of high enough quality were obtained for **1S**, **2**, and **4**. The crystal structures are discussed in the following. The mononuclear iron(II) complexes **1** and **2** are especially air sensitive in solution and also in the solid state. For comparison purpose, the oxidation product, the corresponding dinuclear iron(III) $\mu\text{-O}$ -complex **4**, was synthesized independently and fully characterized, as well.

6.4.2 Mössbauer measurements

Mössbauer spectroscopy is a useful tool to analyze the purity of the iron(II) complexes with regard to the observation of oxidation products, especially if the differences in C, H and N values of the iron(II) and iron(III) complexes expected for elemental analysis are small. In **Figure 1**, the ^{57}Fe Mössbauer spectra of the four complexes **1***, **2**, **3**, and **4** at room temperature are shown and in **Table 2** the corresponding Mössbauer parameters are summarized. **2** and **3** clearly show a pure

iron(II) HS species with a characteristic chemical shift δ of 0.882 and 0.939 mms^{-1} and a quadrupole splitting ΔE_Q of 2.277 and 2.167 mms^{-1} , respectively.^[46,47] The sample of **1** used for the measurements is partially oxidized to the corresponding μ -O complex **4**, either during the sample preparation or during the Mössbauer measurement and is therefore called **1***. The iron(III) HS site has a δ of 0.373 mms^{-1} and a ΔE_Q of 0.974 mms^{-1} , while the iron(II) HS site has values of δ of 0.948 mms^{-1} and ΔE_Q of 2.34 mms^{-1} .^[46,47] The ratio between the iron(III) and iron(II) sites is 70% to 30%. The iron(III) μ -O-complex **4** has a δ of 0.363 mms^{-1} and a ΔE_Q of 1.01 mms^{-1} , which is very similar to the values of the iron(III) HS site of **1***.

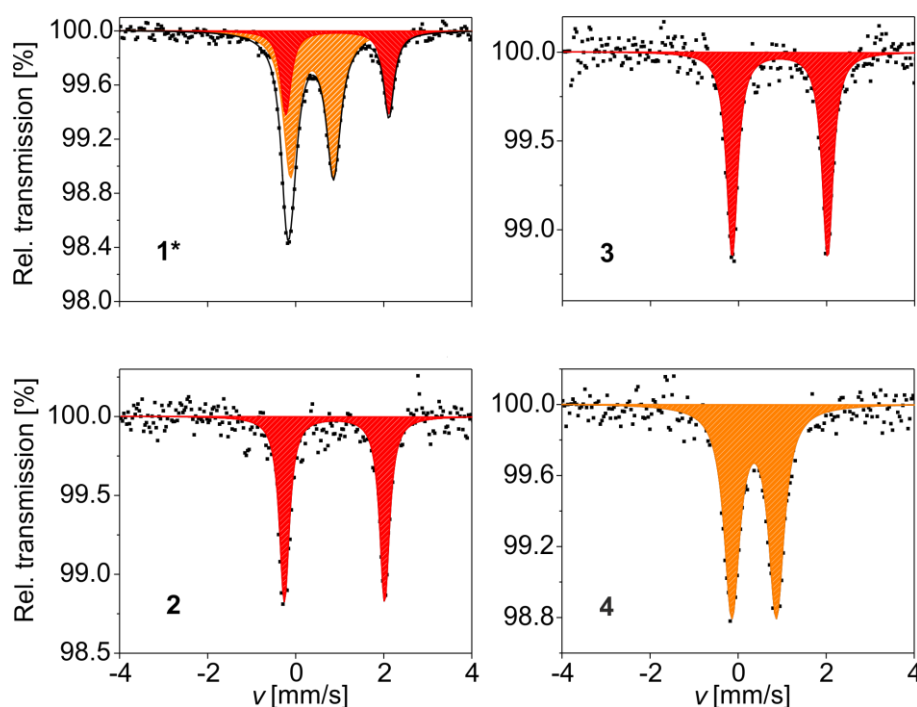


Figure 1: ^{57}Fe Mössbauer spectra of **1*** (partially oxidized **1**), **2**, **3**, and **4** measured at room temperature.

Table 2: ^{57}Fe Mössbauer data of **1***, **2**, **3**, and **4**.

Compound	Species	δ [mms^{-1}]	ΔE_Q [mms^{-1}]	$\Gamma/2$ [mms^{-1}]	Area [%]
1*	Fe(II) HS	0.948(11)	2.34(2)	0.142(16)	30(3)
	Fe(III) HS	0.373(8)	0.974(16)	0.198(11)	70(3)
2	Fe(II) HS	0.882(8)	2.277(16)	0.134(13)	100
3	Fe(II) HS	0.939(9)	2.167(18)	0.148(14)	100
4	Fe(III) HS	0.363(11)	1.01(2)	0.207(15)	100

6.4.3 X-ray structure analysis

Platelet-like crystals of **1S**, **2**, and **4** suitable for X-ray crystal structure were obtained directly from the synthesis. The crystal data were collected at 133 K for **1S** and **4** and at 100 K for **2** and the details are summarized in the Supporting Information **Table S1**. Due to the comparably long lattice

constants and resulting peak overlap it was impossible to find suitably large single crystals of **2** for measurement on a home source. **2** was therefore measured at the SLS synchrotron in Villigen (Switzerland) which enabled a successful structure solution and refinement. All complexes crystallized in the triclinic space group $P\bar{1}$. It is noteworthy that for all complexes a large asymmetric unit is obtained. This could be due to disorder of the alkyl chains, the methyl ester side groups or the axial ligand, in contrast to complexes with longer alkyl chains or a smaller head group, where such a disorder is rarely observed.^[14,45,48] As a result of this, the wR^2 and S values are comparably high. Nevertheless, the first coordination sphere around the iron center is always unaffected by the disorder and will be discussed in the following together with the packing in the crystal. However, details about intermolecular interactions, like hydrogen bonds, can only be provided in some of the structures.

ORTEP drawings of the first coordination sphere of complexes **1S**, **2**, and **4** are given in **Figure 2**. In the Supporting Information, **Figure S1** (**1S**), **Figure S2** (**2**), and **Figure S3** (**4**), ORTEP drawings of the complete asymmetric units including disorder are given. In **Table 3** selected bond lengths and angles of the three complexes are summarized.

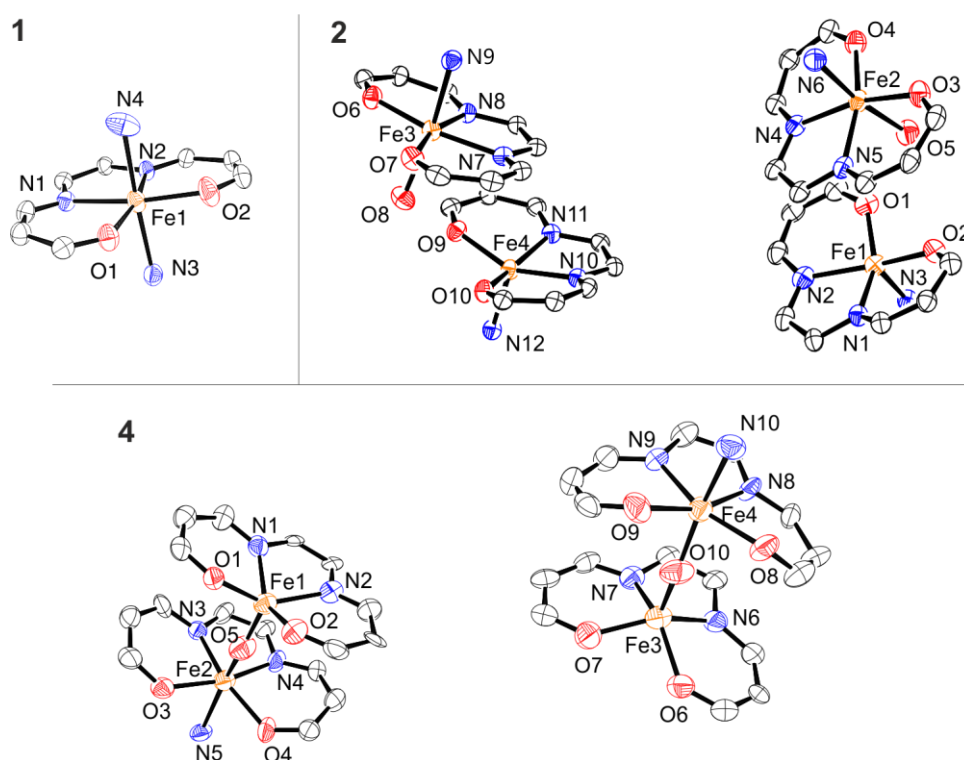


Figure 2: ORTEP drawings of the different coordination spheres of the complexes observed in the crystal structure of **1S** (top, left), **2** (top, right), and **4** (bottom). The alkyl chains and substituents at the chelate cycle were deleted for clarity. Furthermore, hydrogen atoms and disordered parts were also omitted for clarity. The complete asymmetric units including disordered parts are shown in the Supporting Information, **Figure S1** (**1S**), **Figure S2** (**2**), and **Figure S3** (**3**). Thermal ellipsoids shown at the 50% probability level.

The iron(II) center of **1S** has an octahedral N_4O_2 coordination sphere, comprising of the N_2O_2 -coordinating Schiff base-like ligand and two axially coordinating dmap molecules (**Figure 2**, top, left). Both methyl ester groups of the equatorial ligand and one of the dmap molecules are disordered. However, this disorder could not be resolved. The average bond lengths within the first coordination sphere are 2.09 Å (Fe–N_{eq}), 2.00 Å (Fe–O_{eq}), and 2.27 Å (Fe–N_{ax}) and the O_{eq}–Fe–O_{eq} angle is 107° (see **Table 3**). Those values are typical for octahedral HS iron(II) complexes of this ligand type.^[15,27,31,32] The L_{ax}–Fe–L_{ax} angle of 176° is very close to the expected 180° for perfect octahedral coordination. The torsion angle between the axial pyridine rings of the dmap molecules is 3°. The remaining electron density of **1** could not be associated with additional solvent molecules or a specific disorder and due to this was not further refined. Therefore for structure **1S** SQUEEZE from PLATON^[36] was used and a total number of 8 electrons were removed from refinement of four voids with a total void volume of 71 Å³. Consequently, intermolecular contacts between the polar head groups are not discussed. The octahedral distortion parameter Σ was calculated as reported in literature.^[3] It is with a value of 48.1° in the range observed for SCO active iron(II) complexes of this ligand type in the HS state.^[10] In comparison with pure HS complexes of this ligand type and especially to other ligand systems the value is relatively low.^[3,10,49]

The asymmetric unit of **2** contains four complex molecules as shown in **Figure 2** (top, right). Two iron(II) centers have a square pyramidal N_3O_2 coordination sphere (coordination number five, one dmap as axial ligand) and the two other iron(II) centers possess an octahedral N_3O_3 coordination sphere (coordination number six, one dmap and one methanol as axial ligand). Additionally, four non-coordinating methanol molecules are included in the crystal packing. The CH₃ groups of the coordinating MeOH, one of the four free MeOH molecules, a CH₂CH₃ alkyl chain end group, and a CH₂O alkyl chain ether group are disordered. The average bond lengths of the penta-coordinated iron(II) centers are 2.07 Å (Fe–N_{eq}), 2.00 Å (Fe–O_{eq}), and 2.12 Å (Fe–N_{ax}) and the O_{eq}–Fe–O_{eq} angle is 102° (see **Table 3**). Those values are comparable to other penta-coordinated iron(II) complexes of this ligand type in the HS state.^[32,48] The average bond lengths of the hexa-coordinated iron(II) center are with 2.11 Å (Fe–N_{eq}), 2.02 Å (Fe–O_{eq}), 2.20 Å (Fe–O_{ax}), and 2.09 Å (Fe–N_{ax}) slightly longer and the O_{eq}–Fe–O_{eq} angle is with 108° slightly larger (see **Table 3**). Those values are again in the region typical for octahedral HS iron(II) complexes of this ligand type.^[48,50] For the six coordinated iron(II) centers the L_{ax}–Fe–L_{ax} angle of 172° is very close to the expected 180° for perfect octahedral coordination.

The μ -O-iron(III) complex **4** contains two iron centers. One iron(III) center has a square pyramidal N_2O_3 coordination sphere (coordination number five), the second iron(III) center an octahedral

N_3O_3 coordination sphere (coordination number six, one additional dmap as sixth ligand). The asymmetric unit is depicted on the bottom of **Figure 2** and consist of two dimers. The average bond lengths of the penta-coordinated iron(III) center are 2.1 Å (Fe–N_{eq}), 2.0 Å (Fe–O_{eq}), and 1.7 Å (Fe–O_{ax}) and the O_{eq}–Fe–O_{eq} angle is 90°. The average bond lengths of the hexa-coordinated iron(III) center are 2.1 Å (Fe–N_{eq}), 2.0 Å (Fe–O_{eq}), 1.8 Å (Fe–O_{ax}), and 2.2 Å (Fe–N_{ax}) and the O_{eq}–Fe–O_{eq} angle is 113° (see **Table 3**). The average Fe–O_{ax}–Fe angle is 162°. Those values are in good agreement with similar μ -O-iron(III) complexes in literature.^[32,48,51] These complexes often crystallized with two penta-coordinated iron(III) sites, however, examples with one penta-coordinated and one octahedral site with one sixth ligand are also known.^[51]

The packing of the amphiphilic complexes in the crystal is shown in **Figure 3**. All three complexes form lipid layer-like arrangements with an approximate layer-layer distance between the alkyl chains of about 4.2 Å. This distance is characteristic for stabilizing Van der Waals interactions (London dispersion forces) and was also observed in related systems.^[48] As already discussed in previous works,^[48] the arrangement of the amphiphilic complexes strongly depends on the relative size of the head group (height H and broadness B) in relation to the overall length L of the molecule. For the complexes **2** and **4** with smaller head groups due to less or smaller axial ligands, a *sap* (self-assembly parameter = $(H + B)/L$) of around 1 is obtained (1.00 and 1.08 for **2** and **4**, respectively, see **Table 3**) that is associated to a lipid-layer like arrangement.

In line with this, the alkyl chains of the two complexes show no pronounced bending (see **Figure 4**, angle α) or shifting (see **Figure 4**, angle β) but an almost linear arrangement. For **2** the average values are $\alpha = 152^\circ$ and $\beta \approx 177^\circ$ and for the iron(III) complex **4** the average values are $\alpha = 169^\circ$ and $\beta \approx 176^\circ$. Here the alkyl chains stand out almost straight from the chelate ring. **1S**, on the other hand, is a special case. It has a *sap* of 1.12 and is therefore on the border of forming a lipid layer-like structure. This can be concluded by comparing **1S** with complexes with an *sap* of 1.20.^[48] The alkyl chains of those complexes spread apart and no lipid layer-like arrangement is formed. The spreading of the alkyl chains is observed for **1S**, but it is not big enough to stop them from forming the lipid layer-like structure. In contrast to **2** and **4**, the alkyl chains of **1S** do not order parallel to each other. One is in the plane of the equatorial Schiff base-like ligand with $\alpha = 176^\circ$ and $\beta \approx 130^\circ$ and the other stands out nearly perpendicular with $\alpha' = 94^\circ$ and $\beta \approx 125^\circ$.

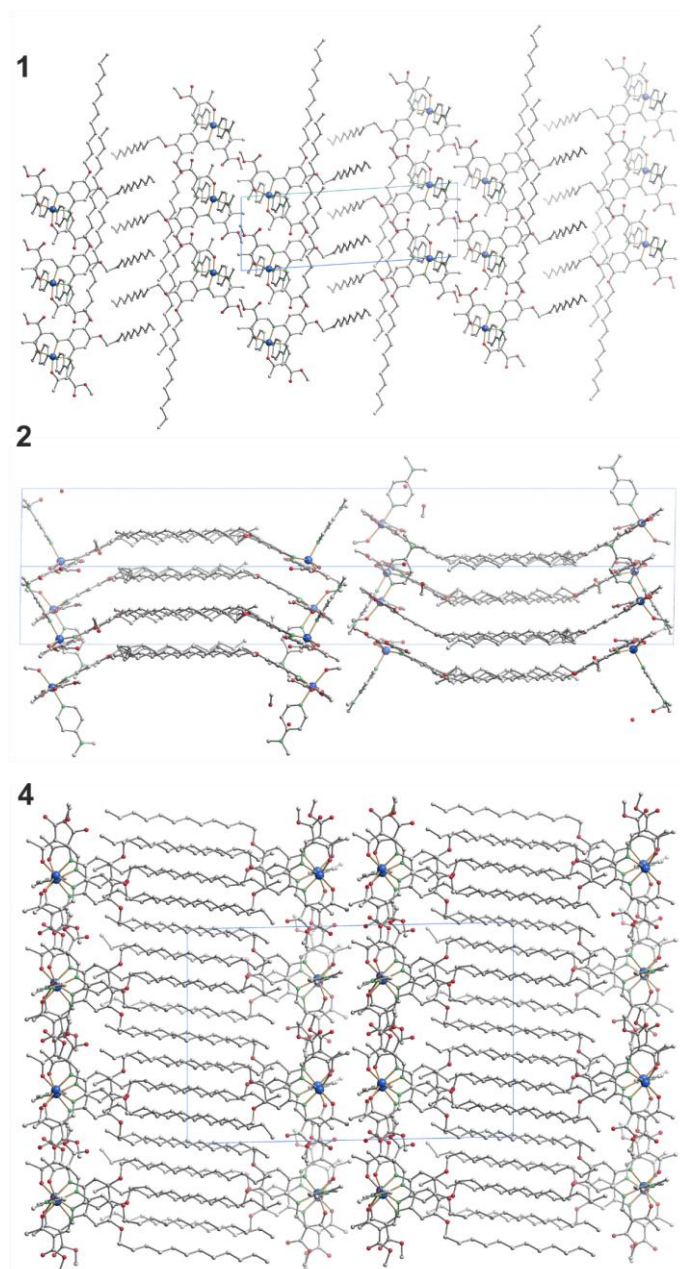


Figure 3: Molecular packing of **1** along $[0\ 1\ 0]$ (top), **2** along $[1\ 1\ 0]$ (center) and **4** along $[1\ 0\ 0]$ (bottom). Hydrogen atoms are omitted for clarity.

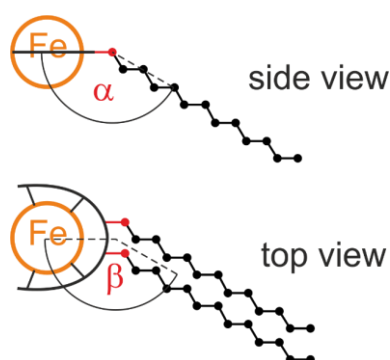


Figure 4: Schematic representation of the angles for the bending α and shifting β between the plane of the chelate cycle and the alkyl chains.

Table 3: Iron sites, coordination number CN, selected bond lengths [\AA] and angles [$^\circ$] of **1**, **2**, and **4** within the first coordination sphere and their dimensions [\AA] and *sap*.^[48]

	Fe site	CN	Fe–N _{eq}	Fe–O _{eq}	Fe–O _{ax} /N _{ax}	O _{eq} –Fe– O _{eq}	L _{ax} –Fe– L _{ax}	\angle L _{ax} ^{a)}	α	β	<i>H</i>	<i>B</i>	<i>L</i>	<i>sap</i>
1	Fe1/Fe(II)	6	2.089(3), 2.099(3)	2.008(3), 1.994(3)	2.261(4), 2.284(5)	107.49(12)	175.95(15)	3.35	176/94	130/125	14.1	13.9	24.9	1.12
	Fe1 ¹ /Fe(II)	5	2.054(4), 2.087(3)	1.993(5), 2.000(3)	2.111(4) ^{c)}	101.86(16)	-	-	151	177	7.5	13.6	22.0	0.96
2	Fe1 ² /Fe(II)	6	2.099(4), 2.108(3)	2.012(3), 2.019(4)	2.203(4) ^{b)} , 2.211(5) ^{c)}	107.83(15)	172.11(11)	-	148	177	10.1	13.2	22.2	1.05
	Fe1 ³ /Fe(II)	6	2.103(4), 2.111(3)	2.017(3), 2.025(4)	2.196(4) ^{b)} , 2.206(5) ^{c)}	108.91(15)	172.57(10)	-	151	175	10.1	13.2	22.3	1.04
	Fe1 ⁴ /Fe(II)	5	2.059(3), 2.094(3)	1.994(5), 1.999(3)	2.119(4) ^{c)}	102.54(15)	-	-	157	178	7.1	13.9	22.4	0.94
	Fe1/Fe(III)	5	2.042(13), 2.058(12)	1.945(9), 1.934(12)	1.744(11) ^{b)}	90.1(5)	162.4(7) ^{d)}	-	170	174	11.3 ^{e)}	13.4 ^{e)}	22.9 ^{e)}	1.08 ^{e)}
4	Fe2/Fe(III)	6	2.039(12), 2.089(11)	1.986(9), 2.004(10)	1.814(11) ^{b)} , 2.190(11) ^{c)}	112.9(4)	-	-	170	179	11.3 ^{e)}	13.4 ^{e)}	22.9 ^{e)}	1.08 ^{e)}
	Fe3/Fe(III)	5	2.056(12), 2.044(13)	1.972(11), 1.936(10)	1.731(10) ^{b)}	90.7(5)	161.0(6) ^{d)}	-	166	174	11.3 ^{e)}	13.4 ^{e)}	22.8 ^{e)}	1.08 ^{e)}
	Fe4/Fe(III)	6	2.076(11), 2.050(12)	2.025(10), 1.988(12)	1.841(10) ^{b)} , 2.208(14) ^{c)}	114.0(5)	-	-	169	178	11.3 ^{e)}	13.4 ^{e)}	22.8 ^{e)}	1.08 ^{e)}

a) Torsion angle between the axial pyridine rings; b) Fe–O_{ax}; c) Fe–N_{ax}; d) Fe–O–Fe angle instead of L_{ax}–Fe–L_{ax}; e) values for one μ -O-iron(III) complex.

6.4.4 Magnetic properties

Magnetic measurements were carried out for the two SCO active iron(II) complexes **1**, and **3** in the 300 K – 10 K temperature range. The partially oxidized complex **1*** and the pure high spin complex **2** was studied in the temperature range of 300 K – 50 K as shown in **Figure S4** and **S5**. The corresponding results are summarized in **Table 4**. In **Figure 5**, the $\chi_M T$ vs. T plot is displayed for the spin crossover active complexes **1** and **3** (where χ_M is the molar magnetic susceptibility and T the temperature). At room temperature, the $\chi_M T$ product of the three iron(II) complexes **1**, **2** and **3** is in the range of 3.2 to 3.5 $\text{cm}^3 \text{Kmol}^{-1}$, characteristic for iron(II) in the HS state. For complex **2** that is either penta-coordinated or octahedral with an N_3O_3 coordination sphere, this value does not change significantly upon cooling as expected for a pure HS complex (see SI, **Figure S5**). The substitution of one nitrogen by one oxygen reduces the overall ligand field strength and so far, only HS complexes were observed for this type of complexes with an N_3O_3 coordination sphere.^[48,50]

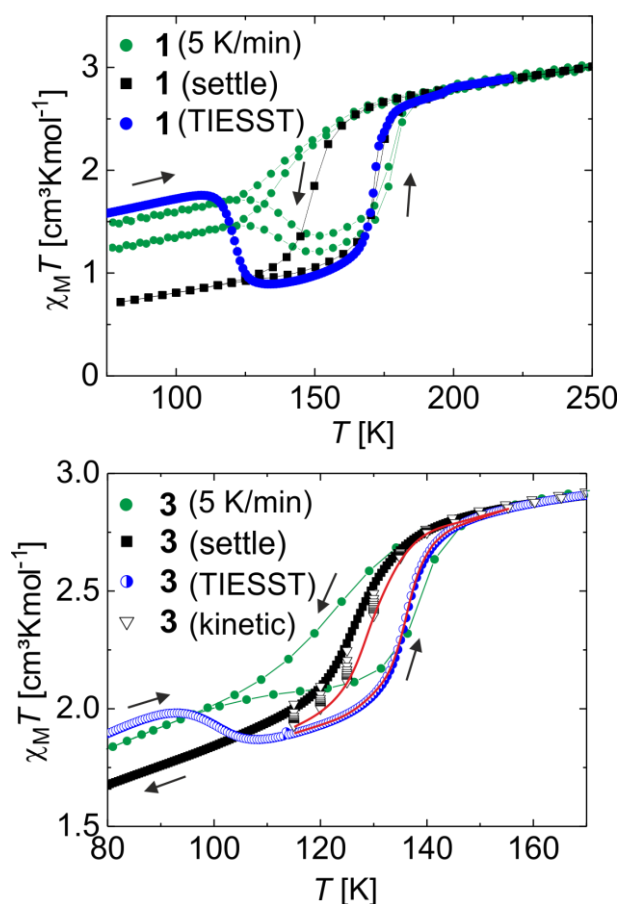


Figure 5: Top: Magnetic measurements of **1** with $\chi_M T$ plotted against T . Bottom: Magnetic measurements of **3** with $\chi_M T$ plotted against T . Green circles: T -dependent measurements in the sweep mode with 5 K/min; Black squares: thermal hysteresis loop measured in the settle mode. Blue circles: TIESST measurement, the sample was rapidly cooled from room temperature to 10 K and then the sample was measured in the heating mode with 0.3 K/min. Open triangles: to determine the real hysteresis width of **3** without of any kinetic effects, the sample was cooled from room temperature to a certain temperature (115 K, 120 K, 125 K, 130 K, 135 K, 140 K) and then kept at this temperature and the magnetic susceptibility was recorded for several hours. The red line obtained from this measurement indicates the real hysteresis width.

Table 4: Magnetic properties of **1**, **1***, **2**, and **3**. For the SCO active complexes the values refer to the measurements done in the settle mode.

Compound	$\chi_M T$ [cm ³ Kmol ⁻¹]	$\chi_M T$ [cm ³ Kmol ⁻¹]	$T_{1/2}^{\downarrow}$ [K]	$T_{1/2}^{\uparrow}$ [K]	Hysteresis width [K]	T_{TIESST} [K]
1	3.25 (300 K)	0.72 (80 K)	150	173	23	121
1*	2.68 (300 K)	1.89 (79 K)	149	156	7	-
2	3.53 (300 K)	3.13 (79 K)	-	-	-	-
3	3.14 (300 K)	1.67 (80 K)	126	136	10	101

The initial measurements on the spin crossover complexes **1** and **3** were done in the sweep mode with a scan rate of 5 K/min. At room temperature, **1** is in the HS state with a $\chi_M T$ product of 3.25 cm³Kmol⁻¹. The complete temperature range of this measurement is given in **Figure S6** in the SI. Upon cooling, the $\chi_M T$ product slowly decreases down to 200 K. Then, an abrupt drop of

the $\chi_{\text{M}}T$ product is observed down to $1.73 \text{ cm}^3\text{Kmol}^{-1}$ indicative of an incomplete spin crossover. Upon further cooling, the $\chi_{\text{M}}T$ product slowly decreases further and finally reaches a value of $1.09 \text{ cm}^3\text{Kmol}^{-1}$ at 10 K. Upon heating, the $\chi_{\text{M}}T$ product follows the curve progression obtained in the cooling mode up to 123 K. Then, a drop of the $\chi_{\text{M}}T$ product is observed in the heating mode reaching a minimum value of $1.36 \text{ cm}^3\text{Kmol}^{-1}$ at 151 K. Above this temperature the $\chi_{\text{M}}T$ product increases abruptly up to 187 K and then again follows the curve progression of the cooling mode. Such a behavior is characteristic of kinetic trapping effects thus the measurement was repeated with the same scan rate; however, the temperature was kept constant at 10 K for eight hours. The only difference observed between those two curves is the HS fraction in the low temperature range. This is most likely due to different amounts of **1S** and **1** in the sample and a transformation of **1S** to **1** upon heating in the SQUID. For the second cooling/heating cycle no differences are observed between the curves in the low temperature range indicating that the trapped HS state is stable at 10 K. An apparent hysteresis width of 44 K is obtained for both measurements. Consequently, the measurement was repeated in the settle mode in the 250 – 75 K temperature range (approx. 0.3 K/min). Upon cooling, an abrupt drop of the $\chi_{\text{M}}T$ product is observed below 160 K with $T_{1/2}^{\downarrow} = 150 \text{ K}$. However, at 80 K **1** is with a $\chi_{\text{M}}T$ value of $0.72 \text{ cm}^3\text{Kmol}^{-1}$, not completely LS. As already discussed before, the mononuclear complexes are highly air sensitive thus a partial oxidation of the complex during sample preparation cannot be ruled out. This is further supported by the results from room temperature Mössbauer spectroscopy, where an even higher fraction of oxidized species is observed, most likely due to the long measurement time. Another indication for this is the slightly tilted curve. This is typical for μ -O-iron(III) species of this general ligand type which show antiferromagnetic coupling.^[51] However, a small amount of **1S** could also contribute to the incomplete nature of the SCO. Upon heating the SCO occurs at a higher temperature with $T_{1/2}^{\uparrow} = 173 \text{ K}$, corresponding to a 23 K wide hysteresis loop. Please note that according to the magnetic measurements the complex is almost in the LS state at 133 K, the temperature where the X-ray structure was determined. However, according to X-ray structure analysis, the iron center is in the HS state. In order to understand those differences, the magnetic measurements were repeated by direct insertion of the sample into the sample chamber that was already cooled down to 10 K. Then the sample was slowly heated up to 220 K (approx. 0.3 K/min) for the TIESST measurement. The whole temperature range (10 K – 22 K) is shown in **Figure S7**. Indeed, using this procedure at 80 K a difference in the $\chi_{\text{M}}T$ value between the un-trapped state ($0.72 \text{ cm}^3\text{Kmol}^{-1}$) and the kinetically trapped, metastable HS state ($1.61 \text{ cm}^3\text{Kmol}^{-1}$) of $\Delta\chi_{\text{M}}T = 0.89 \text{ cm}^3\text{Kmol}^{-1}$ was observed. Upon heating (0.3 K/min) the value remains constant up to 110 K,

where a drop of the $\chi_{\text{M}}T$ value is observed with $T_{\text{TIESST}} = 121$ K. Upon further heating the same curve progression as for the hysteresis measurements is observed. Thus, the differences between the spin state obtained by magnetic measurements and single crystal X-ray diffraction could be due to kinetic trapping effects. A second possibility could be the presence of solvent molecules in the single crystals but not in the fine crystalline sample used for the magnetic measurements. The synthesis of the single crystals of **1** was repeated several times with the aim to obtain a better understanding of those discrepancies. In the supporting Information, **Figure S8**, the results from the magnetic measurements for a separately prepared sample together with the corresponding experimental section is given. According to elemental analysis a 2:1 mixture of **1** and **2** is obtained. Interestingly, for both cooling/heating cycle less than 50% of the iron centers show SCO, thus an evidence is found, that some of the crystals of **1** remain in the HS state in agreement with the results from X-ray structure analysis. Magnetic measurements of **1*** were done again after the Mössbauer measurement to affirm the oxidation and the loss of its SCO properties which are shown in **Figure S4**. At 300 K **1*** is paramagnetic and has a $\chi_{\text{M}}T$ value of $2.68 \text{ cm}^3\text{Kmol}^{-1}$ which is significantly lower than the theoretical value of $4.38 \text{ cm}^3\text{Kmol}^{-1}$. The difference is due to crystallization of dmap after oxidation of the complex that leads to an inhomogeneous compound consisting of iron(III) μ -O-complexes and dmap crystals. However, in the region around 150 K a small step of the SCO can still be seen.

The coordination polymer **3** is paramagnetic at 300 K with a $\chi_{\text{M}}T$ value of $3.14 \text{ cm}^3\text{Kmol}^{-1}$ as shown in the Supporting Information, **Figure S9**. Upon cooling in the sweep mode, a slow drop of the $\chi_{\text{M}}T$ product is observed down to 140 K. Then the $\chi_{\text{M}}T$ value decreases more rapidly. Below 80 K the $\chi_{\text{M}}T$ product does not change significantly with a value of $1.85 \text{ cm}^3\text{Kmol}^{-1}$. This corresponds to about half of the molecules which stay in the HS state with $T_{1/2} = 123$ K. Such a behavior is very frequently observed for iron(II) coordination polymers of this ligand type.^[27,52] Upon heating, the $\chi_{\text{M}}T$ product only slowly increases up to 130 K. Then it increases more rapidly with $T_{1/2} = 138$ K and above 150 K the same curve progression is observed as in the heating mode. An apparent hysteresis width of 15 K is obtained with a strongly tilted hysteresis loop indicative of some kinetic effects. Consequently, the measurement was repeated in settle mode (about 0.3 K/min) resulting in a smaller hysteresis loop (10 K with $T_{1/2}^{\uparrow} = 136$ K and $T_{1/2}^{\downarrow} = 126$ K) that is less tilted, and a slightly lower $\chi_{\text{M}}T$ value of $1.67 \text{ cm}^3\text{Kmol}^{-1}$ at 80 K. Please note that the warming curve of this measurement is identical to the high-temperature region of the TIESST curve and only on graph is shown. This value is characteristic for an equilibrium mixture of HS and LS complexes. However, a single crystal X-ray structure would be needed to further investigate this. After the second heating the sample was rapidly cooled to 10 K with 10 K/min

and then slowly heated up (0.3 K/min). As in the case of **1**, a trapped, metastable HS state is observed that relaxes at around 92 K back to the LS state and the $\chi_M T$ value decreases from 1.98 to 1.87 cm³Kmol⁻¹ with a T_{TIESST} of 101 K, as illustrated in **Figure 5**. The full temperature range investigated is shown in **Figure S10**. Further heating resulted in the same curve progression as for the measurements in the settle mode. Especially in the cooling mode of the settle measurements the hysteresis is still tilted, an indication that the hysteresis width is still influenced by kinetic effects. In order to measure the real width of the hysteresis, **3** was cooled down from 170 K to 145 K, where the temperature was kept for 1 h while every 5 min a data point was measured. After this procedure the temperature was again increased to 170 K and subsequently cooled to 140 K it was measured again for 1 h. This was repeated in the region of the hysteresis in 5 K steps down to 115 K, the results are summarized in **Figure 5**. At each temperature the $\chi_M T$ value is slowly decreasing and stabilizes at a point which is lower compared to the settle measurement. The red line in **Figure 5** illustrates the actual, kinetically corrected hysteresis with a width of about 6 K. PXRD measurements of **3** were done, as shown in **Figure S11** in the region of 2 – 30° 2 θ , to support the statement of a cooperative magnetic behavior. In **Figure 6** a section of the PXRD pattern in the region of 22.5 – 24.0° 2 θ is shown, where a distinct change in the atomic distances during the SCO can be observed. The temperatures, the corresponding 2 θ values, and the $\chi_M T$ values are listed in **Table 5**. The changes in the PXRD pattern are completely reversible in the 100 K to 300 K temperature range. At 130 K the pattern of the heating and the cooling mode vary slightly in line with the appearance of the hysteresis in the magnetic measurements. In **Figure S11**, the PXRD patterns of **3** are compared with the calculated PXRD patterns from the single crystals of **1S**, **2** and **4**. In all patterns, a strong reflex is observed in the 2 – 4° 2 θ region, that can be correlated to the lipid layer like structures observed for the molecule packing in all three crystal structures.

Table 5: Temperatures used for the PXRD measurements of **3** and the corresponding diffraction and magnetic data.

Temperautre [K]	2 θ [°]	$\chi_M T$ [cm ³ Kmol ⁻¹]
300	22.925	3.14
200	23.045	2.99
130	23.255	2.54
100	23.435	1.84
130	23.300	2.06
200	23.045	2.99
300	22.925	3.14

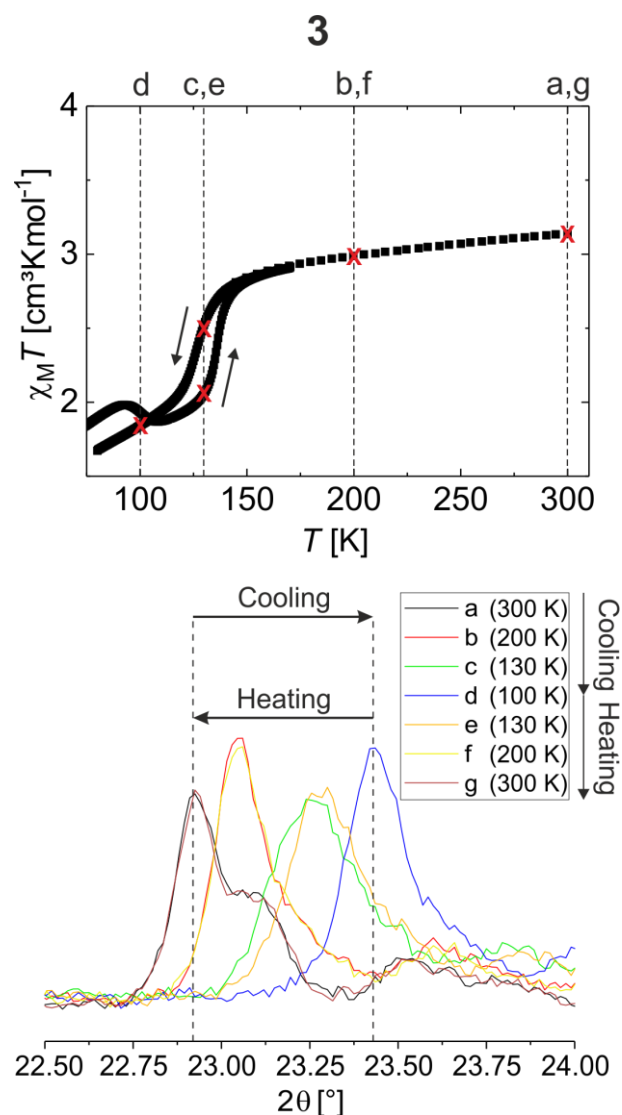


Figure 6: Temperatures used for the PXRD measurements of **3** shown in the $\chi_M T$ vs T plot (top). PXRD pattern in the region of $22.5 - 24.0^\circ 2\theta$, where a distinct change during the SCO can be observed (bottom).

6.5 Discussion

In this work we obtained the crystals suitable for X-ray structure analysis for three different iron(II/III) complexes, all with the same equatorial Schiff base like ligand but with different axial ligands. The crystal packing of those amphiphilic complexes with the sterically less demanding axial ligands **2** and **4** shows lipid layer-like structures while that for **1**, with two relatively large axial dmap ligands is on the border of forming them as predicted by the *sap*.^[48] This is the most likely reason for the difficulties encountered with the synthesis of large amount of pure **1**. The formation of lipid-like layers is a strong driving force for the crystallization of those complexes and consequently mixtures of **1** and **2** were often obtained from the synthesis, almost independently of the [FeL]:dmap ratio used. Additionally, the magnetic properties of **1** and **1S** (including solvent molecules) are different. This is further complicated by the pronounced air

sensitivity of the complexes. Again, the possibility to crystallize in a lipid layer-like structure supports precipitation of **4** compared to **1**. Additionally, the high air sensitivity also in the solid state frequently leads to a partial oxidation of the materials despite careful handling.

With regard to the magnetic properties, both **1** and **3** show a cooperative SCO with hysteresis and kinetic effects, both, with regard to the hysteresis width and the observation of the TIESST effect. Scan rate dependent thermal hysteresis loops and T_{TIESST} above 100 K were so far not observed for SCO complexes of this general N_2O_2 coordinating Schiff base-like ligand type. There are different possible reasons for the observation of high T_{TIESST} values such as a high coordination sphere distortion, order-disorder transitions of the alkyl chains or solvent molecules or a low $T_{1/2}$ value. For the complexes discussed here no solvent molecules are included in the samples showing SCO and the octahedral distortion parameter calculated for **1S** is relatively low and in the region observed for other complexes of this general type.^[10] Thus, those two possibilities can be ruled out. For complexes of this type with very short alkyl chains gradual SCO were observed^[45,53] whereas for longer alkyl chains hysteresis was observed in one case but without indication of any kinetic effects.^[14] Thus, the assumption can be made, that the behavior reported here is due to the presence of alkyl chains and that the length of the alkyl chain is important for tuning the SCO properties. Indeed, this is in line with results on other systems in literature, where kinetic effects associated with a reorientation of alkyl chains are observed for complexes with shorter alkyl chains.^[12] Thus, a similar effect is most likely the reason for the observation of the very pronounced kinetic effects observed for the complexes presented here. Additionally, the $T_{1/2}$ values for the thermal SCO of both complexes are relatively low and can contribute to the high T_{TIESST} value. Considering the difficulties encountered for the mononuclear system **1** with the reproduction of the sample, the synthesis of coordination polymers such as **3** appears to be more promising for further investigations.

6.6 Conclusion

In this article we report the synthesis of a monomeric (**1**) and a polymeric (**3**) iron(II) SCO complex with amphiphilic ligands. Crystal structures of **1S**, the side product **2**, where one of the dmap molecules is exchanged with MeOH, and the oxidized species **4** were obtained showing lipid layer-like structures in all cases. **1** and **3** show SCO with the appearance of a hysteresis around 160 K for the monomeric and 130 K for the polymeric compound, respectively, the magnitude of which strongly depends on the sweep velocity used for the magnetic measurements. The actual hysteresis width without kinetic trapping was obtained for **3** by stabilizing the temperature at different points

in the region of the SCO, in the case of **1** a velocity of 0.3 K/min was sufficient. Both complexes show high T_{TIESST} of 121 K and 101 K for the monomeric and the polymeric complex.

6.7 Associated content

Supporting Information.

The Supporting Information is available free of charge on the ACS Publications website at DOI: 10.1021/acs.inorgchem.8b02763

ORTEP drawings of the full asymmetric units of **1**, **2**, and **4**, the details of the crystallographic data, and additional results from magnetic measurements and powder X-ray diffraction (PDF)

Accession Codes CCDC 1831460, 1857855, and 1857875 contain the supplementary crystallographic data for this paper. These data can be obtained free of charge via www.ccdc.cam.ac.uk/data_request/cif, or by emailing data_request@ccdc.cam.ac.uk, or by contacting The Cambridge Crystallographic Data Centre, 12 Union Road, Cambridge CB2 1EZ, UK; fax: +441223 336033

AUTHOR INFORMATION

Corresponding Author

*E-mail: weber@uni-bayreuth.de.

ORCID

Birgit Weber: 0000-0002-9861-9447

Notes

The authors declare no competing financial interest

ACKNOWLEDGMENTS

Financial support of the University of Bayreuth and the German Science formation (WE 3546/5-1) is gratefully acknowledged. B.D. thanks S. Becker for helpful discussions at the SLS synchrotron and V. Olieric for support using beamline X10SA.

DEDICATION

Dedicated to Prof. Ingo-Peter Lorenz on the occasion of his 75th birthday.

6.8 Supporting Information

Kinetic trapping effects in amphiphilic iron(II) spin crossover compounds

Johannes Weihermüller^a, Stephan Schlamp^a, Birger Dittrich^b, Birgit Weber^{a*}

a) Department of Chemistry, University of Bayreuth, 95440 Bayreuth, Germany, weber@uni-bayreuth.de

b) Anorganische Chemie und Strukturchemie II, Heinrich-Heine University Düsseldorf, Universitätsstr. 1, 40225 Düsseldorf, Germany

Table S1: Crystallographic data of **1**, **2** and **4**.

Compound	1	2	4
CCDC	1857855	1831460	1857875
empirical formula	C ₅₆ H ₈₆ FeN ₆ O ₈	C ₁₀₁ H ₁₆₄ Fe ₂ N ₈ O ₁₉	C ₉₁ H ₁₄₂ Fe ₂ N ₆ O ₁₇
formula weight / g mol ⁻¹	1027.16	1906.09	1703.81
crystal system	triclinic	triclinic	triclinic
space group	<i>P</i> $\bar{1}$	<i>P</i> $\bar{1}$	<i>P</i> $\bar{1}$
<i>a</i> / Å	9.5947(6)	12.473(17)	14.669(3)
<i>b</i> / Å	11.3379(9)	13.05(3)	20.260(3)
<i>c</i> / Å	27.854(2)	66.035(16)	30.735(6)
α / °	78.237(6)	88.68(8)	91.199(14)
β / °	83.510(6)	87.71(4)	90.854(14)
γ / °	75.634(6)	76.23(16)	90.175(14)
<i>V</i> / Å ³	2867.4(4)	10429(30)	9131(3)
<i>Z</i>	2	4	4
$\rho_{\text{calc.}}$ / g cm ⁻³	1.190	1.214	1.239
μ / mm ⁻¹	0.318	0.257	0.385
crystal size / mm	0.13×0.20×0.10	0.22×0.02×0.02	0.07×0.10×0.12
<i>T</i> / K	133	100	133
λ / Å	Mo- <i>K</i> α 0.71069	SLS Synchrotron 0.6358	Mo- <i>K</i> α 0.71069
θ -range / °	2.99-56.09	0.85-25.2	1.2-24.7
measured reflections	13413	305869	97062
independent reflections	13413	46704	30407
parameters	742	2434	2092
<i>R</i> _{int}	0.114	0.062	0.398
<i>R</i>	0.0856	0.0828	0.1002
<i>wR</i> ²	0.2515	0.2414	0.1920
<i>S</i>	0.914	1.940	0.754

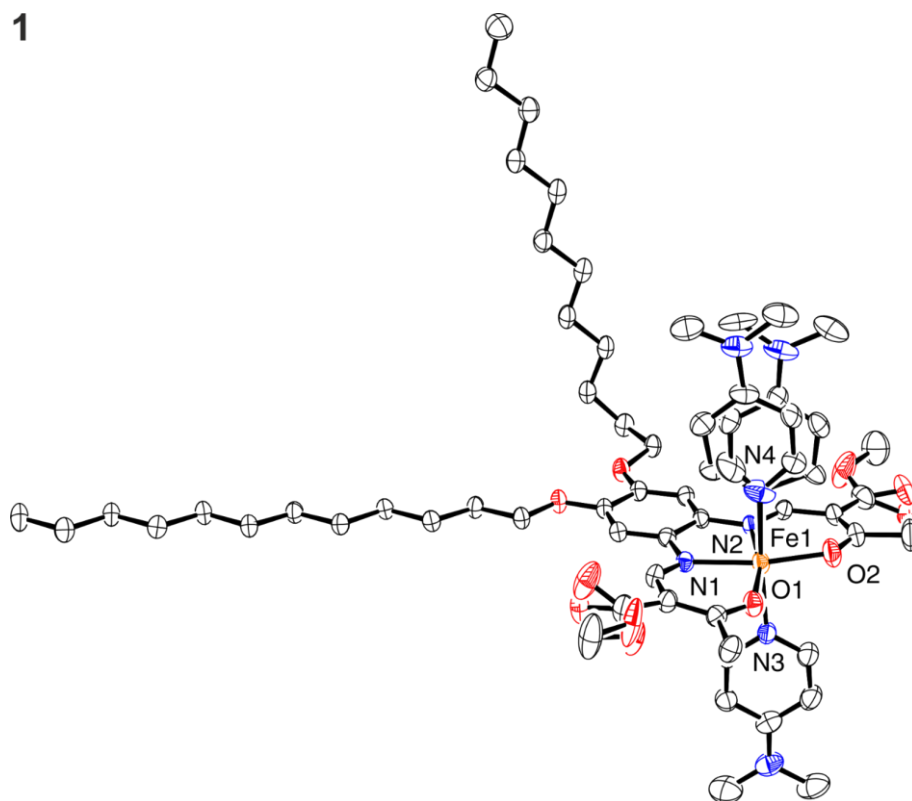


Figure S1: ORTEP drawing of the asymmetric unit including disorder of the crystal structure of **1**. Hydrogen atoms are omitted for clarity. Thermal ellipsoids shown at the 50% probability level.

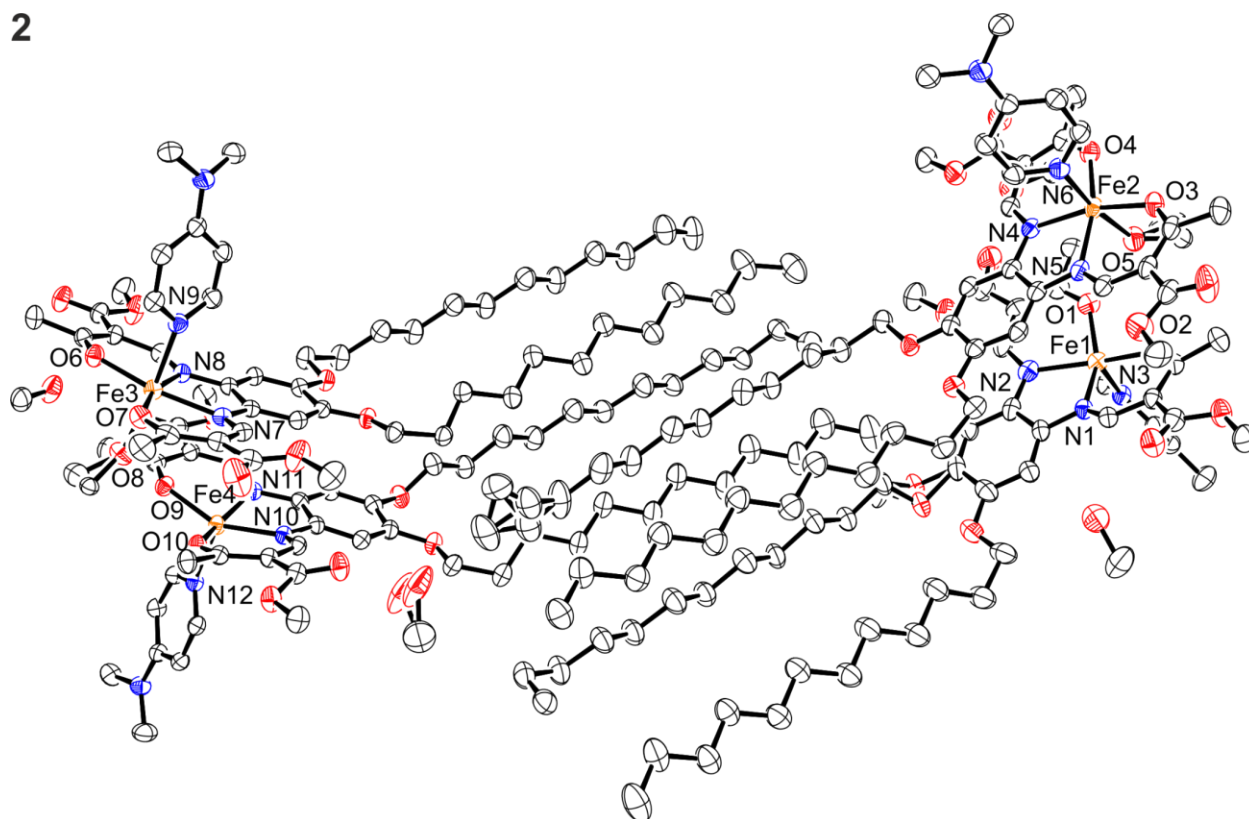


Figure S2: ORTEP drawing of the asymmetric unit including disorder of the crystal structure of **2**. Hydrogen atoms are omitted for clarity. Thermal ellipsoids shown at the 50% probability level.

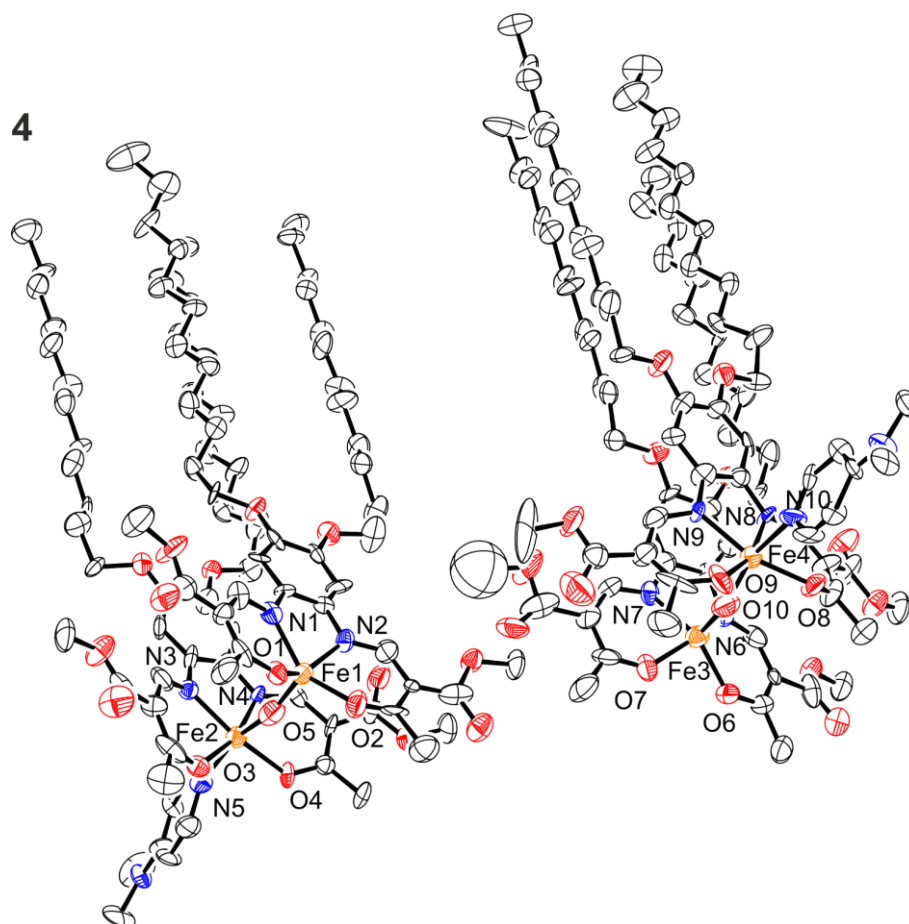


Figure S3: ORTEP drawing of the asymmetric unit including disorder of the crystal structure of **4**. Hydrogen atoms are omitted for clarity. Thermal ellipsoids shown at the 50% probability level.

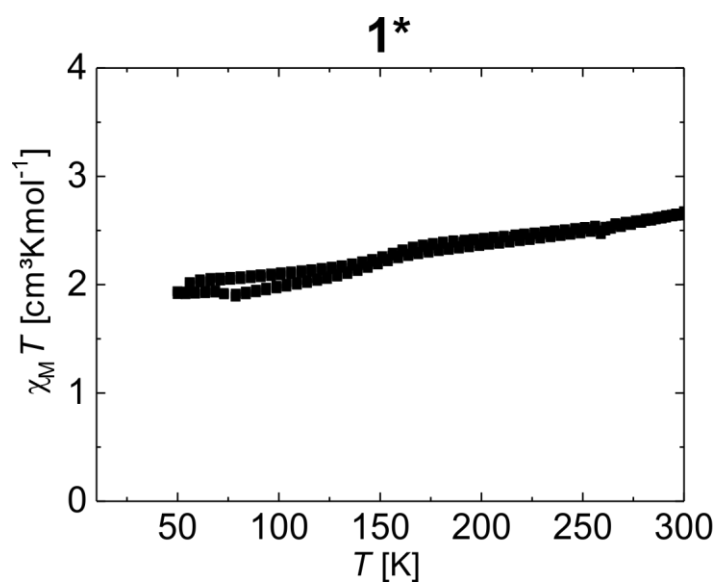


Figure S4: Magnetic measurement of **1***.

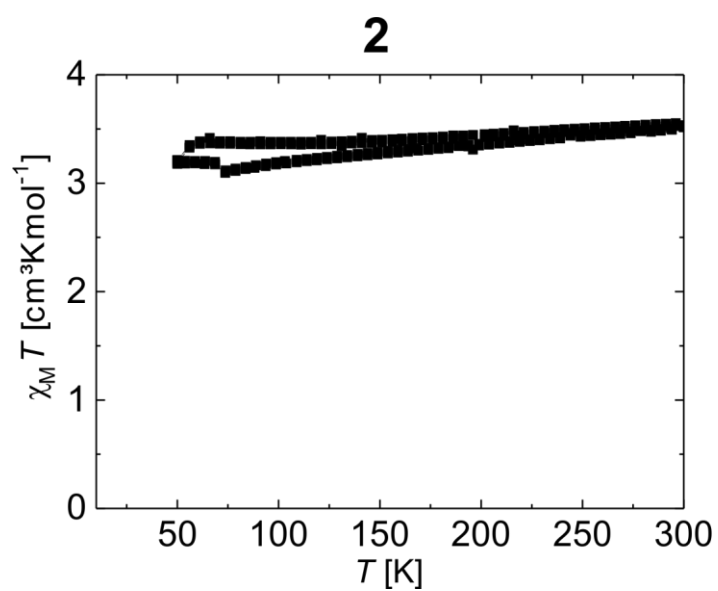


Figure S5: Magnetic measurement of **2**.

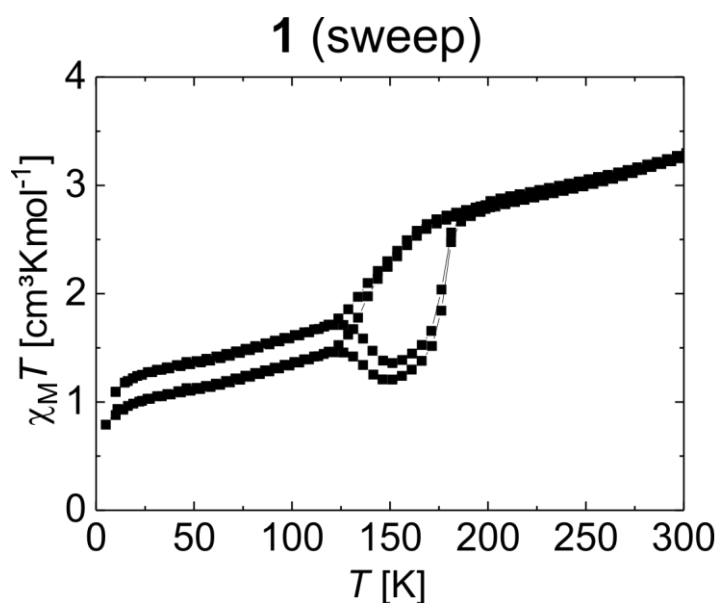


Figure S6: Magnetic measurement of **1** in sweep mode (5 K/min). The cooling/heating cycle was measured two times. The difference of the remaining HS fraction between those two cycles is most likely due to conversion of crystals of **1S** (HS complex according to X-Ray structure analysis) in the sample to **1**. During the second cycle the temperature was kept at 10 K for eight hours to check if there is a difference between the cooling and the heating curve in the low temperature region due to kinetic trapping effects, however, at 10 K the trapped HS state appears to be very stable.

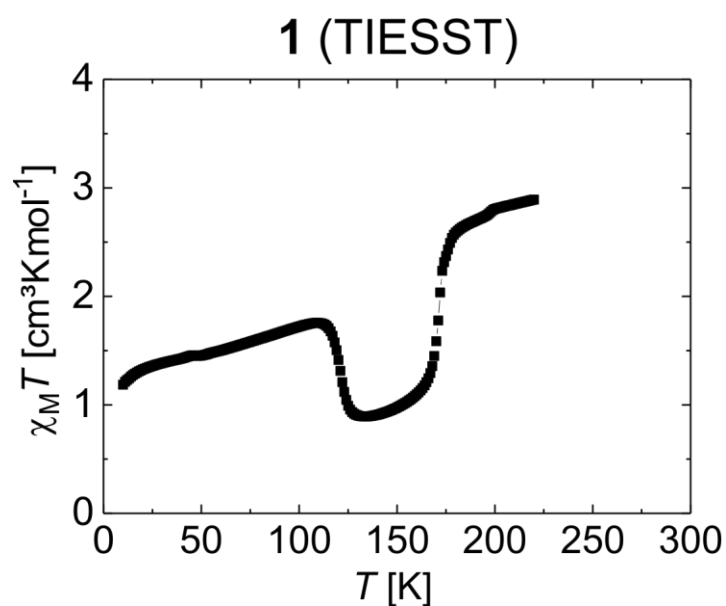


Figure S7: Magnetic measurement of **1** in settle mode (0.3 K/min) with fast cooling to 10 K through direct insertion to the precooled measurement chamber.

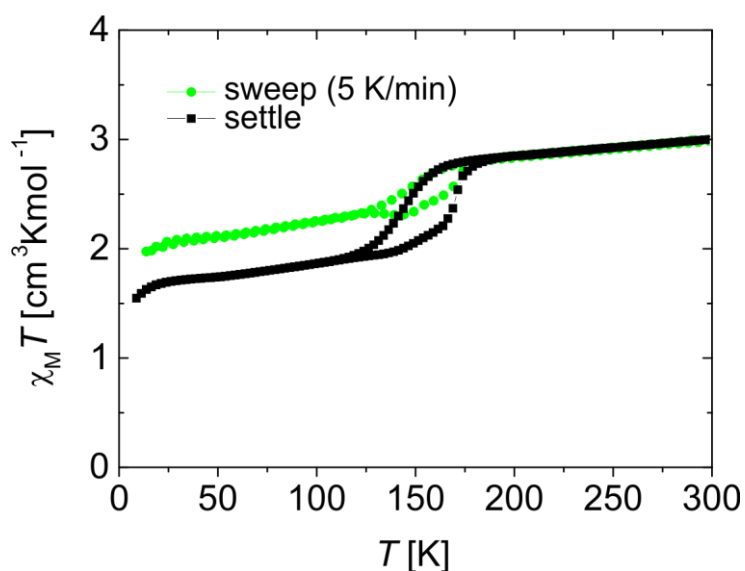


Figure S8: Magnetic measurement of a mixture of **1** (+ **1SC**) and **2**, obtained as one of the attempts to reproduce **1SC**, in sweep mode (5 K/min) and settle mode (0.3 K/min). Synthesis: 0.25 g $[\text{FeL}(\text{MeOH})_2]$ (1 eq, 0.25 mmol, 846.47 $\text{g}\cdot\text{mol}^{-1}$) and 1.08 g dmap (30 eq, 8.85 mmol, 122.08 $\text{g}\cdot\text{mol}^{-1}$) were dissolved in 10 mL methanol and the dark-red solution was heated to reflux for one hour. After storage over night at room temperature and then for five days at 6 °C black needles were obtained that were filtered off, washed with 3 mL methanol and dried carefully. Yield: 0.09 g (35 %). $\text{C}_{56}\text{H}_{86}\text{FeN}_6\text{O}_8$ (1027.18): calcd. C 65.48, H 8.44, N 8.18; found: C 64.64/64.80, H 8.48/8.51, N 7.53/7.37. The nitrogen content is lower than expected for **1** and would fit best assuming a mixture of **1** (possibly including **1SC**) and **2**. Theory calcd. for a 2:1 ratio of **1** and **2**: C 64.75, H 8.53, N 7.41. Please note that more than 50% of the molecules remain in the HS state, especially for the first cycle measured in the sweep mode. This could be an indication that a part of the crystals (presumably **1SC**) did not lose the included solvent and are pure HS complexes, in agreement with the results from X-ray structure analysis.

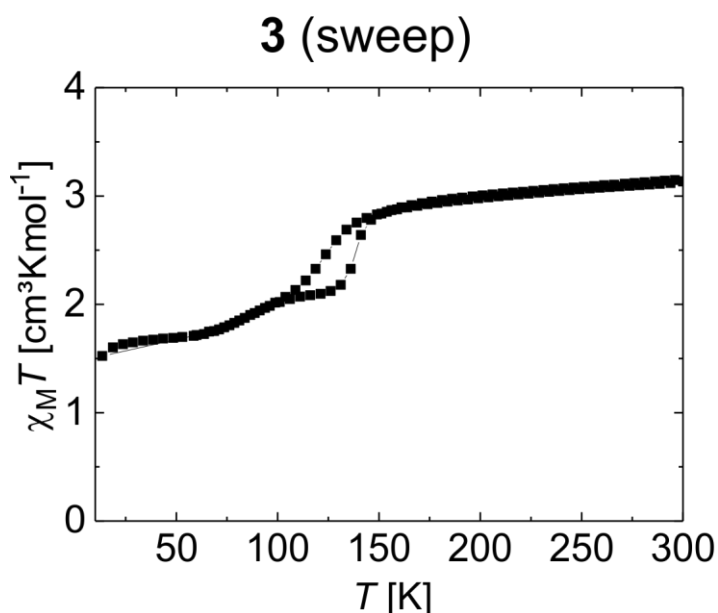


Figure S9: Magnetic measurement of **3** in sweep mode (5 K/min). The apparent two-step character of the SCO curve can be explained with kinetic effects influencing the curve progression below 100 K.

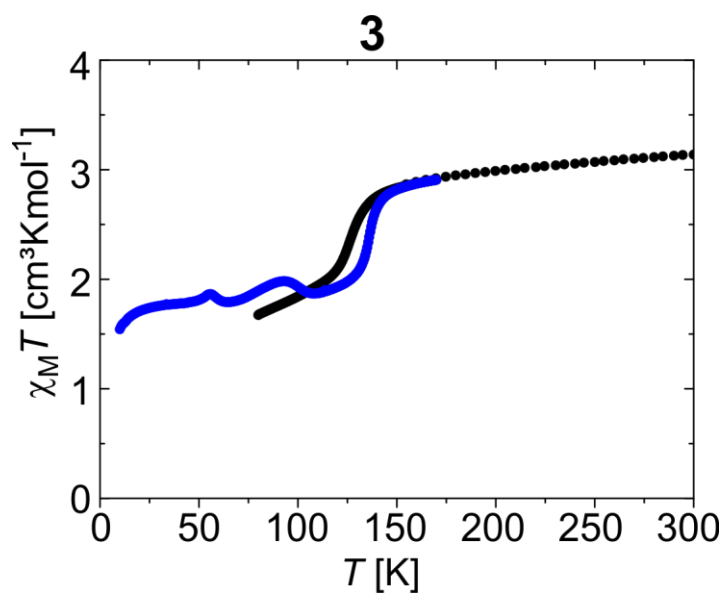


Figure S10: The complete magnetic measurements of **3** in the settle mode (0.3 K/min). Black: cooling mode; blue: heating mode after fast cooling including the TIESST experiment (10 K – 110 K) and the warming branch of the hysteresis curve (110 K – 180 K).

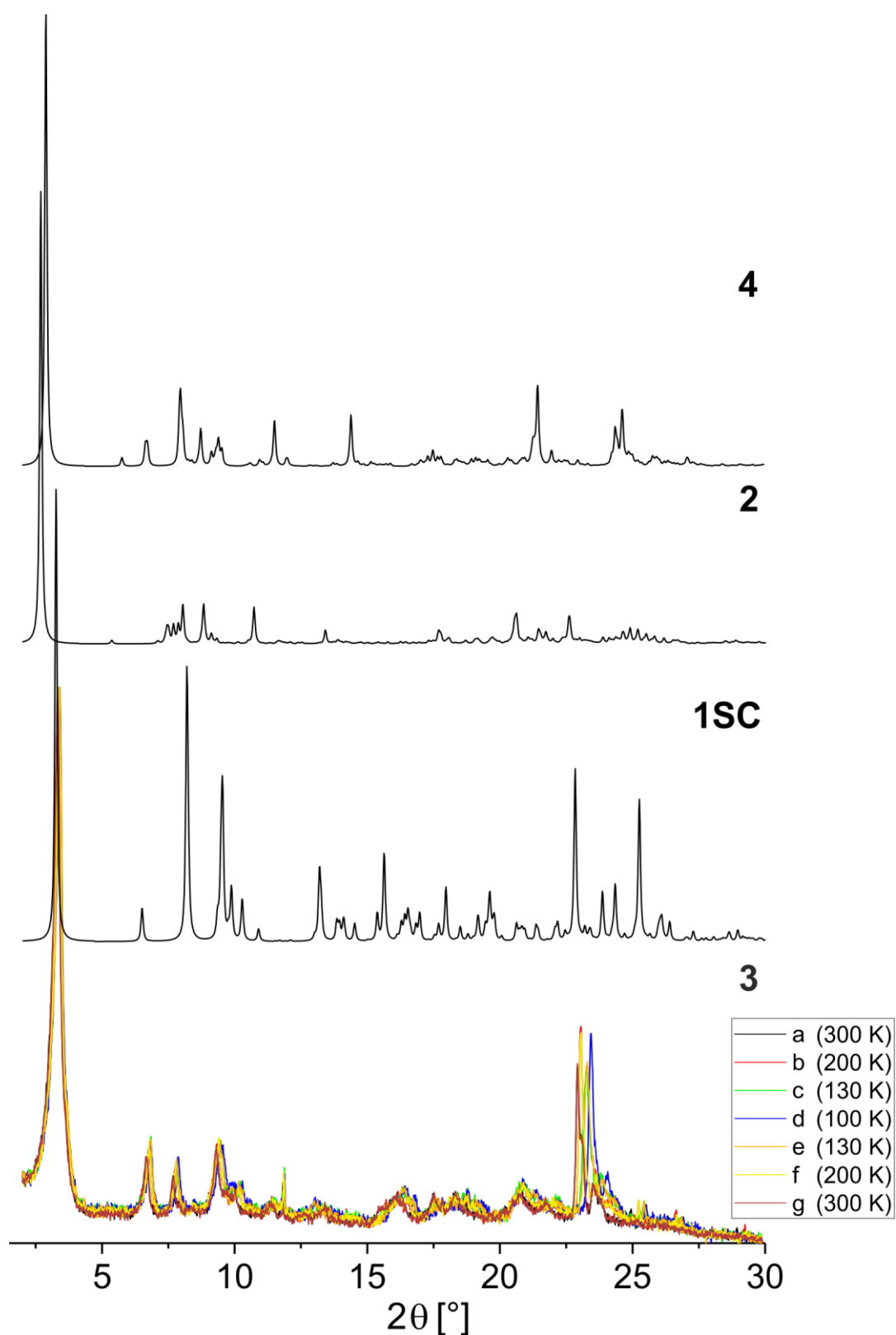


Figure S11: The complete temperature dependent powder X-ray diffraction pattern of **3** in the range of $2 - 30^\circ 2\theta$. The temperature was varied in correlation with the magnetic properties between 300 and 100 K. For comparison purpose, the calculated PXRD patterns of **1**, **2** and **4** are given as well. Please note the strong reflex below $5^\circ 2\theta$ that can be assigned to the lipid-layer like structure in the crystal packing and that is also observed for **3**.

6.9 References

- [1] M. A. Halcrow (Ed.) *Spin-crossover materials. Properties and applications*, Wiley, Chichester **2013**.
- [2] B. Sieklucka, D. Pinkowicz, *Molecular Magnetic Materials: Concepts and Applications*, John Wiley and Sons Inc, Weinheim **2017**.
- [3] P. Gütlich, H. A. Goodwin, *Spin Crossover in Transition Metal Compounds I-III, Vols. 234*, Springer, Berlin, Heidelberg **2004**.
- [4] a) O. Kraieva, C. M. Quintero, I. Suleimanov, E. M. Hernandez, D. Lagrange, L. Salmon, W. Nicolazzi, G. Molnár, C. Bergaud, A. Bousseksou, *Small* **2016**, *12*, 6325–6331; b) R. G. Miller, S. Brooker, *Chem. Sci.* **2016**, *7*, 2501–2505; c) J. Linares, E. Coddjovi, Y. Garcia, *Sensors* **2012**, *12*, 4479–4492.
- [5] a) O. Kahn, *Science* **1998**, *279*, 44–48; b) M. Cavallini, I. Bergenti, S. Milita, G. Ruani, I. Salitros, Z.-R. Qu, R. Chandrasekar, M. Ruben, *Angew. Chem. Int. Ed.* **2008**, *47*, 8596–8600.
- [6] R. N. Muller, L. Vander Elst, S. Laurent, *J. Am. Chem. Soc.* **2003**, *125*, 8405–8407.
- [7] a) K. Senthil Kumar, M. Ruben, *Coord. Chem. Rev.* **2017**, *346*, 176–205; b) G. Molnár, L. Salmon, W. Nicolazzi, F. Terki, A. Bousseksou, *J. Mater. Chem. C* **2014**, *2*, 1360–1366; c) R. Nowak, E. A. Prasetyanto, L. de Cola, B. Bojer, R. Siegel, J. Senker, E. Rössler, B. Weber, *Chem. Commun.* **2017**, *53*, 971–974; d) C. Atmani, F. El Hajj, S. Benmansour, M. Marchivie, S. Triki, F. Conan, V. Patinec, H. Handel, G. Dupouy, C. J. Gómez-García, *Coord. Chem. Rev.* **2010**, *254*, 1559–1569.
- [8] S. Brooker, *Chem. Soc. Rev.* **2015**, *44*, 2880–2892.
- [9] a) J. Olguín, S. Brooker, *Coord. Chem. Rev.* **2011**, *255*, 203–240; b) H. L.C. Feltham, A. S. Barltrop, S. Brooker, *Coord. Chem. Rev.* **2017**, *344*, 26–53; c) D. J. Harding, P. Harding, W. Phonsri, *Coord. Chem. Rev.* **2016**, *313*, 38–61; d) A. Bousseksou, G. Molnár, L. Salmon, W. Nicolazzi, *Chem. Soc. Rev.* **2011**, *40*, 3313–3335; e) M.-L. Boillot, B. Weber, *Comptes Rendus Chimie* **2018**; f) Z.-P. Ni, J.-L. Liu, M. N. Hoque, W. Liu, J.-Y. Li, Y.-C. Chen, M.-L. Tong, *Coord. Chem. Rev.* **2017**, *335*, 28–43; g) P. Guionneau, *Dalton Trans.* **2014**, *43*, 382–393; h) O. Roubeau, *Chemistry* **2012**, *18*, 15230–15244; i) J. Tao, R.-J. Wei, R.-B. Huang, L.-S. Zheng, *Chem. Soc. Rev.* **2012**, *41*, 703–737; j) M. C. Muñoz, J. A. Real, *Coord. Chem. Rev.* **2011**, *255*, 2068–2093.
- [10] M. A. Halcrow, *Chem. Soc. Rev.* **2011**, *40*, 4119–4142.
- [11] A. B. Gaspar, M. Seredyuk, *Coord. Chem. Rev.* **2014**, *268*, 41–58.
- [12] M. Seredyuk, M. C. Muñoz, M. Castro, T. Romero-Morcillo, A. B. Gaspar, J. A. Real, *Chem. Eur. J.* **2013**, *19*, 6591–6596.

- [13] a) A. B. Gaspar, M. Seredyuk, P. Gütllich, *Coord. Chem. Rev.* **2009**, *253*, 2399–2413; b) T. Romero-Morcillo, M. Seredyuk, M. C. Muñoz, J. A. Real, *Angew. Chem. Int. Ed.* **2015**, *54*, 14777–14781; c) G. Schwarz, Y. Bodenthin, Z. Tomkowicz, W. Haase, T. Geue, J. Kohlbrecher, U. Pietsch, D. G. Kurth, *J. Am. Chem. Soc.* **2011**, *133*, 547–558; d) Y. Komatsu, K. Kato, Y. Yamamoto, H. Kamihata, Y. H. Lee, A. Fuyuhiko, S. Kawata, S. Hayami, *Eur. J. Inorg. Chem.* **2012**, 2769–2775; e) P. N. Martinho, Y. Ortin, B. Gildea, C. Gandolfi, G. McKerr, B. O’Hagan, M. Albrecht, G. G. Morgan, *Dalton Trans.* **2012**, *41*, 7461–7463.
- [14] S. Schlamp, B. Weber, A. D. Naik, Y. Garcia, *Chem. Commun.* **2011**, *47*, 7152–7154.
- [15] C. Lochenie, K. Schötz, F. Panzer, H. Kurz, B. Maier, F. Puchtler, S. Agarwal, A. Köhler, B. Weber, *J. Am. Chem. Soc.* **2018**, *140*, 700–709.
- [16] a) B. Schäfer, T. Bauer, I. Faus, J. A. Wolny, F. Dahms, O. Fuhr, S. Lebedkin, H.-C. Wille, K. Schlage, K. Chevalier et al., *Dalton Trans.* **2017**, *46*, 2289–2302; b) O. Kraieva, I. Suleimanov, G. Molnár, L. Salmon, A. Bousseksou, *Magnetochemistry* **2016**, *2*, 11; c) L. J. Kershaw Cook, M. A. Halcrow, *Polyhedron* **2015**, *87*, 91–97; d) I. Suleimanov, O. Kraieva, G. Molnár, L. Salmon, A. Bousseksou, *Chem. Commun.* **2015**, *51*, 15098–15101.
- [17] H.-Y. Wang, J.-Y. Ge, C. Hua, C.-Q. Jiao, Y. Wu, C. F. Leong, D. M. D’Alessandro, T. Liu, J.-L. Zuo, *Angew. Chem. Int. Ed.* **2017**, *56*, 5465–5470.
- [18] a) B. Weber, *Chemistry* **2017**, *23*, 18093–18100; b) O. Klimm, C. Göbel, S. Rosenfeldt, F. Puchtler, N. Miyajima, K. Marquardt, M. Drechsler, J. Breu, S. Förster, B. Weber, *Nanoscale* **2016**, *8*, 19058–19065; c) Y.-H. Luo, Q.-L. Liu, L.-J. Yang, Y. Sun, J.-W. Wang, C.-Q. You, B.-W. Sun, *J. Mater. Chem. C* **2016**, *4*, 8061–8069; d) J. Dugay, M. Aarts, M. Giménez-Marqués, T. Kozlova, H. W. Zandbergen, E. Coronado, H. S. J. van der Zant, *Nano Lett.* **2017**, *17*, 186–193; e) K. Otsubo, T. Haraguchi, H. Kitagawa, *Coord. Chem. Rev.* **2017**, *346*, 123–138; f) K. Bairagi, O. Iasco, A. Bellec, A. Kartsev, D. Li, J. Lagoute, C. Chacon, Y. Girard, S. Rousset, F. Miserque et al., *Nat. Commun.* **2016**, *7*, 12212; g) C. Bartual-Murgui, E. Natividad, O. Roubeau, *J. Mater. Chem. C* **2015**, *3*, 7916–7924; h) C. M. Quintero, G. Félix, I. Suleimanov, J. Sánchez Costa, G. Molnár, L. Salmon, W. Nicolazzi, A. Bousseksou, *Beilstein J. Nanotech.* **2014**, *5*, 2230–2239.
- [19] M. A. Halcrow, *Chem. Lett.* **2014**, *43*, 1178–1188.
- [20] a) C. Lochenie, W. Bauer, A. P. Railliet, S. Schlamp, Y. Garcia, B. Weber, *Inorg. Chem.* **2014**, *53*, 11563–11572; b) B. Weber, W. Bauer, J. Obel, *Angew. Chem. Int. Ed.* **2008**, *47*, 10098–10101.

- [21] a) J.-F. Létard, P. Guionneau, E. Codjovi, O. Lavastre, G. Bravic, D. Chasseau, O. Kahn, *J. Am. Chem. Soc.* **1997**, *119*, 10861–10862; b) Z. J. Zhong, J.-Q. Tao, Z. Yu, C.-Y. Dun, Y.-J. Liu, X.-Z. You, *J. Chem. Soc., Dalton Trans.* **1998**, 327–328.
- [22] I. y. A. Gural'skiy, B. O. Golub, S. I. Shylin, V. Ksenofontov, H. J. Shepherd, P. R. Raithby, W. Tremel, I. O. Fritsky, *Eur. J. Inorg. Chem.* **2016**, 3191–3195.
- [23] R. G. Miller, S. Narayanaswamy, J. L. Tallon, S. Brooker, *New J. Chem.* **2014**, *38*, 1932.
- [24] a) R. Kulmaczewski, J. Olguín, J. A. Kitchen, Feltham, Humphrey L C, Jameson, Guy N L, J. L. Tallon, S. Brooker, *J. Am. Chem. Soc.* **2014**, *136*, 878–881; b) R. Traiche, M. Sy, H. Oubouchou, G. Bouchez, F. Varret, K. Boukheddaden, *J. Phys. Chem. C* **2017**, *121*, 11700–11708; c) T. Ueno, Y. Ii, T. Fujinami, N. Matsumoto, S. Iijima, Y. Sunatsuki, *Polyhedron* **2017**, *136*, 13–22.
- [25] H. Toftlund, E. Pedersen, S. Yde-Andersen, M. Westdahl, *Acta Chem. Scand.* **1984**, *38a*, 693–697.
- [26] E. Buhks, G. Navon, M. Bixon, J. Jortner, *J. Am. Chem. Soc.* **1980**, *102*, 2918–2923.
- [27] W. Bauer, W. Scherer, S. Altmannshofer, B. Weber, *Eur. J. Inorg. Chem.* **2011**, 2803–2818.
- [28] a) R. E. DeSimone, R. S. Drago, *J. Am. Chem. Soc.* **1970**, *92*, 2343–2352; b) J.-F. Létard, S. Asthana, H. J. Shepherd, P. Guionneau, A. E. Goeta, N. Suemura, R. Ishikawa, S. Kaizaki, *Chemistry* **2012**, *18*, 5924–5934; c) N. Paradis, G. Chastanet, J.-F. Létard, *Eur. J. Inorg. Chem.* **2012**, 3618–3624.
- [29] S. Schönfeld, C. Lochenie, P. Thoma, B. Weber, *CrystEngComm* **2015**, *17*, 5389–5395.
- [30] V. Gómez, C. Sáenz de Pipaón, P. Maldonado-Illescas, J. C. Waerenborgh, E. Martin, J. Benet-Buchholz, J. R. Galán-Mascarós, *J. Am. Chem. Soc.* **2015**, *137*, 11924–11927.
- [31] B. Weber, *Coord. Chem. Rev.* **2009**, *253*, 2432–2449.
- [32] B. Weber, E.-G. Jäger, *Eur. J. Inorg. Chem.* **2009**, 465–477.
- [33] H. G. O. Becker, *Organikum. Organisch-chemisches Grundpraktikum*, 19th ed., Barth, Ed. Dt. Verl. der Wiss., Leipzig, Berlin, Heidelberg **1993**.
- [34] a) A. Altomare, M. C. Burla, M. Camalli, G. L. Casciarano, C. Giacovazzo, A. Guagliardi, A. G. G. Moliterni, G. Polidori, R. Spagna, *J. Appl. Crystallogr.* **1999**, *32*, 115–119; b) M. C. Burla, R. Caliendo, B. Carrozzini, G. L. Casciarano, C. Cuocci, C. Giacovazzo, M. Mallamo, A. Mazzone, G. Polidori, *J. Appl. Crystallogr.* **2015**, *48*, 306–309.
- [35] G. M. Sheldrick, *Acta Crystallogr., A, Found. Crystallogr. (Acta crystallographica. Section A, Foundations of crystallography)* **2008**, *64*, 112–122.

- [36] A. L. Spek, *PLATON - A Multipurpose Crystallographic Tool*, Utrecht University, The Netherlands **2008**.
- [37] G. M. Sheldrick, *Acta Crystallogr. A Found. Adv.* **2015**, *71*, 3–8.
- [38] W. Kabsch, *Acta Crystallogr. D Biol. Crystallogr.* **2010**, *66*, 125–132.
- [39] G. M. Sheldrick, *Acta Crystallogr. C Struct. Chem.* **2015**, *71*, 3–8.
- [40] C. B. Hübschle, G. M. Sheldrick, B. Dittrich, *J. Appl. Crystallogr.* **2011**, *44*, 1281–1284.
- [41] L. J. Farrugia, *J. Appl. Crystallogr.* **1997**, *30*, 565.
- [42] E. Keller, *Schakal-99*, University of Freiburg, Germany **1999**.
- [43] O. Kahn, *Molecular magnetism*, VCH, New York **1993**.
- [44] K. Lagarec, D. G. Rancourt, *Recoil, mössbauer spectral analysis software for windows 1.0*, Department of Physics, University of Ottawa, Canada **1998**.
- [45] S. Schlamp, P. Thoma, B. Weber, *Eur. J. Inorg. Chem.* **2012**, 2759–2768.
- [46] W. Bauer, C. Lochenie, B. Weber, *Dalton Trans.* **2014**, *43*, 1990–1999.
- [47] B. Weber, E. Kaps, J. Weigand, C. Carbonera, J.-F. Létard, K. Achterhold, F. G. Parak, *Inorg. Chem.* **2008**, *47*, 487–496.
- [48] S. Schlamp, P. Thoma, B. Weber, *Chem. Eur. J.* **2014**, *20*, 6462–6473.
- [49] a) A. Craze, N. Sciortino, M. Badbhade, C. Kepert, C. Marjo, F. Li, *Inorganics* **2017**, *5*, 62; b) M. Marchivie, P. Guionneau, J. A. K. Howard, G. Chastanet, J.-F. Létard, A. E. Goeta, D. Chasseau, *J. Am. Chem. Soc.* **2002**, *124*, 194–195.
- [50] W. Bauer, B. Weber, *Acta Crystallogr. C* **2008**, *64*, m237-m239.
- [51] B. Weber, E. Kaps, K. Dankhoff, *Z. Anorg. Allg. Chem.* **2017**, *643*, 1593–1599.
- [52] a) W. Bauer, M. M. Dîrtu, Y. Garcia, B. Weber, *CrystEngComm* **2012**, *14*, 1223–1231; b) T. M. Pfaffeneder, S. Thallmair, W. Bauer, B. Weber, *New J. Chem.* **2011**, *35*, 691–700.
- [53] S. Schlamp, K. Dankhoff, B. Weber, *New J. Chem.* **2014**, *38*, 1965–1972.

7. Amphiphilic Iron(II) Spin Crossover Coordination Polymers: Crystal Structures and Phase Transition Properties

Johannes Weihermüller,^a Stephan Schlamp,^a Wolfgang Milius,^b Florian Puchtler,^b Josef Breu,^b Philipp Ramming,^c Sven Hüttner,^c Seema Agarwal,^d Christoph Göbel,^a Markus Hund,^e Georg Papastavrou^e and Birgit Weber*^a

^aDepartment of Chemistry, Inorganic Chemistry IV, Universität Bayreuth, Universitätsstrasse 30, NW I, 95440 Bayreuth, Germany E-mail: weber@uni-bayreuth.de.

^bDepartment of Chemistry, Inorganic Chemistry I, Universität Bayreuth, Universitätsstrasse 30, NW I, 95440 Bayreuth, Germany.

^cDepartment of Chemistry, Macromolecular Chemistry I, Universität Bayreuth, Universitätsstrasse 30, NW I, 95440 Bayreuth, Germany.

^dDepartment of Chemistry, Macromolecular Chemistry II, Universität Bayreuth, Universitätsstrasse 30, NW I, 95440 Bayreuth, Germany.

^eDepartment of Chemistry, Physical Chemistry II, Universität Bayreuth, Universitätsstrasse 30, NW I, 95440 Bayreuth, Germany.

Electronic Supplementary Information (ESI) available: Experimental section, powder X-ray diffraction data and single crystal X-ray diffraction data, Mössbauer spectra of **7-10** and magnetic measurements of **2**, TGA and DSC measurements, POM micrographs of all complexes, AFM images of thin films of **7**. See DOI: 10.1039/c8tc05580g

Reproduced from *J. Mater. Chem. C*, **2019**,*7*, 1151-1163 with permission from the Royal Society of Chemistry

7.1 Abstract

Iron(II) coordination polymers with an N₂O₂ coordinating Schiff base-like equatorial ligand bearing different alkyl chain lengths (C16, C18, C20, and C22) and 1,2-di(4-pyridyl)ethyne, 1,2-bis(4-pyridyl)ethene or 1,2-bis(4-pyridyl)ethane as bridging ligand are synthesized. All complexes display a rather similar abrupt spin transition above room temperature, which is investigated using magnetic measurements and Mössbauer spectroscopy. Variation of the bridging ligand and the alkyl chain lengths allows fine tuning of the transition temperature in the range between 338 K

and 357 K. Single crystal X-ray structure analysis of two coordination polymers and one of the starting complexes reveals the formation of a lipid layer-like arrangement of the amphiphilic complexes in all cases. Further characterization by thermal gravimetric analysis, differential scanning calorimetry, X-ray powder diffraction, and polarized optical microscopy show in all cases solid-solid phase transitions. Those transitions determine the spin crossover behavior and depend on the crystal packing that is controlled by the alkyl chains in the outer periphery of the ligand. Thus, with the presented system the spin crossover properties are controlled by small alterations of the ligand structures. With respect to technological applications, spin coating is shown to be suitable for the processing of the complexes as thin films and furthermore thin platelets of the complexes can be generated by delamination techniques

7.2 Introduction

Bistability is a property frequently observed for hexa-coordinated complexes of 3d transition metals with d^4 - d^7 electron configuration.^[1-3] Through external perturbations like changes in temperature, pressure, by electromagnetic irradiation, or through chemical stimuli, the spin state of the metal center can be switched between a high spin (HS) and a low spin (LS) state, a phenomenon known as spin crossover (SCO). Due to the pronounced property changes upon SCO, these switchable molecular materials have a high potential for a variety of different applications.^[2,4] One example would be bio-sensors for nano-thermometry^[5] or the detection of biologically relevant parameters such as pH. In order to achieve such applications, the synthesis of nanostructured and/or composite materials is investigated very actively.^[6] Alternatively, attempts are made to combine the SCO with additional properties like softness (metallomesogens, amphiphilic molecules)^[7,8,9] leading to multifunctionality, new patterning possibilities, and by this enlarging the range of potential SCO applications. The structural changes upon spin state change could trigger a LC phase transition or, alternatively, the phase transition could trigger the spin transition.^[1,8,10] With regard to this, Seredyuk *et al.* demonstrated that the SCO can be influenced by crystal-liquid crystal phase transitions (PTs) of metal complexes functionalized with long alkyl chain substituents^[8,11] Hayami and co-workers observed interesting phenomena like a reverse ST due to PTs for amphiphilic cobalt complexes.^[1,12] Further approaches by the group of Real yielded scan rate dependent cooperative spin transitions for complexes with short alkyl chains^[13] and a more gradual SCO and crystal-liquid crystal phase transition for complexes with longer alkyl chains.^[14] Further optimization of the system showed that a phase transition in meltable complexes can be used to control the spin transition.^[15] Investigations of Albrecht *et al.* on amphiphilic iron(III) complexes in solution^[16] and in the solid^[17] revealed that an increase of the length of the

alkyl chains did lead to higher cooperativity of the spin crossover due to an improved self-assembly. Furthermore, the combination of LC and SCO properties offers the opportunity of an orientation of the complexes via the electrical field. In the case of amphiphilic systems new strategies to process bulk SCO compounds into thin films also motivated such studies. Those could be obtained by techniques such as the Langmuir-Blodgett, spin coating, or drop casting.^[9,16,18] Such self-assembled monolayers of SCO molecules as thin films can be studied by scanning tunneling microscopy (STM).^[19] Self-assembling spin crossover complexes based on alkylated ligands reported so far are either based on mononuclear complexes (e.g. Langmuir-Blodgett film formation of the $[\text{Fe}(\text{L}_2)(\text{NCS})_2]$ or $[\text{Fe}(\text{L})_3]^{2+} 2\text{NCS}^-$ system with $\text{L} = 2,2'$ -bipyridine substituted in position 4 and 4' with long alkyl chains),^[20,21] triazole-based coordination polymers with the triazole carrying alkyl trails (Langmuir-Blodgett film formation, solid state properties),^[22] or complexes with amphiphilic counter ions (thin film formation).^[23]

Please note that the SCO may be modified by the functionalization of ligands with long alkyl chains and by the processing, thus a prediction of the results so far is highly difficult.^[20] However, for a purposeful synthesis of SCO-based materials, it is indispensable to be able to predict the impact of changes in the ligand structure on the SCO parameters.

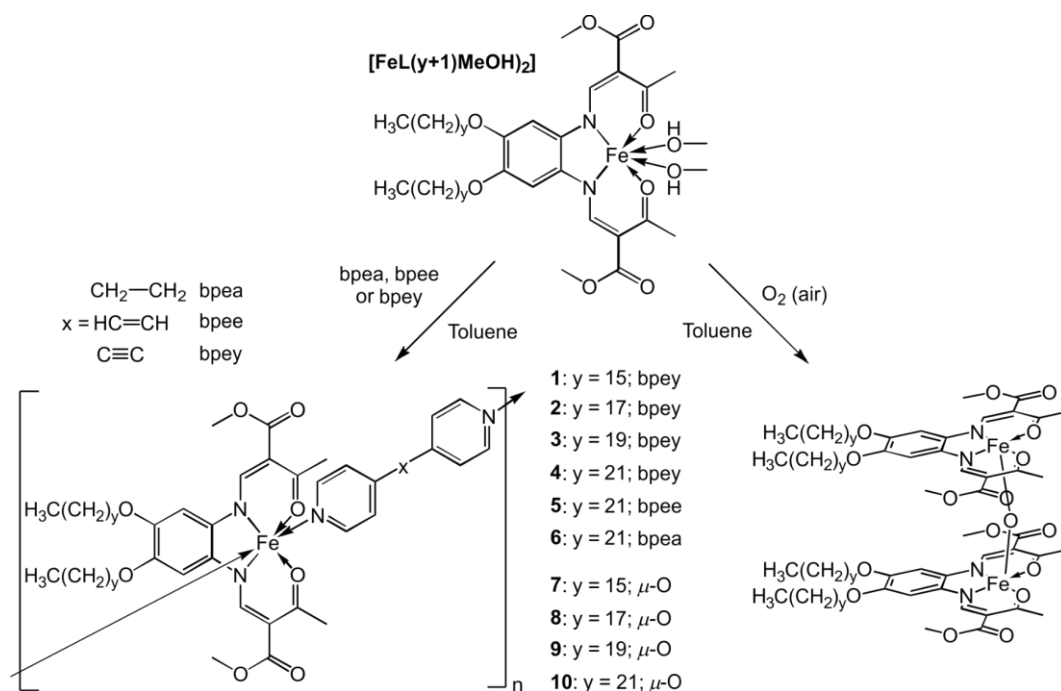
For iron(II) complexes with amphiphilic Schiff base-like ligands used in our group, self-assembly behavior was observed but no LC properties.^[24,25] The complexes crystallize in lipid layer like structures. In agreement with the results from Albrecht *et al.* longer alkyl chains support the formation of lipid layers and by this lead to improved spin crossover properties.^[26] In one case an over 20 K wide thermal hysteresis loop is observed.^[27] So far we were not able to investigate the PT properties of those complexes as they decompose at higher temperatures (above 350 K), a typical behavior for mono- and dinuclear complexes of this type. For the synthesis of more stable coordination polymers, relatively large bridging ligands as 1,2-bis(4-pyridyl)ethane (bpea), 1,2-bis(4-pyridyl)ethene (bpee), or 1,2-bis(4-pyridyl)ethyne (bpey) are necessary.^[28,29] For the realization of those systems the self-assembly parameter (*sap*) needs to be considered, where interplay of the coordination number, the size of the axial ligands attached at the iron(II) center, and the alkyl chain length is summarized.^[24] Through application of this parameter, we are now able to predict the successful synthesis of the coordination polymers with Schiff base-like ligand with 16 - 22 carbon atoms in the alkyl chain that crystallize in a lipid-layer like arrangement. Please note that despite of the number of examples it is still difficult for a given system to predict the packing of the molecules in the crystal and by this the spin crossover properties. Here we show that we are able to fine-tune the SCO parameters through control of the crystal packing – an essential point for future applications. Additionally, the investigation of amphiphilic SCO systems

is one step further towards synthesis of self-assembled (mono-)layers of SCO molecules. In contrast to the coordination polymers with amphiphilic ligands reported so far, the system presented here comprised neutral polymer chains. The influence of these differences on the SCO properties and film formation will be discussed.

7.3 Results and Discussion

7.3.1 Synthesis

In **Scheme 1**, the general structure of the ligands and complexes discussed in this work and the used abbreviations are given. The ligands **H₂L(y+1)** were synthesized following procedures described in literature for similar systems.^[26] The reaction with iron(II) acetate^[30] in methanol yielded the corresponding parent complexes **[FeL(y+1)(MeOH)₂]** with two methanol molecules as axial ligand. For **[FeL(20)(MeOH)₂]**, single crystals of high enough quality were obtained to determine the crystal structure that is discussed in the following. In the next step the axial ligands (MeOH) were substituted by 1,2-di(4-pyridyl)ethyne^[31,32] (bpey), 1,2-bis(4-pyridyl)ethene (bpee), or 1,2-bis(4-pyridyl)ethane (bpea), respectively to yield complexes **1 – 6** (Supporting Information, Scheme S1). Single crystals of **4·tol** and **6·tol** were obtained by slow diffusion setups whose structures are also discussed in the following. All iron(II) complexes are very air sensitive in solution and in part also in the solid state. For comparison purpose, the corresponding oxidized μ -O-complexes **7 – 10** were synthesized as well.



Scheme 1: General structure of the coordination polymers and the $\mu\text{-O}$ -complexes discussed in this work and their abbreviations. $(y+1)$ denotes to the number of carbon atoms of the alkyl chain, bpea, bpee, and bpey denote to the bridging ligands 1,2-bis(4-pyridyl)ethane, 1,2-bis(4-pyridyl)ethene and 1,2-bis(4-pyridyl)ethyne.

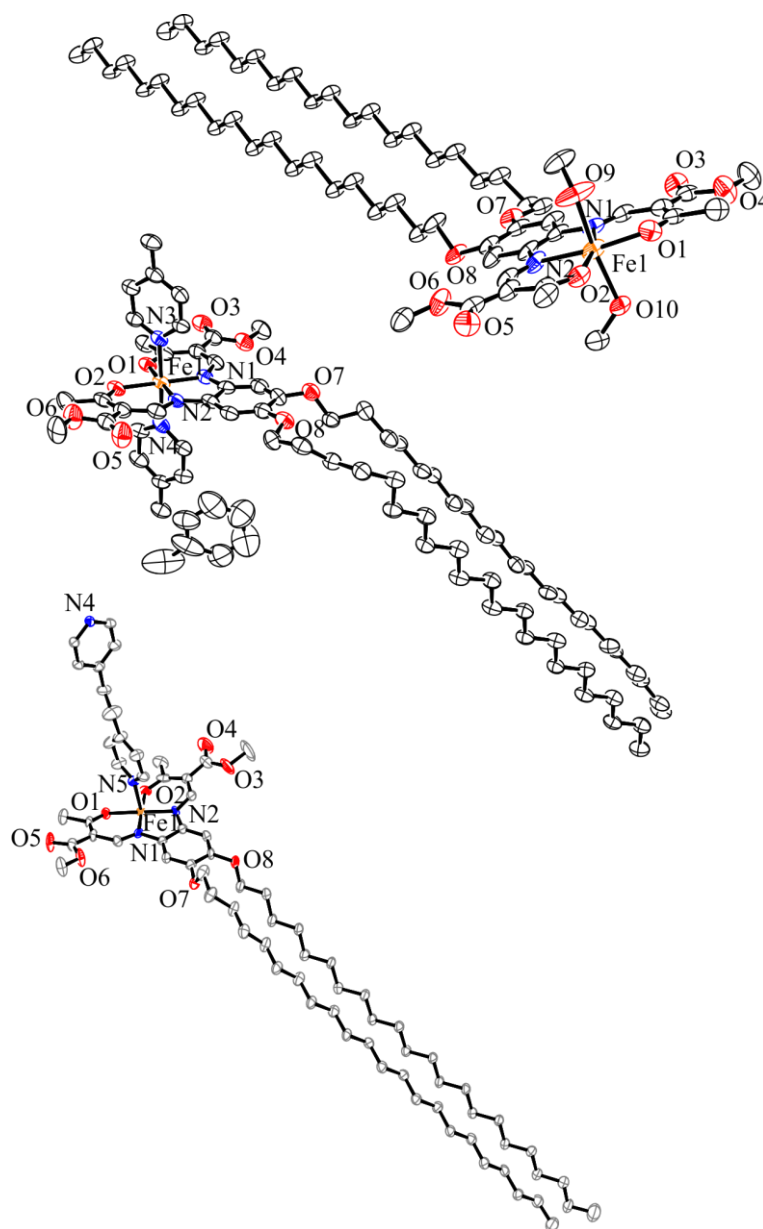
7.3.2 X-ray Structure Analysis

Platelet-like crystals of $[\text{FeL}(\mathbf{20})(\text{MeOH})_2]$ and $\mathbf{4}\cdot\text{tol}$ and spicular crystals of $\mathbf{6}\cdot\text{tol}$ suitable for X-ray structure analysis were obtained either directly from the synthesis or by slow diffusion setups. The crystal data were collected at 133 K ($[\text{FeL}(\mathbf{20})(\text{MeOH})_2]$ and $\mathbf{4}\cdot\text{tol}$) and 200 K ($\mathbf{6}\cdot\text{tol}$) and are summarized in the Supporting Information, **Table S1**. For $\mathbf{4}\cdot\text{tol}$ a non-mathematical twin was obtained. Therefore, the refinement of the crystal structure is incomplete and it will be discussed as a structural motif only. Thus, only the general packing of the molecules is considered but no exact bond lengths or angles are given. Please note that it is very difficult to obtain large enough single crystals of such amphiphilic complexes and that the molecular weight per iron center is with more than 1000 g/mol very high. Thus, the R values are in all cases larger than the ones usually obtained for smaller molecules. All complexes crystallized in the triclinic space group $P\bar{1}$. Selected bond lengths and angles within the first coordination sphere of the iron center are listed in **Table 1**. An ORTEP drawing of the asymmetric unit is given in **Figure 1**.

Table 1: Selected bond lengths [Å] and angles [°] of **[FeL(20)(MeOH)₂]***, **4·tol**, and **6·tol** within the first coordination sphere and their dimensions [Å] and *sap*.^[24]

Compound	Fe–N _{eq}	Fe–O _{eq}	Fe–O _{ax} /N _{ax}	O _{eq} –Fe–O _{eq}	L _{ax} –Fe–L _{ax}	∠L _{ax} ^{a)}	α	β	H	B	L	sap
[FeL(20)(MeOH)₂]	2.097(4)	1.990(4)	2.199(4)	109.38(14)	166.88(11)	---	162	176	8	15	33	0.7
	2.100(4)	2.019(3)	2.184(3)									
4·tol	1.9	2.0	2.0	86	176	5	112	131	14	15	29	1.0
	1.9	1.9	2.0									
6·tol	1.885(4)	1.917(3)	2.012(3)	90.05(10)	175.91(16)	88	140	158	13	14	29	0.9
	1.908(3)	1.953(3)	2.003(4)									

a) Torsion angle between the axial pyridine rings

**Figure 1:** ORTEP drawing of the asymmetric unit of the crystal structure of **[FeL(20)(MeOH)₂]** (top), **4·tol** (center) and **6·tol** (bottom). Hydrogen atoms are omitted for clarity. Thermal ellipsoids shown at the 50% probability level

The iron center of **[FeL(20)(MeOH)₂]** has an N₂O₄ coordination sphere build by the equatorial N₂O₂-coordinating Schiff base-like ligand and two axially coordinating methanol, as shown at the top of **Figure 1**. The average bond lengths are 2.10 Å (Fe–N_{eq}), 2.00 Å (Fe–O_{eq}), and 2.19 Å (Fe–O_{ax}) and the O–Fe–O angle is 109°. Those values are in the region typical for octahedral HS iron(II) complexes of this ligand type.^[28,33] The L_{ax}–Fe–L_{ax} angle of 166° deviates slightly of the expected 180° for a perfect octahedral coordination sphere. An analysis of the packing of the molecules in the crystal, given at the top of **Figure 2**, reveals that they are ordered in a lipid layer-like arrangement. The alkyl chains build parallel layers with an approximate layer to layer distance of about 4.2 Å. This distance is typical for stabilizing Van der Waals interactions (London Dispersion forces) between the alkyl chains and a similar behavior is observed for other amphiphilic complexes, not only for this general ligand type, but also for others that are less related.^[24] The iron containing head groups are oriented to each other between the layers of the alkyl chains. Two intermolecular hydrogen bonds are observed within the layer of the head groups. The hydrogen bond O(9)–H(9)⋯O(3) connects the complex molecule in the same lipid-like layer to form infinite chains along [1 0 0] and O(10)–H(10A)⋯O(2) connects the head groups of two opposite layers through the formation of dimers. The details (distances and angles) of the hydrogen bonds are given in **Table 2**.

Table 2: Distances [Å] and angles [°] of the hydrogen bonds of **[FeL(20)(MeOH)₂]***.

Bond	D–H	H⋯A	A⋯D	D–H⋯A
O(9)–H(9)⋯O(3) ^{a)}	0.84	1.87	2.672(7)	161
O(10)–H(10A)⋯O(2) ^{b)}	0.84	1.95	2.767(4)	165

a) 1+x,y,z. b) 1-x,2-y,2-z

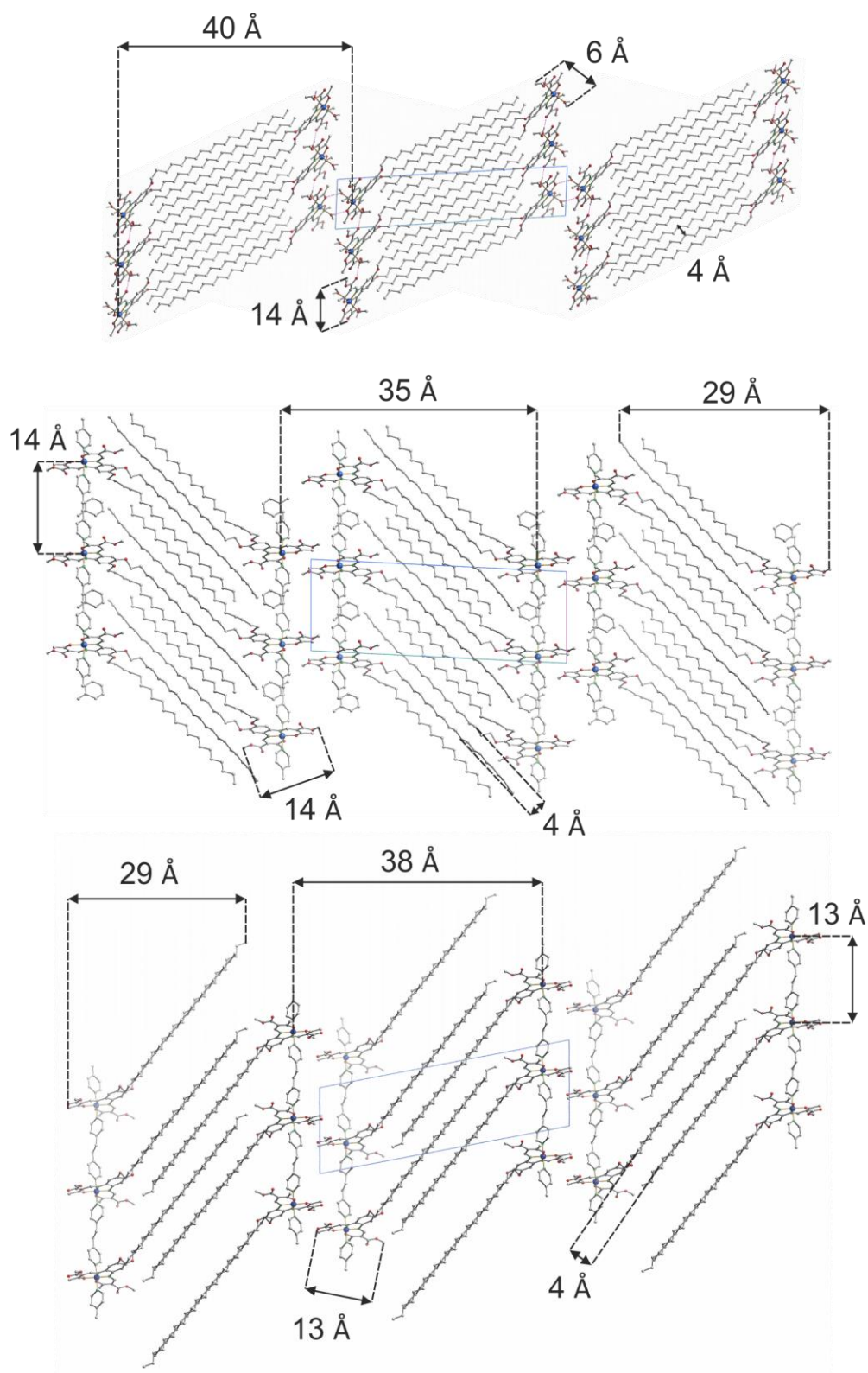


Figure 2: Molecular packing of $[\text{FeL}(\mathbf{20})(\text{MeOH})_2]$ along $[0.3\ 2.3\ 0]$ (top), $\mathbf{4}\text{-tol}$ along $[1\ 0\ 0]$ (center) and $\mathbf{6}\text{-tol}$ along $[1\ 0\ 0]$ (bottom) illustrating selected intermolecular distances discussed in the manuscript. Hydrogen atoms are omitted for clarity.

ORTEP drawings of the asymmetric unit of **4·tol** and **6·tol** are given in the center and at the bottom of **Figure 1**. In both cases the iron center has an N_4O_2 coordination sphere build of the equatorial N_2O_2 coordinating ligand and the bridging N coordinating ligand. The average bond lengths within the first coordination sphere are 1.89 Å / 1.90 Å (Fe–N_{eq}), 1.96 Å / 1.94 Å (Fe–O_{eq}), and 1.99 Å / 2.01 Å (Fe–N_{ax}), respectively. The O–Fe–O angles are 88° in average. Those values are in the region typical for LS iron(II) complexes of this ligand type.^[32,34] The L_{ax}–Fe–L_{ax} angle of 176° (**4·tol** and **6·tol**) deviates only slightly of the expected 180° for a perfect octahedral coordination sphere. The torsion angle between the axial pyridine rings is 5° for **4·tol** and 88° for **6·tol**. The remaining electron density of **6·tol** indicates included solvent molecules. However, due to a strong disorder, they could not be further refined and therefore SQUEEZE from PLATON^[35] was used. A total number of 97 electrons were removed from the refinement with a void volume of 946 Å³. Consequently, intermolecular contacts between the polar head groups cannot be discussed for both complexes.

The packing of the molecules in the crystal is for both complexes very similar to that of **[FeL(20)(MeOH)₂]**. The distances between the alkyl chains correspond to a maximum of stabilizing Van der Waals interactions (approx. 4.2 Å), in good agreement with the particular high ordering of the alkyl chains without major bending. As shown in **Figure 2** (center and bottom), the molecules are ordered in the crystal in a lipid-layer like arrangement. One significant difference between the three structures are the angles between the plain of the chelate cycle and the alkyl chains. Here we can define two angles: the bending of the alkyl chains relative to the plane of the equatorial ligand (angle α) and the shift sideward in the plane of the chelate cycle (angle β). A schematic presentation of the angles is shown in **Figure 3**. For **[FeL(20)(MeOH)₂]** the bending α is 162° and the shifting β is 176°. This bending and shifting is more pronounced for the two complexes **4·tol** and **6·tol** with the longer chains. The values for **4·tol** are $\alpha = 112^\circ$ and $\beta = 131^\circ$ and for **6·tol** $\alpha = 140^\circ$ and $\beta = 158^\circ$, respectively. This deviation of an ideal linear arrangement along the equatorial ligand (both angles 180°) is responsible for the possibility of the complexes to crystallize in a hexa-coordinated fashion. The orientation compensates the sterical demand of the axial ligand and, therefore, provides a lipid layer-like ordering.

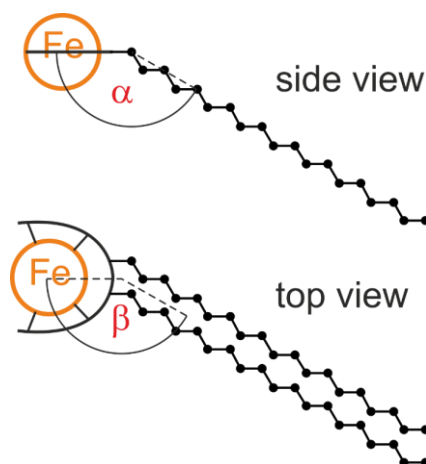


Figure 3: Schematic representation of the angles for the bending α and shifting β between the plane of the chelate cycle and the alkyl chains.

As discussed in a previous work,^[24] there is a relation between the size of the head group (height H plus broadness B) and the length L of the molecule which is called *sap* (self-assembly parameter):

$$sap = \frac{(H + B)}{L}$$

A lipid layer-like arrangement can be expected for a $sap \approx 1$. The calculated values for **[FeL(20)(MeOH)₂]**, **4•tol** and **6•tol** are shown in **Table 1**. **4•tol** and **6•tol** have a *sap* of around 1 which fits very well to the obtained lipid layer-like structure in the crystal packing. However, **[FeL(20)(MeOH)₂]** also shows this kind of arrangement despite of having a *sap* of 0.7. In literature, so far all examined complexes have values around 1 or higher, so it is possible that values below 1 can also lead to lipid layer-like structures. Another reason might be, that for **[FeL(20)(MeOH)₂]** the structure is additionally stabilized by the intermolecular hydrogen bond network. A similar behavior is observed for other methanol complexes of this ligand type with shorter alkyl chains.^[26]

In order to analyze, if the fine crystalline samples of **1 – 6** assume similar structures, the calculated X-ray powder diffraction pattern of **4•tol** and **6•tol** are compared with the measured XRPD patterns of **1 – 6**. The results are given in **Figure 4**. Indeed, in the region of $6^\circ - 8^\circ 2\theta$ and $20^\circ - 25^\circ 2\theta$ strong similarities in the diffraction patterns are observed. This can be used as first indication that in all cases coordination polymers were formed that assemble in a lipid layer like arrangement of the amphiphilic molecules with an approximate distance between the iron centers within the polymer chain of 13 – 14 Å and a distance between the layers of the alkyl chain in the region of 4.3 Å.^[24,36] Especially for the coordination polymers **1 – 4** with bpey as bridging ligand strong similarities are observed thus a very similar packing of the molecules in the crystal is likely. For the more flexible ligands bpee and bpea, the obtained samples are less crystalline with slightly

broader reflexes. However, the overall pattern is still very similar to that observed for **1** – **4** and to that of the calculated patterns from the single crystals. For comparison purpose, the XRPD spectra of the corresponding the μ -O-complexes **7** – **10** were recorded as well and are given in the SI, **Figure S1**.

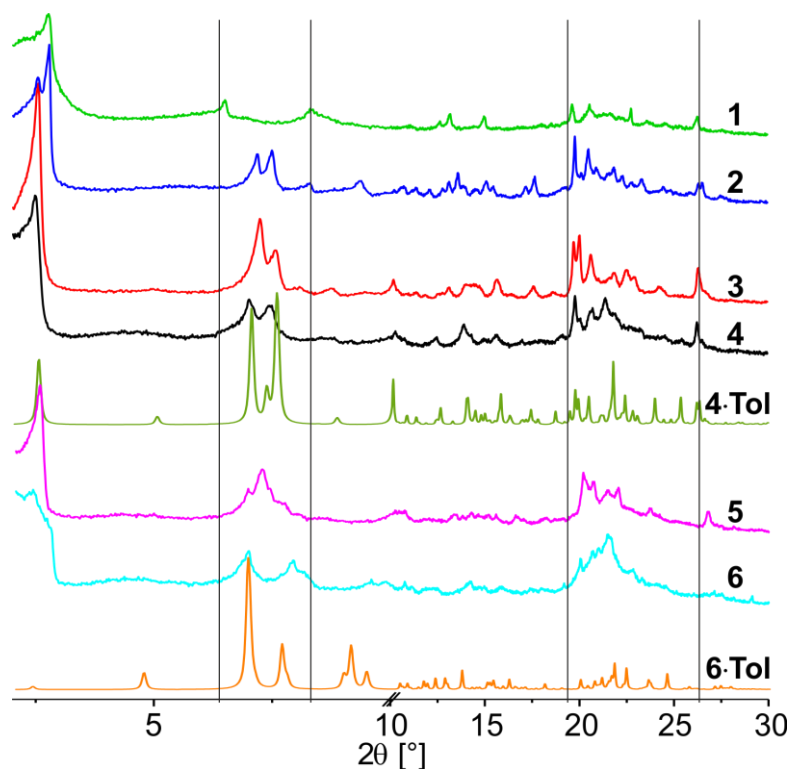


Figure 4: XRPD spectra of **1** – **6** in the range of 2° – 30° 2θ at room temperature and the calculated XRPD data of the single crystal of **4-tol** and **6-tol**. The vertical lines were included as guide for the eye.

Table 3: XRPD data and the calculated interplanar distances of **1** – **6**.

Compound	2θ [°]	d [Å]
1	2.750	32
2	2.525/2.765	35/32
3	2.540	35
4	2.465	36
4-tol	2.503 [#]	35 [#]
5	2.510	35
6	2.360	37
6-tol	2.316 [#]	38 [#]

[#] calculated values from the single crystal X-ray structure using Mercury^[37]

In contrast to the XRPD spectra of **1** – **6**, for the μ -O-complexes **7** – **10** a set of reflexes is observed in the region of $3.5^\circ - 6.5^\circ 2\theta$, whereas in the region $6.5^\circ - 8^\circ 2\theta$ no reflexes are observed. In the $20^\circ - 25^\circ 2\theta$, on the other side, some reflexes are observed as in the case of the coordination polymers. For all samples strong reflexes are observed below $3.5^\circ 2\theta$. In the case of the coordination polymers, the signal appears around $2.5^\circ 2\theta$. By using Bragg's law ($n\lambda = 2d\sin\theta$, $n = 1$, $\lambda = 1.54184 \text{ \AA}$, $d =$ interplanar distance, $\theta =$ scattering angle) the related distances can be calculated and correlated with distances observed in the crystal packing of **4-tol** and **6-tol** (**Table 3** and **Figure 2**). They fit very well to the Fe-Fe distance in the lipid layer-like structure. Furthermore, the trend for **1**, **3**, **4**, **5**, and **6** shows that the distance depends on the alkyl chain length which determines the thickness of the layer. Only **2** deviates slightly with two signals appearing, one a bit lower and one a bit higher than expected. It is possible that during the crystallization process two slightly different phases were formed. However, results from Mössbauer spectroscopy and magnetic measurements indicate that only one independent iron species is present.

7.3.3 Magnetic properties

Magnetic measurements were done for all coordination polymers (**1** – **6**), the results are displayed in **Figure 5** as plot of the HS fraction χ_{HS} vs. T . The $\chi_{\text{M}}T$ vs. T plot is shown in **Figure S2**. At room temperature the complexes **1** – **5** are clearly diamagnetic with a $\chi_{\text{M}}T$ product in the range between 0.02 and $0.27 \text{ cm}^3\text{Kmol}^{-1}$. **6** undergoes already a partial spin transition at this temperature and has a $\chi_{\text{M}}T$ value of $0.89 \text{ cm}^3\text{Kmol}^{-1}$. The spin state is confirmed by room temperature Mössbauer spectroscopy, the details are summarized in **Table 4**. For the complexes **1** – **5** the average values determined at room temperature are $\delta = 0.342 \text{ mm/s}$ and $\Delta E_{\text{Q}} = 1.193 \text{ mm/s}$. Those are characteristic for a low spin Fe(II) in an octahedral N_4O_2 coordination sphere.^[38] For complex **6**, on the other hand, two quadrupole split doublets are observed (**Figure 6** left, **Table 4**), of which one is characteristic for iron(II) in the low spin state, while the other one is characteristic for iron(II) in the HS state. Analysis of the relative area of the two doublets reveals a HS fraction of 0.17. Considering the differences of the Lamb-Mössbauer parameters for iron(II) in the HS and the LS state, this is in good agreement with the results from the magnetic measurement which show a χ_{HS} value of 0.26 at room temperature.

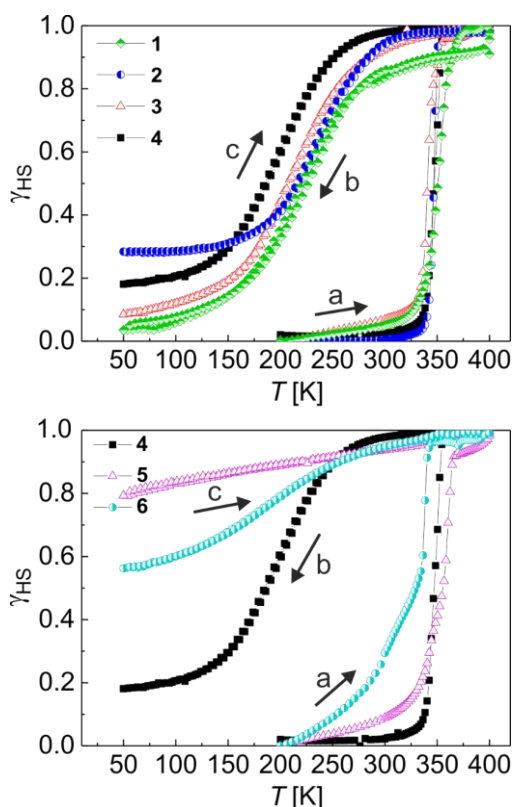


Figure 5: Magnetic measurements of **1** – **4** (top) and **4** – **6** (bottom) with γ_{HS} plotted against T . Temperature sequence: first heating (a), cooling (b), second heating (c).

Table 4: Magnetic properties of **1** – **10**. The magnetic susceptibility data of **1** – **6** is summarized on the left side. $T_{1/2}$ is used for the first heating and $T^*_{1/2}$ is used for the following cooling/heating cycles after annealing. On the right side the room temperature ^{57}Fe Mössbauer data are summarized for **1** – **10**. The SCO coordination polymers **1** – **6** were measured before and after annealing.

Compound	Magnetic measurements				Mössbauer studies				
	$\chi_M T$ (rt) [cm ³ Kmol ⁻¹]	γ_{HS} (rt)	γ_{HS} (50 K)	$T_{1/2}$ and $T^*_{1/2}$ [K]	Species	δ [mm/s]	ΔE_Q [mm/s]	I_{72} [mm/s]	Area [%]
1	0.15	0.05	-	354	Fe(II) LS	0.338(5)	1.173(10)	0.163(7)	100
1 _{annealed}	2.58	0.86	0.04	225	Fe(II) HS	0.96(8)	2.11(16)	0.238(6)	69(14)
					Fe(III) HS	0.3(3)	0.8(6)	0.3(2)	31(14)
2	0.02	0.01	-	347	Fe(II) LS	0.331(4)	1.175(8)	0.160(6)	100
2 _{annealed}	2.83	0.94	0.28	238	Fe(II) HS	0.936(18)	2.21(4)	0.18(3)	77(8)
					Fe(III) HS	0.35(9)	0.81(17)	0.22(12)	22(8)
3	0.21	0.07	-	340	Fe(II) LS	0.343(2)	1.203(3)	0.142(2)	100
3 _{annealed}	2.79	0.92	0.08	216	Fe(II) HS	0.924(4)	2.181(8)	0.158(6)	100
4	0.07	0.02	-	344/351	Fe(II) LS	0.345(4)	1.206(8)	0.141(6)	100
4 _{annealed}	2.94	0.98	0.18	199	Fe(II) HS	0.951(12)	2.14(3)	0.178(19)	100
5	0.27	0.09	-	340/369	Fe(II) LS	0.355(3)	1.207(5)	0.155(4)	100
5 _{annealed}	2.82	0.94	0.79	-	Fe(II) HS	0.879(7)	2.220(14)	0.178(11)	100
6	0.89	0.26	-	338	Fe(II) LS	0.389(17)	1.10(3)	0.231(14)	83(4)
					Fe(II) HS	0.90(7)	2.24(17)	0.21(6)	17(4)
6 _{annealed}	2.85	0.95	0.56	199	Fe(II) HS	0.94(3)	2.23(6)	0.19(5)	100
7	-	-	-	-	Fe(III) HS	0.334(16)	0.77(3)	0.17(2)	100
8	-	-	-	-	Fe(III) HS	0.335(13)	0.74(2)	0.200(18)	100
9	-	-	-	-	Fe(III) HS	0.330(16)	0.75(3)	0.18(2)	100
10	-	-	-	-	Fe(III) HS	0.31(4)	0.73(6)	0.23(5)	100

Upon heating to 400 K the complexes **1** – **4** with different alkyl chain lengths and bpey as bridging ligand show a very similar abrupt, irreversible SCO from LS to HS with $T_{1/2}$ of 354 K for **1**, 347 K for **2**, 340 K for **3** and 344/351 K for **4** (Top of **Figure 5**). The room temperature $\chi_{\text{M}}T$ product after annealing is with an average value of $2.79 \text{ cm}^3\text{Kmol}^{-1}$ lower than expected for an iron(II) in the HS state (details see **Table 4**). This is most likely due to the phase transition observed by temperature dependent polarized optical microscopy and powder XRD. The now observed gradual SCO already starts around room temperature and by this leads to reduced $\chi_{\text{M}}T$ values. In order to confirm that a spin transition took place and to check if it is complete or not, Mössbauer spectra were recorded of the annealed (heating to 380 K for a few minutes) complexes at room temperature. Those measurements confirm that after the first heating the samples are in the HS state at room temperature (see **Figure 6** and **Table 4**). After heating to 380 K (above SCO temperature, but below the melting point, see below), for the complexes **3** – **6** a single HS site is observed. However, in the case of **1** and **2** a second doublet is observed whose parameters cannot be related to iron(II) in the HS or the LS state. Comparison with the room temperature Mössbauer parameters of the oxidized complexes **7** – **10** (Supporting Information, **Figure S3** and **Table 4**) confirms that this doublet belongs to a Fe(III) HS species. This indicates that the compound oxidized either during the heating process or during the Mössbauer measurement itself (around 5 days at room temperature). During the magnetic measurements in the SQUID magnetometer, no indications for the formation of oxidized species during the heating progress are observed. Here, subsequent cooling of the complexes to 50 K reveals a gradual, reversible SCO from HS to LS for all complexes with $T^*_{1/2}$ values of 225 K for **1**, 238 K for **2**, 216 K for **3**, and 199 K for **4**. This SCO is incomplete and at 50 K χ_{HS} varies between 0.04 for **1**, 0.28 for **2**, 0.08 for **3**, and 0.18 for **4**, respectively.

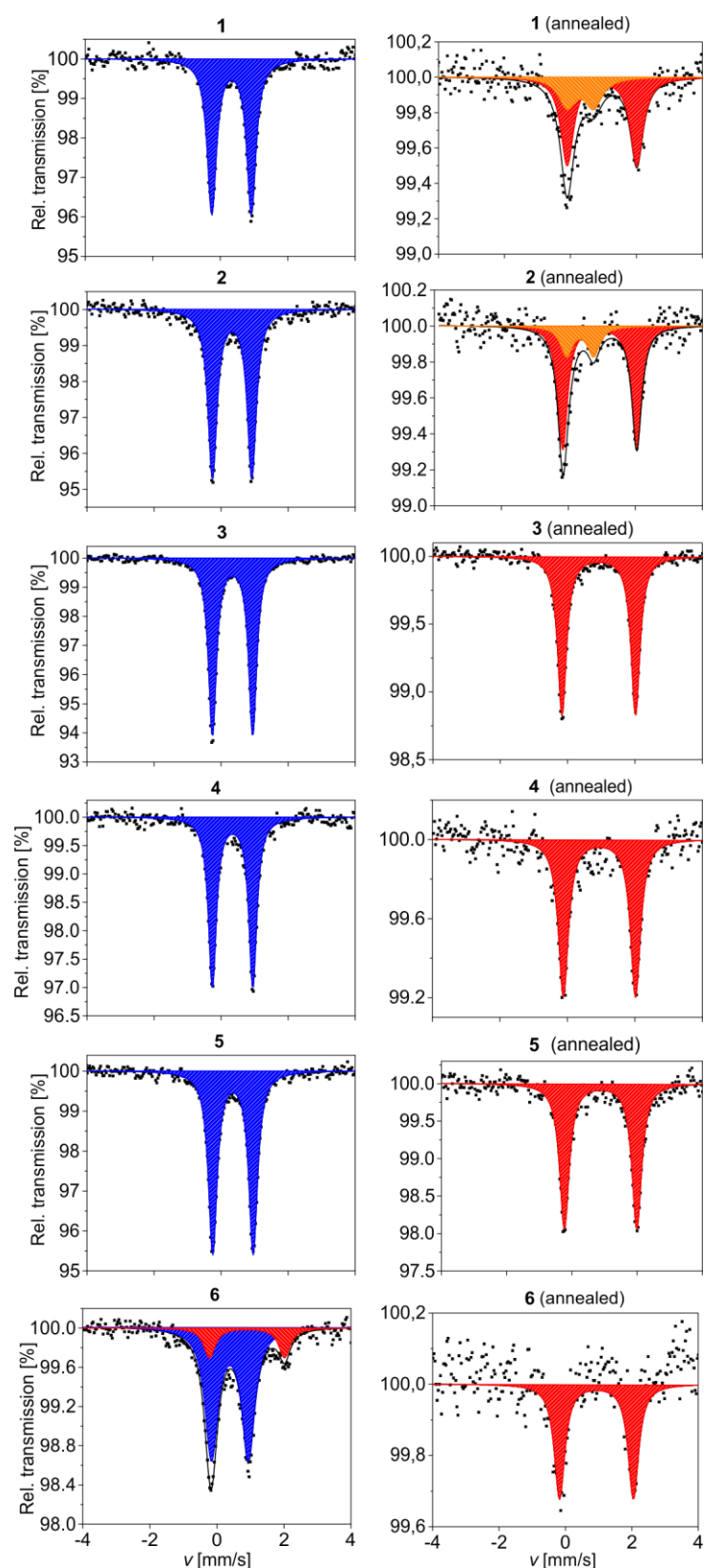


Figure 6: Mössbauer spectra of **1** – **6** measured at room temperature (left: before annealing, right: after annealing at 380 K for about 10 min). The blue doublet corresponds to iron(II) in the low spin state and the red doublet corresponds to iron(II) in the high spin state. The orange doublet is characteristic for the corresponding μ -O-iron(III) species (high spin state). The corresponding parameters are summarized in **Table 4**.

For **4** – **6** the alkyl chain length of C22 was kept constant, but the axial ligand was varied from bpey, to bpee and bpea. At the bottom of **Figure 5** the results from the temperature dependent measurement are given that show that the influence of the bridging ligand on the SCO behavior is stronger in comparison to a change of the alkyl chain length. This is due to stronger interactions of the iron center with the bridging ligand than with the alkyl chains at the outer periphery. From bpey (**4**) to bpee (**5**) and bpea (**6**) the SCO of the first heating becomes more and more gradual. This can be explained with the decreasing rigidity of the bridging ligand. A more rigid system tends to have a more abrupt SCO. $T_{1/2}$ of the abrupt part of the SCO is 344/351 K for **4**, 340/369 K for **5**, and 338 K for **6**. Upon cooling to 50 K, the second SCO is incomplete for bpey (**4**) and bpea (**6**) with a χ_{HS} fraction of 0.18 and 0.56, respectively, and almost disappears for bpee (**5**) with a χ_{HS} fraction of 0.79. In order to analyze the spin crossover and potential phase transition behavior in more detail, the magnetic measurements were repeated for **2** using slightly varied conditions. The sample was heated up to 354 K (only slightly above $T_{1/2}$ and significantly below any further phase transitions, see TGA/DSC) with three repeating heating and cooling cycles (**Figure S4**). Independent of this, the same initial abrupt SCO is observed followed by a gradual SCO during the subsequent cooling and heating cycles. Thus, the SCO behavior is not influenced by any subsequent phase transitions/melting of the sample above 354 K. When **2** is measured for three heating and cooling cycles it can be seen that at 50 K χ_{HS} increases after each cycle from 0.30 to 0.56 to 0.76 and the gradual SCO is slowly disappearing.

7.3.4 TGA and DSC

In both single crystal X-ray structures of **4·tol** and **6·tol** solvent molecules were observed in the crystal packing. From the literature it is known that SCO phenomena can be triggered or influenced by a solvent loss.^[39] Consequently, TGA measurements of the fine crystalline samples **1** – **6** were performed to analyze if solvent is included in the crystal packing that could influence the SCO behavior and explain the differences between the first and all subsequent heating modes. Please note that the complexes were dried in vacuum for several hours prior to all characterization to remove as much solvent as possible to reduce such effects. The results of the TGA measurements are displayed in the Supporting Information, **Figure S5**. In the case of **2**, **3**, **5** and **6**, the TGA shows a small step around the SCO temperature which can be associated with some solvent loss. On the other side, for the complexes **1** and **4** no indications for the presence of additional solvent in the sample is observed (Supporting Information, **Table S2**). The temperature range and percentage of the weight loss corresponds best to the inclusion of 0.5 to 1 methanol molecules per repeating unit of the coordination polymer (probably from the starting material). However,

according to elemental analysis, the inclusion of toluene is more likely. As the magnetic properties of all SCO coordination polymers is similar independent of the presence or absence of included solvent molecules, an influence of the solvent molecules can be ruled out. An irreversible phase transition accompanying the spin transition could be another reason for the different SCO properties for the first heating and all subsequent cycles. In order to analyse this, DSC measurements were performed with two heating and cooling cycles. The results are summarized in the Supporting Information, **Figure S6** and in **Table 5**. While there are no differences between the first and the second cooling cycle, in the heating mode pronounced differences between the first and the second cycle are observed. For the first heating, each coordination polymer undergoes an endothermic process around the $T_{1/2}$ of the SCO, as illustrated in **Figure 7**. The calculated enthalpy (ΔH) and entropy (ΔS) changes exceed by far the expected values for an iron(II) SCO ($\Delta H = 10 \text{ kJ mol}^{-1}$ and $\Delta S = 40 \text{ J K}^{-1} \text{ mol}^{-1}$, **Table 5**).^[1,2,40] This points towards a phase transition taking place during the spin transition. Either the spin crossover triggers the phase transition or vice versa. The absolute values of ΔH and ΔS strongly depend on the chain length of the equatorial ligand and increase with the extension of the alkyl chain (**1 – 4**). Thus, the spin transition is most likely triggered by a phase transition related to those alkyl chains. Furthermore, the values of ΔH and ΔS increase by decreasing flexibility of the bridging ligand (**4 – 6**) (**Figure 8**), however, here the changes are not as pronounced. The evaporation of additional solvent molecules also has an influence on ΔH and ΔS . However, in our case the influence is too small to be observable as only the number of C atoms appears to be relevant for the correlation shown in **Figure 8**. The two cooling cycles and the second heating cycle confirm the assumption that additional phase transitions take place next to the spin transition. The related structural changes were investigated further using temperature dependent powder XRD.

Table 5: Spin-crossover temperature $T_{1/2}$ obtained from magnetic measurements and thermodynamic parameters calculated from DSC for **1 – 6**.

Compound	SCO $T_{1/2}$ [K]	DSC T_{\max} [K]	ΔH [kJ mol ⁻¹]	ΔS [J K ⁻¹ mol ⁻¹]
1	354	354	30.15	84.26
2	347	351	45.18	125.19
3	340	351	69.57	213.49
4	344/351	353	78.83	237.57
5	340/369	336/362	73.24	203.33
6	338	340	67.85	197.32

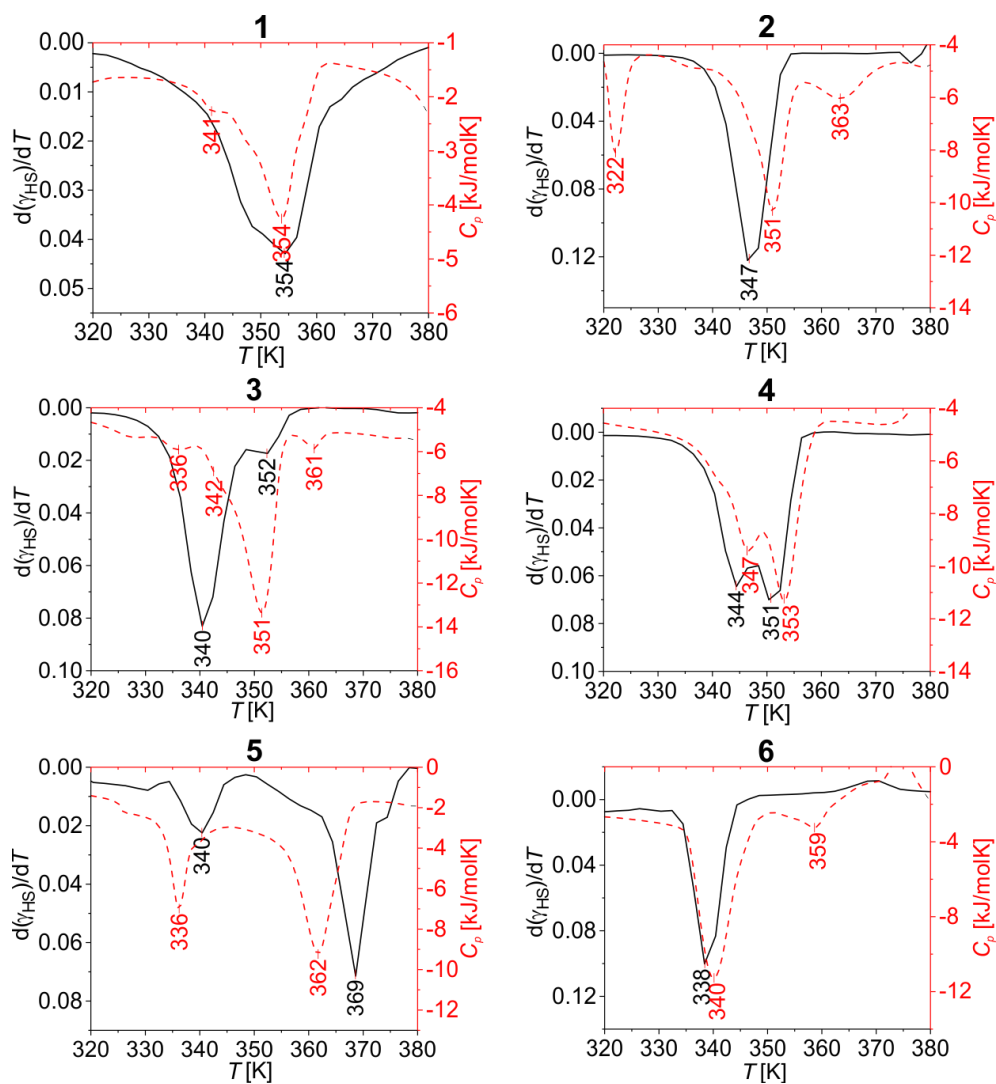


Figure 7: DSC measurements (red, dashed line) and the first derivative of the magnetic measurements (black, solid line) of **1** – **6** in the temperature range between 320 and 380 K illustrating a good agreement between both methods. The slight difference between the temperatures is most likely due to the different measurement velocities of the two methods.

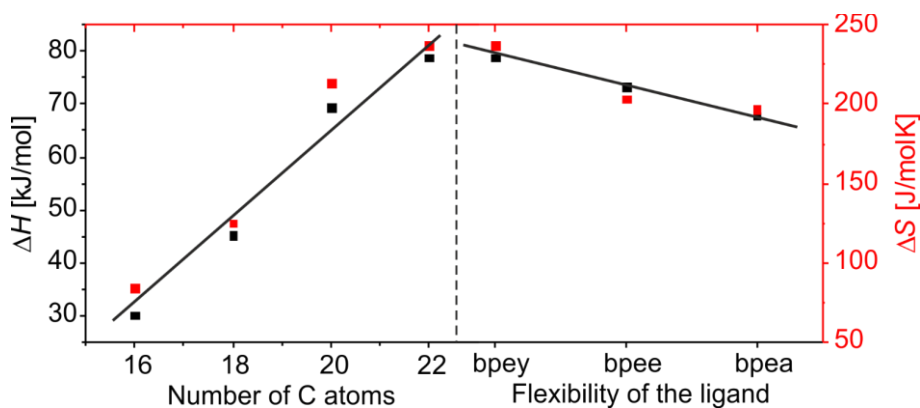


Figure 8: Influence of the chain length and of the flexibility of the bridging ligand on the enthalpy ΔH and entropy ΔS .

Temperature dependent XRPD measurements were carried out to analyze the structural changes associated to the combined spin and phase transition. Those will be reflected in changes in the XRPD patterns and can be related to characteristic Fe-Fe distances in the crystal packing (e.g. between the layers or interchain). Please note that the XRPD measurements mentioned in the previous paragraph were measured in a capillary, whereas the temperature dependent XRPD measurements were measured on a flat plate. Thus, small differences in the 2θ values between those two methods can occur. In **Figure 9**, the temperature dependent changes in the $2.0 - 3.5 2\theta$ region is displayed for the complexes **2**, **4** and **5** as typical examples. The corresponding powder diffraction patterns of the other three complexes together with the diffraction patterns in the whole 2θ range are given in the Supporting Information, **Figure S7** and **Figure S8**. As already discussed in the X-ray structure analysis section and illustrated in **Table 3**, the $2.0 - 3.5 2\theta$ region is characteristic for the distance between the layers of the lipid-like structure. Upon heating of **4**, three different phases are observed. Starting at room temperature upon heating to 338 K a first phase with a peak maximum at $2.5^\circ 2\theta$ is observed. At 343 K a second peak appears at $2.7^\circ 2\theta$, that increases in intensity at 348 K while the intensity of the first peak decreases. At 358 K the first peak disappeared completely and a third peak starts to appear at $3.0^\circ 2\theta$. At 363 K this is the only peak. The increase in the 2θ values upon increasing temperature corresponds to a decrease of the distances between the layers, thus a rearrangement of the alkyl chains of the complexes takes place. The other complexes show similar phase transitions with either two (**2** and **5**) or three (**1**, **3**, **4**, and **6**) different phases. No systematic trend can be observed if the peak maximum shifts to higher (**4** and **5**) or lower (**2** and **6**) 2θ values. In the case of **3** the intermediate phase at 363 K is shifted to higher 2θ values and upon further heating it goes back to almost the original value, whereas for **1** an opposite trend is observed with the highest temperature peak in the middle between the two others. Thus, the statement that can be derived from those results is that the phase transition is accompanied by an irreversible rearrangement of the alkyl chains leading to changes in the distances between the polymer chains. Those changes are always in the $2.4 - 2.9 2\theta$ region corresponding to distance changes in the range between 36.8 to 30.5 Å. The numbers indicate that this involves a significant structural re-organization that leads to a loss of cooperativity (and crystallinity) and a gradual SCO is observed afterwards. Those significant rearrangements also lead to a shift of peaks in the other 2θ regions, as illustrated in the Supporting Information, **Figure S8**. In order to analyze the irreversible nature of this rearrangement in more detail, in the case of **1** two subsequent heating and cooling cycles were investigated. In the Supporting Information, **Figure S9**, the room temperature XRD pattern before annealing (1st cycle), after

heating to 413 K (2nd cycle) and after heating to 373 K (3rd cycle) are given. It can be seen that after the first heating the XRPD pattern did change, however no further changes are observed for subsequent heating cycles.

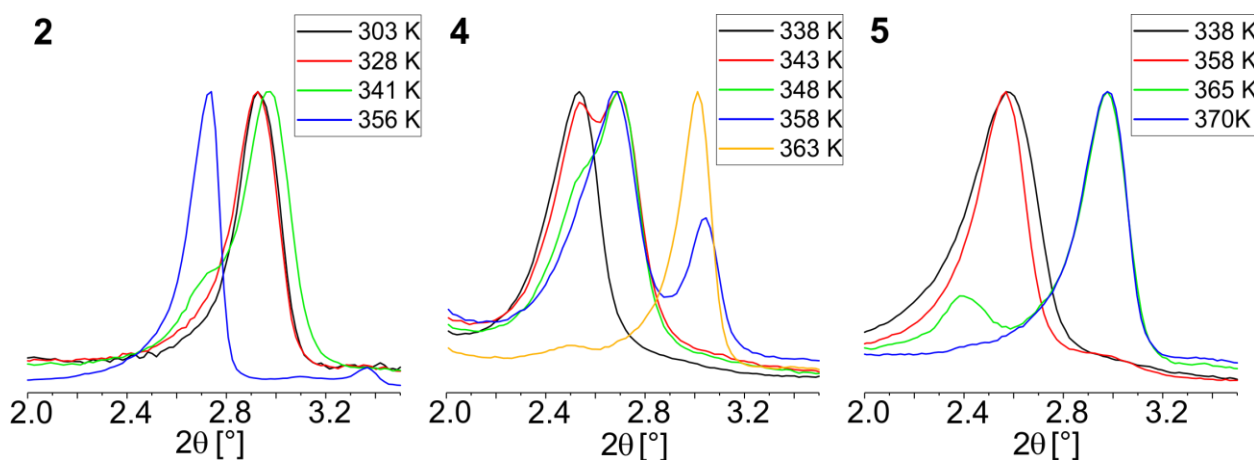


Figure 9: Temperature dependent XRPD spectra of **2**, **4** and **5** displayed in the 2.0° – 3.5° 2θ range. The temperatures were selected based on the DSC measurements and the phase transitions observed therein.

7.3.5 Polarized Optical Microscopy

In order to analyze the phase transitions observed by DSC and XRPD in more detail, polarized optical microscopy (POM) pictures of all coordination polymers (**1** – **6**) were taken at different temperatures in the heating and cooling mode. The micrographs were recorded with and without a retardation plate (first order). In **Figure 10**, the different phases of **4** as function of temperature are shown as typical example. In **Figure 10A** and **B** the crystalline phase at room temperature is shown. Upon heating above the SCO temperature (**Figure 10C** and **Figure 10D**), the solid-solid phase transition detected by DSC measurements is reflected in changes in the POM micrograph. Further heating resulted in a melting of the sample around 384 K (**Figure 10E** and **Figure 10F**), in line with the outcomes of the DSC measurements. When the sample is cooled down after the initial melting, the formation of ordered, birefringent domains is observed (**Figure 10G** and **Figure 10H**). Thus, from the melt the complex crystallizes in a different phase compared to the crystallization from solution. This is in good agreement with the differences in the magnetic properties after the first heating and for all subsequent heatings. For the samples **1** – **3**, **5** and **6** a similar behavior is observed that is illustrated in the Supporting Information, **Figures S10** – **S14**. In all cases the phase transition associated to the spin transition is reflected in changes of the POM micrographs. A chain length dependent difference is observed for the final structures. For the complexes **1**, **2**, and **3** with C16 – C20 alkyl chains, spherulites are observed after cooling down from the melt, while for the complexes **4** – **6** with 22 carbon atoms in the alkyl chain, birefringent

domains are observed after cooling. The corresponding POM micrographs are summarized in **Figure 11**. The changes of the crystalline phase after heating to 400 K were additionally investigated using scanning electron microscopy for complex **4**. The results are shown in the Supporting Information, **Figure S15**. After crystallization from solution, the sample consists of plate-like crystals with a thickness of about 65 nm. After heating and crystallization from the melt, again plate-like crystals are observed with a similar average thickness (82 nm).

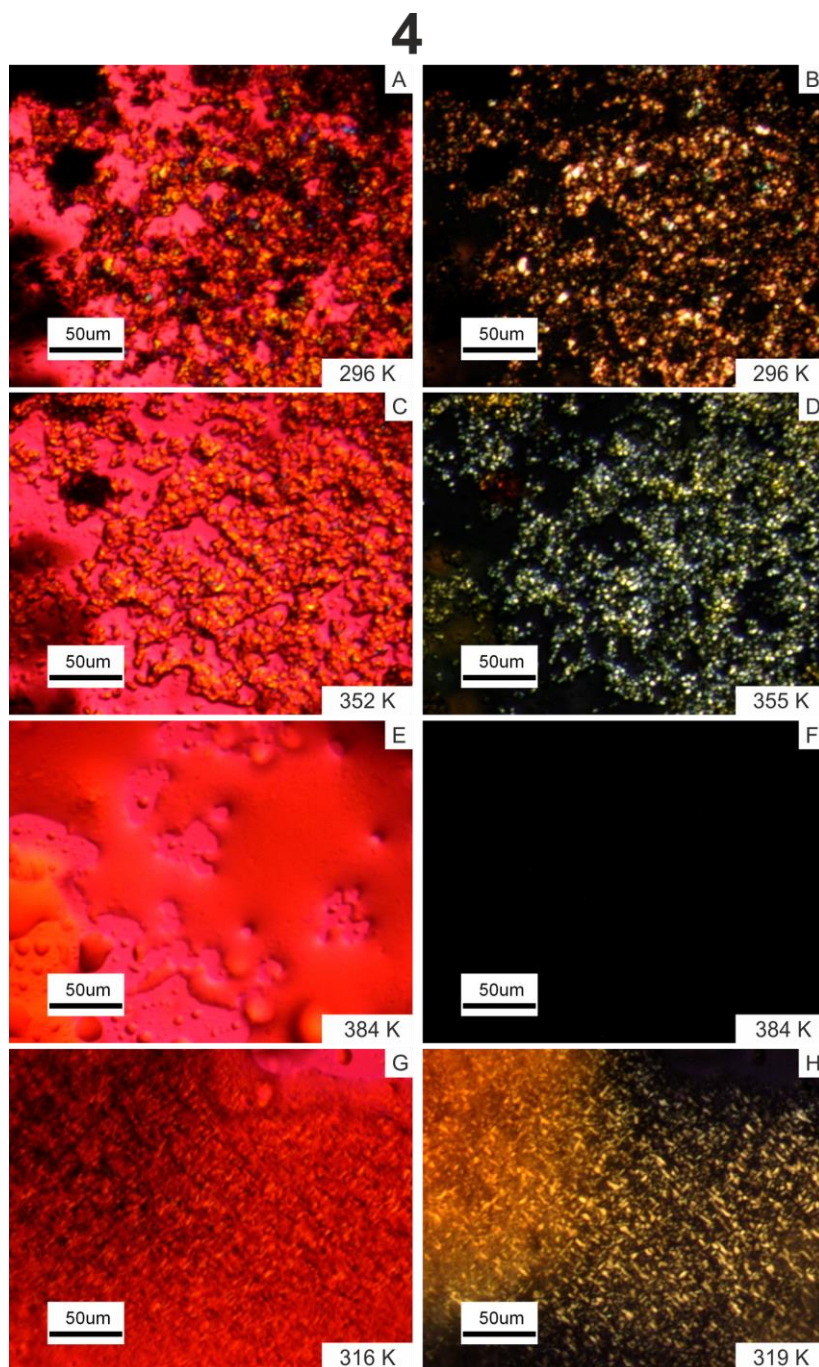


Figure 10: POM micrographs of **4**. All images were taken under crossed polarized light. Left: with retardation plate, right: without retardation plate. A) and B): crystalline powder from synthesis; C) and D): after combined SCO and phase transition; E) and F): melted sample; G) and H): formation of birefringent domains after cooling down.

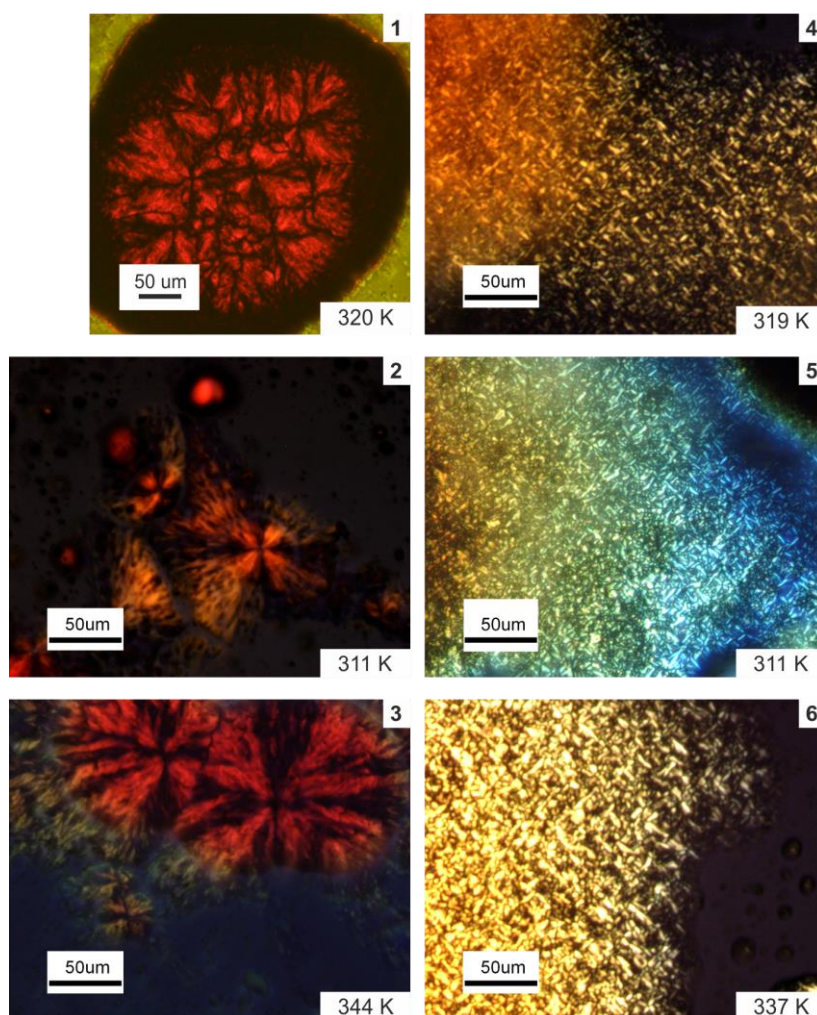


Figure 11: POM micrographs with cross shaped spherulites of **1 – 3** and the birefringent domains of **4 – 6** after the first heating.

7.3.6 Processing as thin films

One of the advantages of amphiphilic complexes is that they offer an easy approach towards thin film formation. This is of importance for potential applications and the construction of functional devices. Consequently, the suitability of the complexes described in this work for film formation was tested using the spin coating approach. Due to the air sensitivity of the iron(II) complexes **1 – 6**, the corresponding μ -O-complex **7** was used for first preliminary investigations on the general suitability of these complexes for spin coating experiments. **7** was dissolved in toluene and spin coated with different concentrations and spin coating speeds on silicon wafers (**Table 6**). Spin coating on glass slides and ODTS functionalized silicon wafers was also tested, but did not result in a homogeneous film and is therefore not further discussed. The morphology of the films was then analyzed by atomic force microscopy (AFM) in tapping mode (**Figure S16**). Images with a resolution of 20x20 μm and 1x1 μm or 10x10 μm were recorded. To be able to measure the film

thickness a small scratch was carved in the film with a needle. Due to this some of the removed material was deposited next to the edge and will be disregarded. Height profiles at different locations of the film were extracted and the film thickness and the RMS (root mean square) roughness was determined. With a concentration of 0.2 mg/mL (**Figure S16 A1**) no film formation can be observed. However, a network is formed with bridges of about 2 nm height. By increasing the concentration to 1.0 mg/mL a film with cavities is formed. The film thickness is 4 nm (**Figure S16 B2**) and the film RMS roughness is 1.4 nm (**Figure S16 B1**). A concentration of 5 mg/mL increases the film thickness up to 22 nm (**Figure S16 C2**) while the number of cavities decreases (**Figure S16 C1**). The cavities still reach down to the surface of the silicon wafer. Thus, the RMS roughness increases to 4.8 nm. By further increasing the concentration to 10 mg/mL the film thickness increases up to 30 nm (**Figure S16 D2**). At this concentration the cavities don't reach the silicon wafer anymore and the RMS roughness is decreased to 1.3 nm. The film becomes more and more homogenous (**Figure S16 D1**). For a concentration of 10 mg/mL the influence of the spin speed was investigated, too. An increase from 2000 rpm to 5000 rpm still resulted in the formation of a thin film with a thickness of 15 nm (**Figure S16 E2**) and an RMS roughness of 1.2 nm (**Figure S16 E1**).

Table 6: Spin coating parameters and film properties of **7**.

Concentration [mg/mL]	Spin speed [rpm]	Average film thickness [nm]	RMS roughness [nm] (image)
0.2	2000	-	1.5 (A1)
1.0	2000	4	1.4 (B1)
5.0	2000	22	4.8 (C1)
10.0	2000	30	1.3 (D1)
10.0	5000	15	1.2 (E1)

Motivated by those results in the following the iron(II) spin crossover complex **4** was characterized with regard to film formation. TEM samples of **4** were prepared to analyze if the same behavior is observed as for the iron(II) coordination polymers and to investigate the structure of the film in more detail. Furthermore, the complex was dissolved in toluene or suspended in *iso*-octane to investigate the impact of the solvent on the film formation. The results are illustrated in **Figure 12**. An incomplete film formation with gaps between the patterns was observed for the sample of **4** from toluene. The results are similar to those obtained for the AFM measurements done with **7** with low concentrations (**Figure S16 A1** and **B1**). It appears that a similar film formation behavior is observed for both, the coordination polymer and the dimeric iron(III) complex if toluene is used

as solvent. As **4** was insoluble in *iso*-octane the suspension was vortexed and ultrasonicated for some minutes. In the corresponding TEM pictures thin platelets and agglomerates of thin platelets are observed. In comparison to the SEM measurements (**Figure S15**) done for the same complex before and after annealing at 400 K, the platelets appear to be much thinner and separated layers can be identified as seen in **Figure 12 B**. It is possible that the ultrasonication procedure in the nonpolar solvent triggered a delamination of the layer-structure observed in the single crystal XRD. For the dried TEM sample the formation of agglomerates of the thin plates, as seen on the left side in **Figure 12 B**, was observed, too. To determine the thickness of the platelets AFM measurements of **4** dispersed in *iso*-octane were conducted. The results are illustrated in **Figure 13** and further images are given in the SI, **Figure S17**. The images show again small agglomerates where the platelets are not perfectly stacked above each other but are piled up in a random way. This can be seen in the height profiles as some slopes are increasing constantly while others increase step-wise. The thickness of the platelets is roughly between 75 nm (**Figure S17 C**) and 260 nm (**Figure S17 A**). However, for the height of 260 nm it was difficult to distinguish between multistacking and thicker platelets. Please note that for the untreated sample the SEM images (**Figure S15**) do not reveal such very thin platelets and the crystallites appear to be thicker.

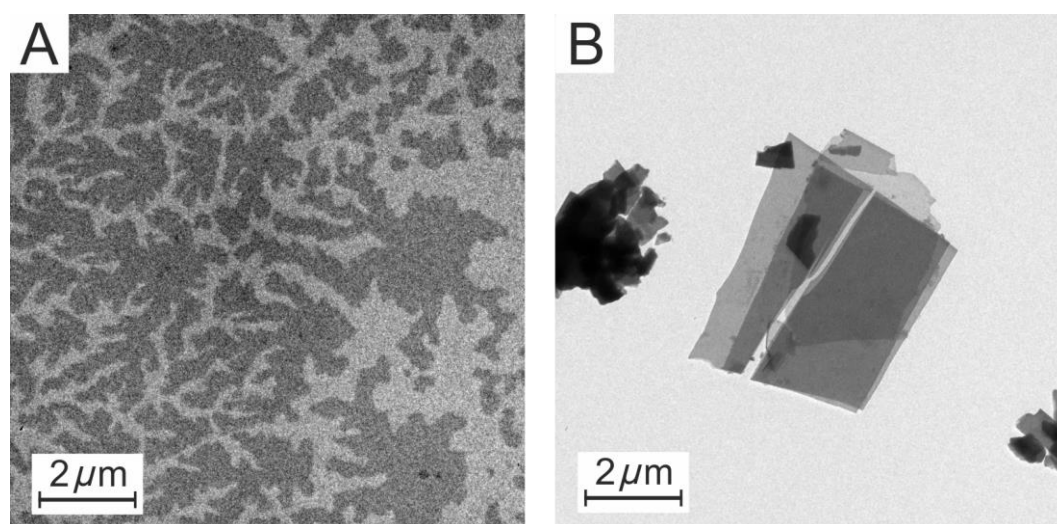


Figure 12: TEM images of **4** prepared in toluene (A) and *iso*-octane (B).

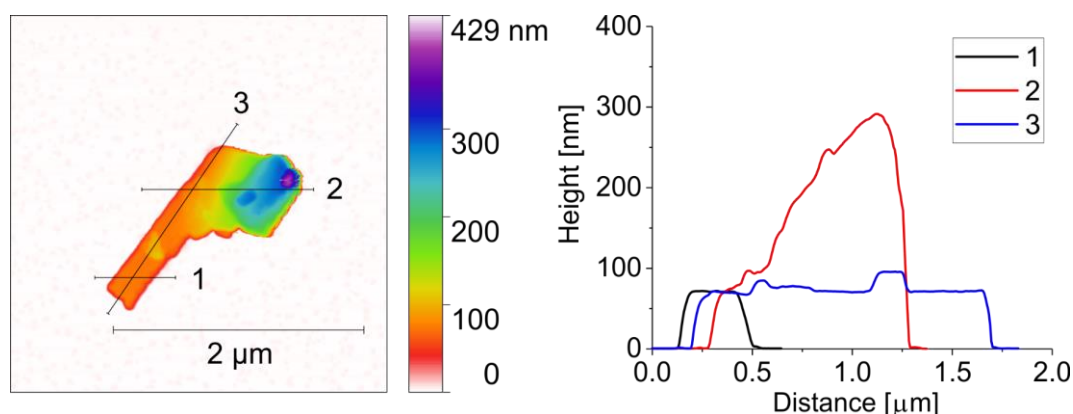


Figure 13: AFM images of **4** prepared in *iso*-octane with the corresponding height profiles.

7.4 Conclusion

In this manuscript the synthesis of six new iron(II) coordination polymers (**1** – **6**) with amphiphilic ligands is reported. All of them show an abrupt SCO above room temperature. After initial heating, **1** – **5** show a gradual and incomplete SCO at lower temperatures, while **6** remains in the HS state. The spin state before and after the first heating was confirmed by room temperature Mössbauer spectroscopy. DSC measurements of the six complexes reveal ΔH and ΔS values around the SCO temperature which are too high to be only associated with a spin transition. In addition, ΔH and ΔS increases with increasing alkyl chain length. This indicates the occurrence of a second process, namely a phase transition that is coupled to the spin transition and depends on the alkyl chain length and by this on the crystal packing. Single crystal X-ray structure analysis of three complexes (**[FeL(20)(MeOH)₂]**, **4-tol** and **6-tol**) reveals a lipid layer-like packing of the complexes in the crystal. The very similar PXRD patterns of all six coordination polymers indicates a similar packing in all cases that is dominated by the Van der Waals interactions between the alkyl chains. Thus, by ligand design it is possible to predict the packing of the molecules in the crystal. The Fe–Fe distance between the layers depends on the length of the alkyl chains. Temperature dependent XRPD supports the assumption that the spin transition is coupled to a phase transition which is triggered by a rearrangement of the alkyl chains. This rearrangement is also observable in POM micrographs and in addition to that ordered, birefringent domains appear in the solid phase after the melting process. The film formation behavior was tested for complex **7** using spin coating. By increasing the concentration from 0.2 mg/ml to 10 mg/mL the properties of the film significantly improved and with 10 mg/mL a homogenous film with a thickness of 30 nm and a RMS roughness of 1.3 nm was formed. As expected, an increase of the spin speed resulted in a reduction of the film thickness. Preliminary TEM and AFM measurements were done on films and delaminated

crystalline layers of the coordination polymer **4**. Further studies on the film vs. platelet formation and the corresponding magnetic properties are in progress.

7.5 Conflicts of interest

There are no conflicts to declare.

7.6 Acknowledgements

Financial support of the University of Bayreuth and the German Science formation (WE 3546/5-1 and SFB 840) is gratefully acknowledged. L. Peng, P. Pineda, J. Kronawitt and K. Küspert (MC, University of Bayreuth) are thanked for help with the calorimetric measurement and the polarized optical microscopy. We thank P. Mayer (University of Munich) for the collection of single crystal XRD data of **6•tol**.

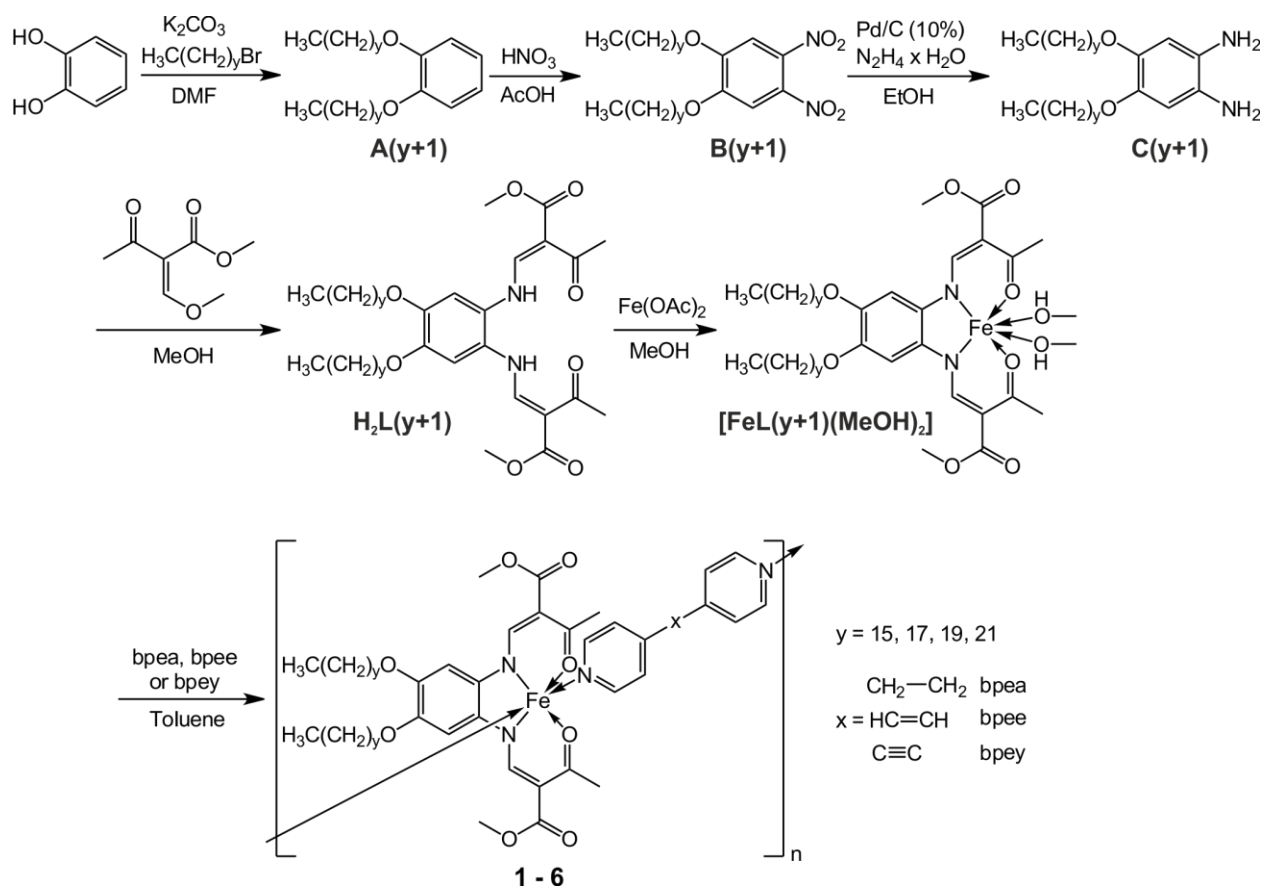
7.7 Supporting Information

Amphiphilic Iron(II) Spin Crossover Coordination Polymers: Crystal Structures and Phase Transition Properties

Johannes Weihermüller,^a Stephan Schlamp,^a Wolfgang Milius,^b Florian Puchtler,^b Josef Breu,^b Philipp Ramming,^c Sven Hüttner,^c Seema Agarwal,^d Christoph Göbel,^a Markus Hund,^e Georg Papastavrou^e and Birgit Weber*^a

- a. Department of Chemistry, Inorganic Chemistry VI, Universität Bayreuth, Universitätsstrasse 30, NW I, 95440 Bayreuth, Germany E-mail: weber@uni-bayreuth.de.
- b. Department of Chemistry, Inorganic Chemistry I, Universität Bayreuth, Universitätsstrasse 30, NW I, 95440 Bayreuth, Germany.
- c. Department of Chemistry, Macromolecular Chemistry I, Universität Bayreuth, Universitätsstrasse 30, NW I, 95440 Bayreuth, Germany.
- d. Department of Chemistry, Macromolecular Chemistry II, Universität Bayreuth, Universitätsstrasse 30, NW I, 95440 Bayreuth, Germany.
- e. Department of Chemistry, Physical Chemistry II, Universität Bayreuth, Universitätsstrasse 30, NW I, 95440 Bayreuth, Germany.

iron; spin crossover; ligand-design; self-assembly; phase transition



Scheme S1: Synthesis of the ligands and the resulting complexes 1 – 6.

Experimental Section

Infrared Spectroscopy: Transmission infrared spectra were collected using a PerkinElmer Spectrum 100 FT-IR (ATR). The samples were measured as solids.

Elemental Analysis: Carbon, hydrogen and nitrogen contents were measured using a Vario EL III. The samples were prepared in tin boats. All samples were measured at least twice and the average was used. Acetanilide (Merck) was used as standard.

Mass Spectrometry: Mass spectra were recorded with a MS8500 sector field mass spectrometer from Thermo Finnigan. Direct injection was used and the measurement was done in a temperature range of room temperature to 330 °C.

Nuclear Magnetic Resonance Spectroscopy: The NMR spectra were recorded with a Varian Unity Inova 300 spectrometer from Agilent Technologies at 300 MHz. The samples were dissolved in CDCl₃ and their signals were calibrated to the residual signals of the solvent.

Magnetic Measurements: Magnetic measurements were collected using a SQUID MPMS-XL5 instrument from Quantum Design. A field of 1.0 T was applied and the samples were measured from 200 K to 400 K to 50 K to 400 K in sweep mode with a sweep velocity of 2K/min. Gelatine capsules in a plastic straw were used for sample preparation. Moreover, K₃[Fe(CN)₆] was added as a paramagnetic standard to bypass center problems. The diamagnetic parts of the sample holder, the organic ligand and additional paramagnetic parts of the standard were corrected afterwards by using tabulated Pascal's constants (ligand)^[41] or measured values (sample holder, K₃[Fe(CN)₆]).

Mössbauer Spectroscopy: ⁵⁷Fe Mössbauer spectra were recorded in transmission geometry at constant acceleration using a conventional Mössbauer spectrometer with a 50 mCi ⁵⁷Co(Rh) source. The samples were prepared under argon atmosphere. The spectra were fitted using Recoil 1.05 Mössbauer analysis software.^[42] Isomer shift values were reported with respect to α -Fe as a reference at room temperature.

Thermogravimetric Analysis: Thermogravimetric analysis was done with a Netzsch TG 209 F1 Libra under nitrogen atmosphere using 4 mg – 10 mg of the sample with a heating rate of 10 K min⁻¹.

Differential Scanning Calorimetry: The samples were measured with a Mettler Toledo 821c calorimeter under nitrogen atmosphere (50 mL min⁻¹). 5 mg – 10 mg of the samples were prepared in an aluminum boat (0.04 mL) and the heat rate was set to 10 K min⁻¹.

Single Crystal X-ray Diffraction: The X-ray crystal analysis of [FeL(20)(MeOH)2] and 4•tol were done on a STOE StadiVari diffractometer, the one of 6•tol was done on a Bruker D8 Quest diffractometer. Both were using graphite-monochromatic Mo-K α radiation. The data were

corrected for Lorentzian and polarization effects. The structures were solved by direct methods (SIR-97, SIR2014)^[43] and refined by full matrix-least square techniques against F_o^2 (SHELXL-97)^[44] Hydrogen atoms were included at calculated positions with fixed displacement parameters. Due to a strong disorder in **6•tol** the included solvent could not be solved and was squeezed with PLATON.^[35] ORTEP-III^[45] was used for the presentation of the asymmetric unit of the crystal structure, SCHAKAL-99^[46] to illustrate the molecular packing. Powder pattern were calculated from the x-ray crystal data by using Mercury.^[37] The supplementary crystallographic data for **[FeL(20)(MeOH)₂]** (CCDC number 1835195), for **6•tol** (CCDC number 1835196), and for **6•tol** (CCDC number 1044903) can be obtained free of charge from The Cambridge Crystallographic Data Centre via www.ccdc.cam.ac.uk/data_request/cif.

X-ray Powder Diffraction: XRPD measurements were done on a STOE Stadi P diffractometer in transmission geometry with Cu- K_α radiation and a Mythen1K detector. The grinded samples were prepared in glass capillaries under argon flow. Temperature dependent XRPD measurements were done on an X'Pert MPD Pro diffractometer from Panalytical (Bragg-Brentano geometry). Cu- K_α radiation was used. The samples were measured on a flat plate under nitrogen atmosphere in an XRK-900 chamber from Anton Paar.

Polarized Optical Microscopy: The micrographs were taken on a Nikon DIAPHOT 300 microscope using a Nikon Digital Camera DXM1200 and Nikon ACT-1 software. For temperature control a Mettler Toledo FP82HT Hot Stage was used. The samples were prepared between two glass plates and sealed with glue under argon atmosphere.

Scanning Electron Microscope: Scanning electron microscopy images were taken with a Zeiss LEO 1530. The samples were prepared on carbon tape.

Spin coating: Spin coating was done with 0.2 mg/mL, 1.0 mg/mL, 5 mg/mL, and 10 mg/mL solutions of **7** in toluene. The spin speed was 2000 rpm or 5000 rpm. The substrates were silicon wafers or glass slides (Menzel glass) which were first cleaned with acetone under ultrasonication for 10 min, then with a 1 vol% Hellmanex III (Hellma, Müllheim, Germany) solution at room temperature under ultrasonication for 10 min, then ultrasonicated twice in Milli-Q water for 10 min and finally ultrasonicated in iso-propanol for another 10 min. They were dried under nitrogen flow and then either put on a hotplate or put in an ozone oven. Some of them were then functionalized with octadecyltrichlorosilane (ODTS) after the ozone treatment and also dried on the hotplate.

Delamination procedure: **4** was dispersed in degassed *iso*-octane, vortexed, and ultrasonicated for about 1 min. One drop of the dispersion was then applied on a freshly prepared mica plate and used for AFM measurements.

AFM measurements: AFM measurements of **7** were done on a commercially available Dimension™ 3100 AFM from Veeco Instruments equipped with a Nanoscope® V controller (USA) and a hybrid XYZ closed loop scanner. The micro cantilevers (OTESPA-R3) were purchased from Bruker. The images were recorded with 512 rows and 512 pixels. The set point amplitude was 500 mV and the drive amplitude 380 mV. The scan rate was 0.4 Hz for the images with a resolution of 20x20 μm and 10x10 μm , and 1.0 Hz for the images with a resolution of 1x1 μm . AFM images were processed with Gwyddion 2.50.^[47] The data was leveled by mean plane subtraction and flattened by subtracting a third order polynomial background. The fast scanning x-axis was corrected with a median of differences algorithm. The minimum of the data values was then shifted to zero. AFM measurements of the delaminated crystals of **4** were done on a commercially available Dimension Icon from Bruker in tapping mode under air. The micro cantilevers (AC160TS) were purchased from Oxford Instruments. The images were recorded with 512 rows and 512 pixels. AFM images were first processed with NanoScope Analysis 1.80. The data was leveled with a first order plane fit and a first order flattening in histogram mode. The data was then further processed with Gwyddion 2.50^[47] where the minimum of the data values was shifted to zero.

Transmission electron microscopy: Transmission electron microscopy was made at a Zeiss CEM902 electron microscope (Zeiss, Oberkochen, Germany). The complex was dissolved/dispersed in toluene/*iso*-octane applying vortex. The solution was dropped on a copper grid (mesh 200, Science Services, Munich). Electron acceleration voltage was set to 80 kV. Micrographs were taken with a MegaView III / iTEM image acquiring and processing system from Olympus Soft Imaging Systems (OSIS, Münster, Germany) and an Orius 830 SC200W / DigitalMicrograph system from Gatan (Munich, Germany).

General: The syntheses of the iron complexes were carried out under an argon atmosphere (argon 5.0) using Schlenk tube techniques. Apart from this, the μ -O-complexes were dissolved in toluene under air. The solvents were purified as described in the literature^[48] and distilled under an atmosphere of argon or saturated with argon over one hour. When argon is used for the synthesis of the intermediate products, it is described in the text. The alkylbromide, bpea and bpee are commercial products (Sigma-Aldrich) and were used as received. The syntheses of 1,2-di(4-pyridyl)ethyne,^[31] methoxymethylenemethylacetoacetate,^[49] iron(II) acetate,^[30] and **[FeL(16)(MeOH)₂]**^[27] are described in literature.

1,2-Dioctadecyloxybenzene (A(18)): 1,2-dihydroxybenzene (5.03 g, 45.68 mmol) was mixed with K₂CO₃ (15.90 g, 115.05 mmol, 2.5 eq.) in DMF (500 mL) and stirred for 1 h at room

temperature. 1-bromooctadecane (33.50 g, 100.48 mmol, 2.2 eq.) was added and it was heated to 100 °C for 35 h. The mixture was filtrated, washed with H₂O (3x200 mL). It was recrystallized from an EtOH/H₂O (120 mL/60 mL) solution, filtrated, washed with EtOH (60 mL) and dried on air to obtain a white powder. Yield: 18.09 g (65%) C₄₂H₇₈O₂ (615.07): calcd. C 82.02, H 12.78; found C 81.74, H 12.71. MS (DEI-(+)): *m/z* (%) 614 (92) [M]⁺, 362 (20), 110 (100). ¹H-NMR (300 MHz, CDCl₃, 296 K): δ = 0.88 (t, *J* = 6.5 Hz, 6 H, CH₃), 1.18-1.40 (m, 56 H, CH₂), 1.41-1.52 (m, 4 H, CH₂), 1.74-1.87 (m, 4 H, CH₂), 3.99 (t, *J* = 6.6 Hz, 4 H, CH₂O), 6.88 (s, 4 H, H_{ar}) ppm. ¹³C-NMR (75 MHz, CDCl₃, 296 K): δ = 14.3 (CH₃), 22.8 (CH₂), 26.2 (CH₂), 29.5 (CH₂), 29.5 (CH₂), 29.6 (CH₂), 29.8 (CH₂), 29.8 (CH₂), 29.9 (CH₂), 32.1 (CH₂), 69.4 (CH₂O), 114.2 (C_{ar}), 121.1 (C_{ar}), 149.4 (C_{ar}-O) ppm.

1,2-Diicosyloxybenzene (A(20)): 1,2-dihydroxybenzene (2.37 g, 21.52 mmol) was mixed with K₂CO₃ (7.52 g, 54.41 mmol, 2.5 eq.) in DMF (250 mL) and stirred for 45 min at room temperature. 1-bromoeicosane (17.00 g, 47.03 mmol, 2.2 eq.) was added and it was heated to 95 °C for 44 h. The mixture was filtrated, washed with H₂O (2x50 mL) and EtOH (100 mL). It was recrystallized from an EtOH/H₂O (80 mL/40 mL) solution, filtrated, washed with EtOH (30 mL) and dried on air to obtain a white powder. Yield: 11.10 g (77 %). C₄₆H₈₆O₂ (671.17): calcd. C 82.32, H 12.92; found C 79.78, H 12.85. MS (DEI-(+)): *m/z* (%) 671 (100) [M]⁺, 324 (93), 110 (53). ¹H-NMR (300 MHz, CDCl₃, 296 K): δ = 0.88 (t, *J* = 6.0 Hz, 6 H, CH₃), 1.18-1.40 (m, 64 H, CH₂), 1.41-1.52 (m, 4 H, CH₂), 1.74-1.87 (m, 4 H, CH₂), 3.99 (t, *J* = 6.5 Hz, 4 H, CH₂O), 6.88 (s, 4 H, H_{ar}) ppm. ¹³C-NMR (75 MHz, CDCl₃, 296 K): δ = 14.3 (CH₃), 22.8 (CH₂), 26.2 (CH₂), 29.5 (CH₂), 29.6 (CH₂), 29.8 (CH₂), 29.8 (CH₂), 29.9 (CH₂), 32.1 (CH₂), 69.4 (CH₂O), 114.3 (C_{ar}), 121.1 (C_{ar}), 149.4 (C_{ar}-O) ppm.

1,2-Didocosyloxybenzene (A(22)): 1,2-dihydroxybenzene (10 g, 0.09 mol) was mixed with K₂CO₃ (31.21 g, 0.226 mol, 2.5 eq.) in DMF (650 mL) and stirred for 1 h at room temperature. 1-bromodocosane (70.75 g, 0.182 mol, 2 eq.) was added and it was heated to 80 °C for 17 h. The mixture was poured into 6 L H₂O and stirred for 4 days at room temperature. After filtrating and washing the white precipitate with H₂O (100 mL) and EtOH (200 mL), it was recrystallized 4 times in EtOH (500 mL) to obtain white fine crystalline powder. Yield: 38.6 g (58.9 %). C₅₀H₉₄O₂ (727.28): calcd. C 82.57, H 13.03; found C 82.68, H 13.58. MS (DEI+): *m/z* (%) = 727 (100) [M]⁺, 419 (14), 110 (47). ¹H-NMR (300 MHz, CDCl₃, 296 K): δ = 0.86 (t, *J* = 6.3 Hz, 6H, CH₃), 1.21–1.30 (m, 72 H, CH₂), 1.41–1.47 (m, 4H, CH₂), 1.74–1.83 (m, 4H, CH₂), 3.97 (t, 4H, *J* = 6.0 Hz CH₂O) 6.81–6.85 (m, 4 H, H_{ar}) ppm.

1,2-Dinitro-4,5-dioctadecyloxybenzene (B(18)): **A(18)** (17.65 g, 28.70 mmol) was suspended in acetic acid (215 mL) and stirred for 1 h. Nitric acid (68 %, 50 mL) was added dropwise. Then

fuming nitric acid (>90 %, 180 mL) was added dropwise over 1 h and it was heated shortly to 60 °C to obtain a yellow suspension. The mixture was stirred for 25 h at room temperature. It was poured over ice water (4 L) and stirred for some minutes. It was filtrated, washed neutral with H₂O (5 L) and recrystallized from EtOH (280 mL). It was filtrated again, washed with EtOH (60 mL) and dried on air to obtain a yellow powder. Yield: 17.36 g (86 %). C₄₂H₇₆N₂O₆ (705.06): calcd. C 71.55, H 10.86, N 3.97; found C 71.52, H 11.40, N 3.92. MS (DEI-(+)): *m/z* (%) 704 (55) [M]⁺, 57 (100) [C₄H₉]⁺. ¹H-NMR (300 MHz, CDCl₃, 296 K): δ = 0.88 (t, *J* = 6.9 Hz, 6 H, CH₃), 1.16-1.41 (m, 64 H, CH₂), 1.42-1.54 (m, 4 H, CH₂), 1.79-1.93 (m, 4 H, CH₂), 4.10 (t, *J* = 6.4 Hz, 4 H, CH₂O), 7.29 (s, 2 H, H_{ar}) ppm. ¹³C-NMR (75 MHz, CDCl₃, 296 K): δ = 14.3 (CH₃), 22.8 (CH₂), 26.0 (CH₂), 28.9 (CH₂), 29.4 (CH₂), 29.5 (CH₂), 29.7 (CH₂), 29.7 (CH₂), 29.8 (CH₂), 29.8 (CH₂), 29.9 (CH₂), 32.1 (CH₂), 70.4 (CH₂O), 108.1 (C_{ar}-H), 136.6 (C_{ar}-NO₂), 151.9 (C_{ar}-O) ppm.

1,2-Dinitro-4,5-diicosyloxybenzene (B(20)): A(20) (10.70 g, 15.94 mmol) was suspended in acetic acid (130 mL) and stirred for 1 h. Nitric acid (68 %, 30 mL) was added dropwise and it was heated shortly to 60 °C to obtain a yellow suspension. Then fuming nitric acid (>90 %, 110 mL) was added dropwise over 45 min and the mixture was stirred for 20 h at room temperature. It was poured over ice water (3 L) and stirred for some minutes. It was filtrated, washed neutral with H₂O (3 L) and recrystallized from EtOH (170 mL). It was filtrated again, washed with EtOH (40 mL) and dried on air to obtain a yellow powder. Yield: 9.95 g (82 %). C₄₆H₈₄N₂O₆ (761.17): calcd. C 72.58, H 11.12, N 3.68; found C 73.62, H 11.68, N 2.81. MS (DEI-(+)): *m/z* (%) 761 (19) [M]⁺, 325 (95), 57 (100). ¹H-NMR (300 MHz, CDCl₃, 296 K): δ = 0.88 (t, *J* = 6.4 Hz, 6 H, CH₃), 1.15-1.41 (m, 64 H, CH₂), 1.42-1.54 (m, 4 H, CH₂), 1.79-1.91 (m, 4 H, CH₂), 4.09 (t, *J* = 6.2 Hz, 4 H, CH₂O), 7.29 (s, 2 H, H_{ar}) ppm. ¹³C-NMR (75 MHz, CDCl₃, 296 K): δ = 14.3 (CH₃), 22.8 (CH₂), 26.0 (CH₂), 28.8 (CH₂), 29.4 (CH₂), 29.5 (CH₂), 29.6 (CH₂), 29.7 (CH₂), 29.7 (CH₂), 29.8 (CH₂), 29.9 (CH₂), 32.1 (CH₂), 70.3 (CH₂O), 108.0 (C_{ar}-H), 136.6 (C_{ar}-NO₂), 151.9 (C_{ar}-O) ppm.

1,2-Dinitro-4,5-didocosyloxybenzene (B(22)): A(22) (25.02 g, 0.03 mol) was suspended in acetic acid (300 mL) for 1 h. nitric acid (68%, 70 mL) was added dropwise and heated shortly to 60 °C to obtain a yellow suspension. Over 1.5 h, fuming nitric acid (>90 %, 250 mL) was added dropwise and the mixture was stirred for 2 d at room temperature. It was poured into ice water (2.5 L) and stirred for 15 min. It was filtered off, washed neutral and dried on air. Recrystallization from EtOH (700 mL) gave a yellow powder. Yield: 24.1 g (85.0 %). C₅₀H₉₂N₂O₆ (817.28): calcd. C 73.48, H 11.35, N 3.43; found C 72.85, H 11.80, N 3.95. MS (DEI+): *m/z* (%) = 817 (100) [M]⁺, 476 (10). ¹H NMR (300 MHz, CDCl₃, 296 K.): δ = 0.81 (t, *J* = 7.0 Hz, 6 H, CH₃), 1.05–1.51 (m, 80 H, CH₂), 1.80 (quint, *J* = 7.0 Hz, 4 H, CH₂), 4.02 (t, *J* = 7.0 Hz, 4 H, CH₂O), 7.3 (s, 2 H, H_{ar}).

1,2-Diamino-4,5-dioctadecyloxybenzene (C(18)): B(18) (17.10 g, 24.25 mmol) and Pd/C (1.21 g, 10 %) were suspended in degassed EtOH (600 mL) under argon. Hydrazine monohydrate (65 mL, 1.24 mol, 50 eq.) was added dropwise and it was heated to reflux for 22 h. The Pd/C was removed by hot filtration over Celite[®] 545. After 1 d at -30 °C, the yellow-white precipitate was filtrated, washed with EtOH (3x15 mL) and dried under vacuum to obtain a white powder. Yield: 13.03 g (83 %). C₄₂H₈₀N₂O₂ (645.10): calcd. C 78.20, H 12.50, N 4.34; found C 78.18, H 13.44, N 4.37. MS (DEI-+): *m/z* (%) 644 (100) [M]⁺, 629 (9) [M - NH₂]⁺, 392 (16) [M - C₁₈H₃₇]⁺.

1,2-Diamino-4,5-diicosyloxybenzene (C(20)): B(20) (9.50 g, 12.48 mmol) and Pd/C (0.60 g, 10 %) were suspended in degassed EtOH (300 mL) under argon. Hydrazine monohydrate (30 mL, 625 mmol, 50 eq.) was added dropwise and it was heated to reflux for 23 h. The Pd/C was removed by hot filtration over Celite[®] 545. After 1 d at -30 °C, the yellow-white precipitate was filtrated, washed with EtOH (2x10 mL) and dried under vacuum to obtain a pale yellow powder. Yield: 6.40 g (73 %). C₄₆H₈₈N₂O₂ (701.20): calcd. C 78.79, H 12.65, N 4.00; found C 78.00, H 12.77, N 3.49. MS (DEI-+): *m/z* (%) 700 (100) [M]⁺, 685 (25) [M - NH₂]⁺, 420 (8) [M - C₂₀H₄₁]⁺.

1,2-Diamino-4,5-didocosyloxybenzene (C(22)): B(22) (12.25 g, 14.99 mmol) and Pd/C (0.75 g, 10 %) were suspended in degassed EtOH (350 mL) under argon. Hydrazine monohydrate (35 mL, 722 mmol, 48 eq.) was added dropwise and it was heated to reflux for 18 h. The Pd/C was removed by hot filtration over Celite[®] 545. After 2 d at -30 °C, the white precipitate was filtrated, washed with EtOH (2x10 mL) and dried under vacuum to obtain a white powder. Yield: 7.59 g (67 %). C₅₀H₉₆N₂O₂ (757.31): calcd. C 79.30, H 12.78, N 3.70; found C 78.94, H 12.52, N 3.77.

H₂L(18): C(18) (4.00 g, 6.20 mmol) and methoxymethylenemethylacetoacetate (3.00 g, 18.97 mmol) were suspended in MeOH (500 mL) under argon and it was heated to reflux for 16 h. After 1 d at 4 °C, the product was filtrated, washed with MeOH (2x50 mL) and dried on air to obtain a yellow powder. Yield: 5.35 g (96 %). C₅₄H₉₂N₂O₈ (897.32): calcd. C 72.28, H 10.33, N 3.12; found C 72.08, H 10.60, N 3.17. MS (DEI-+): *m/z* (%) 896 (5) [M]⁺, 755 (100) [M - C₆H₈NO₃]⁺. IR: $\tilde{\nu}$ = 1706 (s) (C=O), 1629 (s) (N-H), 1603 (s) (C=O) cm⁻¹. ¹H-NMR (300 MHz, CDCl₃, 296 K): δ = 0.88 (t, *J* = 6.5 Hz, 6 H, CH₃), 1.14-1.41 (m, 64 H, CH₂), 1.42-1.55 (m, 4 H, CH₂), 1.75-1.90 (m, 4 H, CH₂), 2.55 (s, 6 H, CH₃), 3.78 (s, 6 H, CH₃), 4.01 (t, *J* = 6.3 Hz, 4 H, CH₂O), 6.74 (s, 2 H, H_{ar}), 8.26 (d, *J* = 12.3 Hz, 2 H, CH), 12.89 (d, *J* = 12.4, 2 H, NH) ppm. ¹³C-NMR (75 MHz, CDCl₃, 296 K): δ = 14.3 (CH₃), 22.8 (CH₂), 26.2 (CH₂), 29.4 (CH₂), 29.5 (CH₂), 29.6 (CH₂), 29.8 (CH₂), 29.8 (CH₂), 29.9 (CH₂), 31.2 (CH₃), 32.1 (CH₂), 51.4 (CH₃), 70.3 (CH₂O), 103.6 (C_q), 106.7 (C_{ar}-H), 125.0 (C_{ar}-N), 148.7 (C_{ar}-O), 154.3 (CH), 167.4 (O-C=O), 200.3 (C=O) ppm.

H₂L(20): C(20) (2.51 g, 3.58 mmol) and methoxymethylenemethylacetoacetate (1.70 g, 10.75 mmol) were suspended in MeOH (300 mL) under argon and it was heated to reflux for 19 h. The product was filtrated, washed with MeOH (2x15 mL) and recrystallized from MeOH (120 mL). It was filtrated again and dried on air to obtain a yellow powder. Yield: 2.48 g (73 %). C₅₈H₁₀₀N₂O₈ (953.42): calcd. C 73.07, H 10.57, N 2.94; found C 73.10, H 10.63, N 2.90. MS (DEI- (+)): *m/z* (%) 952 (5) [M]⁺, 811 (100) [M - C₆H₈NO₃]⁺. IR: $\tilde{\nu}$ = 1712 (s) (C=O), 1619 (s) (N-H), 1600 (s) (C=O) cm⁻¹. ¹H-NMR (300 MHz, CDCl₃, 296 K): δ = 0.88 (t, *J* = 6.3 Hz, 6 H, CH₃), 1.13-1.41 (m, 64 H, CH₂), 1.42-1.55 (m, 4 H, CH₂), 1.75-1.89 (m, 4 H, CH₂), 2.55 (s, 6 H, CH₃), 3.78 (s, 6 H, CH₃), 4.01 (t, *J* = 6.2 Hz, 4 H, CH₂O), 6.74 (s, 2 H, H_{ar}), 8.26 (d, *J* = 12.4 Hz, 2 H, CH), 12.88 (d, *J* = 12.5, 2 H, NH) ppm. ¹³C-NMR (75 MHz, CDCl₃, 296 K): δ = 14.3 (CH₃), 22.8 (CH₂), 26.2 (CH₂), 29.4 (CH₂), 29.5 (CH₂), 29.6 (CH₂), 29.8 (CH₂), 29.8 (CH₂), 29.9 (CH₂), 31.2 (CH₃) 32.1 (CH₂), 51.4 (CH₃), 70.3 (CH₂O), 103.6 (C_q), 106.7 (C_{ar}-H), 125.0 (C_{ar}-N), 148.7 (C_{ar}-O), 154.3 (CH), 167.4 (O-C=O), 200.3 (C=O) ppm.

H₂L(22): C(22) (2.40 g, 3.17 mmol) and methoxymethylenemethylacetoacetate (1.59 g, 10.05 mmol) were suspended in MeOH (250 mL) under argon and it was heated to reflux for 18 h. The product was filtrated, washed with MeOH (2x15 mL) and recrystallized from MeOH (120 mL). It was filtrated again, washed with MeOH (2x15 mL) and dried on air to obtain a yellow powder. Yield: 2.88 g (90 %). C₆₂H₁₀₈N₂O₈ (1009.53): calcd. C 73.76, H 10.78, N 2.77; found C 73.48, H 10.42, N 2.87. IR: $\tilde{\nu}$ = 1706 (s) (C=O), 1620 (s) (N-H), 1603 (s) (C=O) cm⁻¹. ¹H-NMR (300 MHz, CDCl₃, 296 K): δ = 0.88 (t, *J* = 6.0 Hz, 6 H, CH₃), 1.11-1.41 (m, 72 H, CH₂), 1.42-1.54 (m, 4 H, CH₂), 1.74-1.91 (m, 4 H, CH₂), 2.55 (s, 6 H, CH₃), 3.78 (s, 6 H, CH₃), 4.01 (t, *J* = 5.7 Hz, 4 H, CH₂O), 6.74 (s, 2 H, H_{ar}), 8.26 (d, *J* = 12.2 Hz, 2 H, CH), 12.89 (d, *J* = 12.4, 2 H, NH) ppm. ¹³C-NMR (75 MHz, CDCl₃, 296 K): δ = 14.3 (CH₃), 22.8 (CH₂), 26.2 (CH₂), 29.4 (CH₂), 29.5 (CH₂), 29.6 (CH₂), 29.8 (CH₂), 29.9 (CH₂), 31.2 (CH₃) 32.1 (CH₂), 51.4 (CH₃), 70.2 (CH₂O), 103.6 (C_q), 106.6 (C_{ar}-H), 125.0 (C_{ar}-N), 148.7 (C_{ar}-O), 154.3 (CH), 167.4 (O-C=O), 200.3 (C=O) ppm.

[FeL(18)(MeOH)₂]: H₂L(18) (3.01 g, 3.35 mmol) and iron(II) acetate (1.44 g, 8.28 mmol, 2.5 eq.) were suspended in MeOH (190 mL) and heated to reflux for 6 h. It was filtrated and washed with MeOH (2x15 mL) and dried under vacuum to obtain a brown powder. Yield: 3.24 g (96 %): C₅₆H₉₈FeN₂O₁₀ (1015.23): calcd. C 66.25, H 9.73, N 2.76; found C 66.44, H 9.80, N 2.92. MS (DEI- (+)): *m/z* (%) 950 (100) [M - 2xMeOH]⁺, 892 (63) [M - 2xMeOH - C₂H₃O₂]⁺. IR: $\tilde{\nu}$ = 3342 (b) (O-H), 1696 (s) (C=O), 1574 (s) (C=O) cm⁻¹.

[FeL(20)(MeOH)₂]: H₂L(20) (1.00 g, 1.05 mmol) and iron(II) acetate (0.44 g, 2.52 mmol, 2.4 eq.) were suspended in MeOH (55 mL) and heated to reflux for 3 h. It was filtrated and washed with MeOH (2x5 mL) and dried under vacuum to obtain a brown powder. Yield: 0.95 g (84 %):

$C_{60}H_{106}FeN_2O_{10}$ (1071.34): calcd. C 67.27, H 9.97, N 2.61; found C 67.70, H 9.43, N 2.63. MS (DEI-+): m/z (%) 1006 (100) $[M - 2xMeOH]^+$, 948 (63) $[M - 2xMeOH - C_2H_3O_2]^+$. IR: $\tilde{\nu} = 3365$ (b) (O-H), 1698 (s) (C=O), 1576 (s) (C=O) cm^{-1} .

[FeL(20)(MeOH)₂]: 3 (61 mg, 0.05 mmol) was dissolved in toluene (21 mL) and heated to reflux for some minutes. A reservoir with MeOH (20 mL) was put on top and after some days very few crystals suitable for single crystal X-ray diffraction were obtained.

[FeL(22)(MeOH)₂]: H₂L(22) (2.59 g, 2.57 mmol) and iron(II) acetate (1.08 g, 6.17 mmol, 2.4 eq.) were suspended in MeOH (130 mL) and heated to reflux for 6 h. It was filtrated and washed with MeOH (2x7 mL) and dried under vacuum to obtain a brown powder. Yield: 2.43 g (84 %): $C_{64}H_{114}FeN_2O_{10}$ (1127.44): calcd. C 68.18, H 10.19, N 2.48; found C 70.85, H 10.57, N 2.75. MS (DEI-+): m/z (%) 1062 (20) $[M - 2xMeOH]^+$, 1004 (28) $[M - 2xMeOH - C_2H_3O_2]^+$, 43 (100) $[C_3H_7]^+$. IR: $\tilde{\nu} = 3360$ (b) (O-H), 1696 (s) (C=O), 1571 (s) (C=O) cm^{-1} .

[FeL(16)bpey]_n (1): [FeL(16)(MeOH)₂ (515 mg, 0.54 mmol) and bpey (390 mg, 2.16 mmol, 4.0 eq.) were dissolved in toluene (7 mL) and heated to reflux for 2 h. After 2 days at room temperature it was filtrated and washed with toluene (2x1.5 mL) and dried under vacuum to obtain a black, crystalline powder. Yield: 267 mg (46 %): $C_{62}H_{90}FeN_4O_8$ (1075.25): calcd. C 69.26, H 8.44, N 5.21; found C 68.69, H 7.82, N 5.32. MS (DEI-+): m/z (%) 894 (18) $[M - bpey]^+$, 836 (8) $[M - bpey - C_2H_3O_2]^+$, 44 (100) $[C_3H_7]^+$. IR: $\tilde{\nu} = 1685$ (s) (C=O), 1595 (s) (C=O) cm^{-1} .

[FeL(18)bpey]_n (2): [FeL(18)(MeOH)₂ (636 mg, 0.63 mmol) and bpey (471 mg, 6.17 mmol, 4.2 eq.) were dissolved in toluene (8 mL) and heated to reflux for 5 h. After 2 days at room temperature it was filtrated and washed with toluene (2x1.5 mL) and dried under vacuum to obtain a black, crystalline powder. Yield: 575 mg (81 %): $C_{66}H_{98}FeN_4O_8 \times 0.25$ toluene (1154.39): calcd. C 70.49, H 8.73, N 4.85; found C 70.57, H 9.06, N 4.93. MS (DEI-+): m/z (%) 950 (62) $[M - bpey]^+$, 892 (17) $[M - bpey - C_2H_3O_2]^+$, 57 (100) $[C_4H_9]^+$. IR: $\tilde{\nu} = 1685$ (s) (C=O), 1600 (s) (C=O) cm^{-1} .

[FeL(20)bpey]_n (3): [FeL(20)(MeOH)₂ (342 mg, 0.32 mmol) and bpey (345 mg, 1.92 mmol, 6.0 eq.) were dissolved in toluene (5 mL) and heated to reflux for 2 h. After 2 days at room temperature it was filtrated and washed with toluene (2x1.0 mL) and dried under vacuum to obtain a black, crystalline powder. Yield: 267 mg (70 %): $C_{70}H_{106}FeN_4O_8 \times 0.50$ toluene (1233.53): calcd. C 71.57, H 8.99, N 4.54; found C 71.79, H 9.09, N 4.59. MS (DEI-+): m/z (%) 1006 (18) $[M - bpey]^+$, 948 (16) $[M - bpey - C_2H_3O_2]^+$, 43 (100) $[C_3H_7]^+$. IR: $\tilde{\nu} = 1688$ (s) (C=O), 1600 (s) (C=O) cm^{-1} .

[FeL(22)bpey]_n (4): [FeL(22)(MeOH)₂ (469 mg, 0.42 mmol) and bpey (456 mg, 2.50 mmol, 6.0 eq.) were dissolved in toluene (6 mL) and heated to reflux for 2 h. After 2 days at room

temperature it was filtrated and washed with toluene (3x1.0 mL) and dried under vacuum to obtain a black, crystalline powder. Yield: 338 mg (67 %): $C_{74}H_{116}FeN_4O_8 \times 1.00$ toluene (1335.70): calcd. C 72.84, H 9.21, N 4.19; found C 72.80, H 9.28, N 4.22. MS (DEI-+): m/z (%) 1062 (6) $[M - bpey]^+$, 1004 (19) $[M - bpey - C_2H_3O_2]^+$, 43 (100) $[C_3H_7]^+$. IR: $\tilde{\nu} = 1682$ (s) (C=O), 1598 (s) (C=O) cm^{-1} .

[FeL(22)bpey]_n-toluene (4·tol): **[FeL(22)(MeOH)₂]** (35 mg, 0.03 mmol) and bpey (34 mg, 0.19 mmol, 6.0 eq.) were dissolved in toluene (15 mL) and heated to reflux for 2 min. A reservoir with acetonitrile (17 mL) was put on top and after some days very few crystals suitable for single crystal X-ray diffraction were obtained.

[FeL(22)bpee]_n (5): **[FeL(22)(MeOH)₂]** (457 mg, 0.41 mmol) and bpee (148 mg, 0.81 mmol, 2.0 eq.) were dissolved in toluene (5 mL) and heated to reflux for 2 h. After 6 days at room temperature it was filtrated and washed with toluene (2x1.0 mL) and dried under vacuum to obtain a black, crystalline powder. Yield: 338 mg (67 %): $C_{74}H_{116}FeN_4O_8 \times 1.00$ toluene (1337.72): calcd. C 72.73, H 9.34, N 4.19; found C 72.87, H 10.04, N 4.00. MS (DEI-+): m/z (%) 1062 (4) $[M - bpee]^+$, 1004 (11) $[M - bpee - C_2H_3O_2]^+$, 43 (100) $[C_3H_7]^+$. IR: $\tilde{\nu} = 1685$ (s) (C=O), 1603 (s) (C=O) cm^{-1} .

[FeL(22)bpea]_n (6): **[FeL(22)(MeOH)₂]** (522 mg, 0.49 mmol) and bpea (182 mg, 0.99 mmol, 2.0 eq.) were dissolved in toluene (5 mL) and heated to reflux for 2 h. After 3 days at room temperature it was filtrated and washed with toluene (2x1.0 mL) and dried under vacuum to obtain a reddish-brown, crystalline powder. Yield: 422 mg (69 %): $C_{74}H_{118}FeN_4O_8 \times 1.00$ toluene (1339.73): calcd. C 72.62, H 9.48, N 4.18; found C 72.84, H 10.08, N 4.13. MS (DEI-+): m/z (%) 1062 (30) $[M - bpea]^+$, 1004 (37) $[M - bpea - C_2H_3O_2]^+$, 57 (100) $[C_4H_9]^+$. IR: $\tilde{\nu} = 1687$ (s) (C=O), 1604 (s) (C=O) cm^{-1} .

[FeL(22)bpea]_n (6·tol): **[FeL(22)(MeOH)₂]** (0.18 g, 0.16 mmol) and bpea (0.35 g, 1.92 mmol, 12.0 eq.) were dissolved in toluene (8.5 mL) and heated to reflux for 1.5 h. After cooling to room temperature, black needle-like crystals were filtrated and dried under vacuum. The crystals obtained were suitable for single crystal X-ray diffraction. Yield: 120 mg (60 %): $C_{74}H_{118}FeN_4O_8 \times 0.3$ toluene (1278.31): calcd. C 71.24, H 9.53, N 4.48; found C 71.72, H 9.51, N 4.38.

[μ -O-((FeL(16))₂)] (7): **[FeL(16)(MeOH)₂]** was dissolved in toluene under air and refluxed for 2 h. After some days the solvent evaporated and a dark brown powder was obtained. Yield: 185 mg (100 %): $C_{100}H_{164}Fe_2N_4O_{17}$ (1806.08): calcd. C 66.50, H 9.15, N 3.10; found C 66.46, H 9.34, N 3.07.

[μ -O-((FeL(18))₂)] (8): [FeL(18)(MeOH)₂] was dissolved in toluene under air and refluxed for 3 h. After some days the solvent evaporated and a dark brown powder was obtained. Yield: 121 mg (89 %): C₁₀₈H₁₈₀Fe₂N₄O₁₇ (1918.29): calcd. C 67.62, H 9.46, N 2.92; found C 67.20, H 9.94, N 3.00.

[μ -O-((FeL(20))₂)] (9): [FeL(20)(MeOH)₂] was dissolved in toluene under air and refluxed for 2 h. After some days the solvent evaporated and a dark brown powder was obtained. Yield: 216 mg (97 %): C₁₁₆H₁₉₆Fe₂N₄O₁₇ (2030.50): calcd. C 68.62, H 9.73, N 2.76; found C 68.05, H 9.67, N 2.78.

[μ -O-((FeL(22))₂)] (10): [FeL(22)(MeOH)₂] was dissolved in toluene under air and refluxed for 2 h. After some days the solvent evaporated and a dark brown powder was obtained. Yield: 156 mg (81 %): C₁₂₄H₂₁₂Fe₂N₄O₁₇ (2142.72): calcd. C 69.51, H 9.97, N 2.61; found C 69.07, H 9.82, N 2.69.

Table S1: Crystallographic data of [FeL(20)(MeOH)₂], 4•tol and 6•tol.

Compound	[FeL(20)(MeOH) ₂]	4•tol	6•tol
CCDC	1835195	1835196	1044903
empirical formula	C ₆₀ H ₁₀₆ FeN ₂ O ₁₀	C ₇₄ H ₁₁₄ FeN ₄ O ₈ ·C ₇ H ₈	C ₇₄ H ₁₁₈ FeN ₄ O ₈
formula weight / g mol ⁻¹	1071.36	1335.73	1247.57
crystal system	triclinic	triclinic	triclinic
space group	<i>P</i> $\bar{1}$	<i>P</i> $\bar{1}$	<i>P</i> $\bar{1}$
<i>a</i> / Å	8.1994(6)	8.9330(6)	8.8292(5)
<i>b</i> / Å	10.9932(8)	13.125(1)	13.3483(8)
<i>c</i> / Å	35.441(2)	35.302(3)	38.144(2)
α / °	87.909(5)	95.974(6)	100.300(3)
β / °	84.165(5)	95.177(6)	90.396(3)
γ / °	68.887(5)	73.555(6)	104.379(3)
<i>V</i> / Å ³	2964.7(4)	3951.0(5)	4278.2(4)
<i>Z</i>	2	2	2
$\rho_{\text{calc.}}$ / g cm ⁻³	1.200	1.123	0.969
μ / mm ⁻¹	0.311	0.245	0.222
crystal size / mm	0.459×0.189×0.169	0.204×0.119×0.115	0.303×0.139×0.024
<i>T</i> / K	133 K	133 K	200 K
λ / Å	Mo- <i>K</i> α 0.71073	Mo- <i>K</i> α 0.71069	Mo- <i>K</i> α 0.71073
θ -range / °	1.2-28.5	1.2-28.6	2.2-23.4
measured reflections	25667	36530	56143
independent reflections	12111	17564	11638
parameters	660	847	790
<i>R</i>	0.0919	0.1706	0.0757
<i>wR</i> ²	0.2604	0.4733	0.1952
<i>S</i>	0.88	1.28	1.00

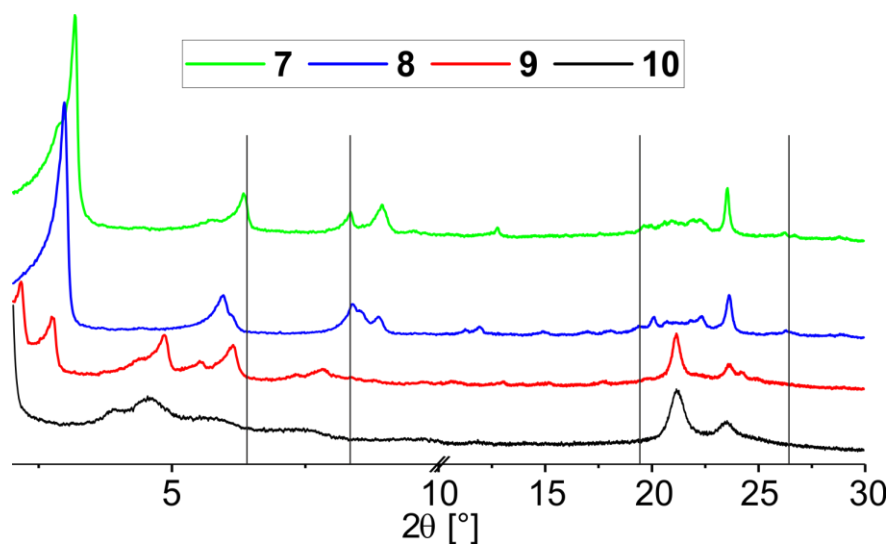


Figure S1: Powder X-ray diffraction patterns of 7 – 10 in the range of 2° – 30° 2θ at room temperature.

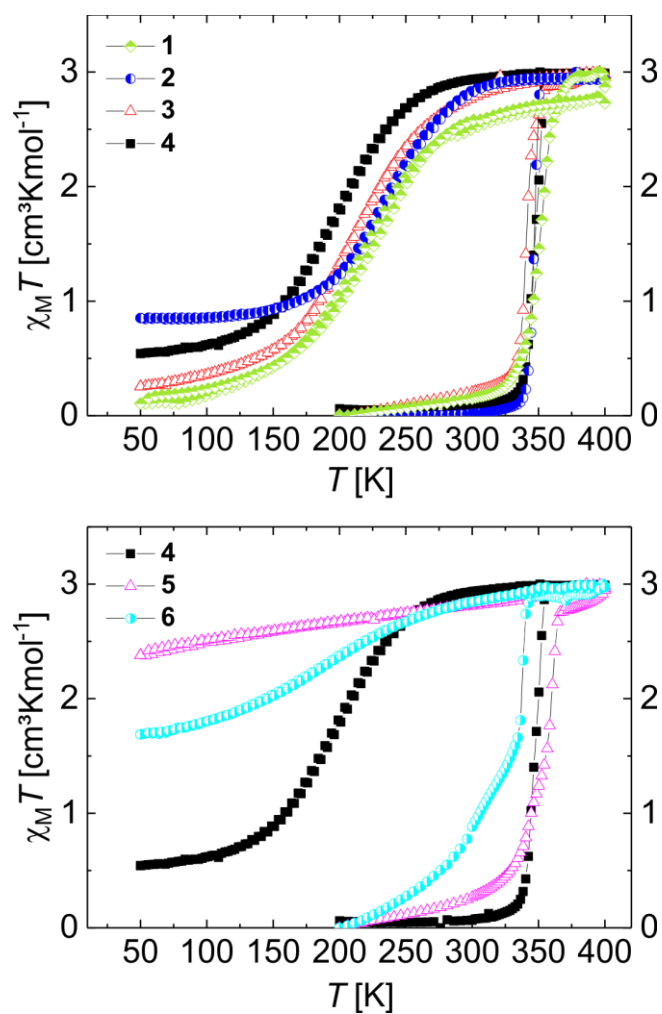


Figure S2: Magnetic measurements of 1 – 4 (top) and 4 – 6 (bottom) with $\chi_M T$ plotted against T .

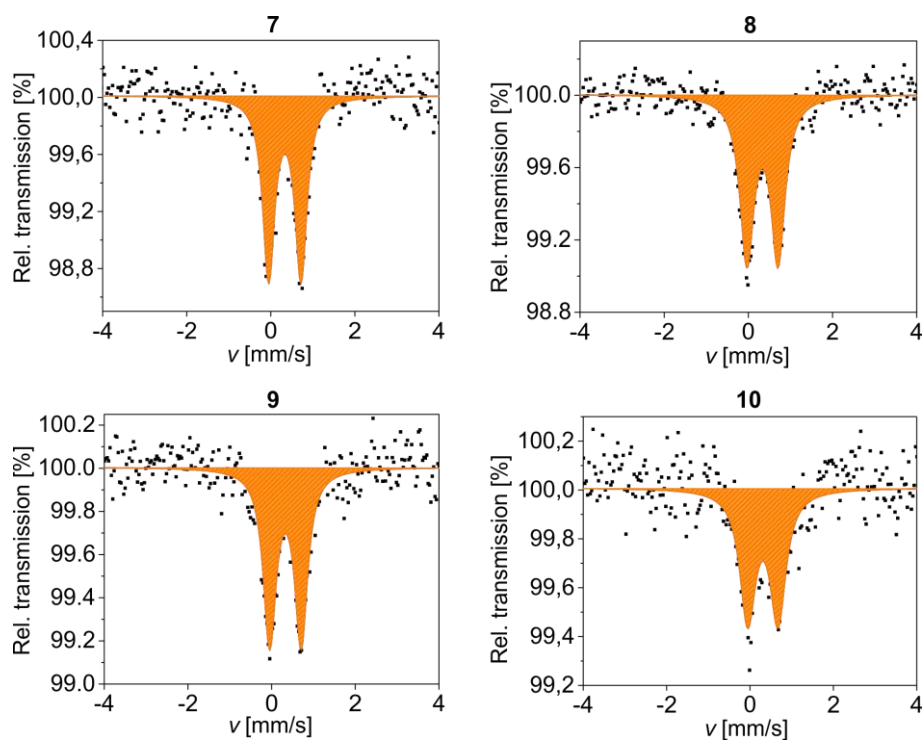


Figure S3: Mössbauer spectra of 7 – 10 measured at room temperature.

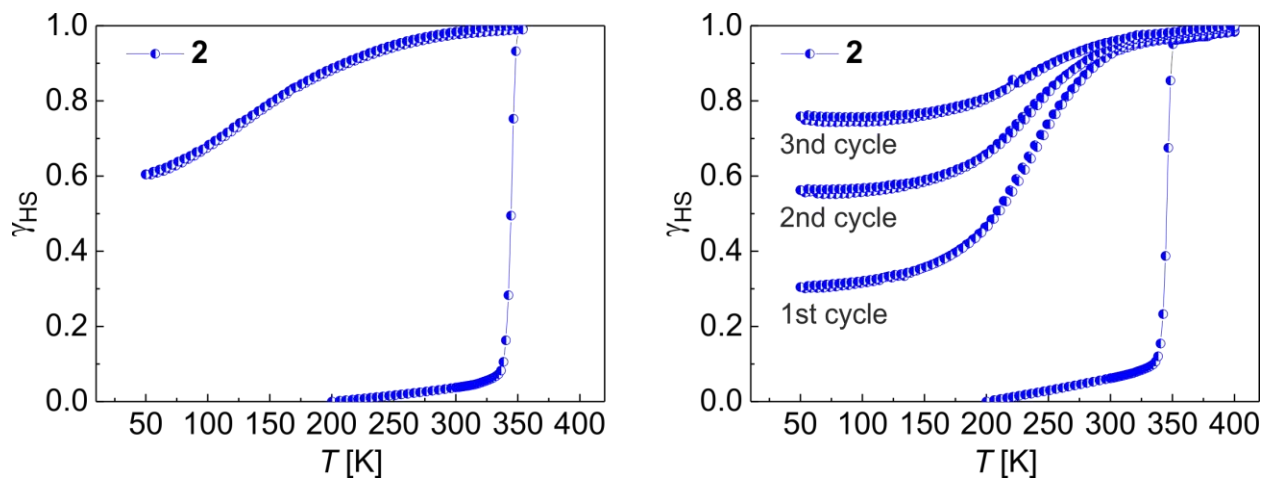


Figure S4: Magnetic measurement of 2 with γ_{HS} plotted against T . Measured only up to 354 K (left) and measured with 3 repeating temperature cycles (right).

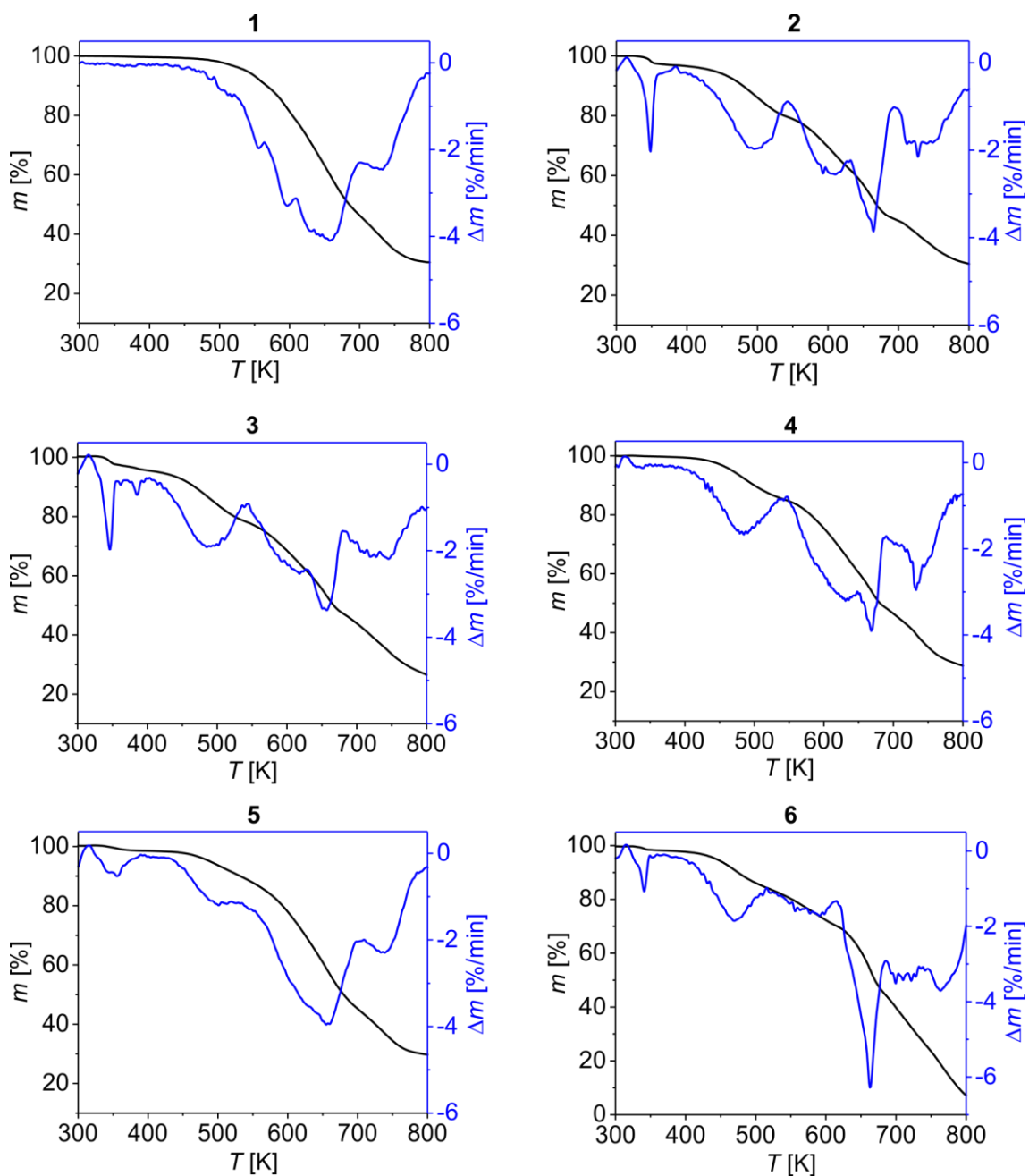
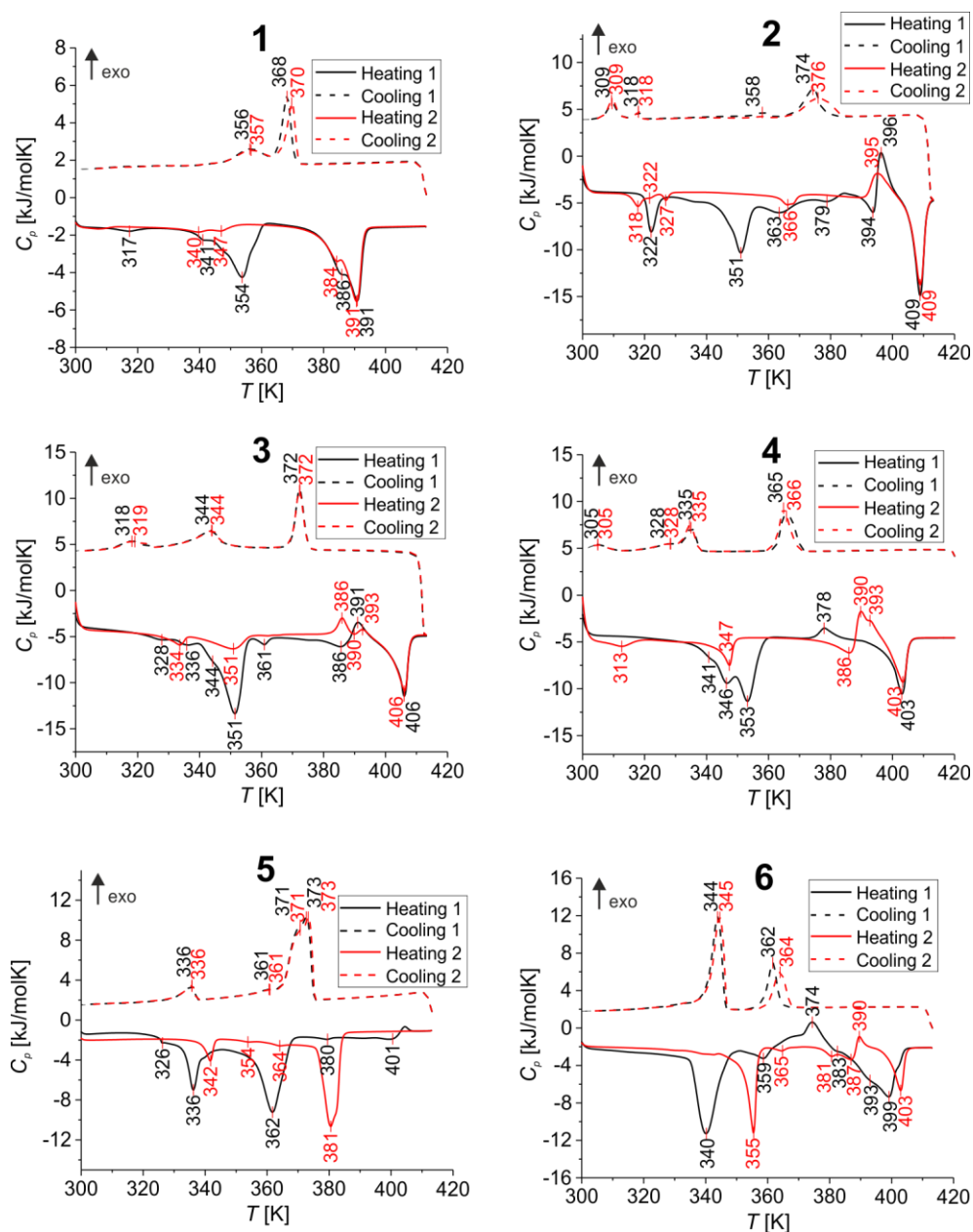


Figure S5: Results from TGA measurements of the complexes **1** – **6**.

Table S2: Correlation between the weight loss due to solvent loss in TGA and elemental analysis.

Compound	Weight loss (TGA) [wt%]	Additional toluene (Elemental Analysis)	Weight portion toluene (Elemental Analysis) [wt%]	Temperature of weight loss (TGA) [K]	$T_{1/2}$ (Magnetic measurement) [K]
1	-	-	-	-	354
2	2.56	0.25	2.00	349	347
3	2.40	0.50	3.73	346	340
4	-	1.00	6.90	-	344/351
5	1.29	1.00	6.89	349	340/369
6	1.27	1.00	6.88	341	338

**Figure S6:** DSC measurements of 1 – 6 in the heating and cooling mode (first cycle: black, second cycle: red).

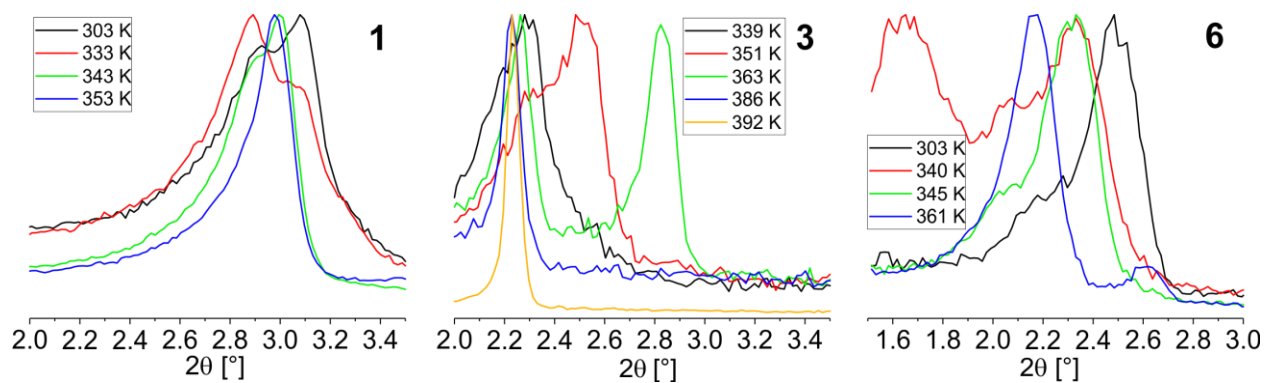


Figure S7: Temperature dependent powder X-ray diffraction patterns of **1** and **3** displayed in the $2.0^\circ - 3.5^\circ$ 2θ range and **6** displayed in the $1.5^\circ - 3.0^\circ$ 2θ range. The temperatures were selected based on the DSC measurements and the phase transitions observed therein.

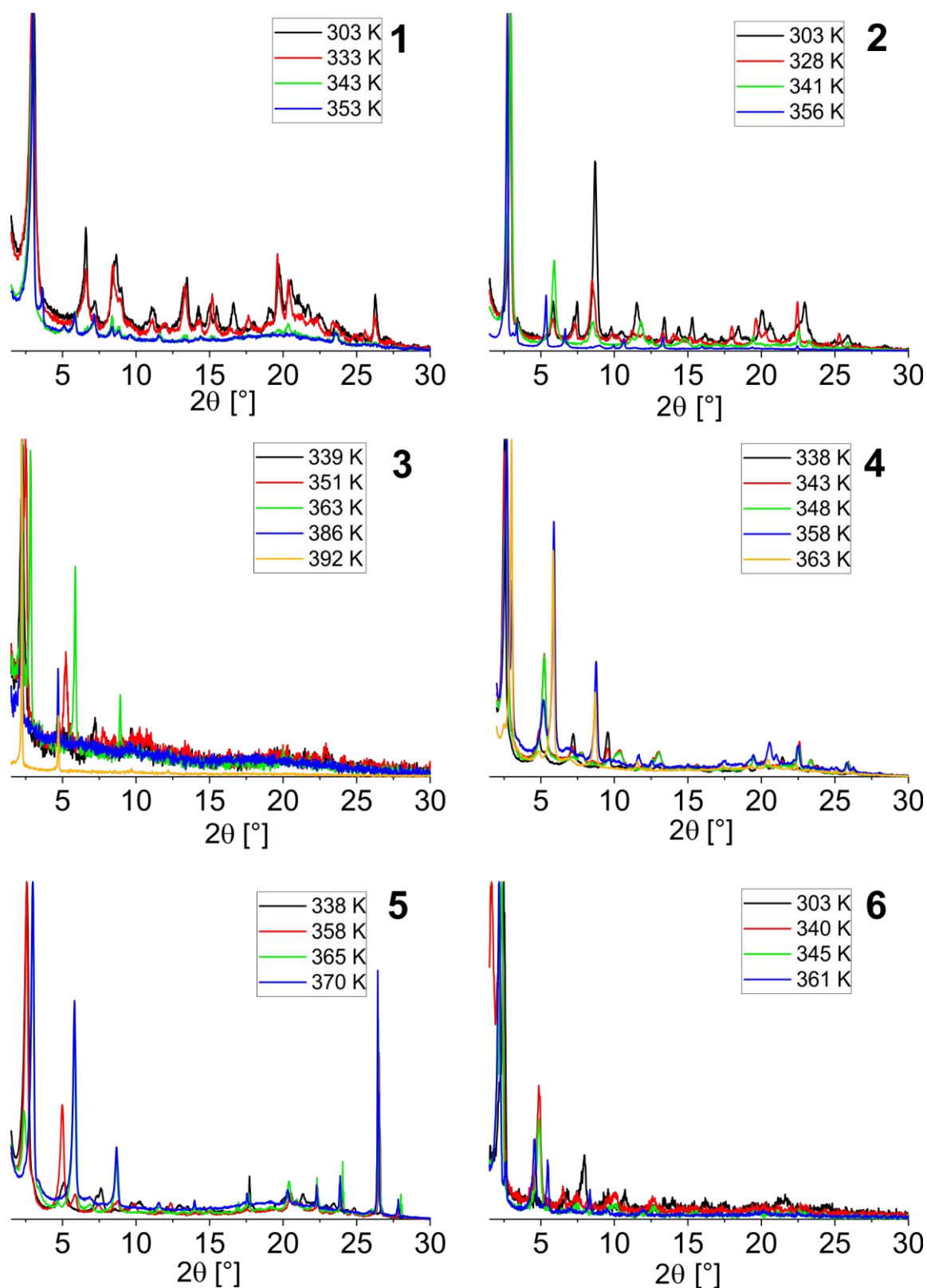


Figure S8: Temperature dependent PXRD patterns of **1 – 6** displayed in the 1.5° – 30° 2θ range.

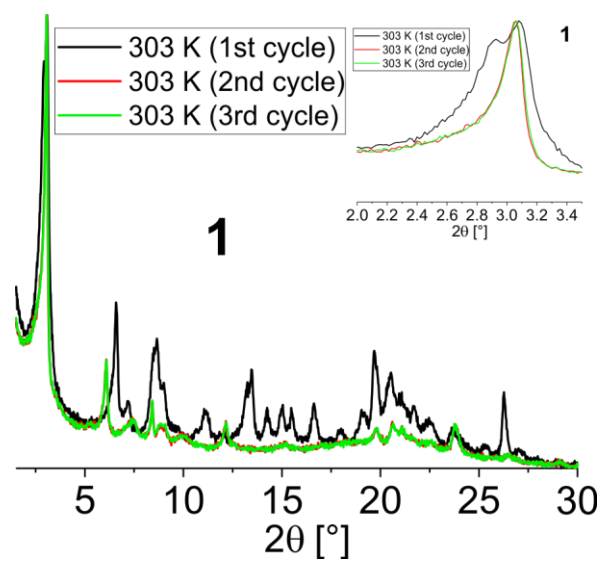


Figure S9: Temperature dependent XRPD patterns of **1** displayed in the $1.5^\circ - 30^\circ$ 2θ range at 303 K before annealing (1st cycle), after annealing at 413 K (2nd cycle) and after second annealing at 373 K (3rd cycle). Inset: zoomed $2.0^\circ - 3.5^\circ$ 2θ range.

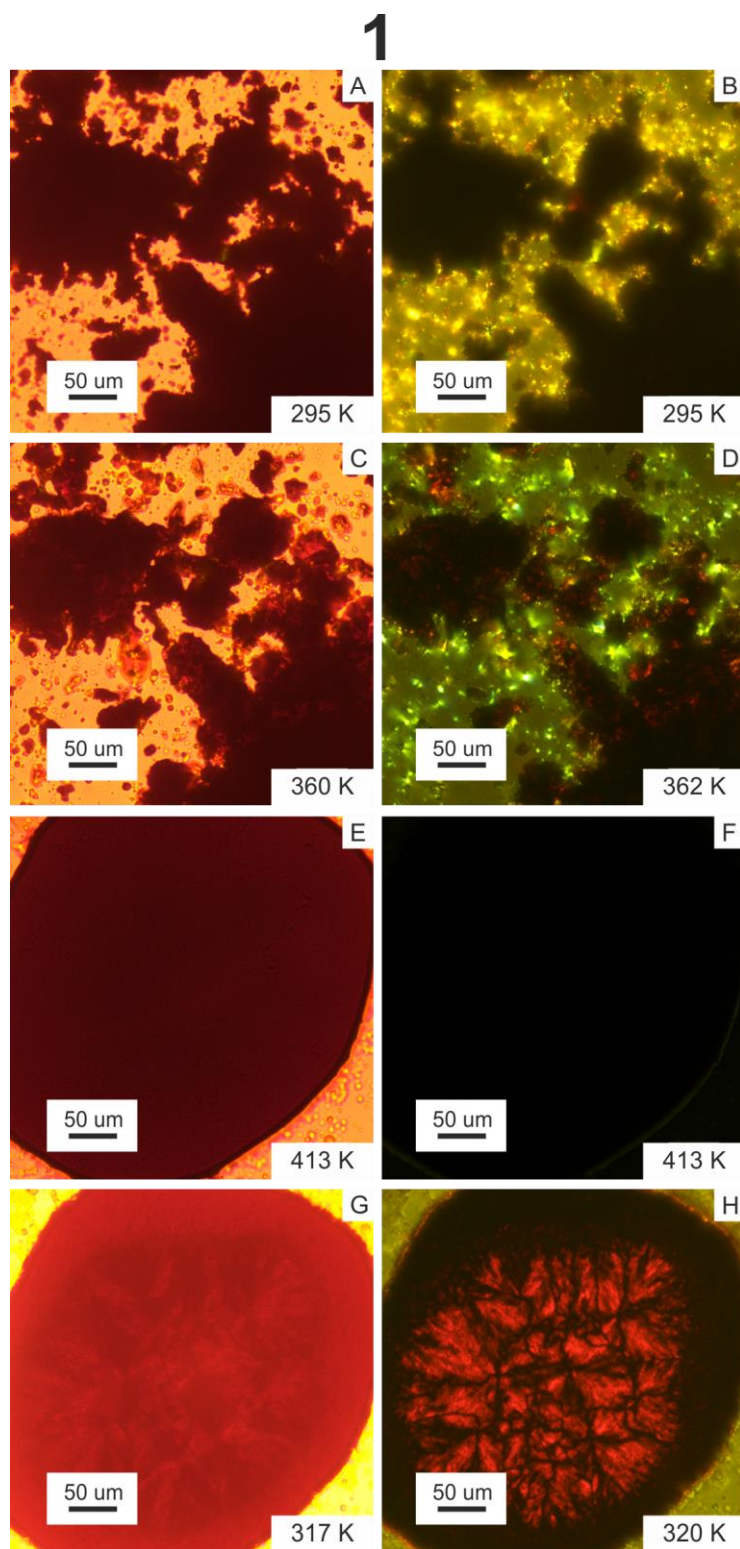


Figure S10: POM micrographs of **1**. All images were taken under crossed polarised light. Left: with retardation plate, right: without retardation plate. A) and B): crystalline powder from synthesis; C) and D): after phase transition; E) and F): melted sample; G) and H): formation of birefringent domains after cooling down.

2

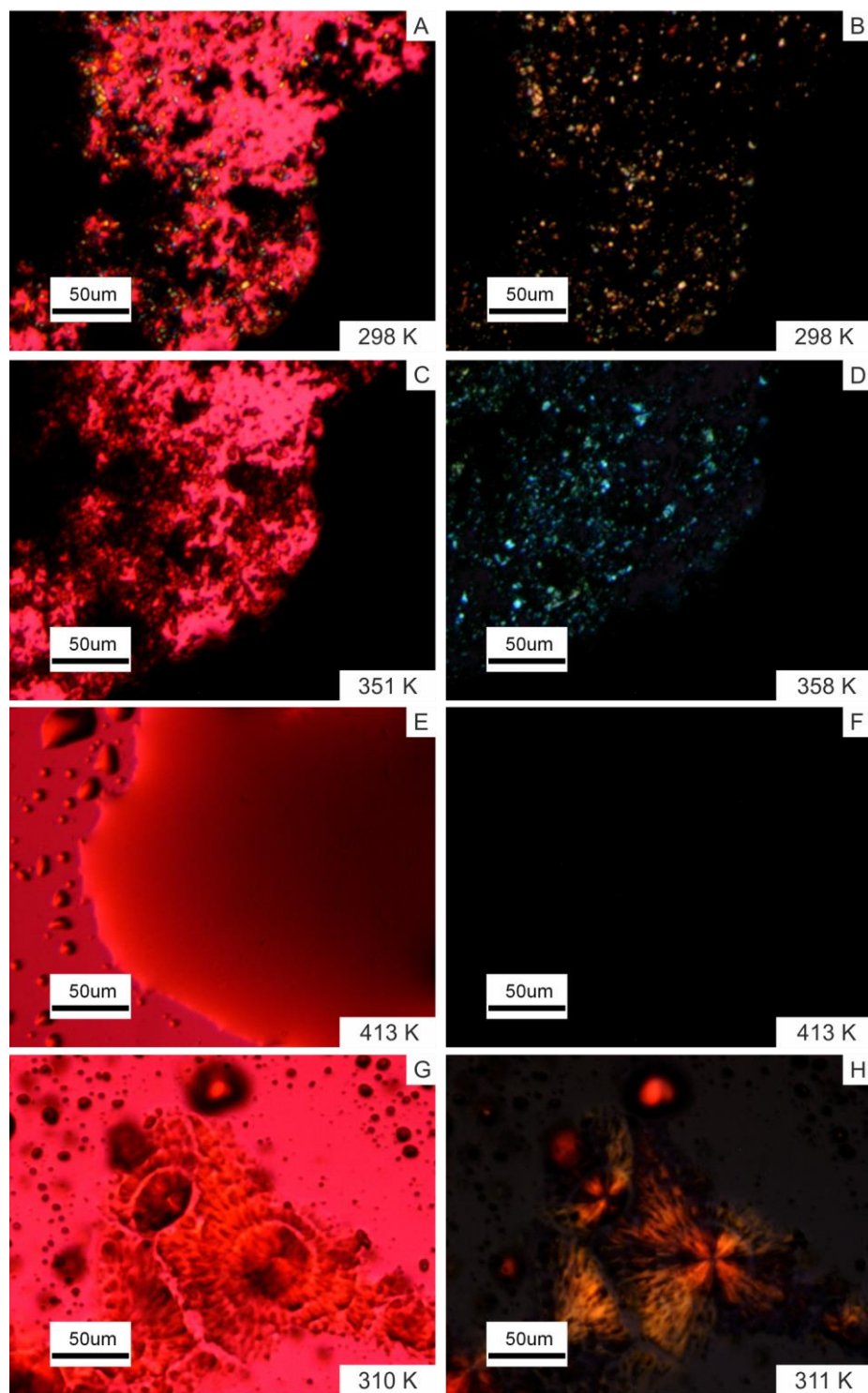


Figure S11: POM micrographs of **2**. All images were taken under crossed polarised light. Left: with retardation plate, right: without retardation plate. A) and B): crystalline powder from synthesis; C) and D): after phase transition; E) and F): melted sample; G) and H): formation of birefringent domains after cooling down.

3

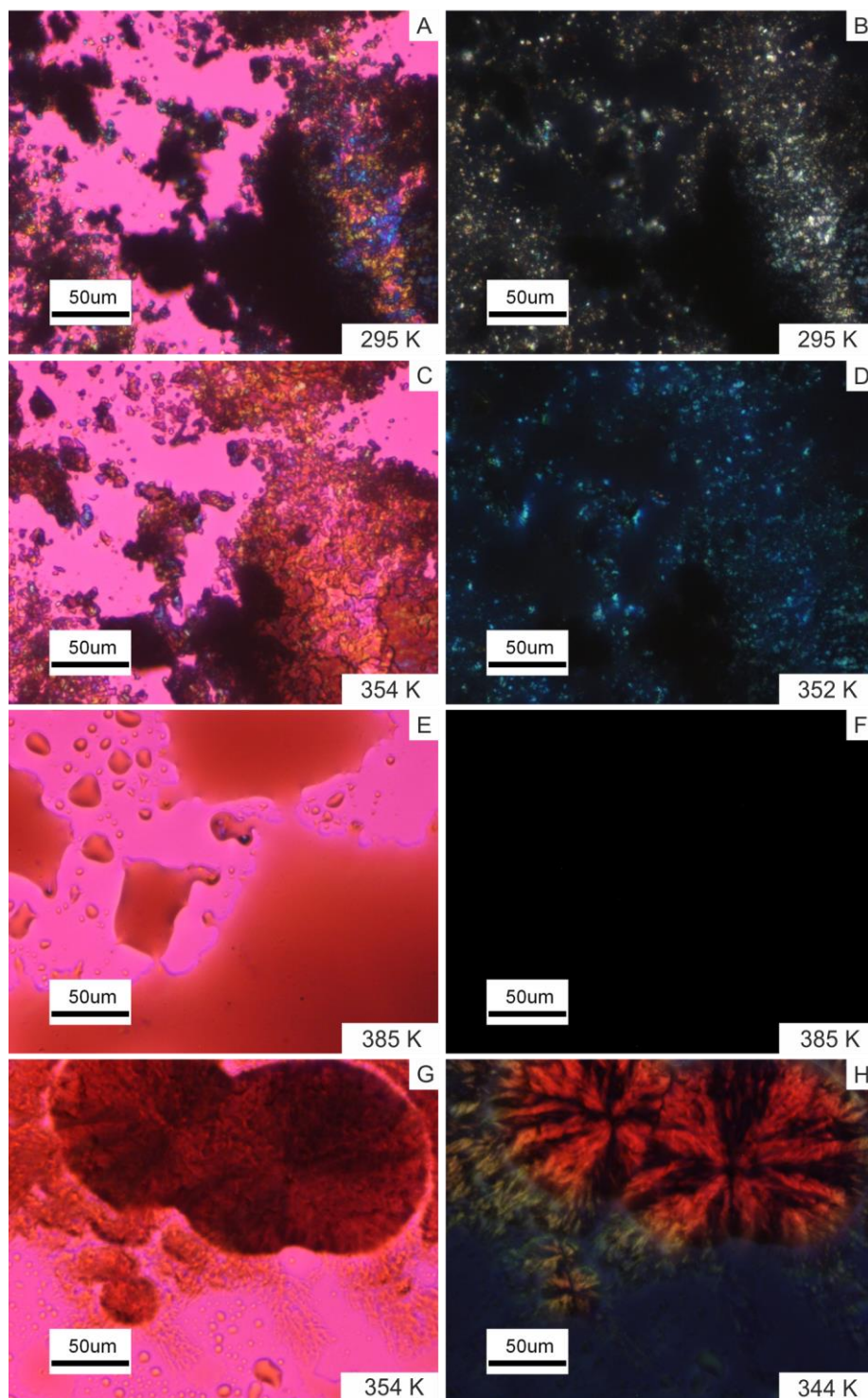


Figure S12: POM micrographs of **3**. All images were taken under crossed polarised light. Left: with retardation plate, right: without retardation plate. A) and B): crystalline powder from synthesis; C) and D): after phase transition; E) and F): melted sample; G) and H): formation of birefringent domains after cooling down.

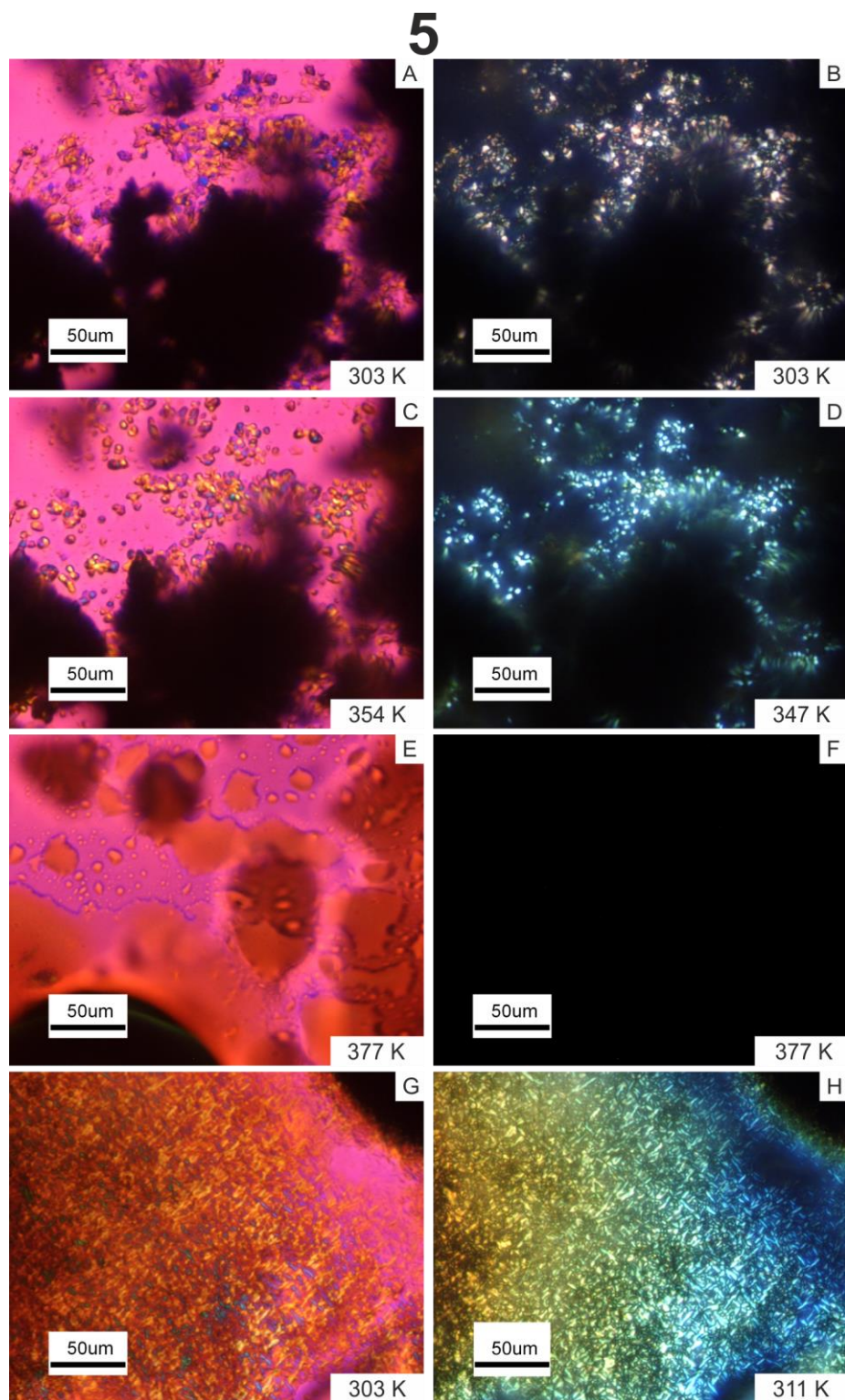


Figure S13: POM micrographs of **5**. All images were taken under crossed polarised light. Left: with retardation plate, right: without retardation plate. A) and B): crystalline powder from synthesis; C) and D): after phase transition; E) and F): melted sample; G) and H): formation of birefringent domains after cooling down.

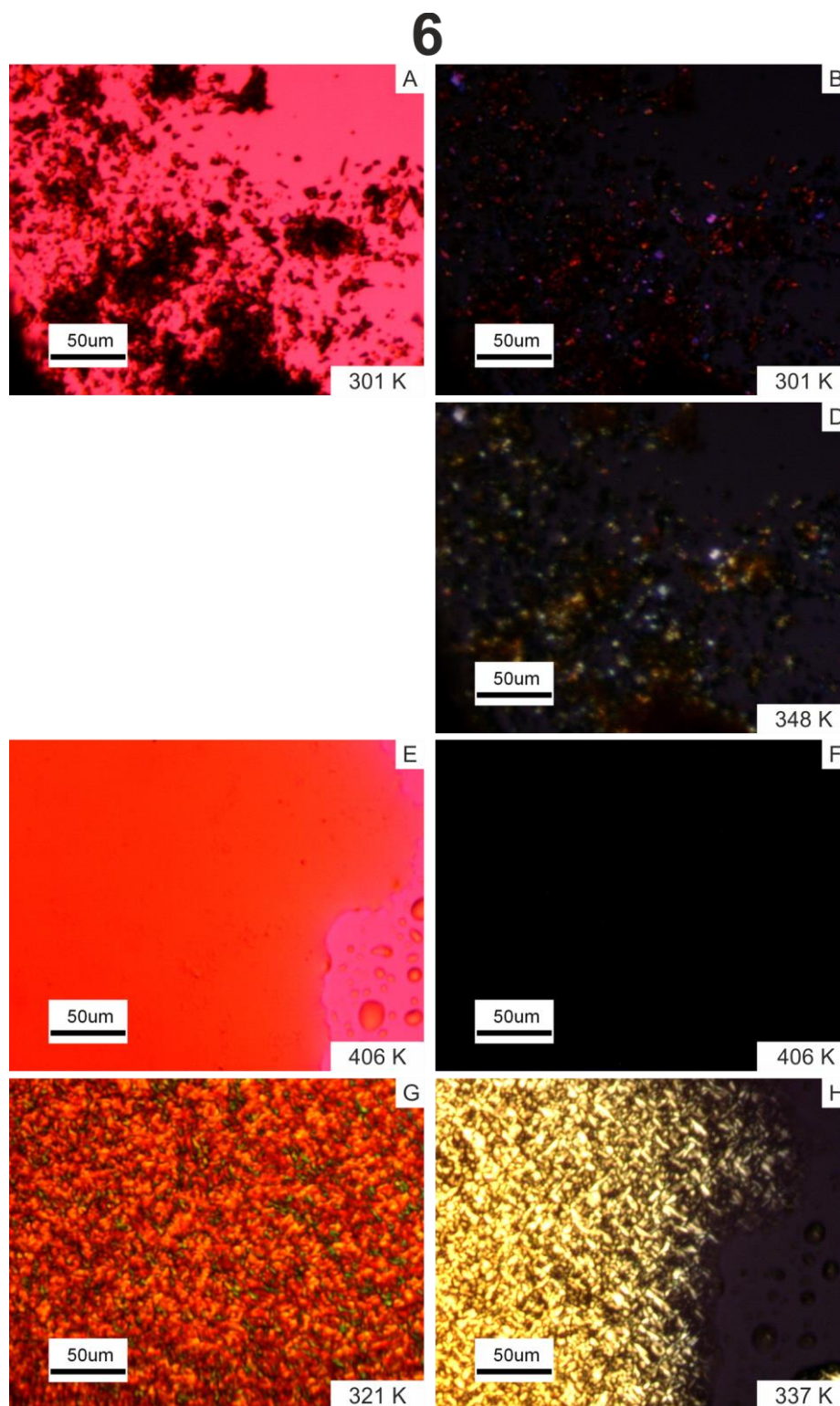


Figure S14: POM micrographs of **6**. All images were taken under crossed polarised light. Left: with retardation plate, right: without retardation plate. A) and B): crystalline powder from synthesis; D): after phase transition; E) and F): melted sample; G) and H): formation of birefringent domains after cooling down.

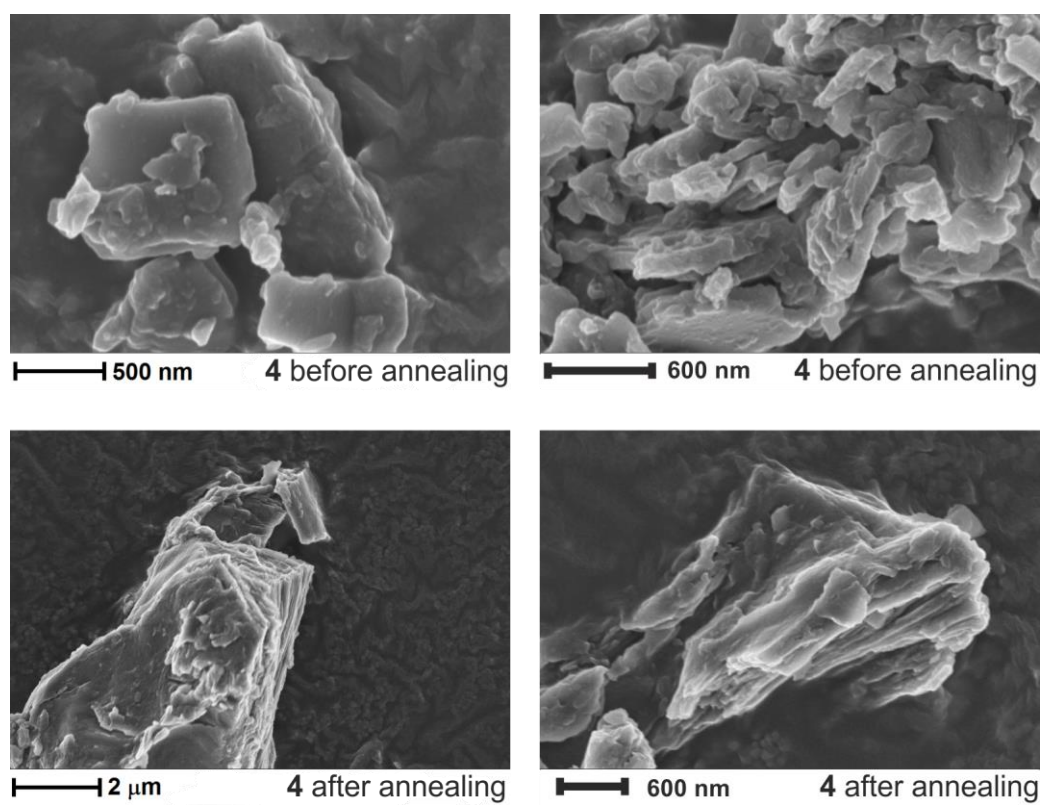


Figure S15: SEM measurements of **4** (top: sample before annealing, bottom: sample after annealing).

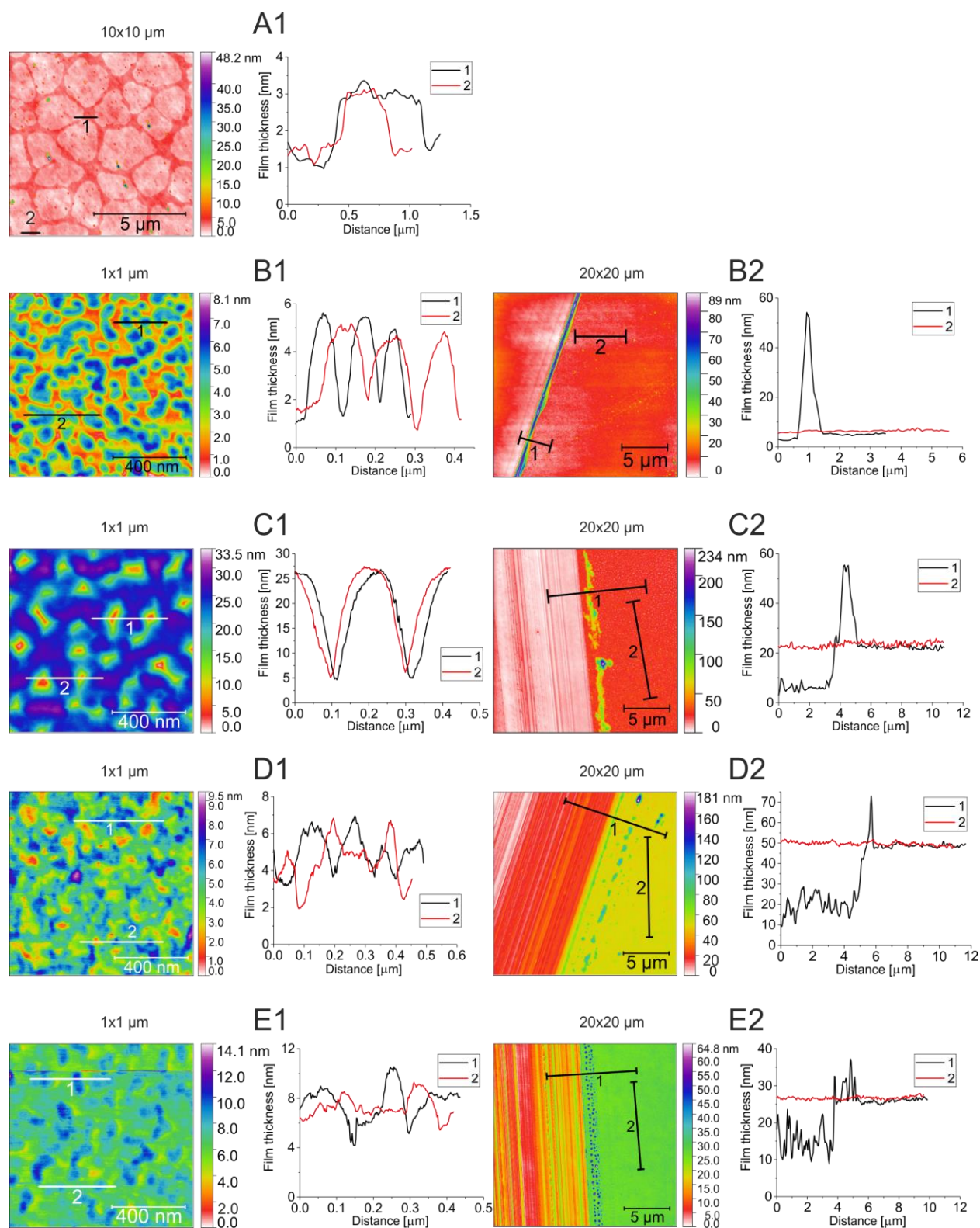


Figure S16: AFM images of **7** with corresponding height profiles and different resolutions. The spin coating parameters were varied from 0.2 mg/mL with 2000 rpm (A1) to 1.0 gm/mL with 2000 rpm (B1 and B2) to 5.0 mg/mL with 2000 rpm (C1 and C2) to 10.0 mg/mL with 2000 rpm (D1 and D2) to 10.0 mg/mL with 5000 rpm (E1 and E2).

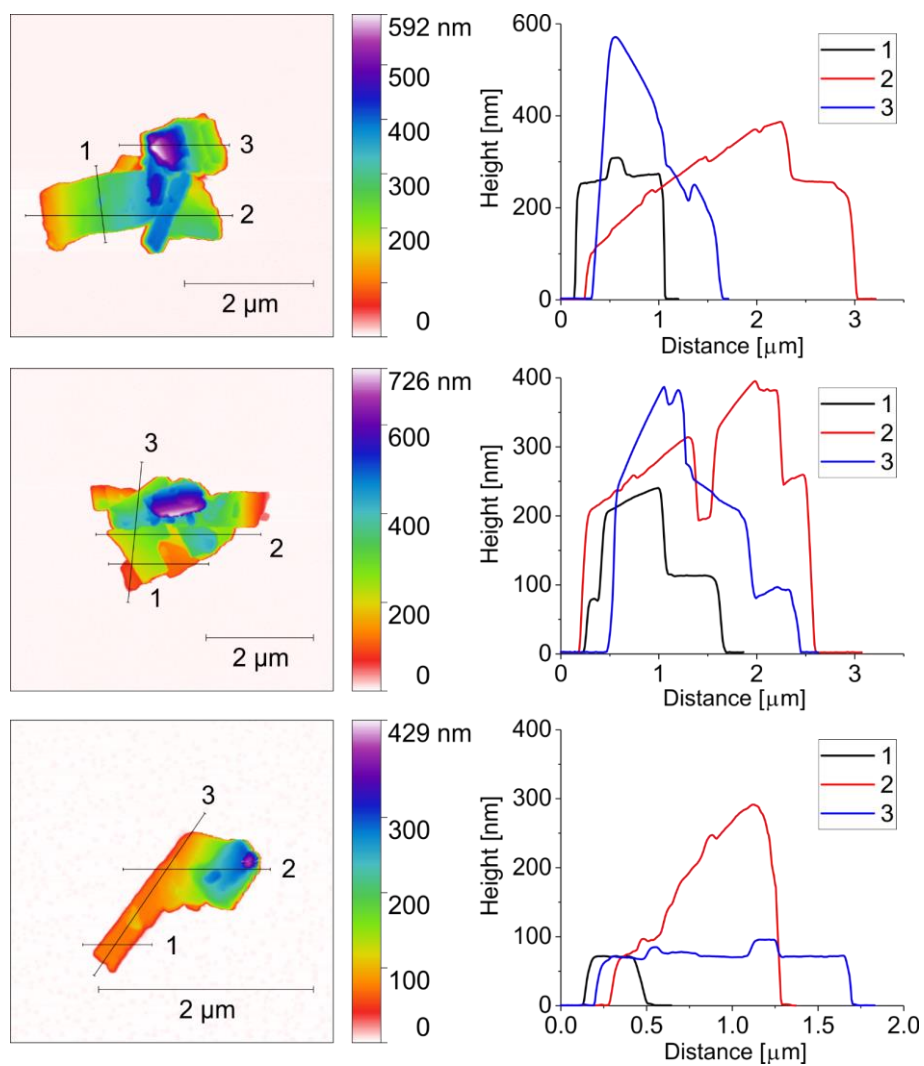


Figure S17: AFM images of **4** with the corresponding height profiles.

7.8 References

- [1] M. A. Halcrow (Ed.) *Spin-crossover materials. Properties and applications*, Wiley, Chichester **2013**.
- [2] P. Gütllich, H. A. Goodwin, *Spin Crossover in Transition Metal Compounds I-III, Vols. 234*, Springer, Berlin, Heidelberg **2004**.
- [3] P. Gütllich, A. B. Gaspar, Y. Garcia, *Beilstein J. Org. Chem.* **2013**, *9*, 342–391.
- [4] a) O. Kahn, C. J. Martinez, *Science* **1998**, *279*, 44–48; b) A. Galet, A. B. Gaspar, M. C. Muñoz, G. V. Bukin, G. Levchenko, J. A. Real, *Adv. Mater.* **2005**, *17*, 2949–2953; c) J. Linares, E. Codjovi, Y. Garcia, *Sensors* **2012**, *12*, 4479–4492; d) O. Kahn, C. Jay, J. Krober, R. Claude, F. Groliere, *Spin-transition chemical compounds, and devices comprising read-, memory-, and erase-units, active medium which contains at least one of those compounds*, EP0666561 **1995**.
- [5] a) O. Kraieva, C. M. Quintero, I. Suleimanov, E. M. Hernandez, D. Lagrange, L. Salmon, W. Nicolazzi, G. Molnár, C. Bergaud, A. Bousseksou, *Small* **2016**, *12*, 6325–6331; b) C. D. S. Brites, P. P. Lima, N. J. O. Silva, A. Millán, V. S. Amaral, F. Palacio, L. D. Carlos, *Nanoscale* **2012**, *4*, 4799–4829; c) L. Salmon, G. Molnár, D. Zitouni, C. Quintero, C. Bergaud, J.-C. Micheau, A. Bousseksou, *J. Mater. Chem.* **2010**, *20*, 5499.
- [6] a) S. Cobo, G. Molnár, J. A. Real, A. Bousseksou, *Angew. Chem. Int. Ed.* **2006**, *45*, 5786–5789; b) E. Coronado, J. R. Galán-Mascarós, M. Monrabal-Capilla, J. García-Martínez, P. Pardo-Ibáñez, *Adv. Mater.* **2007**, *19*, 1359–1361; c) M. Cavallini, I. Bergenti, S. Milita, G. Ruani, I. Salitros, Z.-R. Qu, R. Chandrasekar, M. Ruben, *Angew. Chem. Int. Ed.* **2008**, *47*, 8596–8600; d) J. Larionova, L. Salmon, Y. Guari, A. Tokarev, K. Molvinger, G. Molnár, A. Bousseksou, *Angew. Chem. Int. Ed.* **2008**, *47*, 8236–8240; e) A. D. Naik, L. Stappers, J. Snauwaert, J. Fransaer, Y. Garcia, *Small (Weinheim an der Bergstrasse, Germany)* **2010**, *6*, 2842–2846; f) Y. Raza, F. Volatron, S. Moldovan, O. Ersen, V. Huc, C. Martini, F. Brisset, A. Gloter, O. Stéphan, A. Bousseksou et al., *Chem. Commun.* **2011**, *47*, 11501–11503.
- [7] a) B. Sieklucka, D. Pinkowicz, *Molecular Magnetic Materials: Concepts and Applications*, John Wiley and Sons Inc, Weinheim **2017**; b) A. B. Gaspar, M. Seredyuk, *Coord. Chem. Rev.* **2014**, *268*, 41–58.
- [8] A. B. Gaspar, M. Seredyuk, P. Gütllich, *Coord. Chem. Rev.* **2009**, *253*, 2399–2413.
- [9] Y. Bodenthin, G. Schwarz, Z. Tomkowicz, M. Lommel, T. Geue, W. Haase, H. Möhwald, U. Pietsch, D. G. Kurth, *Coord. Chem. Rev.* **2009**, *253*, 2414–2422.
- [10] H. S. Scott, B. Moubaraki, N. Paradis, G. Chastanet, J.-F. Létard, S. R. Batten, K. S. Murray, *J. Mater. Chem. C* **2015**, *3*, 7845–7857.

- [11] a) M. Seredyuk, A. B. Gaspar, V. Ksenofontov, Y. Galyametdinov, J. Kusz, P. Gütllich, *J. Am. Chem. Soc.* **2008**, *130*, 1431–1439; b) M. Seredyuk, A. B. Gaspar, V. Ksenofontov, Y. Galyametdinov, J. Kusz, P. Gütllich, *Adv. Funct. Mater.* **2008**, *18*, 2089–2101.
- [12] S. Hayami, Y. Shigeyoshi, M. Akita, K. Inoue, K. Kato, K. Osaka, M. Takata, R. Kawajiri, T. Mitani, Y. Maeda, *Angew. Chem. Int. Ed.* **2005**, *44*, 4899–4903.
- [13] K. Senthil Kumar, M. Ruben, *Coord. Chem. Rev.* **2017**, *346*, 176–205.
- [14] M. Seredyuk, M. C. Muñoz, V. Ksenofontov, P. Gütllich, Y. Galyametdinov, J. A. Real, *Inorg. Chem.* **2014**, *53*, 8442–8454.
- [15] T. Romero-Morcillo, M. Seredyuk, M. C. Muñoz, J. A. Real, *Angew. Chem. Int. Ed.* **2015**, *54*, 14777–14781.
- [16] P. N. Martinho, Y. Ortin, B. Gildea, C. Gandolfi, G. McKerr, B. O'Hagan, M. Albrecht, G. G. Morgan, *Dalton Trans.* **2012**, *41*, 7461–7463.
- [17] P. N. Martinho, C. J. Harding, H. Müller-Bunz, M. Albrecht, G. G. Morgan, *Eur. J. Inorg. Chem.* **2010**, 675–679.
- [18] a) Y. Bodenthin, U. Pietsch, H. Möhwald, D. G. Kurth, *J. Am. Chem. Soc.* **2005**, *127*, 3110–3114; b) J. A. Kitchen, N. G. White, C. Gandolfi, M. Albrecht, G. N. L. Jameson, J. L. Tallon, S. Brooker, *Chem. Commun.* **2010**, *46*, 6464–6466; c) P. Coronel, A. Barraud, R. Claude, O. Kahn, A. Ruaudel-Teixier, J. Zarembowitch, *J. Chem. Soc., Chem. Commun.* **1989**, 193–194.
- [19] K. Bairagi, O. Iasco, A. Bellec, A. Kartsev, D. Li, J. Lagoute, C. Chacon, Y. Girard, S. Rousset, F. Miserque et al., *Nat. Commun.* **2016**, *7*, 12212.
- [20] H. Soyer, C. Mingotaud, M.-L. Boillot, P. Delhaes, *Langmuir* **1998**, *14*, 5890–5895.
- [21] H. Soyer, E. Dupart, C. J. Gómez-García, C. Mingotaud, P. Delhaès, *Adv. Mater.* **1999**, *11*, 382–384.
- [22] a) T. Fujigaya, D.-L. Jiang, T. Aida, *J. Am. Chem. Soc.* **2003**, *125*, 14690–14691; b) O. Roubeau, B. Agricole, R. Clérac, S. Ravaine, *J. Phys. Chem. B* **2004**, *108*, 15110–15116; c) O. Roubeau, J. M. Alcazar Gomez, E. Balskus, J. J. A. Kolnaar, J. G. Haasnoot, J. Reedijk, *New J. Chem.* **2001**, *25*, 144–150.
- [23] D. G. Kurth, P. Lehmann, M. Schutte, *Chem. Phys. Lett.* **2000**, *97*, 5704–5707.
- [24] S. Schlamp, P. Thoma, B. Weber, *Chem. Eur. J.* **2014**, *20*, 6462–6473.
- [25] S. Schlamp, K. Dankhoff, B. Weber, *New J. Chem.* **2014**, *38*, 1965–1972.
- [26] S. Schlamp, P. Thoma, B. Weber, *Eur. J. Inorg. Chem.* **2012**, 2759–2768.
- [27] S. Schlamp, B. Weber, A. D. Naik, Y. Garcia, *Chem. Commun.* **2011**, *47*, 7152–7154.
- [28] W. Bauer, W. Scherer, S. Altmannshofer, B. Weber, *Eur. J. Inorg. Chem.* **2011**, 2803–2818.

- [29] W. Bauer, S. Schlamp, B. Weber, *Chem. Commun.* **2012**, 48, 10222–10224.
- [30] B. Weber, R. Betz, W. Bauer, S. Schlamp, *Z. Anorg. Allg. Chem.* **2011**, 637, 102–107.
- [31] M. Tanner, A. Ludi, *Chimia* **1980**, 23–24.
- [32] K. Dankhoff, C. Lochenie, F. Puchtler, B. Weber, *Eur. J. Inorg. Chem.* **2016**, 2136–2143.
- [33] a) C. Lochenie, K. Schötz, F. Panzer, H. Kurz, B. Maier, F. Puchtler, S. Agarwal, A. Köhler, B. Weber, *J. Am. Chem. Soc.* **2018**, 140, 700–709; b) B. Weber, *Coord. Chem. Rev.* **2009**, 253, 2432–2449; c) B. Weber, E.-G. Jäger, *Eur. J. Inorg. Chem.* **2009**, 465–477.
- [34] C. Lochenie, J. Heinz, W. Milius, B. Weber, *Dalton Trans.* **2015**, 44, 18065–18077.
- [35] A. L. Spek, *PLATON - A Multipurpose Crystallographic Tool*, Utrecht University, The Netherlands **2008**.
- [36] C. Lochenie, W. Bauer, A. P. Railliet, S. Schlamp, Y. Garcia, B. Weber, *Inorg. Chem.* **2014**, 53, 11563–11572.
- [37] C. F. Macrae, P. R. Edgington, P. McCabe, E. Pidcock, G. P. Shields, R. Taylor, M. Towler, J. van de Streek, *J. Appl. Crystallogr.* **2006**, 39, 453–457.
- [38] a) W. Bauer, T. Pfaffeneder, K. Achterhold, B. Weber, *Eur. J. Inorg. Chem.* **2011**, 3183–3192; b) B. Weber, E. S. Kaps, C. Desplanches, J.-F. Létard, K. Achterhold, F. G. Parak, *Eur. J. Inorg. Chem.* **2008**, 2008, 4891–4898; c) B. Weber, *MERDJ - Mössbauer Effect Reference and Data Journal* **2012**, 35, 238–254.
- [39] a) B. Weber, E. S. Kaps, C. Desplanches, J.-F. Létard, *Eur. J. Inorg. Chem.* **2008**, 2963–2966; b) R. Nowak, W. Bauer, T. Ossiander, B. Weber, *Eur. J. Inorg. Chem.* **2013**, 975–983.
- [40] P. Gütllich, A. Hauser, H. Spiering, *Angew. Chem. Int. Ed.* **1994**, 33, 2024–2054.
- [41] O. Kahn, *Molecular magnetism*, VCH, New York **1993**.
- [42] K. Lagarec, D. G. Rancourt, *Recoil, mössbauer spectral analysis software for windows 1.0*, Department of Physics, University of Ottawa, Canada **1998**.
- [43] a) M. C. Burla, R. Caliandro, B. Carrozzini, G. L. Casciarano, C. Cuocci, C. Giacovazzo, M. Mallamo, A. Mazzone, G. Polidori, *J. Appl. Crystallogr.* **2015**, 48, 306–309; b) A. Altomare, M. C. Burla, M. Camalli, G. L. Casciarano, C. Giacovazzo, A. Guagliardi, A. G. G. Moliterni, G. Polidori, R. Spagna, *J. Appl. Crystallogr.* **1999**, 32, 115–119.
- [44] G. M. Sheldrick, *Acta Crystallogr., A, Found. Crystallogr. (Acta crystallographica. Section A, Foundations of crystallography)* **2008**, 64, 112–122.
- [45] L. J. Farrugia, *J. Appl. Crystallogr.* **1997**, 30, 565.
- [46] E. Keller, *Schakal-99*, University of Freiburg, Germany **1999**.
- [47] D. Nečas, P. Klapetek, *Open Physics* **2012**, 10, 99.

[48] H. G. O. Becker, *Organikum. Organisch-chemisches Grundpraktikum*, 19th ed., Barth, Ed. Dt. Verl. der Wiss., Leipzig, Berlin, Heidelberg **1993**.

[49] W. Bauer, T. Ossiander, B. Weber, *Z. Naturforsch. B* **2010**, 323–328.

8. Behaviour of Cu(II) and Ni(II) Schiff base-like complexes with long, branched alkyl chains in solution and in the solid state: Micelle formation, CISSS, and liquid crystallinity

Johannes Weihermüller,^a Stella Buchmann,^a Victoria Müller,^a Wolfgang Milius,^b and Birgit Weber^{a*}

^aDepartment of Chemistry, Inorganic Chemistry IV, Universität Bayreuth, Universitätsstrasse 30, NW I, 95440 Bayreuth, Germany, E-mail: weber@uni-bayreuth.de.

^bDepartment of Chemistry, Inorganic Chemistry I, Universität Bayreuth, Universitätsstrasse 30, NW I, 95440 Bayreuth, Germany.

8.1 Abstract

A novel Schiff base-like ligand system with long, branched alkyl chains was synthesised over eight steps and used to form the corresponding charge-neutral Cu(II) and Ni(II) complexes without counter ion. The properties of the complexes were studied using magnetic measurements, TGA, DSC, NMR, UV-Vis, DLS, TEM, POM, PXRD, and SEM. The Ni(II) complex shows a coordination-induced spin state switch in solution. Both complexes form micelles in a hexane/MeOH mixture upon the addition of NaCN. POM measurements reveal liquid crystalline phases during the cooling mode. The system also exhibits promising properties for the facile approach to form thin films through a melting process.

8.2 Introduction

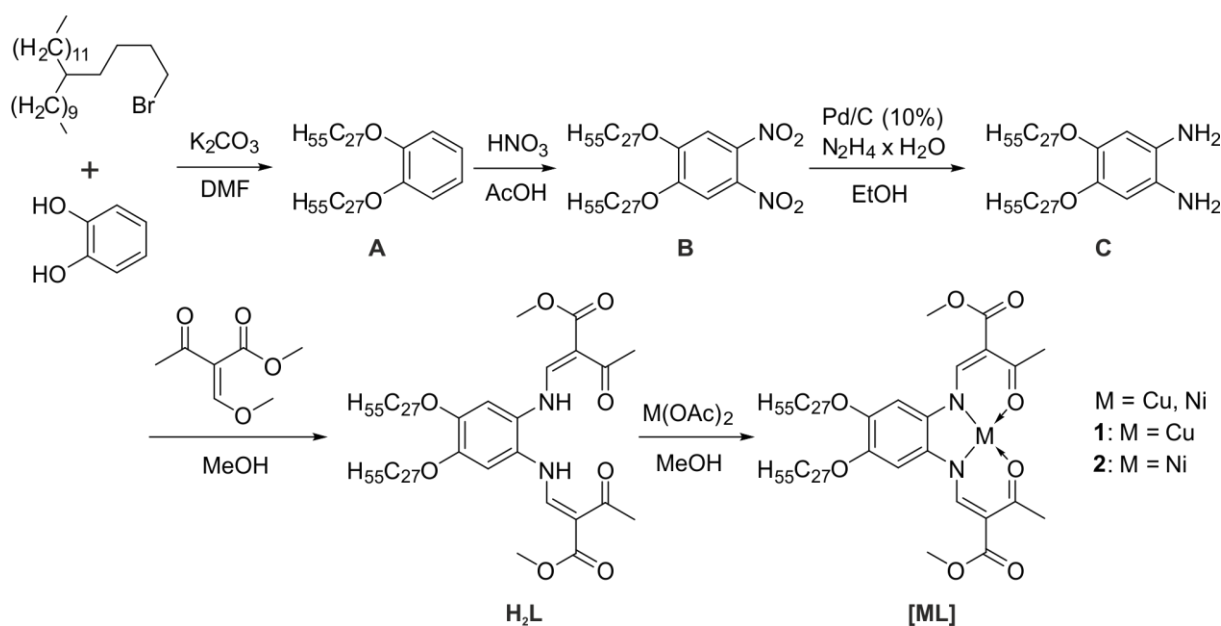
Multifunctional responsive materials are of great interest for future applications. One of those materials are spin crossover (SCO) complexes which can switch between a diamagnetic and a paramagnetic state. Most SCO phenomena can be triggered by a change of temperature, pressure, or pH or by light irradiation.^[1] In this case, no change of the coordination number takes place. However, it is also possible to trigger a similar phenomenon where the spin state changes, the coordination induced spin state switch (CISSS). Here, the coordination sphere is chemically altered and with it the electronic occupation of the orbitals. This was shown in 2010 by Thies *et al.* using a porphyrin-based system.^[2] In a non-coordinating solvent the Ni(II) complex was in a square planar coordination sphere and diamagnetic ($S = 0$). The addition of pyridine resulted in its coordination onto the Ni(II) centre and the formation of the paramagnetic ($S = 1$) penta- or hexacoordinated Ni(II) complex. By introducing a covalently attached azopyridine or

azoimidazole group to the porphyrin unit the system could be switched with light.^[3,4] The water solubility of these complexes and their magnetic properties, in particular the CISSS, make them attractive for the application as functional magnetic resonance imaging (MRI) contrast agent.

A new multifunctional system can be obtained by combining the CISSS with other properties, such as amphiphilicity and liquid crystallinity. To realise this, long alkyl chains are introduced to the CISSS active unit to form an amphiphilic metal complex. Fe(II),^[5,6] Fe(III),^[7,8] and Co(II)^[9] based amphiphilic SCO systems were reported in literature. Some of them show micelle formation in solution which drastically improved cooperative effects in solution.^[6,10] An advantage of the micellar systems is that they are nanosized structures and bear the possibility to be used in various ways for future applications. In general, Israelachvili *et al.* thoroughly discussed the basic principles of the self-assembly of ionic amphiphiles in 1976.^[11] The discussion was focused primarily on spherical or cylindrical micelles and vesicular or lamellar bilayers. It was outlined that the interacting forces, the entropy, and the geometric component can be applied to a simple model for ionic and zwitterionic amphiphiles. However, moving to more complicated systems it is still challenging to predict the self-assembly behaviour. To date, only lipid layer-like arrangements were observed in the solid state for the electronic neutral Schiff base-like system investigated by our group.^[12,13–15] After the crystallisation of several similar complexes the self-assembly parameter (*sap*) was introduced to better understand the formation of the lipid layer-like arrangements.^[14] Yet, the self-assembly behaviour in solution still needs to be investigated. This work will focus on the effect of using long, branched alkyl chains to improve the geometric packing of the complex structure. The necessity of introducing a charge at the head group as this enhances the phase separation properties and with it the self-assembly to inverse micelles will be discussed, as well. In addition, the introduction of the charge can be coupled with the CISSS effect.

8.3 Synthesis

The general synthesis route for the Cu(II) and the Ni(II) complexes is presented in **Scheme 1**. In a first step, the alkyl chain had to be elongated as reported in literature^[8] which is omitted in **Scheme 1**. Prior tests showed that, without the elongation, the steric hindrance is too strong for two branched alkyl chains to react with catechol. The next four steps were performed in a similar way as shown in literature with an unbranched system^[13] to obtain the ligand **H₂L** with branched alkyl chains. **H₂L** was further reacted with the corresponding metal acetate to form **[CuL]** (**1**) and **[NiL]** (**2**), respectively. The purity of the intermediates and the compounds was confirmed by elemental analysis, NMR spectroscopy, mass spectrometry, and IR spectroscopy. Small amounts of unreacted ligand were found in the ¹H-NMR of **2**.



Scheme 1: General synthesis route for compounds **[CuL]** (**1**) and **[NiL]** (**2**).

8.4 Results and discussion

8.4.1 ¹H-NMR spectroscopy

H₂L and **2** were characterised by ¹H-NMR spectroscopy, as shown in **Figure 1** and **Table 1**. The complete spectra are shown in the Supporting Information in **Figure S1** - **Figure S3**. The chemical shifts δ and the coupling constants J of **H₂L** are in agreement with similar ligand systems with unbranched alkyl chains from literature measured in CDCl_3 .^[13] Due to *cis-trans* isomers the protons at e) and at f) position cause the weak additional signals e') and f'). By introducing Ni(II) into the chelate ligand to obtain **2** the appearance of the geometric isomers is suppressed and the additional signals e') and f') as well as the signal of the amine protons a) disappear. In addition, the signals b) and c), that represent protons are close to the Ni(II) centre, are slightly shifted. The chemical shifts of signals d) to j) are the same as for **H₂L**. The ¹H-NMR of **2** was additionally measured in pyridine-*d*₅, where the pyridine molecules can coordinate to the nickel centre and trigger a coordination induced spin state switch (CISSS).^[2,3] As a result, the square planar, diamagnetic Ni(II) system ($S = 0$) converts to either a square pyramidal, paramagnetic system ($S = 1$) by coordinating one pyridine molecule or to an octahedral, paramagnetic system ($S = 1$) by coordinating two pyridine molecules.^[16] The change in magnetism can be followed in the ¹H-NMR spectra through a line broadening and a shift of the signals, which is stronger for protons close to the Ni(II) centre. Both can be clearly seen for b), c), d), and f). Interestingly, weak signals are still observed and labelled d*), e*), and f*) that could belong to a diamagnetic Ni(II) complex or to residues of unreacted ligand. The signals are still slightly shifted due to a change of solvent,

but very sharp which is in better agreement with a diamagnetic species. The other diamagnetic signals are located below the paramagnetic signals. A reason for a diamagnetic Ni(II) species could be the high complex concentration needed for the paramagnetic $^1\text{H-NMR}$ measurement. An excess of only around 300 eq. of pyridine could have been too low to coordinate all Ni(II) complex molecules and push the equilibrium towards the paramagnetic Ni(II) species. In the case of ligand impurities, the complex synthesis could be repeated with more than 1.4 eq. excess of $\text{Ni}(\text{OAc})_2$ and a longer reaction time. The workup could be then improved by extracting the higher excess of $\text{Ni}(\text{OAc})_2$ with H_2O , separating it with an *n*-hexane phase, drying it over Na_2SO_4 , and removing the solvent under vacuum. By repeating the synthesis under improved conditions, it would be possible to verify which case occurred.

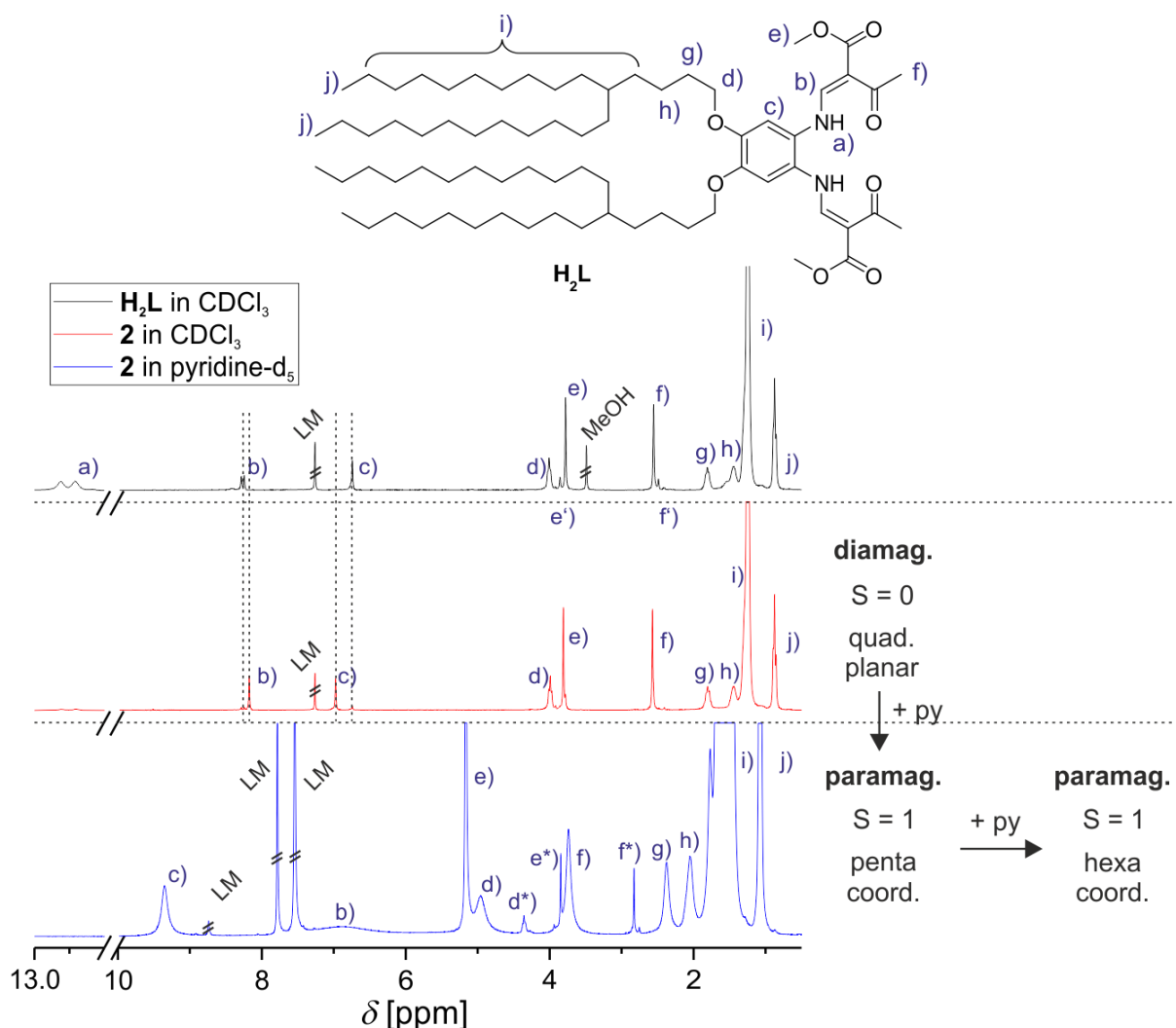


Figure 1: Top: Structure of the ligand H_2L with assigned signals from the $^1\text{H-NMR}$ spectroscopy measurements. Bottom left: $^1\text{H-NMR}$ spectra of H_2L in CDCl_3 , $\mathbf{2}$ in CDCl_3 , and $\mathbf{2}$ in pyridine-d_5 at room temperature. Bottom right: magnetic state of complex $\mathbf{2}$ in relation to its coordination sphere.

Table 1: Chemical shifts of the ¹H-NMR measurements of **H₂L** in CDCl₃, **2** in CDCl₃, and **2** in pyridine-d₅.

Signal	H ₂ L in CDCl ₃ [ppm]	2 in CDCl ₃ [ppm]	2 in pyridine-d ₅ [ppm]
a)	12.88	-	-
b)	8.27	8.17	6.86
c)	6.74	6.97	9.35
d)	4.01	4.00	4.96/4.35**
e)	3.86/3.78*	3.81	5.16/3.85**
f)	2.56/2.49*	2.57	3.74/2.83**
g)	1.81	1.80	2.38
h)	1.45	1.44	2.05
i)	1.25	1.25	1.77/1.64/1.68/1.47/1.59**
j)	0.88	0.88	1.08

* E/Z-isomers; ** dia- and paramagnetic signals

8.4.2 DLS measurements

The amphiphilic properties of **1** and **2** were used for the synthesis of inverse micellar structures in solution which were characterised by DLS. Anions can weakly coordinate on the metal centre of complexes **1** or **2**. In addition to that, the counterion will be located in close proximity to the anion in the MeOH phase. Therefore, the head group becomes more polar which should improve the inverse micelle formation. For this reason, the complexes were first dissolved in *n*-hexane (*c* = 0.5 mg/mL) and then either pure MeOH, a solution of KSCN in MeOH, or a solution of NaCN in MeOH was added. A schematic presentation of this process is shown in **Figure 2**. The saturation of NaCN in MeOH was reached with about 4 mg/mL. Therefore, tests with pure H₂O instead of MeOH were done to increase the concentration of NaCN in the solvent, too, but resulted in a complete separation of the water and the organic phase and in weakly pronounced correlation functions in the DLS measurement. Tests with H₂O/salt mixtures are still in progress.

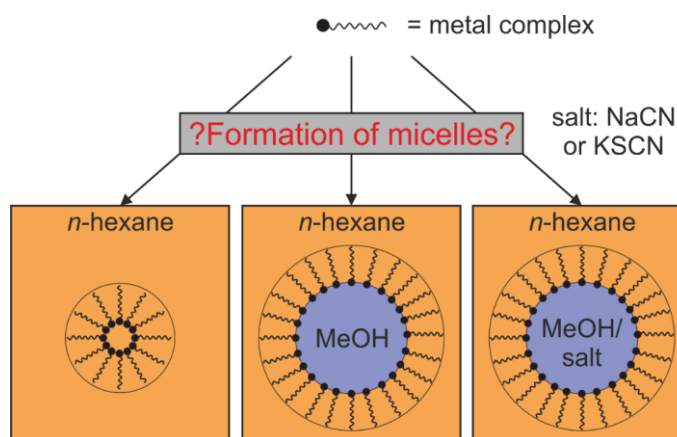


Figure 2: Schematic presentation of the possible ways of micelle formation tested in this work.

The salt concentration in MeOH was selected that 10 μL of the MeOH solution contained 2 eq. of anion for each complex molecule when 1 mL of *n*-hexane solution was used. The addition of more than 20 μL of MeOH solution to 1 mL of *n*-hexane solution resulted in the appearance of a second phase. Consequently, the maximum miscibility of *n*-hexane and MeOH was reached at that point. Complexes **1** or **2** in pure *n*-hexane or with the addition of 10 μL MeOH per 1 mL of *n*-hexane solution resulted in no proper inverse micelle formation as shown in the autocorrelation functions in **Figure 3**. The addition of 10 μL MeOH/2 eq. KSCN and 20 μL MeOH/4 eq. KSCN per mL of *n*-hexane solution did not improve the formation, as well. However, increasing the ligand strength of the anion, by changing the salt to NaCN, had a positive effect on the inverse micelle formation. With the addition of 10 μL MeOH/2 eq. NaCN a mirrored sigmoidal curve as correlation function was obtained for complex **1** as shown in **Figure 3**. This suggests the formation of inverse micelles with hydrodynamic diameters of 744 ± 203 nm and 6593 ± 1289 nm. The size distribution of the hydrodynamic diameters of **1** is shown in **Figure 4** on the left side and **Table 2**. It is important to note that DLS measurements are not necessarily well suited for bimodal distributions. Increasing the MeOH solution to 20 μL MeOH/4 eq. NaCN per mL of *n*-hexane solution resulted in a decrease in quality of the correlation function. Either the inverse micelles became multidisperse or they formed non-spherical structures, *e.g.* layers or tubes. Both possibilities are disadvantageous for DLS measurements. For complex **2** the addition of 10 μL MeOH/2 eq. KSCN and 20 μL MeOH/4 eq. KSCN per mL of *n*-hexane solution did again result in invalid correlation functions. In contrast to this, the addition of 10 μL MeOH/2 eq. NaCN and 20 μL MeOH/4 eq. NaCN per mL of *n*-hexane to a solution with complex **2** resulted in very distinct mirrored sigmoidal curves as correlation functions as shown in **Figure 3**. The calculated size distributions are monomodal as shown in **Figure 4** on the right side and in **Table 2**. The hydrodynamic diameters are 772 ± 159 nm and 1173 ± 273 nm, respectively. This showed that increasing the volume of MeOH also increases the size of the inverse micelles.

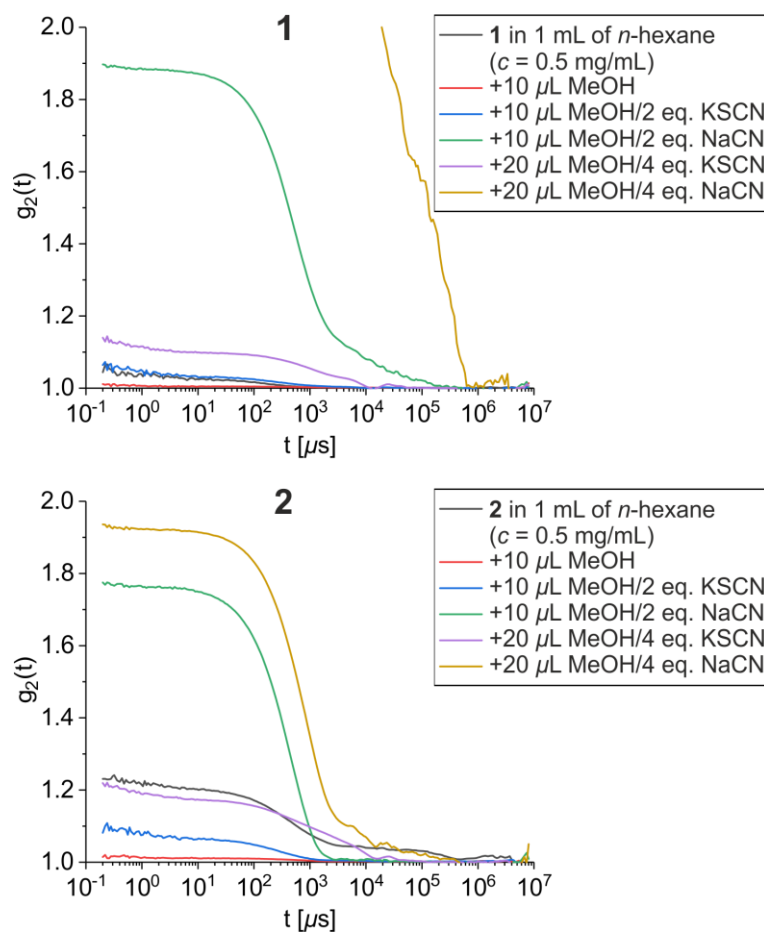


Figure 3: Autocorrelation functions of the DLS measurements of **1** (top) and **2** (bottom) in *n*-hexane, with the addition of MeOH, and with different amounts of MeOH and salts added.

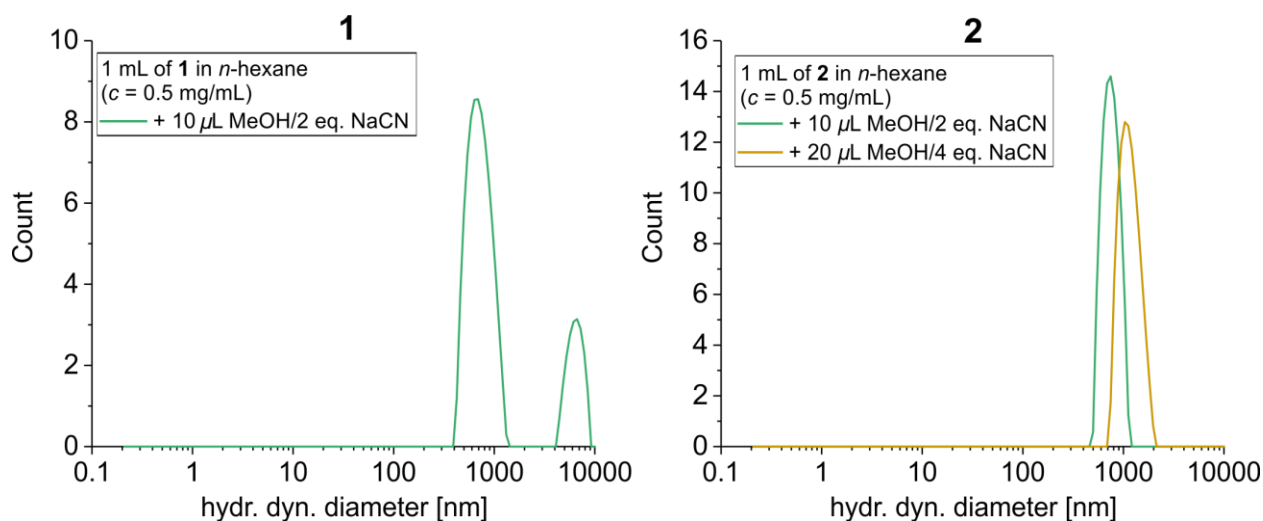


Figure 4: Size distributions of the hydrodynamic diameter obtained from the autocorrelation functions of the DLS measurements for **1** and **2**. The corresponding amounts of MeOH and salt were added to 1 mL of the *n*-hexane stock solution.

Table 2: DLS measurements of **1** and **2** done with different salts and volumes of MeOH including the resulting hydrodynamic diameter and the polydispersity index (PDI).

Compound	Salt	MeOH [μ L]	hydr. dyn. diameter 1 [nm]	hydr. dyn. diameter 2 [nm]	PDI
1	-	-	-	-	0.255
	KSCN (2 eq.)	10	-	-	0.480
	NaCN (2 eq.)	10	744 \pm 203	6593 \pm 1289	0.223
	KSCN (4 eq.)	20	-	-	0.493
	NaCN (4 eq.)	20	-	-	3.621
2	-	-	-	-	0.223
	KSCN (2 eq.)	10	-	-	0.285
	NaCN (2 eq.)	10	772 \pm 159	-	0.103
	KSCN (4 eq.)	20	-	-	0.224
	NaCN (4 eq.)	20	1173 \pm 273	-	0.287

8.4.3 TEM measurements

The solutions used for the DLS measurements were further investigated by TEM. Only various undefined structures were observed for the measurements of **1** and **2** in *n*-hexane and in *n*-hexane with MeOH. However, both complexes formed spherical structures in *n*-hexane upon the addition of MeOH/NaCN as shown in **Figure 5**. All spheres have at least one dark spot which is supposed to be NaCN that was in excess in the MeOH phase within the micelles and crystallised there upon drying. The sizes of the micelles are 775 \pm 561 nm for **1** and 578 \pm 386 nm for **2**. The values fit with the sizes obtained from the DLS measurements considering the standard deviation. In addition to that, micelles with a diameter of 4241 nm and 8513 nm were found for **1**. A similar size was observed in the DLS measurements as a second signal in the size distribution.

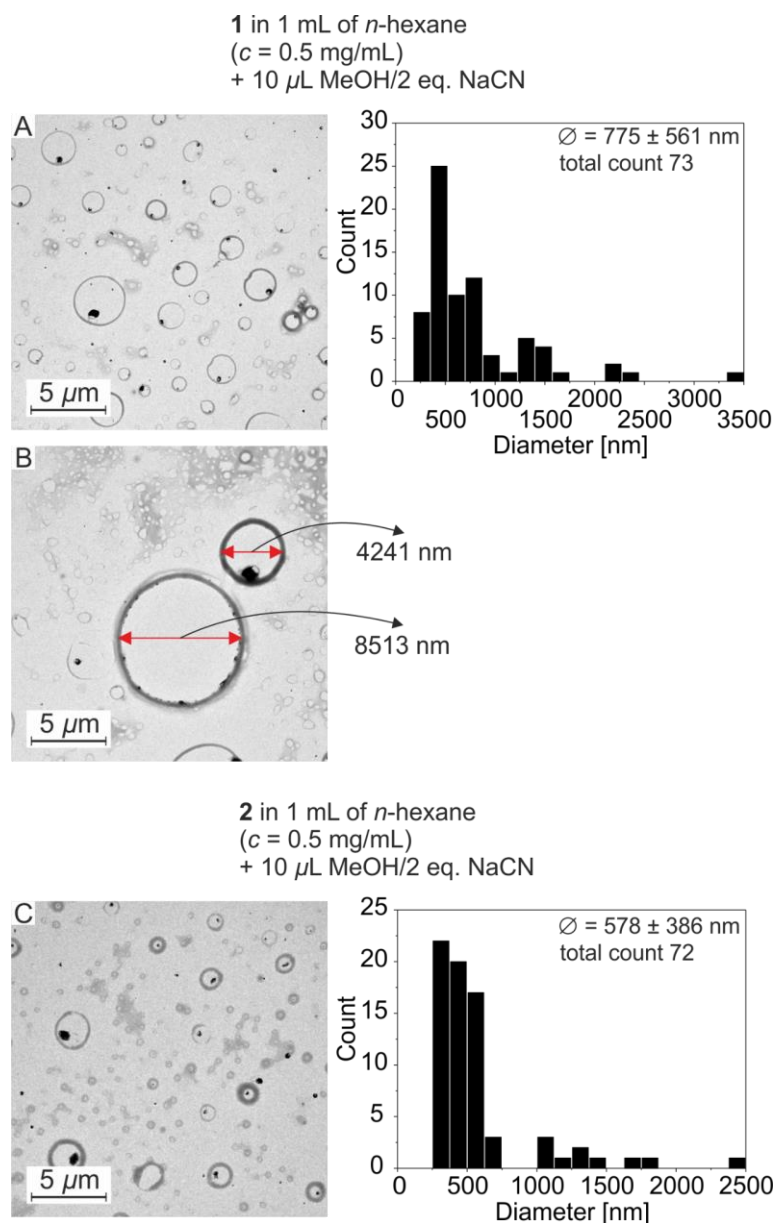


Figure 5: TEM measurements (left) of **1** (A and B) and **2** (C) prepared with solutions used in the DLS measurement. The size distributions are shown on the right side.

8.4.4 UV-Vis spectroscopy

The optical absorption properties of **1** and **2** were studied with UV-Vis spectroscopy. Both complexes were very soluble in CHCl_3 , a weakly coordinating solvent, and pyridine, a strongly coordinating solvent. The colours of the solutions are already distinguishable with the bare eye, as shown in **Figure 6**.

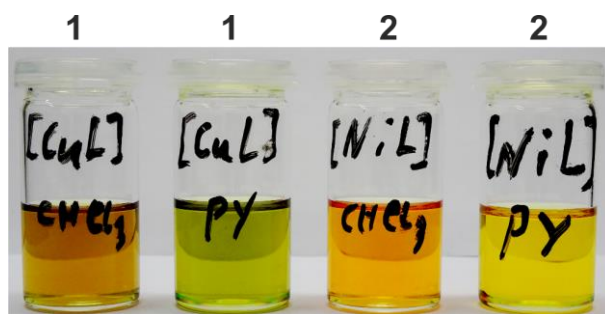


Figure 6: The solutions used in the UV-Vis measurements of **1** (left, left centre) and **2** (right centre, right) in CHCl_3 and pyridine (py).

The UV-Vis spectra were recorded in correlation to the concentration of added pyridine as shown in **Figure 7**. The data obtained from the UV-Vis measurements are listed in **Table 3**. The gradient of the measurements started in pure CHCl_3 and finished in pure pyridine. The concentration of the complexes was always kept constant for the different CHCl_3 /pyridine ratios. However, two different concentrations were used to better identify charge transfer processes in the range of 300 – 600 nm and d-d transitions processes in the range of 450 – 1000 nm which strongly vary in intensity. With increasing equivalents of pyridine **1** shows only a weak increase in intensity for π - π^* transitions with broad bands (including shoulders) at 339 and 389 nm. At higher wavenumbers a red shift of the d-d transition band from 540 to 586 nm can be observed. This solvatochromic effect is caused by a higher coordination strength of pyridine in comparison to CHCl_3 .^[17] The values agree with similar Cu(II) complexes from literature.^[18–20] The influences of the different solvents on the absorption properties are more pronounced for **2**. In the region for π - π^* transition processes the intensities of the weak shoulder at 341 nm increases strongly and the intensity of the absorption band at 375 nm decreases and is shifted to 388 nm with increasing equivalents of pyridine. Here, no distinct isosbestic point can be observed for **2** which indicates that more than one species exists. This can be explained by an equilibrium between a penta- and a hexacoordinated Ni(II) centre.^[2] At higher wavenumbers a shoulder for d-d transitions at 515 nm weakens with the addition of pyridine, while two new absorption bands appear at 766 and 814 nm, as observed for similar Ni(II) complexes.^[20]

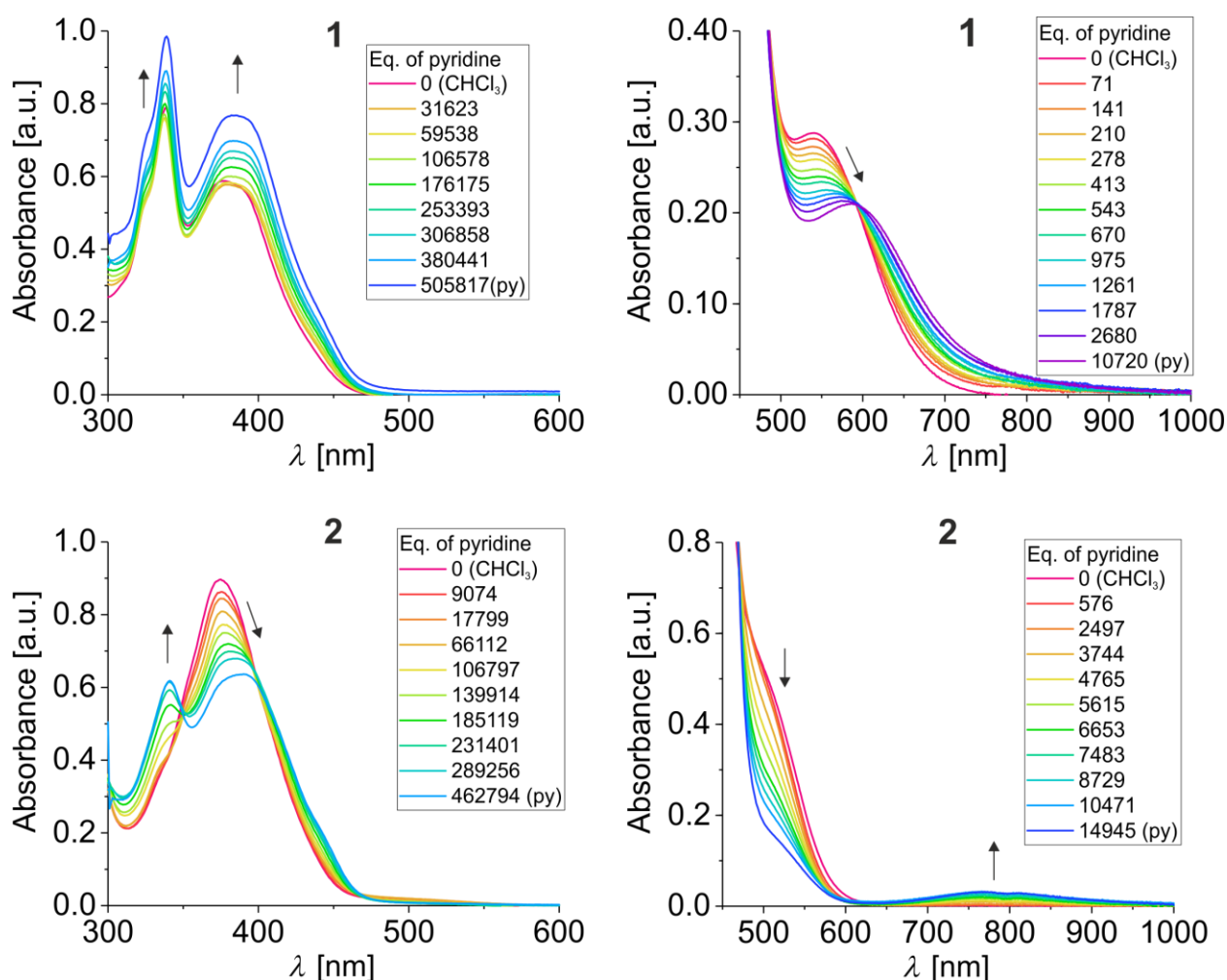


Figure 7: UV-Vis absorption spectra of compounds **1** and **2** in the range of 300 – 600 nm and 450 – 1000 nm in CHCl₃ and pyridine. The first measurement started in pure CHCl₃, then pyridine was added stepwise between each measurement until the last measurement which was done in pure pyridine. During this, the concentration of the complexes was always kept constant. However, to better identify charge transfer processes and $\pi \pi^*$ transitions two measurement sets with different concentrations (left and right) were done. The arrows show the change of absorption in relation to the addition of different equivalents of pyridine.

With regards to the DLS measurements the UV-Vis measurements of **1** and **2** were also carried out in *n*-hexane, with the addition of pure MeOH, and with the addition of a MeOH/NaCN solution ($c(\text{NaCN}) = 2.77 \text{ mg/mL}$) in the range of 300 – 600 nm ($c(\mathbf{1}) = 0.0296 \text{ mg/mL}$ and $c(\mathbf{2}) = 0.0323 \text{ mg/mL}$) and of 450 – 1000 nm ($c(\mathbf{1}) = 1.4 \text{ mg/mL}$ and $c(\mathbf{2}) = 1.0 \text{ mg/mL}$) as shown in **Figure 8** and in **Table 3**. Please note, that different concentrations were used for the DLS and the UV-Vis measurements as the precision of the detectors differed. This also influenced the number of added equivalents of NaCN. Therefore, it was not possible to obtain high numbers of equivalents as shown for the DLS measurements. Due to the formation of a second phase above 140 μL MeOH/NaCN solution the addition of more was not possible, as well. However, CN⁻ is a stronger ligand than pyridine and it was to be expected that less equivalents were needed to observe a change in the electronic properties. For complex **1** a significant change was observed neither in

the region of charge transfers of 300 – 600 nm (46 equivalents of NaCN) nor in the region of the d-d transitions of 450 – 1000 nm (7 equivalents of NaCN). It is possible that the number of equivalents was too small. In CHCl₃ and in *n*-hexane complex **1** showed very similar maxima with absorption bands at 337, 374, and 541 nm in *n*-hexane in comparison to 339, 384, and 540 nm in CHCl₃. Nevertheless, small changes in intensity are visible for **2** at 337 and 373 nm corresponding to a charge transfer process. Compared to **2** in CHCl₃ the absorption bands are around the same wavelength (339 and 384 nm). In the region of the d-d transition processes **2** behaves different with NaCN than with pyridine. Instead of a constant decrease of the intensity at 515 nm with pyridine the intensity of the shoulder starts to increase at around 493 nm and to decrease at around 572 nm with NaCN.

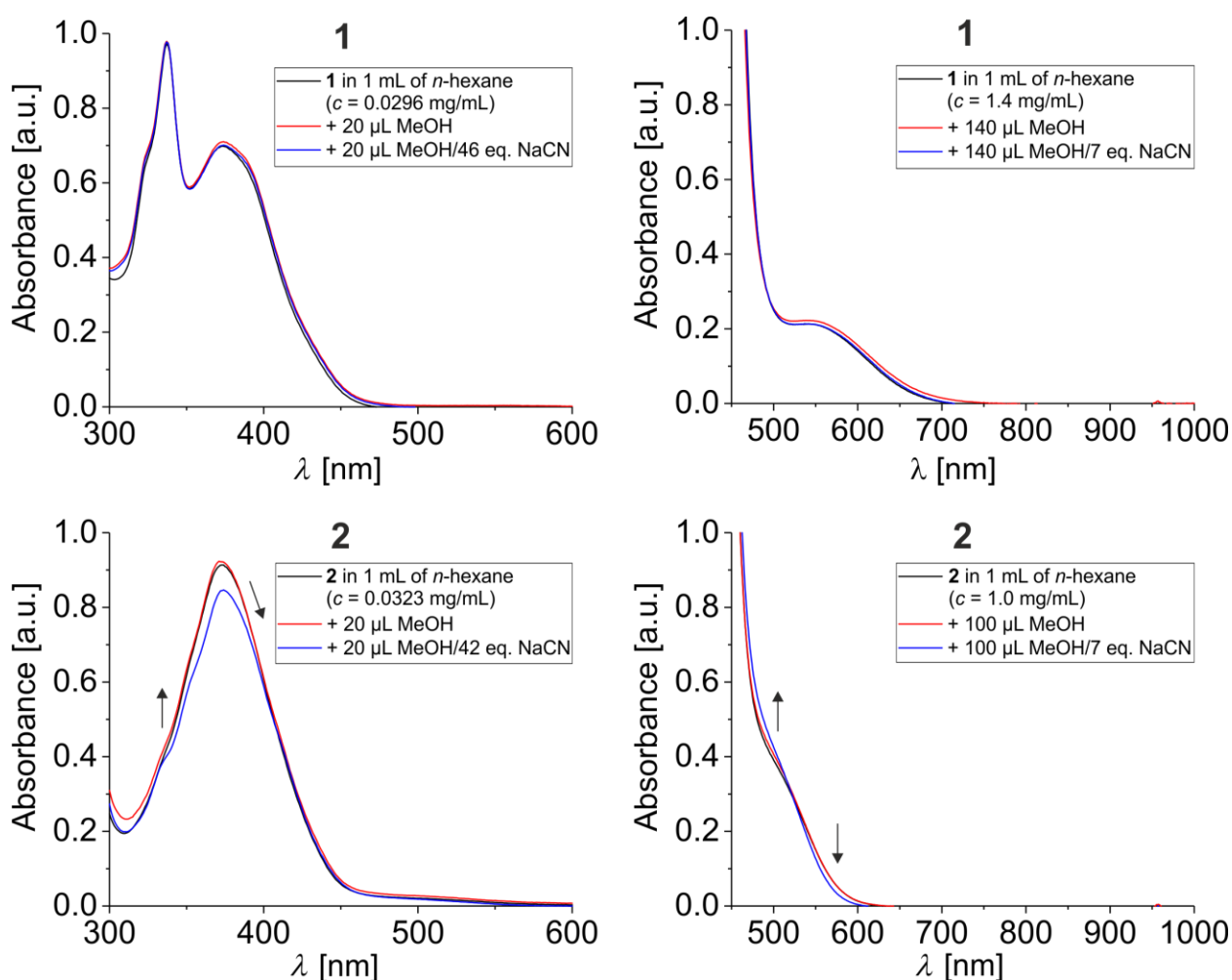


Figure 8: UV-Vis absorption spectra of compounds **1** and **2** in the range of 300 – 600 nm and 450 – 1000 nm in *n*-hexane and with the addition of pure MeOH or a MeOH/NaCN solution. To better identify charge transfers and π π^* transitions two measurement sets with different concentrations (left and right) were done. The arrows show the change of absorption in relation to the addition of different equivalents of NaCN.

Table 3: Obtained data of the UV-Vis measurements in CHCl₃;pyridine and *n*-hexane;MeOH/NaCN: Concentrations *c*, maximum absorption wavelengths λ_{abs} , and the molar attenuation coefficients ϵ of **1** and **2**.

Compound	$c(300 - 600 \text{ nm}) = 2.45 \cdot 10^{-5} \text{ mmol mL}^{-1}$			$c(450 - 1000 \text{ nm}) = 1.16 \cdot 10^{-3} \text{ mmol mL}^{-1}$		
1	$\lambda_{\text{abs.}}$	$\epsilon(\text{CHCl}_3)$	$\epsilon(\text{py})$	$\lambda_{\text{abs.}}$	$\epsilon(\text{CHCl}_3)$	$\epsilon(\text{py})$
	[nm]	[Lmol ⁻¹ cm ⁻¹]	[Lmol ⁻¹ cm ⁻¹]	[nm]	[Lmol ⁻¹ cm ⁻¹]	[Lmol ⁻¹ cm ⁻¹]
	339	31429	40204	540	248	166
	384	23633	31306	586	194	181
	$\lambda_{\text{abs.}}$	$\epsilon(n\text{-hexane})$	$\epsilon(\text{MeOH/NaCN})$	$\lambda_{\text{abs.}}$	$\epsilon(n\text{-hexane})$	$\epsilon(\text{MeOH/NaCN})$
	[nm]	[Lmol ⁻¹ cm ⁻¹]	[Lmol ⁻¹ cm ⁻¹]	[nm]	[Lmol ⁻¹ cm ⁻¹]	[Lmol ⁻¹ cm ⁻¹]
337	39975	39975	541	184	184	
374	28480	28480	-	-	-	
	$c(300 - 600 \text{ nm}) = 2.68 \cdot 10^{-5} \text{ mmol mL}^{-1}$			$c(450 - 1000 \text{ nm}) = 8.29 \cdot 10^{-4} \text{ mmol mL}^{-1}$		
2	$\lambda_{\text{abs.}}$	$\epsilon(\text{CHCl}_3)$	$\epsilon(\text{py})$	$\lambda_{\text{abs.}}$	$\epsilon(\text{CHCl}_3)$	$\epsilon(\text{py})$
	[nm]	[Lmol ⁻¹ cm ⁻¹]	[Lmol ⁻¹ cm ⁻¹]	[nm]	[Lmol ⁻¹ cm ⁻¹]	[Lmol ⁻¹ cm ⁻¹]
	341	15597	23060	515	542	182
	375	33470	22836	766	1	40
	388	29776	23731	814	1	36
	$\lambda_{\text{abs.}}$	$\epsilon(n\text{-hexane})$	$\epsilon(\text{MeOH/NaCN})$	$\lambda_{\text{abs.}}$	$\epsilon(n\text{-hexane})$	$\epsilon(\text{MeOH/NaCN})$
[nm]	[Lmol ⁻¹ cm ⁻¹]	[Lmol ⁻¹ cm ⁻¹]	[nm]	[Lmol ⁻¹ cm ⁻¹]	[Lmol ⁻¹ cm ⁻¹]	
337	15724	14971	493	509	563	
373	34094	31594	572	75	49	

8.4.5 Magnetic properties

Magnetic measurements were done for **1** and **2** which are presented in **Figure 9**. The samples were heated from 200 K to 400 K, cooled to 50 K and again heated up to 400 K. In the case of **1**, centering of the sample in the SQUID magnetometer was difficult as neither a clear diamagnetic nor paramagnetic signal was obtained. This appeared to be a similar problem as in literature.^[15] Consequently, the calibration standard K₃[Fe(CN)₆] was added in the measurement of **1** to always ensure a paramagnetic signal which is better traceable by the magnetometer. The additional magnetisation of the calibration standard was corrected afterwards. The measured $\chi_M T$ and μ_{eff} values of **1** were 0.36 cm³Kmol⁻¹/1.69 at 50 K and 0.42 cm³Kmol⁻¹/1.84 at 300 K. These values agree with the theoretical value of $\mu_{\text{so}} = 1.73$ for one unpaired electron. The magnetic measurement of **2** showed a diamagnetic signal over the complete temperature range. The $\chi_M T$ and μ_{eff} values at 50 K and at 300 K were 0.01 cm³Kmol⁻¹ and 0.28.

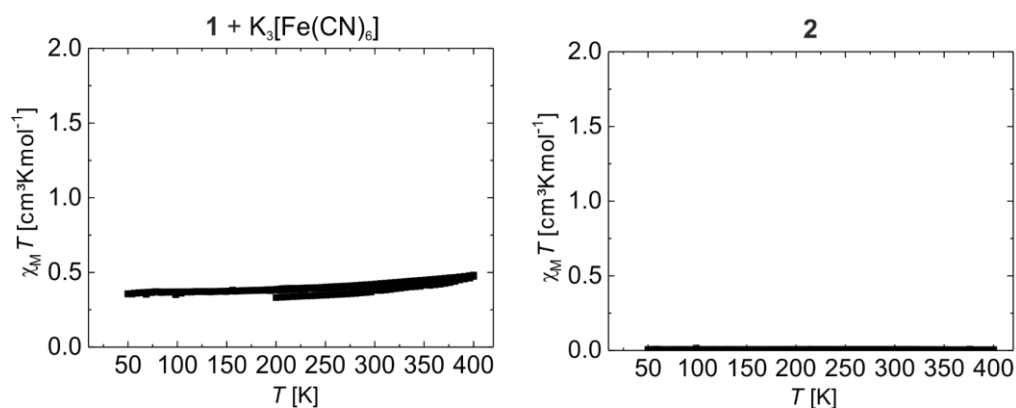


Figure 9: Magnetic measurement of **1** (left) and **2** (right). **1** was measured with $K_3[Fe(CN)_6]$ as a calibration standard. The temperature sequence was 200 to 400 to 50 to 400 K.

8.4.6 TGA and DSC measurements

1 and **2** were characterised using TGA and DSC. The TGA measurements showed first indications of decomposition for **1** and **2** at approximately 568 K and 539 K, respectively (**Figure 10**). Consequently, both samples were never heated above those temperatures during any other measurements.

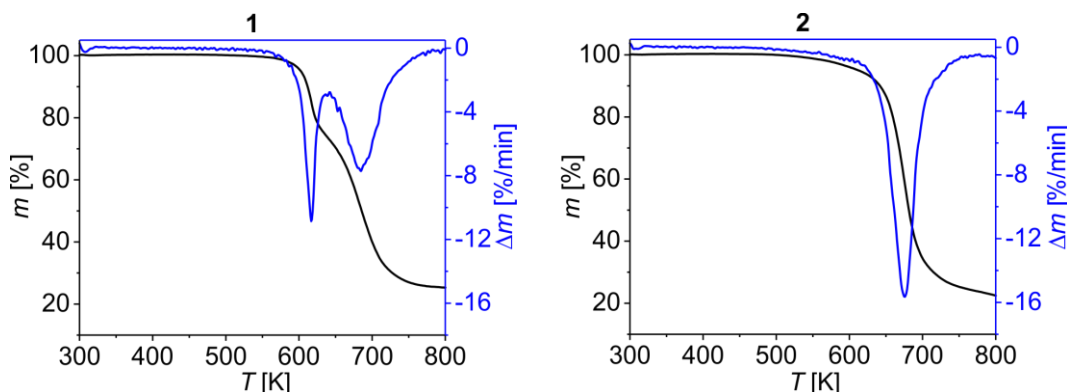


Figure 10: TGA measurements of samples **1** and **2**.

The DSC measurements of **1** and **2** are shown in **Figure 11**. Due to the slow scan rate of 1 K/min the measurement curves are sloped. Therefore, a manual baseline correction was applied before the peaks were picked. Faster scan rates lead to a blurring of the peaks in the background. The measurements should be repeated on a DSC device which can measure with slower scan rates to reduce the sloping effect.

The samples run twice through a cooling-heating cycle in the temperature range of 193 K to 473 K. During the first heating **1** and **2** showed a peak at 228 K and 232 K/242 K, respectively, in the range of about 50 K, which originated most likely from a solid-solid phase transition. Further heating resulted in a very broad signal for both. For **1** it started at 336 K and ended at 421 K, whereas for **2** the signal was in the range of 354 K to roughly 367 K. In this region the sample

underwent melting processes which was also observed in the POM measurements that are discussed in the next part. When the samples were cooled down **1** and **2** showed more than one crystallisation process in the range of approximately 397 K to 355 K and 389 K to 366 K, respectively. At lower temperatures both samples showed one signal at 229 K or 231 K corresponding to the solid-solid phase transition in the heating mode. In addition to that, a very sharp signal at 203 K and 202 K was observed.

In the second cycle the peaks of the solid-solid phase transition in the heating mode became better defined and at least two different phase transitions could be observed for each sample at 226 K and 238 K for **1** and 231 K and 241 K for **2**. Further heating did not result in a very broad signal as during the first heating. Nevertheless, weaker signals for **1** and **2** were found at around 393 K, 410 K, and 418 K and at 378 K and 461 K, respectively. During the second cooling the crystallisation processes were also better defined and found at 403 K and 388 K for **1** and 426 K and 375 K for **2**.

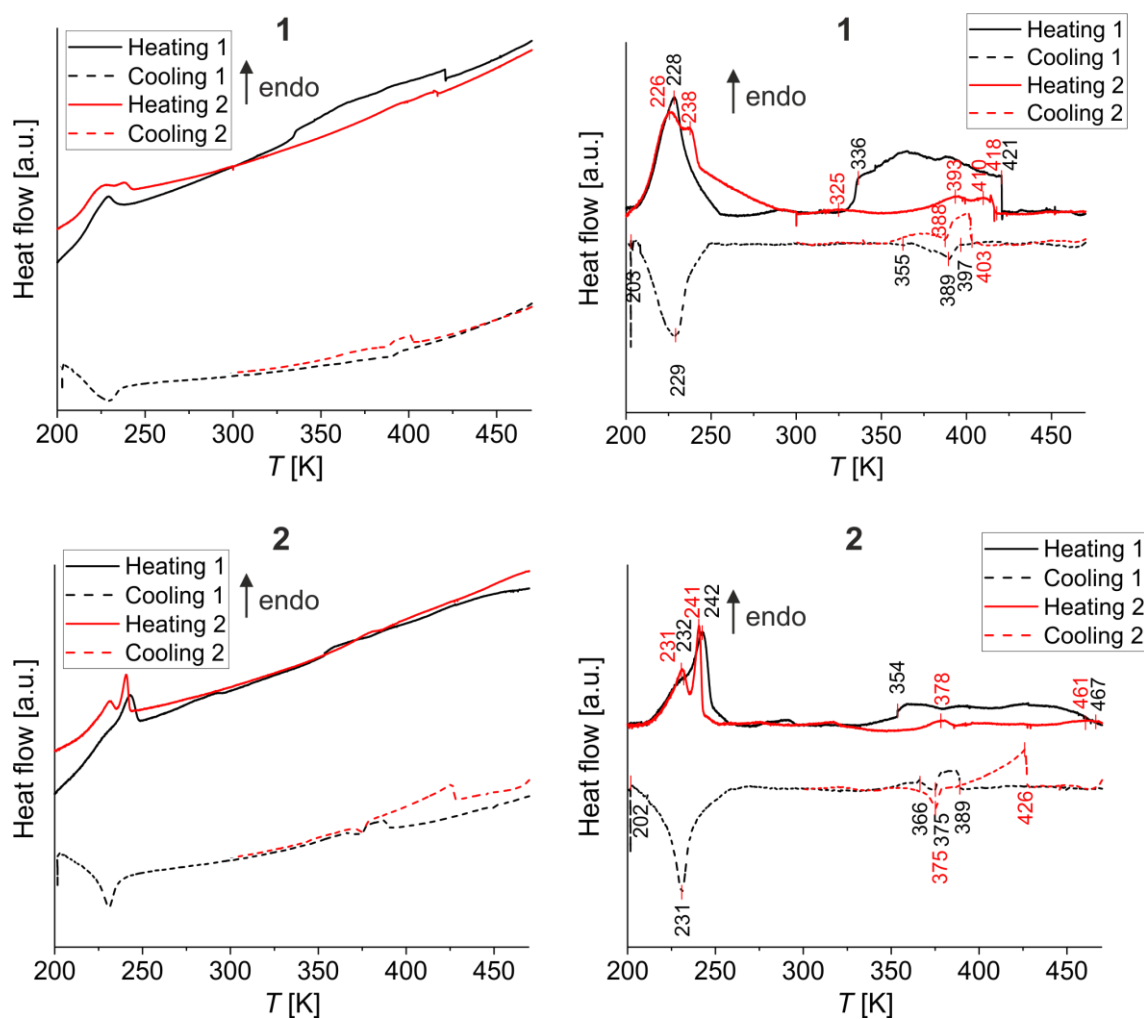


Figure 11: DSC measurements of samples **1** and **2**. Left: uncorrected graphs as obtained from the measurement. Right: DSC graphs with applied baseline correction.

8.4.7 Polarised optical microscopy

The phase transition behaviour of **1** and **2** was additionally characterised by polarised optical microscopy (POM) with a scan rate of 2 K/min in the temperature range between room temperature and 415 K for **1** and 381 K for **2**, respectively. A retardation plate (first order) was used for some images to better observe the recrystallisation process. POM micrographs of the Cu(II) complex **1** are shown in **Figure 12**. **Figure 12A - Figure 12C** show the melting of the birefringent samples during the heating process. At 294 K (**Figure 12A**) **1** was a wax-like, inhomogeneous compound. Heating resulted in a slow melting process over a broad temperature range (**Figure 12B**) starting from around 358 K until the sample was completely molten at 411 K (**Figure 12C**). The DSC measurement showed a different temperature range of the melting process of 336 K to 421 K (**Figure 11**). A reason for this could be that kinetic effects, such as the different scan rates used in both measurements, have an influence on the properties of complex **1**. Additionally, it is also possible that the small window of the POM oculus did not give a sufficiently accurate view of the state of the sample. When **1** was cooled down the first signs of crystallisation appeared at 400 K (**Figure 12D**) which is in agreement with a signal at 403 K during the second cooling process in the DSC measurement. At 391 K (**Figure 12E**) the appearance of two different kinds of structures can be observed. One having a well-defined six-armed star form and the other one having fan-like form with birefringent properties. Cooling further down (**Figure 12F**) lead to more crystal growth and also to a partial conversion from the six-armed crystals to the birefringent phase. At 381 K (**Figure 12G**) nearly all crystals changed to the birefringent state, some conserving their six-armed star form. Interestingly, at this point there were still areas which remained in the liquid state until the temperature came close to room temperature. At 304 K (**Figure 12H**) **1** turned completely solid and only the birefringent phase can be observed. Some structures still resemble grown together six-armed stars while there are also spherulitic structures which are characteristic for a liquid crystalline phase. Afterwards, shear stress was applied to the sample (**Figure 12I**). Consequently, the soft crystals deformed and then resembled strongly the freshly prepared compound as shown in **Figure 12A**.

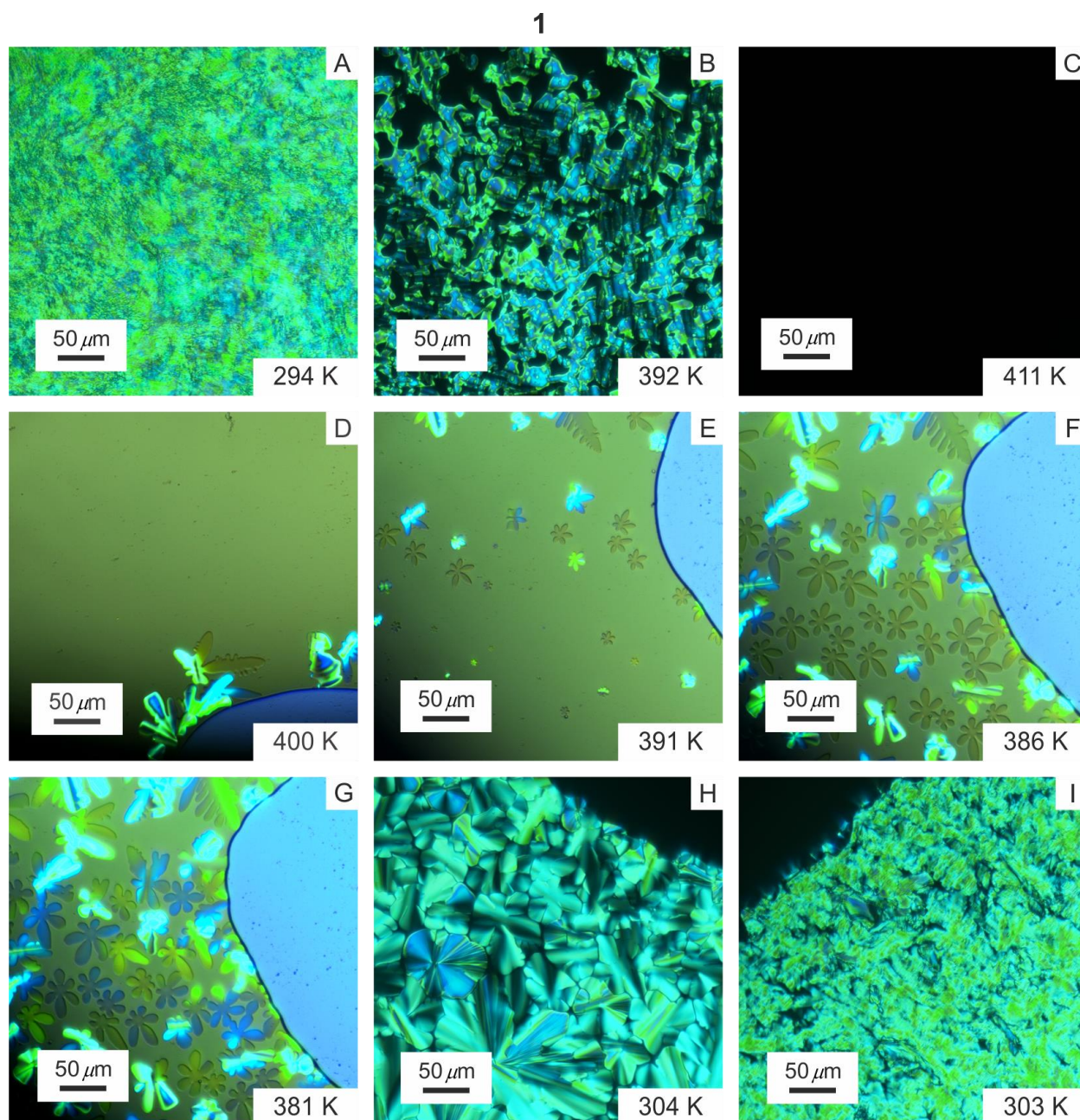


Figure 12: POM micrographs of **1**. All images were taken under cross polarised light at the indicated temperature. A retardation plate was used for some micrographs to better observe the crystallisation process. The melting of the sample during the heating process is shown in images A – C without retardation plate. The crystallisation during the cooling process is shown in images D – G with retardation plate and in image H without retardation plate. Image I shows the soft crystals after shear stress was applied without retardation plate.

The POM micrographs of the Ni(II) complex **2** are shown in **Figure 13**. In **Figure 13A** the pristine sample can be seen which looks very similar to **1** at room temperature. During the heating process the sample started to flow slowly at around 336 K and started to melt at 353 K. This agrees with the data obtained in the DSC measurement, where a signal can be observed at 354 K (**Figure 11**). The melting process was faster than for **2** and took until 378 K (**Figure 13C** and **Figure 13D**). Cooling down leads to a crystallisation process which starts at 374 K (**Figure 13E**). The formation

of different sizes of birefringent structures can be observed until 353 K (**Figure 13F** – **Figure 13G**) where most of the sample solidified. In **Figure 13H** the texture shows spherulites which can be attributed to a liquid crystalline phase. The spherulitic structures of **Figure 13H** are magnified in **Figure 13I**. In comparison to **1** the spherulites of **2** are better defined which can originate from **2** possessing only one type of crystals during the cooling process.

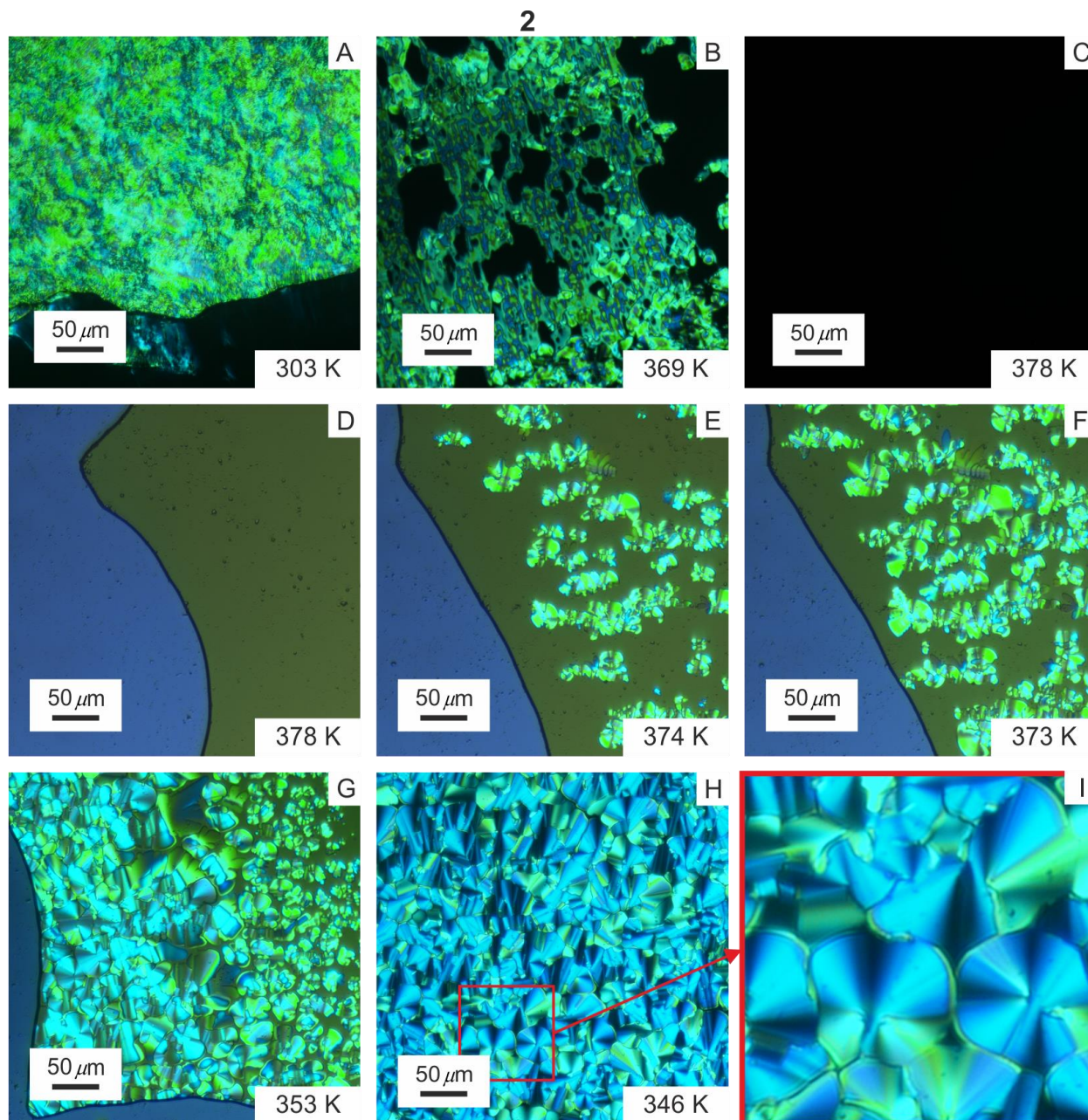


Figure 13: POM micrographs of **2**. All images were taken under cross polarised light at the indicated temperature. A retardation plate was used for some micrographs to better observe the crystallisation process. The melting of the sample during the heating process is shown in images A – C without retardation plate. The crystallisation during the cooling process is shown in images D – G with retardation plate and in image H without retardation plate. Image I shows a magnification of spherulitic structures of image H.

8.4.8 PXRD patterns

PXRD measurements were done of **1** and **2** in the region of 1.5° to 30.0° 2θ at different temperatures which were based on the DSC and the POM measurements. Sections of the powder patterns of both complexes are split in the heating (**1** is shown in **Figure 14** and **2** is shown in **Figure 16**) and the cooling (**1** is shown in **Figure 15** and **2** is shown in **Figure 17**) mode for clarity. The complete patterns are shown in the Supporting Information in **Figure S4** to **Figure S7**. Interestingly, both complexes show powder patterns with only five signals over the whole temperature range. The obtained 2θ values were calculated to distances in the crystal packing based on the *Bragg's law*. The obtained and the calculated data is shown in **Table 4**.

During the heating mode all the distances in the structure of **1** increase and decrease during the cooling mode (**Figure 14** and **Figure 15**). This occurs most probably due to *Brownian motion*. For an unknown reason a line broadening is observed for the low temperatures at 193 K and 206 K in the range of 1.5° to 8.0° 2θ which is contrary to the expectations. Although strong signals were observed in the DSC measurements around 230 K only slight shifts were observed in the powder patterns of different temperatures. No PXRD measurements could be carried out of the melt as the measurement device was not able to heat up to 411 K.

In the powder pattern complex **2** behaved very similar as complex **1** (**Figure 16** and **Figure 17**). However, at 193 K and 260 K one additional signal at around 3° 2θ was observed, while a noticeable change of the powder pattern, as expected from the DSC measurements, is again not occurring. During the heating mode the distances in the range of 1.5° to 8.0° 2θ decrease from 193 K to 300 K and increase until 386 K. In the melt at 386 K a strong line broadening occurs and only three of the five signals can be found. Nevertheless, this showed that the melt still possessed order. In the cooling mode the changes of the distance occur in reverse to the heating mode. Yet, no second signal around 3° 2θ appears at 193 K. A reason for this could be a kinetic effect resulting from a difference of cooling directly from room temperature down to 193 K and cooling stepwise with measurement points in between.

The signals at 3.86° 2θ (22.9 Å) for **1** and 3.84° 2θ (23.0 Å) for **2** are of special interest. In literature similar complexes with long alkyl chains were studied.^[15] These complexes formed lipid layer-like structures, where the alkyl chains ordered straight in one direction and it was shown that the signals belonged to the metal-metal distance from one layer to the next one. A complex with a C16 alkyl chain showed distances of 2.75° 2θ (32 Å). For complex **1** and **2** the longest straight alkyl chains are a C17 chains which should be in a similar range. However, the calculated distances are much smaller and fit better to C12 alkyl chains or shorter ones. This could be a consequence

of either no formation of the lipid-like arrangements or of no ordering of the alkyl chains in a straight line. The signals at $18.71^\circ 2\theta$ (4.7 Å) for **1** and $19.17^\circ 2\theta$ (4.6 Å) for **2** could belong to van der Waals interactions (around 4.2 Å). The crystal data of a similar system with the same head group and a Ni(II) centre was studied in literature.^[19] The data showed that the distances between centroids containing the Ni(II) centre are of around 3.3 Å. This fits very well with the distances found for **1** at $27.17^\circ 2\theta$ (3.3 Å) and for **2** at $26.94^\circ 2\theta$ (3.3 Å) and could indicate a stacking of the head groups.

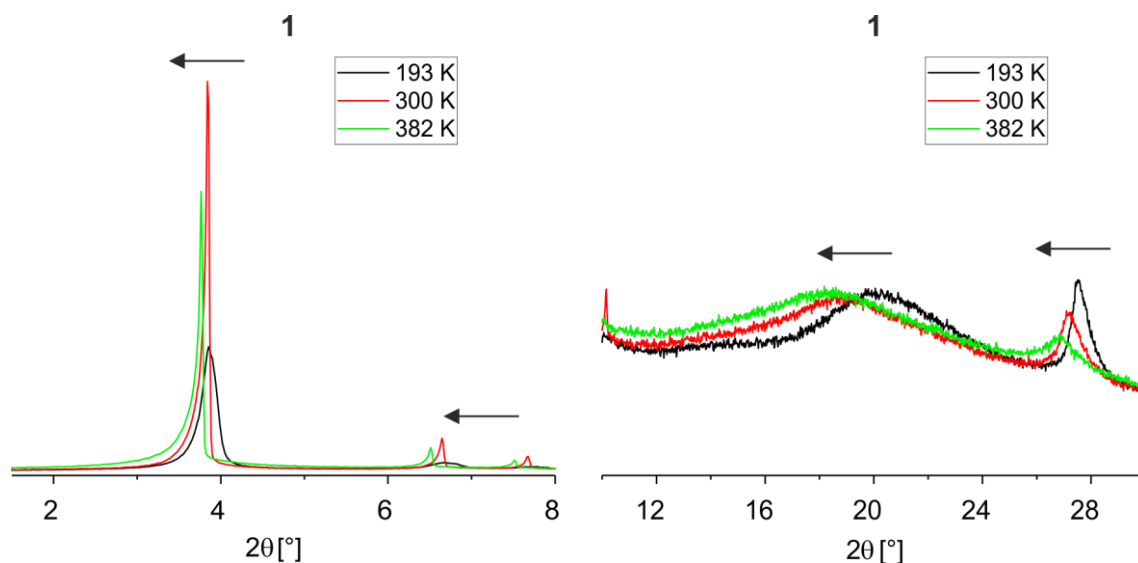


Figure 14: Temperature dependent PXRD patterns of **1** in the range of 1.5° to $8.0^\circ 2\theta$ (left) and 10.0° to $30.0^\circ 2\theta$ (right) during the heating mode. The arrows show the trend in relation to the temperature. The complete data is shown in the Supporting Information in **Figure S4**.

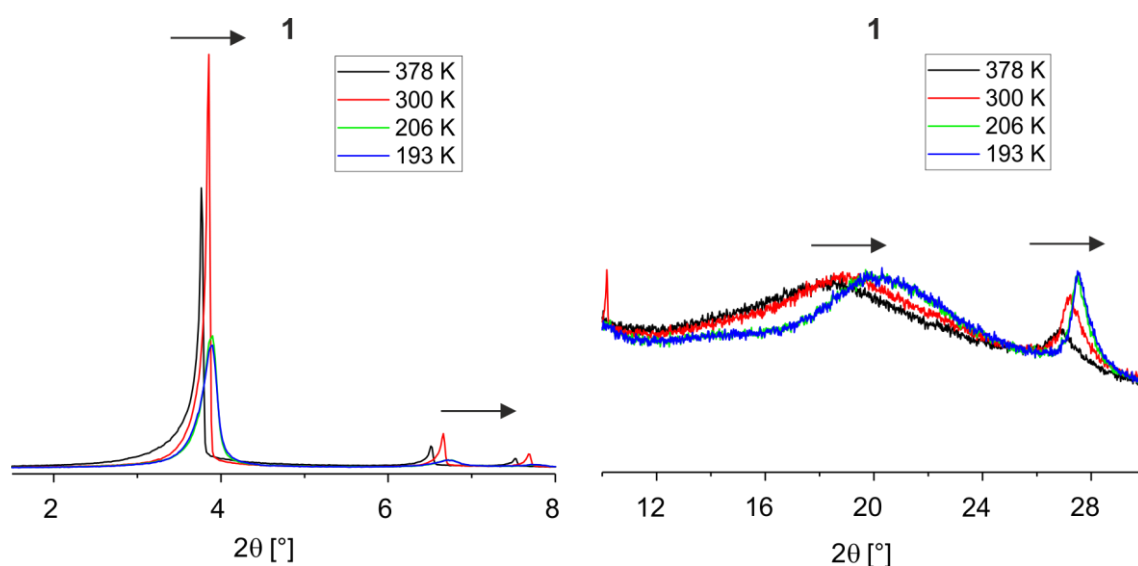


Figure 15: Temperature dependent PXRD patterns of **1** in the range of 1.5° to $8.0^\circ 2\theta$ (left) and 10.0° to $30.0^\circ 2\theta$ (right) during the cooling mode. The arrows show the trend in relation to the temperature. The complete data is shown in the Supporting Information in **Figure S5**.

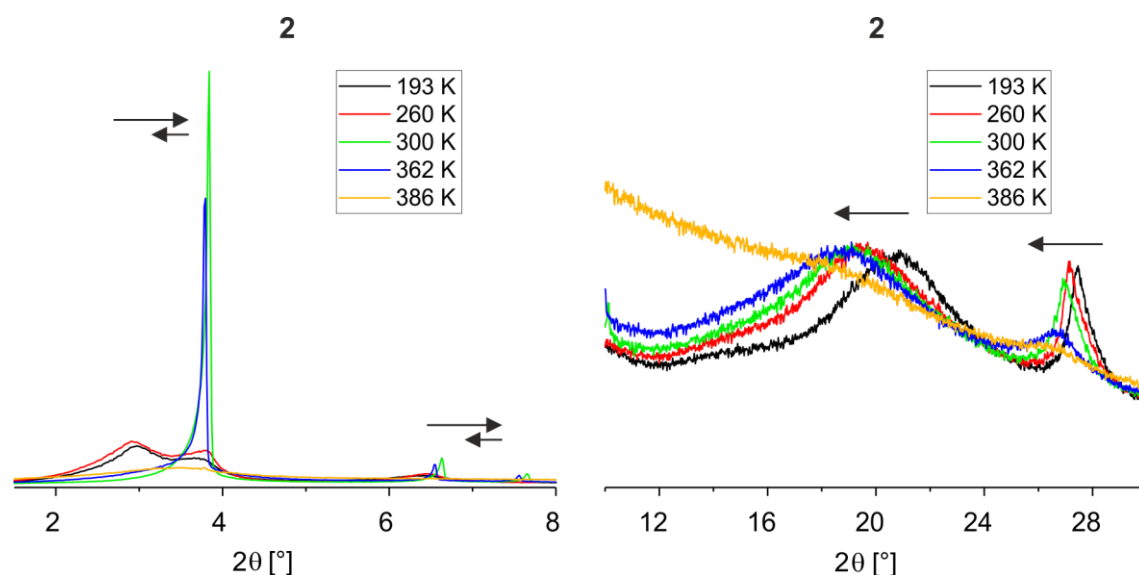


Figure 16: Temperature dependent PXRD patterns of **2** in the range of 1.5° to 8.0° 2θ (left) and 10.0° to 30.0° 2θ (right) during the heating mode. The arrows show the trend in relation to the temperature. The complete data is shown in the Supporting Information in **Figure S6**.

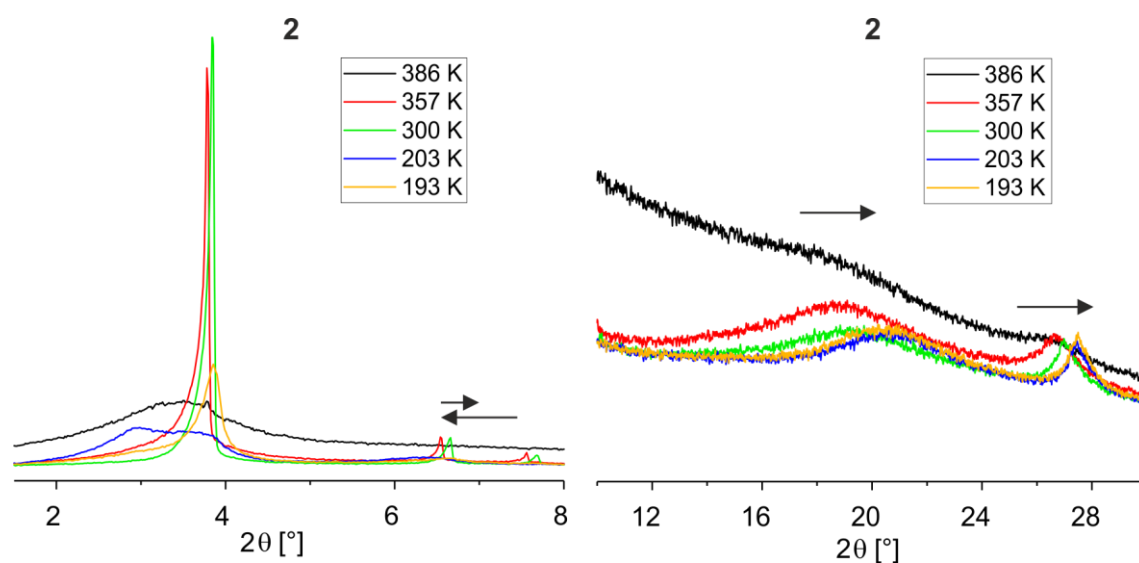


Figure 17: Temperature dependent PXRD patterns of **2** in the range of 1.5° to 8.0° 2θ (left) and 10.0° to 30.0° 2θ (right) during the cooling mode. The arrows show the trend in relation to the temperature. The complete data is shown in the Supporting Information in **Figure S7**.

Table 4: Data of the PXRD measurements at 300 K and the calculated distances of **1** and **2**.

Compound	Unit	Signal 1	Signal 2	Signal 3	Signal 4	Signal 5
1	2θ [°]	3.86	6.65	7.67	18.71	27.17
	Distance [Å]	22.9	13.3	11.5	4.7	3.3
2	2θ [°]	3.84	6.63	7.65	19.17	26.94
	Distance [Å]	23.0	13.3	11.5	4.6	3.3

8.4.9 SEM measurements

Additionally, the surface of **1** and **2** was investigated using scanning electron microscopy (SEM) as shown in **Figure 18** and **Figure 19**, respectively. The wax-like properties can be noticed in **Figure 18A**, **Figure 19A**, and **Figure 19B** of the samples of **1** and **2**. Zooming in showed a smooth surface for **1** (**Figure 18B** and **Figure 18C**) and a wrinkled surface for **2** (**Figure 19C**). After annealing at 423 K both complexes melted and were measured again. During the annealing process they spread to a thin film and obtained a very smooth surface as shown in **Figure 18D** and **Figure 18E** for **1** and **Figure 19D** and **Figure 19E** for **2**. Atomic force microscopy (AFM) is needed to further investigate the roughness of the surface and will be done in future work.

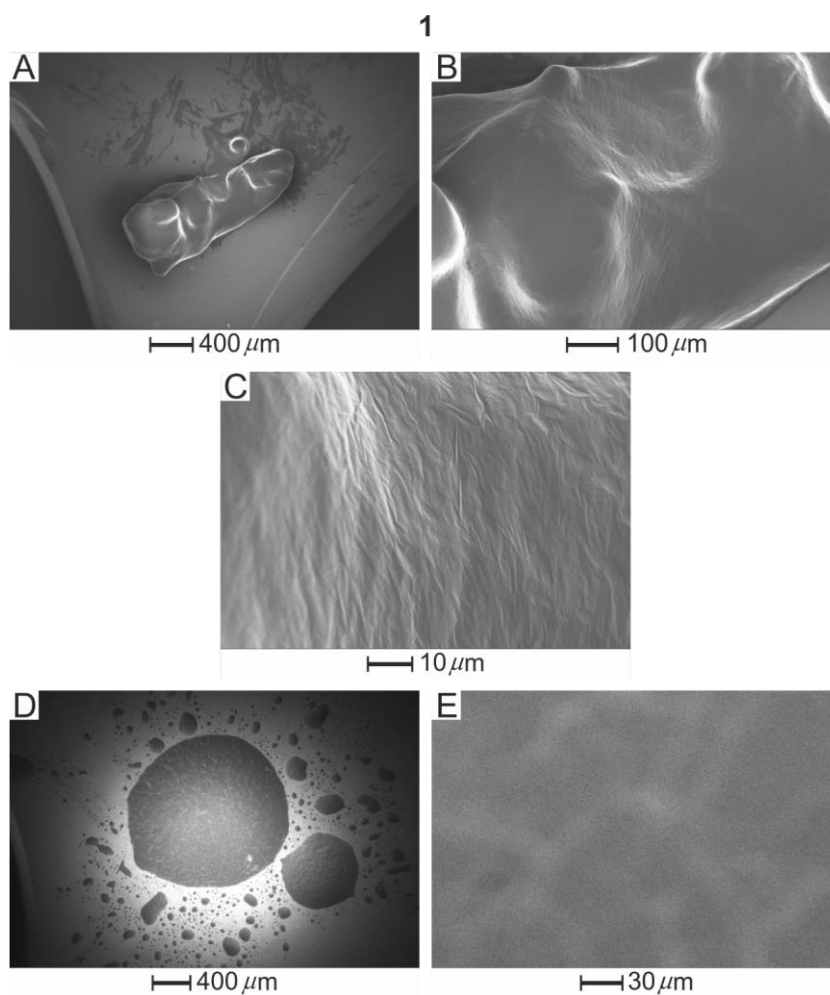


Figure 18: SEM measurement of **1**. Images A, B, and C before the melting process at 423 K, images D and E after the melting process.

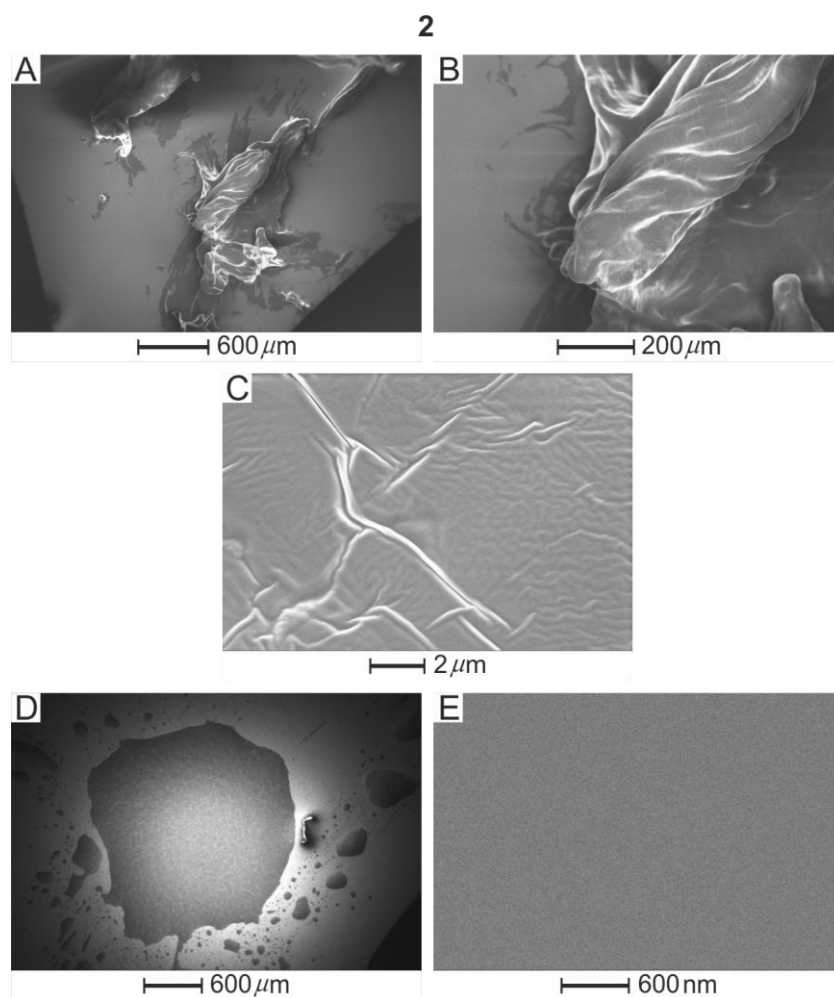


Figure 19: SEM measurement of **2**. Images A, B, and C before the melting process at 423 K, images D and E after the melting process.

8.5 Conclusion

In this work, we presented the synthesis of a new Schiff base-like ligand with long, branched alkyl chains and the corresponding Cu(II) (**1**) and Ni(II) (**2**) complexes. Small amounts of ligand were found in the $^1\text{H-NMR}$ of **2**. Therefore, the synthesis should be improved by increasing the amount of eq. of $\text{M}(\text{OAc})_2$ and extending the reaction time. Both complexes showed unique behaviour in solution by forming inverse micelles in *n*-hexane in the presence of MeOH and NaCN. This was confirmed with DLS and TEM measurements. Further tests with other solvents, *e.g.* toluene or ethyl acetate, have to be carried out in the next step to find better parameter for the formation of monodisperse micelles. **2** exhibited a CISSS as shown with $^1\text{H-NMR}$ and UV-Vis studies. The characterisation of the CISSS properties, where NaCN was used, could benefit from test with other solvents, as well. In the solid state **1** and **2** showed in the DSC measurement wide temperature ranges where phase transitions occurred which was supported by POM. Here, some of the phases were identified as a liquid crystalline phase with the occurrence of spherulites. However, the DSC

measurements were sloped and therefore difficult to interpret. The measurements should be repeated with a better DSC device which can measure more accurately with slower scan rates. Characterisation by SQUID magnetometry showed paramagnetic properties for **1** and diamagnetic properties for **2** over the whole temperature range as expected. Temperature dependent PXRD measurements showed weak changes in the powder pattern for **1** and stronger changes for **2**. The longest observed distances were unusually short for systems with C17 alkyl chains as longest chains and would fit better to alkyl chains with C12 chains or shorter chains. The wax-like properties of both complexes were further studied by SEM before and after annealing. The formation of smooth, thin films was observed. Nevertheless, the roughness has to be determined in more detail by AFM measurements in future studies. As the melting procedure is a very facile approach for the preparation of thin films these properties can be beneficial for the application of functional materials in surface coating.

8.6 Experimental Part

Infrared Spectroscopy: Transmission infrared spectra were collected using a PerkinElmer Spectrum 100 FT-IR (ATR). The samples were measured as solids or oils.

Elemental Analysis: Carbon, hydrogen and nitrogen contents were measured using a Vario EL III. The samples were prepared in tin boats. All samples were measured at least twice, and the average was used. Acetanilide (Merck) was used as standard.

Mass Spectrometry: Mass spectra were recorded with a MS8500 sector field mass spectrometer from Thermo Finnigan. Direct injection was used and the measurement was done in a temperature range of room temperature to 330 °C.

Nuclear Magnetic Resonance Spectroscopy: The NMR spectra were recorded with a Varian Unity Inova 300 spectrometer from Agilent Technologies at 300 MHz. The samples were dissolved in CDCl₃ or pyridine-d₅ as indicated and their signals were calibrated to the residual signals of the solvent. A Bruker Avance III HD spectrometer at 500 MHz was also used for some samples when indicated.

Magnetic Measurements: Magnetic measurements were done on a SQUID MPMS-XL5 instrument from Quantum Design. Gelatine capsules in a plastic straw were used for sample preparation. K₃[Fe(CN)₆] was added as a paramagnetic standard for one measurement of compound **1** as indicated in the main text to bypass centre problems. The diamagnetic parts of the sample holder, the organic ligand, and additional paramagnetic parts of the standard (if used) were corrected afterwards by using Pascal's constants (ligand)^[21] or measured values (sample holder, standard).

Thermogravimetric Analysis: Thermogravimetric analysis was done with a Netzsch TG 209 F1 Libra under nitrogen atmosphere using 4 mg – 10 mg of the sample with a heating rate of 10 K min⁻¹.

Differential Scanning Calorimetry: The samples were measured with a Mettler Toledo DSC 2 Star System calorimeter under nitrogen atmosphere (50 mL min⁻¹). 17.51 mg of **1** and 9.71 mg of **2** were prepared in an aluminium boat (0.04 mL) and the heat rate was set to 1 K min⁻¹.

Polarized Optical Microscopy: The micrographs were taken on a Nikon DIAPHOT 300 microscope using a Nikon DS-Ri2 digital camera and NIS-Elements F 4.60 software. For temperature control a Mettler Toledo HS82 Hot Stage with a HS1 Hot Stage Controller was used. The samples were prepared between two glass plates (Menzel-Gläser) from Thermo Scientific.

UV-Vis spectroscopy: UV-Vis measurements were done on a Cary 60 UV-Vis from Agilent Technologies with a Cary WinUV Scan Application 5.0 software. High precision cells made of high performance quartz glass with a 10 mm light path from Hellma Analytics were used for the measurement.

Dynamic Light Scattering: DLS measurements were done on a Particle Analyzer Litesizer 500 and a Kalliope Professional 1.8.4 software from Anton Paar. High precision cells made of high performance quartz glass with a 10 mm light path from Hellma Analytics were used for the measurement.

Transmission Electron Microscopy: Transmission electron microscopy was carried out at a Zeiss CEM902 electron microscope (Zeiss, Oberkochen, Germany). The complex was dissolved in *n*-hexane and either nothing, MeOH or MeOH/NaCN was added. The solutions were then dropped on a copper grid (mesh 200, Science Services, Munich). Electron acceleration voltage was set to 80 kV. Micrographs were taken with a MegaView III / iTEM image acquiring and processing system from Olympus Soft Imaging Systems (OSIS, Münster, Germany) and an Orius 830 SC200W / DigitalMicrograph system from Gatan (Munich, Germany). The micelle sizes in the micrographs were evaluated with “ImageJ” image processing software by Wayne Rasband (National Institutes of Health, USA).

Scanning Electron Microscopy: Scanning electron microscopy images were taken with a Zeiss Ultra Plus SEM. The samples were prepared on a silica wafer.

Powder X-ray Diffraction: The wax-like complexes were melted for the sample preparation and absorbed into glass capillaries of which both sides were sealed with a lighter afterwards. Temperature dependent PXRD measurements were done on a STOE Stadi P diffractometer in transmission geometry with Cu-*K*_α radiation.

General: 11-(4-bromobutyl)tricosane^[8] and methoxymethylenemethylacetoacetate^[22] were reproduced as reported in literature. The syntheses of **C** and **H₂L** were carried out under an argon atmosphere (argon 5.0) using Schlenk tube techniques. The solvents were purified as described in the literature^[23] and distilled under an atmosphere of argon or saturated with argon over one hour. Cu(ac)₂·H₂O and Ni(ac)₂·4xH₂O are commercial products (Fluka) and were used as received.

1,2-bis((5-decylheptadecyl)oxy)benzene (A): 1,2-dihydroxybenzene (3.27 g, 29.70 mmol) was mixed with K₂CO₃ (10.25 g, 74.17 mmol, 2.5 eq.) in DMF (320 mL) and stirred for 90 min at room temperature. 11-(4-bromobutyl)tricosane (30.34 g, 66.03 mmol, 2.2 eq.) was added and it was heated to 100 °C for 43 h. The mixture was extracted with hexane, dried over Na₂SO₄ and the solvent was removed under vacuum. The oil was purified by column chromatography over silica gel with hexane:DCM (4:1) to give 7.52 g (29%) of colourless oil. C₆₀H₁₁₄O₂ (867.57): calc. C 83.07, H 13.25, N 0.00; found C 82.75, H 13.21, N 0.23. MS (DEI+): *m/z* (%) = 867 (100) [M]⁺, 489 (17), 110 (51). ¹H-NMR (300 MHz, CDCl₃, 296 K): δ = 0.88 (t, *J* = 7.2 Hz, 12 H, CH₃), 1.15-1.36 (m, 86 H, CH₂, CH), 1.43 (m, 4 H, CH₂), 1.79 (quintet, *J* = 7.2 Hz, 4 H, CH₂), 3.99 (t, *J* = 6.6 Hz, 4 H, CH₂O), 6.89 (s, 4 H, H_{ar}) ppm. ¹³C-NMR (126 MHz, CDCl₃, 296 K): δ = 14.1 (CH₃), 22.7 (CH₂), 23.1 (CH₂), 26.7 (CH₂), 29.4 (CH₂), 29.7 (CH₂), 29.8 (CH₂), 29.8 (CH₂), 29.8 (CH₂), 30.2 (CH₂), 32.0 (CH₂) 33.5 (CH₂), 33.6 (CH₂), 37.4 (CH), 69.3 (CH₂O), 114.2 (C_{ar}-H), 121.0 (C_{ar}-H), 149.3 (C_{ar}-O) ppm.

1,2-bis((5-decylheptadecyl)oxy)-4,5-dinitrobenzene (B): **A** (14.38 g, 16.58 mmol) was suspended in acetic acid (125 mL) and nitric acid (68%, 29 mL) was added dropwise. Then fuming nitric acid (>90 %, 100 mL) was added dropwise over 2 h and it was stirred for 20 h at room temperature. It was poured over ice water, extracted with hexane and dried over Na₂SO₄. The solvent was removed under vacuum to give 15.55 g (98%) of yellow oil. C₆₀H₁₁₂N₂O₆ (957.56): calc. C 75.26, H 11.79, N 2.93; found C 75.48, H 11.81, N 2.68. MS (DEI+): *m/z* (%) = 956 (17) [M]⁺, 579 (4), 379 (17), 57 (100). ¹H-NMR (300 MHz, CDCl₃, 296 K): δ = 0.88 (t, *J* = 7.2 Hz, 12 H, CH₃), 1.15-1.35 (m, 86 H, CH₂, CH), 1.44 (m, 4 H, CH₂), 1.85 (quintet, *J* = 7.0 Hz, 4 H, CH₂), 4.10 (t, *J* = 6.1 Hz, 4 H, CH₂O), 7.29 (s, 2 H, H_{ar}) ppm. ¹³C-NMR (75 MHz, CDCl₃, 296 K): δ = 14.1 (CH₃), 22.7 (CH₂), 22.9 (CH₂), 26.7 (CH₂), 29.1 (CH₂), 29.4 (CH₂), 29.7 (CH₂), 29.7 (CH₂), 29.8 (CH₂), 30.2 (CH₂), 31.9 (CH₂) 33.3 (CH₂), 33.5 (CH₂), 37.3 (CH), 70.2 (CH₂O), 107.9 (C_{ar}-H), 136.5 (C_{ar}-N), 151.8 (C_{ar}-O) ppm.

4,5-bis((5-decylheptadecyl)oxy)benzene-1,2-diamine (C): **B** (5.68 g, 5.93 mmol) and Pd/C (337 mg, 10 %) were suspended in degassed EtOH (140 mL) under argon. Hydrazine monohydrate (14 mL, 297 mmol, 50 eq.) was added dropwise and it was heated to reflux for 19 h. The Pd/C was removed by hot filtration over Celite[®] 545. The supernatant EtOH was removed with a tube and

the oil was washed with degassed H₂O (5x100 mL). It was dried under vacuum. The highly air sensitive product was directly used in the next step without further characterization.

H₂L: **C** (5.33 g, 5.93 mmol) and methoxymethylenemethylacetoacetate (2.63 g, 16.63 mmol) were suspended in MeOH (490 mL) under argon and it was heated to reflux for 23 h. The supernatant MeOH was removed by decanting and the yellow oil was dried under vacuum to give 3.68 g (54%) of product. C₇₂H₁₂₈N₂O₈·2 hexane (1322.18): calc. C 76.31, H 11.89, N 2.12; found C 76.20, H 11.63, N 2.45. MS (ESI⁺): *m/z* (%) 1171.956 (100) [M + Na]⁺, 1149.974 (20) [M]⁺. IR: $\tilde{\nu}$ = 1714 (s) (C=O), 1623 (s) (N-H), 1581 (s) (C=O) cm⁻¹. ¹H-NMR (300 MHz, CDCl₃, 296 K): δ = 0.88 (t, *J* = 6.8 Hz, 12 H, CH₃), 1.11-1.37 (m, 86 H, CH₂, CH), 1.39-1.59 (m, 4 H, CH₂), 1.81 (quintet, *J* = 7.1 Hz, 4 H, CH₂), 2.56 (s, 6 H, CH₃), 3.78 (s, 6 H, CH₃), 4.01 (t, *J* = 6.2 Hz, 4 H, CH₂O), 6.74 (s, 2 H, H_{ar}), 8.27 (d, *J* = 12.3 Hz, 2 H, CH), 12.88 (d, *J* = 12.5 Hz, 2 H, NH) ppm. ¹³C-NMR (75 MHz, CDCl₃, 296 K): δ = 14.3 (CH₃), 22.8 (CH₂), 26.2 (CH₂), 29.4 (CH₂), 29.5 (CH₂), 29.6 (CH₂), 29.8 (CH₂), 29.8 (CH₂), 29.9 (CH₂), 29.9 (CH₃), 30.4 (CH₂) 32.1 (CH₂), 51.4 (CH₃), 70.3 (CH₂O), 103.6 (C_q), 106.7 (C_{ar}-H), 125.0 (C_{ar}-N), 148.7 (C_{ar}-O), 154.3 (CH), 167.4 (O-C=O), 200.3 (C=O) ppm.

[CuL] (1): **H₂L** (297 mg, 0.26 mmol) and Cu(ac)₂·H₂O (73 mg, 0.37 mmol, 1.4 eq.) were dispersed in EtOH (11 mL) and heated to reflux for 1 h. It was filtrated, washed with MeOH (20 mL) and dried under vacuum to give 252 mg (81%) of dark, yellow wax. C₇₂H₁₂₆CuN₂O₈ (1211.35): calc. C 71.39, H 10.48, N 2.31; found C 70.92, H 10.36, N 2.31. MS (DEI-(+)): *m/z* (%) 1209 (100) [M]⁺, 831 (8) [M - C₂₇H₅₅]⁺, 452 (31) [M - 2xC₂₇H₅₅]⁺. IR: $\tilde{\nu}$ = 1707 (s) (C=O), 1604 (s) (C=O) cm⁻¹

[NiL] (2): **H₂L** (542 mg, 0.47 mmol) and Ni(ac)₂·4xH₂O (168 mg, 0.66 mmol, 1.4 eq.) were dispersed in MeOH (20 mL) and heated to reflux for 1 h 30 min. It was filtrated, washed with MeOH (2x20 mL) and dried under vacuum. The organic phase was dried under vacuum to give 541 mg (95%) of a red wax. C₇₂H₁₂₆NiN₂O₈ (1206.50): calc. C 71.68, H 10.53, N 2.32; found C 71.71, H 10.85, N 2.71. MS (DEI-(+)): *m/z* (%) 1204 (100) [M]⁺, 826 (8) [M - C₂₇H₅₅]⁺, 447 (42) [M - 2xC₂₇H₅₅]⁺. IR: $\tilde{\nu}$ = 1703 (s) (C=O), 1604 (s) (C=O) cm⁻¹

8.7 Supporting Information

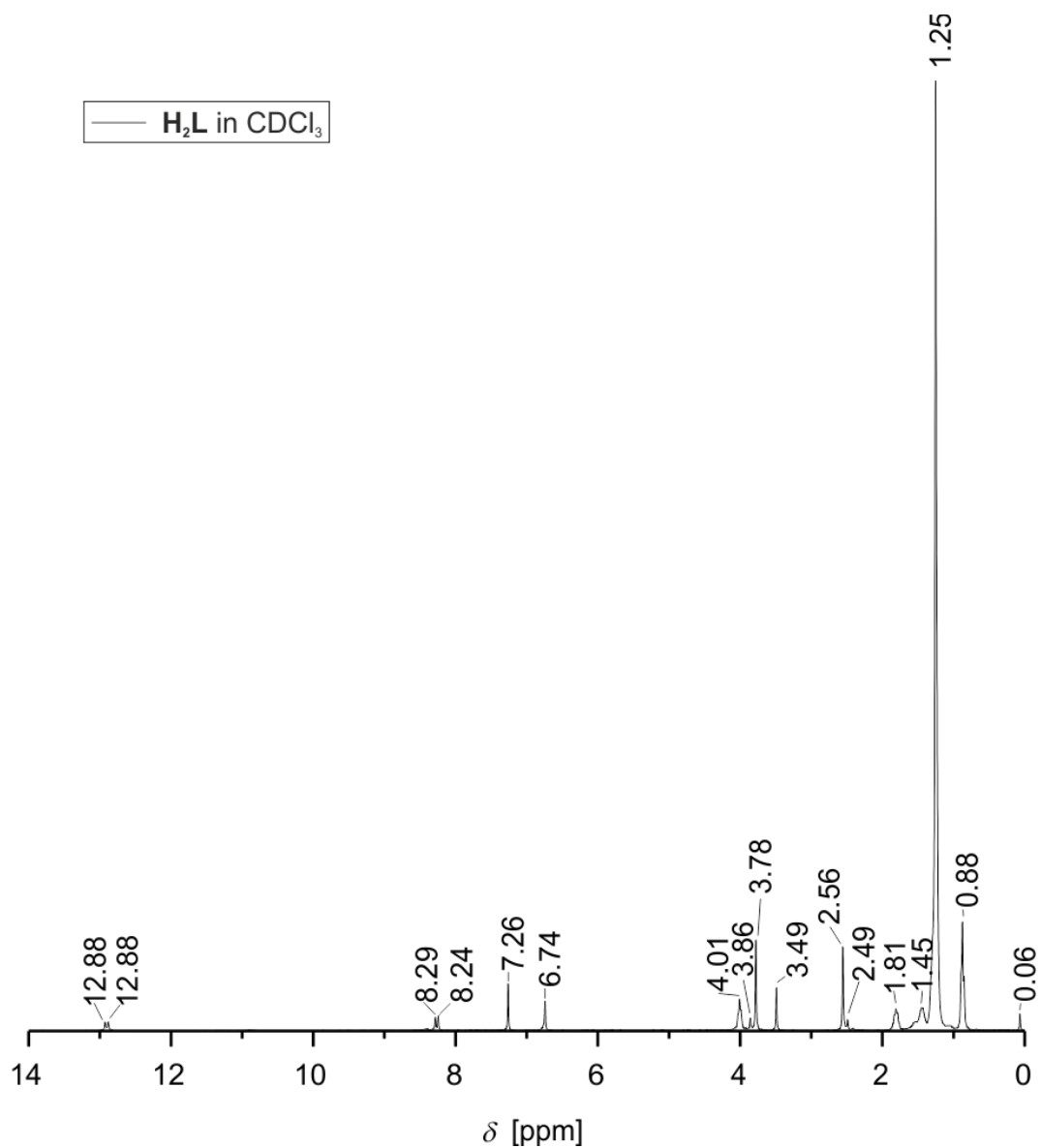


Figure S1: Complete $^1\text{H-NMR}$ spectra of H_2L in CDCl_3 .

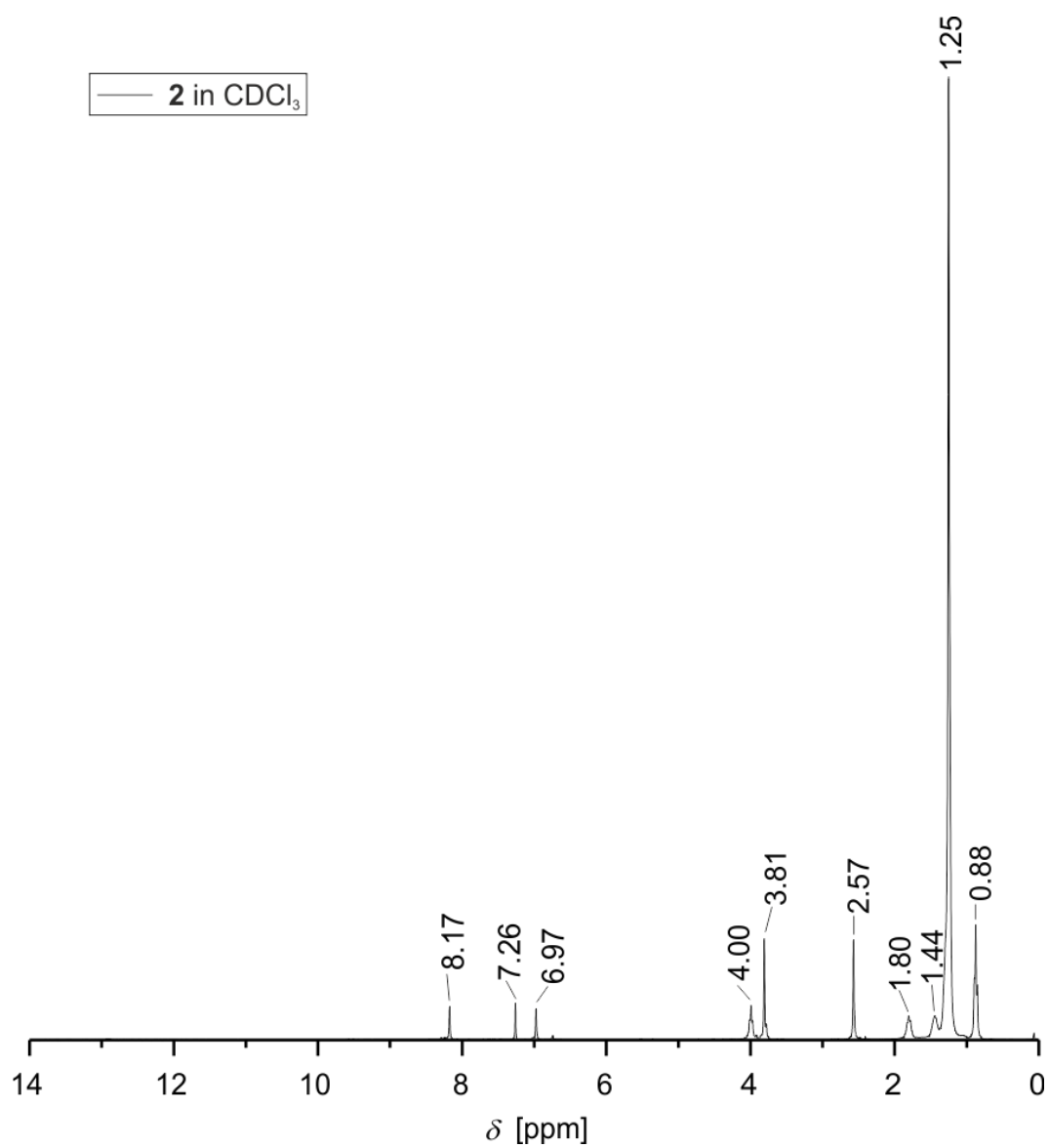


Figure S2: Complete ¹H-NMR spectra of **2** in CDCl₃.

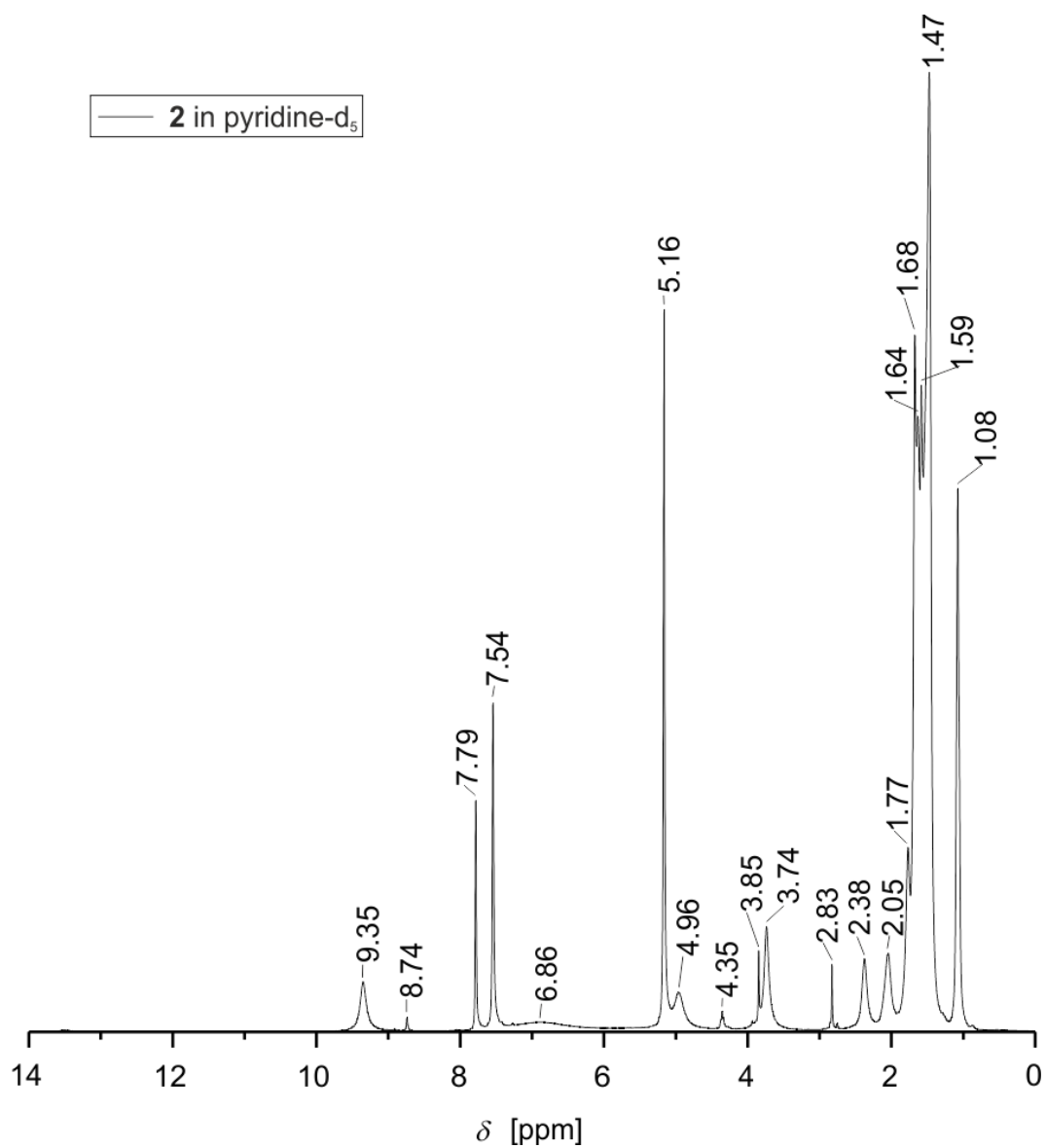


Figure S3: Complete ¹H-NMR spectra of 2 in pyridine-d₅.

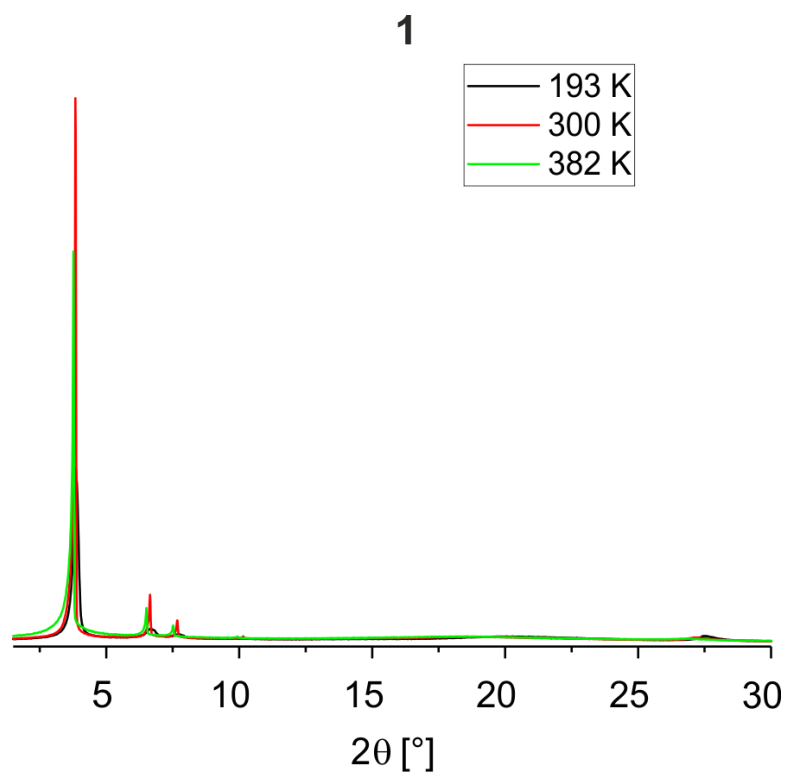


Figure S4: Complete PXRD spectra of **1** in the heating mode.

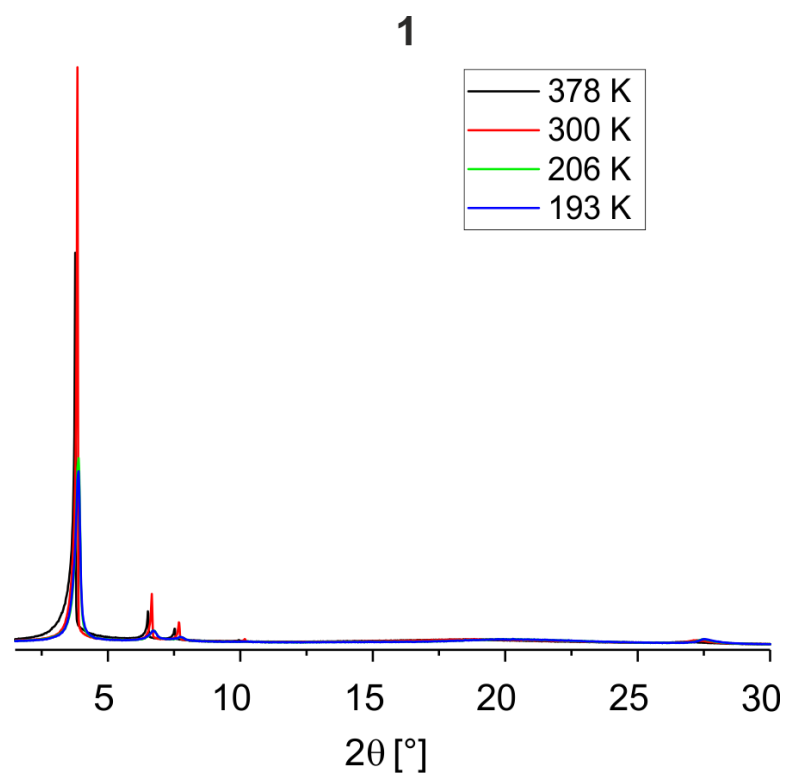


Figure S5: Complete PXRD spectra of **1** in the cooling mode.

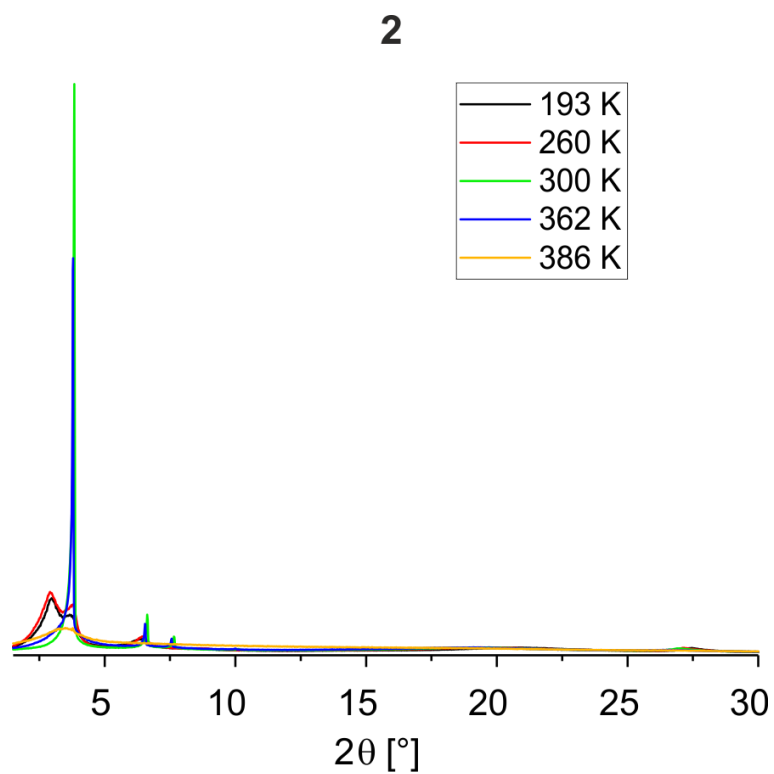


Figure S6: Complete PXRD spectra of **2** in the heating mode.

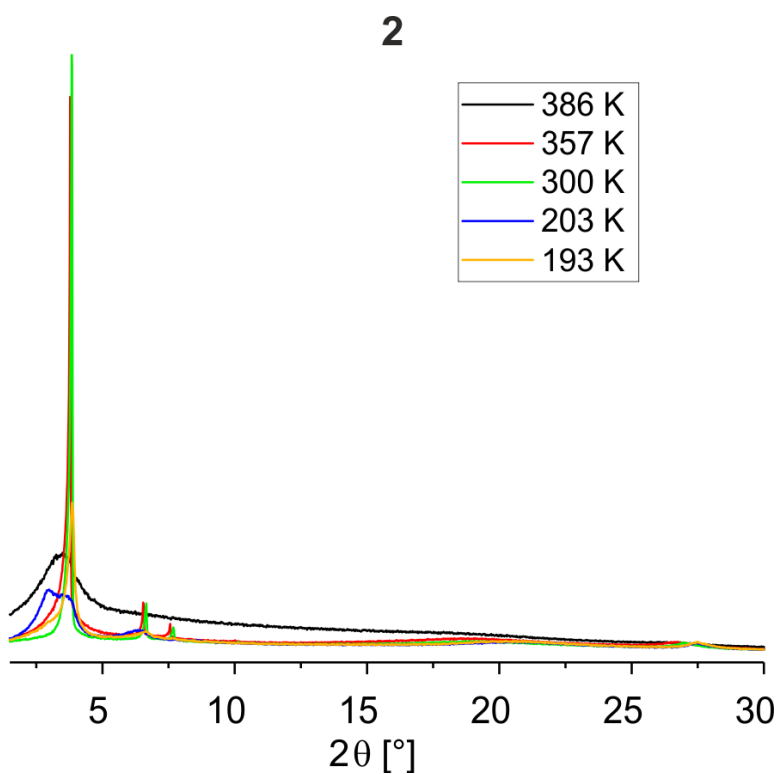


Figure S7: Complete PXRD spectra of **2** in the cooling mode.

8.8 References

- [1] a) M. A. Halcrow (Ed.) *Spin-crossover materials. Properties and applications*, Wiley, Chichester **2013**; b) B. Sieklucka, D. Pinkowicz, *Molecular Magnetic Materials: Concepts and Applications*, John Wiley and Sons Inc, Weinheim **2017**; c) P. Gütllich, H. A. Goodwin, *Spin Crossover in Transition Metal Compounds I-III, Vols. 234*, Springer, Berlin, Heidelberg **2004**; d) K. Senthil Kumar, M. Ruben, *Coord. Chem. Rev.* **2017**, *346*, 176–205; e) G. Molnár, L. Salmon, W. Nicolazzi, F. Terki, A. Bousseksou, *J. Mater. Chem. C* **2014**, *2*, 1360–1366; f) R. Nowak, E. A. Prasetyanto, L. de Cola, B. Bojer, R. Siegel, J. Senker, E. Rössler, B. Weber, *Chem. Commun.* **2017**, *53*, 971–974.
- [2] S. Thies, C. Bornholdt, F. Köhler, F. D. Sönnichsen, C. Näther, F. Tuzcek, R. Herges, *Chemistry* **2010**, *16*, 10074–10083.
- [3] M. Dommaschk, M. Peters, F. Gutzeit, C. Schütt, C. Näther, F. D. Sönnichsen, S. Tiwari, C. Riedel, S. Boretius, R. Herges, *J. Am. Chem. Soc.* **2015**, *137*, 7552–7555.
- [4] a) G. Heitmann, C. Schütt, J. Gröbner, L. Huber, R. Herges, *Dalton Trans.* **2016**, *45*, 11407–11412; b) G. Heitmann, C. Schütt, R. Herges, *Eur. J. Org. Chem.* **2016**, *2016*, 3817–3823.
- [5] a) A. Ruaudel-Teixier, A. Barraud, P. Coronel, O. Kahn, *Thin Solid Films* **1988**, *160*, 107–115; b) F. Armand, C. Badoux, P. Bonville, A. Ruaudel-Teixier, O. Kahn, *Langmuir* **1995**, *11*, 3467–3472; c) S. Hayami, N. Motokawa, A. Shuto, N. Masuhara, T. Someya, Y. Ogawa, K. Inoue, Y. Maeda, *Inorg. Chem.* **2007**, *46*, 1789–1794; d) H. Soyer, E. Dupart, C. J. Gómez-García, C. Mingotaud, P. Delhaès, *Adv. Mater.* **1999**, *11*, 382–384.
- [6] Y.-H. Luo, Q.-L. Liu, L.-J. Yang, Y. Sun, J.-W. Wang, C.-Q. You, B.-W. Sun, *J. Mater. Chem. C* **2016**, *4*, 8061–8069.
- [7] a) Y. Galyametdinov, V. Ksenofontov, A. Prosvirin, I. Ovchinnikov, G. Ivanova, P. Gütllich, W. Haase, *Angew. Chem. Int. Ed.* **2001**, *40*, 4269–4271; b) P. N. Martinho, C. J. Harding, H. Müller-Bunz, M. Albrecht, G. G. Morgan, *Eur. J. Inorg. Chem.* **2010**, 675–679.
- [8] Y. H. Lee, A. Ohta, Y. Yamamoto, Y. Komatsu, K. Kato, T. Shimizu, H. Shinoda, S. Hayami, *Polyhedron* **2011**, *30*, 3001–3005.
- [9] a) S. Hayami, R. Moriyama, A. Shuto, Y. Maeda, K. Ohta, K. Inoue, *Inorg. Chem.* **2007**, *46*, 7692–7694; b) N. Abdullah, N. L. M. Noor, A. R. Nordin, M. A. Halcrow, D. R. MacFarlane, M. A. Lazar, J. M. Pringle, D. W. Bruce, B. Donnio, B. Heinrich, *J. Mater. Chem. C* **2015**, *3*, 2491–2499.
- [10] a) C. Gandolfi, C. Moitzi, P. Schurtenberger, G. G. Morgan, M. Albrecht, *J. Am. Chem. Soc.* **2008**, *130*, 14434–14435; b) C. Gandolfi, G. G. Morgan, M. Albrecht, *Dalton Trans.* **2012**, *41*, 3726–3730.

- [11] J. N. Israelachvili, D. J. Mitchell, B. W. Ninham, *J. Chem. Soc., Faraday Trans. 2* **1976**, 72, 1525.
- [12] a) S. Schlamp, B. Weber, A. D. Naik, Y. Garcia, *Chem. Commun.* **2011**, 47, 7152–7154;
b) S. Schlamp, K. Dankhoff, B. Weber, *New J. Chem.* **2014**, 38, 1965–1972.
- [13] S. Schlamp, P. Thoma, B. Weber, *Eur. J. Inorg. Chem.* **2012**, 2759–2768.
- [14] S. Schlamp, P. Thoma, B. Weber, *Chem. Eur. J.* **2014**, 20, 6462–6473.
- [15] J. Weihermüller, S. Schlamp, W. Milius, F. Puchtler, J. Breu, P. Ramming, S. Hüttner, S. Agarwal, C. Göbel, M. Hund et al., *J. Mater. Chem. C* **2019**, 7, 1151–1163.
- [16] H. Kurz, C. Lochenie, K. G. Wagner, S. Schneider, M. Karg, B. Weber, *Chem. Eur. J.* **2018**, 24, 5100–5111.
- [17] C. Lochenie, S. Schlamp, A. P. Railliet, K. Robeyns, B. Weber, Y. Garcia, *CrystEngComm* **2014**, 16, 6213–6218.
- [18] E.-G. Jäger, *Z. Anorg. Allg. Chem.* **1967**, 349, 139–150.
- [19] C. Lochenie, K. G. Wagner, M. Karg, B. Weber, *J. Mater. Chem. C* **2015**, 3, 7925–7935.
- [20] L. Wolf, E.-G. Jäger, *Z. Anorg. Allg. Chem.* **1966**, 346, 76–91.
- [21] O. Kahn, *Molecular magnetism*, VCH, New York **1993**.
- [22] W. Bauer, T. Ossiander, B. Weber, *Z. Naturforsch. B* **2010**, 323–328.
- [23] H. G. O. Becker, *Organikum. Organisch-chemisches Grundpraktikum*, 19th ed., Barth, Ed. Dt. Verl. der Wiss., Leipzig, Berlin, Heidelberg **1993**.

9. Publications

- 1.) Johannes Weihermüller, Stephan Schlamp, Wolfgang Milius, Florian Puchtler, Josef Breu, Philipp Ramming, Sven Hüttner, Seema Agarwal, Christoph Göbel, Markus Hund, Georg Papastavrou, and Birgit Weber, “Amphiphilic iron(II) spin crossover coordination polymers: crystal structures and phase transition properties”, *J. Mater. Chem. C*, **2019**, 7, 1151–1163

- 2.) Johannes Weihermüller, Stephan Schlamp, Birger Dittrich, and Birgit Weber, “Kinetic Trapping Effects in Amphiphilic Iron(II) Spin Crossover Compounds”, *Inorg. Chem.*, **2019**, 58, 1278–1289

10. Conferences

- 22.-24.03.15 **Poster presentation:** “Synthese von Nanopartikeln aus tensidähnlichen Fe(III) und Cu(II) Komplexen”; 11. Koordinationschemie-Treffen, *Paderborn, Germany*
- 20.-21.06.16 **Poster presentation + flash talk:** “Long alkyl chain ligands for Fe²⁺ spin-crossover complexes with phase transition properties”; VW Eisen Symposium „Renaissance of Iron in Functional Materials“, *Hannover, Germany*
- 05.-07.03.17 **Poster presentation:** “Iron(II) spin-crossover complexes with long alkyl chains concerning their magnetic properties and their phase transition behaviour”; 13. Koordinationschemie-Treffen, *Potsdam, Germany*
- 26.-27.06.17 **Poster presentation + flash talk:** “Magnetic and phase transition studies on iron(II) spin crossover complexes with long alkyl chains”; Bordeaux Olivier Kahn Discussions „Spin-Crossover and Switchable Materials Discussions“, *Bordeaux, France*
- 31.08.17 **Oral presentation:** “Magnetic and phase transition studies on iron(II) spin crossover complexes with long alkyl chains”; 15. Mitteldeutsches Anorganiker-Nachwuchssymposium, *Leipzig, Germany*
- 11.-13.03.18 **Oral presentation:** “Magnetic and phase transition studies on iron(II) spin crossover complexes with long alkyl chains”; 14. Koordinationschemie-Treffen, *Heidelberg, Germany*
- 28.-30.07.18 **Oral presentation:** “Studies on iron(II) spin crossover complexes with long alkyl chains: Magnetic properties and phase transition behaviour”; 68th Conference of Japan Society of Coordination Chemistry, *Sendai, Japan*
- 30.07.-04.08.18 **Poster presentation:** “Studies on iron(II) spin crossover complexes with long alkyl chains: Magnetic properties and phase transition behaviour”; 43rd International Conference on Coordination Chemistry, *Sendai, Japan*

11. (Eidesstattliche) Versicherungen und Erklärungen

(§ 8 Satz 2 Nr. 3 PromO Fakultät)

Hiermit versichere ich eidesstattlich, dass ich die Arbeit selbstständig verfasst und keine anderen als die von mir angegebenen Quellen und Hilfsmittel benutzt habe (vgl. Art. 64 Abs. 1 Satz 6 BayHSchG).

(§ 8 Satz 2 Nr. 3 PromO Fakultät)

Hiermit erkläre ich, dass ich die Dissertation nicht bereits zur Erlangung eines akademischen Grades eingereicht habe und dass ich nicht bereits diese oder eine gleichartige Doktorprüfung endgültig nicht bestanden habe.

(§ 8 Satz 2 Nr. 4 PromO Fakultät)

Hiermit erkläre ich, dass ich Hilfe von gewerblichen Promotionsberatern bzw. –vermittlern oder ähnlichen Dienstleistern weder bisher in Anspruch genommen habe noch künftig in Anspruch nehmen werde.

(§ 8 Satz 2 Nr. 7 PromO Fakultät)

Hiermit erkläre ich mein Einverständnis, dass die elektronische Fassung der Dissertation unter Wahrung meiner Urheberrechte und des Datenschutzes einer gesonderten Überprüfung unterzogen werden kann.

(§ 8 Satz 2 Nr. 8 PromO Fakultät)

Hiermit erkläre ich mein Einverständnis, dass bei Verdacht wissenschaftlichen Fehlverhaltens Ermittlungen durch universitätsinterne Organe der wissenschaftlichen Selbstkontrolle stattfinden können.

.....
Ort, Datum, Unterschrift